ALMA MATER STUDIORUM
UNIVERSITÀ DI BOLOGNA

DOTTORATO DI RICERCA IN ASTROFISICA

CICLO 36

Settore Concorsuale: 02/C1 - Astronomia, Astrofisica, Fisica della Terra e dei Pianeti

Settore Scientifico Disciplinare: FIS/05 - Astronomia e Astrofisica

The physics of blazar jets in the context of multi-wavelength and multi-messenger astronomy

Presentata da: **Cristina Nanci**

Coordinatore Dottorato

Prof. **Andrea Miglio**

Supervisore

Dr. **Roberta Zanin**

Co-Supervisore

Dr. **Marcello Giroletti**

Esame finale Anno 2024

This Thesis work was done as part of the research activity of the Istituto di Radioastronomia - Istituto Nazionale di Astrofisica (INAF) in Bologna.

Abstract

Blazars represent a class of active galactic nuclei with powerful jets oriented close to our line of sight. The intense and variable electromagnetic emission observed from blazars is the ultimate manifestation of the accelerated plasma. These accelerated particles can interact with surrounding matter and radiation, generating neutrinos and gamma rays. Recently, the study of blazars has gained significant importance in the realm of multi-messenger astrophysics, the field that explores cosmic phenomena through the combined analysis of different types of signals, including electromagnetic waves, cosmic rays, neutrinos, and gravitational waves. Indeed, the extreme conditions reached in blazar jets make them capable of producing both neutrinos and radiation across the electromagnetic spectrum, from radio waves to gamma rays. Neutrinos, being neutral and nearly massless, provide a unique way to probe the most energetic astrophysical processes, while multi-wavelength (MWL) observations carry information about the extreme conditions in blazar jets and the emission mechanisms in action. In particular, the unique capabilities of very-long-baseline interferometry (VLBI) and very high energy (VHE, $E > 100$ GeV) observations (e.g., with the Major Atmospheric Gamma-ray Imaging Cherenkov, MAGIC, telescopes) allow a privileged view in the compact regions of blazar jets: VLBI provides images of parsec scale regions of these sources; VHE observations through variability analysis probe even more compact emission regions.

The theoretical expectations on blazar jets as neutrino sources were observationally confirmed when the gamma-ray blazar TXS 0506+056 was detected in spatial coincidence with the IceCube-170922A (IC 170922A) neutrino event, highlighting one of the most significant connections between high-energy neutrinos and astrophysical sources to date. Once the first milestone has been reached, now it is crucial to provide more observational insights to support or discard the neutrino-blazar connection hypothesis. To delve into potential blazar counterparts of high-energy neutrinos, this Thesis focuses on the parsec-scale regions of gamma-ray blazars spatially coinciding with neutrino detections from the IceCube Neutrino Observatory. The project aims to explore distinctive radio properties related to neutrino production, such as coincident radio flares or features in jet morphology like limb brightening and transverse structures which have been observed in TXS 0506+056. The study involved detailed multi-frequency VLBI follow-up observations of candidate counterparts associated with four high-energy neutrino events detected by IceCube: IC 190704A, IC 200109A, IC 201021A and IC 201114A. We identified and examined ten potential neutrino-emitting blazars, with emphasis on five of them because of the gamma-ray association, similar to TXS 0506+056. We investigated their radio characteristics shortly after neutrino arrival, comparing them with archival VLBI observations and low-frequency radio data. The results were discussed in the context of previous statistical works and studies on the case of TXS 0506+056. Two of the sources, PKS 1725+123 and TXS 1100+122, show hints of an elevated state of activity emerging as promising neutrino source candidates. While our results to date can not establish a robust connection between the radio activity state and neutrino arrival for the other sources, they stress the need for more extensive VLBI and MWL follow-up observations of neutrino events. Such efforts are crucial to advancing our understanding of neutrino production mechanisms in astrophysical sources.

A crucial tool for unravelling the fundamental processes at play in blazar jets, whether they are connected to neutrino emission or not, is the investigation of their broadband Spectral Energy Distribution (SED). Blazar SED is interpreted as synchrotron radiation in the low-energy regime and radiation produced through inverse Compton scattering (leptonic models) or hadronic processes at high energy. The latter processes are also involved in the neutrino production. Leptonic and hadronic models offer different perspectives, with SED modelling playing a pivotal role in discerning the microphysics of the system. To this purpose, the MAGIC Collaboration coordinates long-term monitoring of blazars in collaboration with lower energy facilities. The blazar 1ES1959+650 serves as an ideal laboratory for the study of the MWL behaviour of blazars, due to its brightness at all wavelengths and peculiar flare episodes. During the last few years, the source has experienced its lowest state ever reached, mainly at VHE. Yet it remained significantly detected on hour time scales by MAGIC. In this Thesis, we discussed the MWL spectral features and variability patterns during this low-state period, with a focus on the VHE data. Taking into account the findings on the VHE and MWL variability and spectral properties, we modelled the broadband SED of the source under the assumption of a leptonic scenario. In particular, to study the source evolution during the 2020-2022 period, we focused on three different states, a high and low state at VHE and a high state in the optical band, one at the beginning, the end and the middle of the period, respectively. We found that the leptonic explanation satisfactorily describes the data during this low-state period. We discussed the differences in the model parameters among the three days of the 2020-2022 low-state period and compared them with past flaring states. The MWL monitoring of 1ES1959+650 is ongoing and the view of the quiescent state that we provided will be useful as a baseline for the investigation of the source evolution with future new data.

This doctoral project aims to enhance our comprehension of particle acceleration in astrophysical settings, with a specific focus on blazars and their potential role as sources of high-energy neutrinos. The research takes advantage of the parallel and complementary insights derived from radio and gamma-ray observations, serving as indicators of relativistic particle acceleration in extreme cosmic environments. Looking ahead, both radio and gamma-ray astronomy fields are experiencing remarkable and innovative developments. The advent of the Square Kilometre Array Observatory (SKAO) in the radio astronomy field and the ongoing construction of the Cherenkov Telescope Array Observatory (CTAO) in the gamma-ray astronomy field promise significant advancements. In this context, this Thesis provides an overview of the use of radio and gamma-ray observations in the study of cosmic accelerators, utilizing data from existing facilities and anticipating the improvements that future instruments will bring to this field.

The Thesis starts with an introduction to blazar physics, discussing blazar characteristics, classification, hypotheses on emission mechanisms, and the radio and gamma-ray view of these sources. It is then divided into two independent parts.

Part I describes the radio astronomy approach for studying acceleration processes in blazars, starting with interferometry and data analysis techniques. The results from radio observations of the sample of blazar candidate neutrino emitters are then presented.

Part II addresses the gamma-ray astronomy approach for investigating blazar emission mechanisms. The observing technique and data analysis are illustrated, followed by a description of current and future instruments. The study of the blazar 1ES 1959+650 represents the application of the MWL approach (driven by the observations in the gamma-ray band).

The conclusions close the Thesis with a summary of the results and considerations for future instrument improvements and scientific outputs.

Contents

Chapter 1

Multi-Messenger astronomy

At the basis of the study of the Universe, photons have always served as carriers of astrophysical information. However, cosmic rays (i.e. atomic nuclei accelerated to close to the speed of light), neutrinos, and gravitational waves can help tell a more complete story of the Universe. In recent decades, multi-messenger (MM) astronomy has emerged as a compelling approach to studying various astrophysical events. The effectiveness of utilizing a broad observational tool set, consisting of different messengers, to understand diverse astrophysical phenomena is nowadays well established (e.g., Mészáros et al. 2019, for a review). In some cases, MM observations have helped validate previous theoretical predictions, like in the case of the groundbreaking discovery of gravitational waves from binary black hole mergers which marked a pivotal moment in this field (Abbott et al. 2016b).

The power of MM astronomy relies on a collaborative effort of various branches of astrophysics and particle astronomy. Task forces are entirely dedicated to the coordination of joint activities among different facilities, from the scheduling of almost simultaneous observations to scientific publications. Online channels like the Astronomer's Telegram (ATel)[1] and Gamma-Ray Burst (GRB) Coordinates Network (GCN)[2] are crucial to shed light on the processes occurring in astrophysical environments.

While mainly based on multi-wavelength (MWL) observations, this Thesis is closely connected to the production of messengers beyond photons. Within the framework of MM astronomy, it serves as a test for the approach involving not only the conventional tool of astronomers, i.e. photons, but also neutrinos and cosmic rays. This Chapter provides an introductory overview of the connection between the three messengers.

1.1 Photons

The purpose of observational astronomy is to collect information about astrophysical objects to understand the processes governing the behaviour of those objects. The recording of photons at all the wavelengths of the electromagnetic spectrum is indeed one of the most powerful tools humanity has to discover and understand the observable Universe.

The electromagnetic spectrum spans a range of frequencies, (or wavelengths, or photon energies). It covers electromagnetic waves with frequencies below 1 Hz to above 10^{27} Hz, corresponding to wavelengths from thousands of kilometres down to fractions of the size of an atomic nucleus. The spectrum is divided into bands, ranging from radio waves and microwaves

[1] https://www.astronomerstelegram.org/

[2] GRB are brief and extremely energetic cosmic explosions, emitting intense bursts of gamma-ray radiation, typically lasting from sub seconds to a few minutes. Despite the name, the GCN archive collects alerts on all kinds of transients, not only on GRB. The archive can be consulted at https://gcn.gsfc.nasa.gov/gcn/gcn3_archive.html.

to infrared, visible light, ultraviolet, X-rays, and gamma rays. Each band requires a different observing technique, depending on the behaviour of the light at that wavelength.

The medium traversed significantly influences photon propagation through absorption or scattering processes. Moreover, photons must pass through the Earth's atmosphere and ionosphere before reaching the ground. Only photons with a wavelength in the range between 3000 Å and 8000 Å (visible window) and the ones with a wavelength in the range from $\sim$ 1 cm to $\sim$ 10 m (radio window) can cross the Earth's atmosphere (see Fig. 1.1). Outside these windows, the only way to collect information is by minimizing the amount of atmosphere between the observer and the source. This is achieved by operating at high altitudes, like on mountains or using balloons flying the upper layers of the atmosphere. Satellites allow observations even beyond Earth's atmosphere. The ultraviolet, far infrared, X-ray, and gamma-ray band windows were opened only in the 1970s thanks to the diffusion of satellites. Instead, the radio band began to be explored as early as the 1930s.

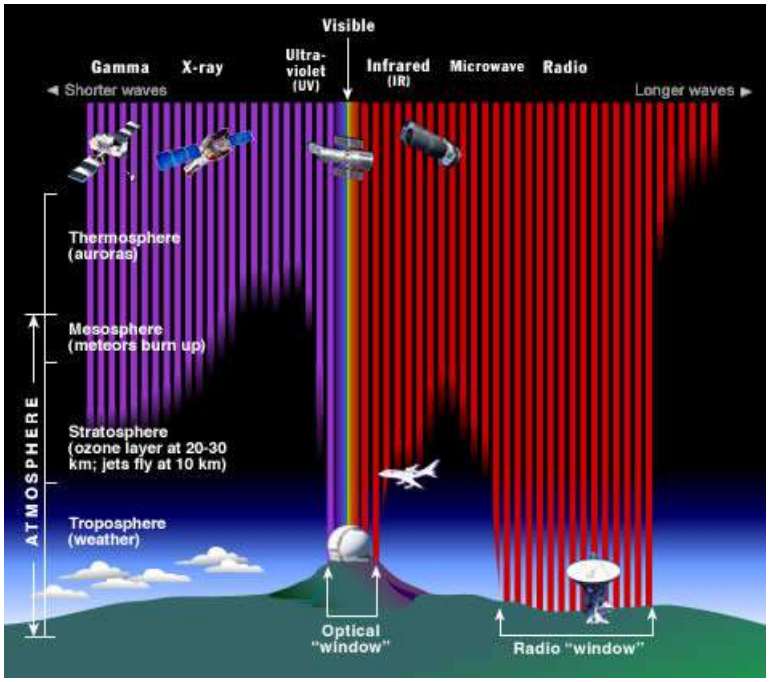

Figure 1.1: The figure shows a schematic representation of the electromagnetic spectrum, illustrating the division in bands and indicating the atmospheric layers that photons within each band can penetrate. The visible window (3000 Å to 8000 Å) and the radio window (1 cm to 10 m) are the only atmosphere windows allowing photons to pass through. Observing outside these windows often requires high-altitude platforms such as satellites, balloons, or mountain-based observatories to minimize atmospheric interference. Credit: STScI/JHU/NASA.

The type of photons produced at each band also heavily depends on the physical conditions of the emission region, such as temperature, pressure, motion, magnetic field strength, etc. Consequently, each phenomenon tends to produce energy primarily at certain wavelengths, depending on the environmental condition. Observing at specific wavelengths means applying a filter to certain objects and phenomena, and studying an object in a single frequency band is therefore limiting. A MWL approach, i.e. a connection between information collected at several wavelengths, is fundamental for a more complete understanding of astrophysical phenomena.

In particular, radio and gamma-ray observations provide two complementary eyes on the *non-thermal* Universe. We refer to non-thermal processes when the particle distribution is not Maxwellian and therefore it is not possible to define a temperature for the emitting system. Non-

thermal processes include, e.g., *synchrotron emission* arising from charged particles spiralling around magnetic field lines at relativistic speeds, and *Compton scatterings* involving inelastic collisions between electrons and photons (Rybicki & Lightman 1986). On the other hand, thermal radiation is characterized by a well-defined emission spectrum, known as the *blackbody spectrum*, which is, for example, a good approximation of the spectrum of ordinary stars. It is derived from Planck's law resulting from quantum mechanical considerations. Non-thermal phenomena are instead all those characterized by an emission spectrum different from that of the thermal black body. For instance, the non-thermal spectra in several sources can be well described by power laws.

Radio and gamma-ray observations sample these kinds of spectra, allowing us to identify and study sources where non-thermal components, such as relativistic electrons and magnetic fields, are present. The project presented in this Thesis is based on radio and gamma-ray observations.

1.2 Cosmic rays

In 1912, Victor Hess discovered that ionization levels of the Earth's atmosphere increased with altitude. Then, he postulated the existence of charged particles of cosmic origin constantly colliding with the Earth's atmosphere, the cosmic rays. According to his theory, this shelling was the source of the highest levels of ionization. Cosmic rays are particles with the highest energy observed in the Universe, surpassing the capabilities of all existing particle accelerators on Earth by over a million times.

Approximately 80% of the cosmic ray composition is represented by protons and approximately 15% by helium nuclei. Additionally, heavier nuclei have been observed. Electrons and positrons contribute approximately 1% to the total particle population constituting cosmic rays. Since Hess's discovery, the cosmic ray spectrum has been studied across about 12 orders of magnitude in energy. At lower energies, this was done by employing balloons and satellites. At higher energies, where the flux is lower, large arrays of air shower detectors deployed on Earth's surface have been used; more details on this detection technique are given in Chapter 1.

The observed cosmic ray spectrum follows a power law function as shown in Fig. 1.2. There are two break points. At around 10^{15} eV is the *knee*, and at around 10^{18} eV the *ankle*. The spectral index of the power law goes from around 2.67 at low energies, below the knee, to 3.10 for intermediate energies, above the knee, and to 2.75 for high energies, above the ankle.

A widely accepted hypothesis, proposed by Fermi (1949), suggests that cosmic rays undergo acceleration by repeatedly crossing shock fronts. The magnetic field strength and the size of the acceleration regions determine the maximum energy at which a cosmic ray can be accelerated by an astrophysical source according to the Hillas criterion. The gyroradius of the accelerated particle must not exceed the physical dimensions of the acceleration region, to ensure the particle's confinement within that region (Hillas 1984). For a particle with charge Z accelerated within a region of radius R and containing a tangled magnetic field of strength B, the maximum energy, $E_{\rm max}$, satisfying the Hillas criterion is given by:

$$E_{\rm max} = Z \frac{B}{30\ {\rm G}} \frac{R}{10^{15}{\rm cm}} 10^{19}\ {\rm eV}. \tag{1.1}$$

While at lower energies, solar cosmic rays dominate the observed flux, supernova remnants are considered one of the primary sources of Galactic cosmic rays at energies above 10^9 eV up to 10^{15} eV, below the ankle. Cosmic rays, being electrically charged, experience deflection due to magnetic fields, making it challenging to precisely determine their origin. The highest-energy cosmic ray particles – so-called Ultra High Energy Cosmic Rays (UHECRs), with $E > 10^{18}$ eV – are generally thought to originate in extragalactic sources like jets of Active Galactic Nuclei (AGN) or GRB. AGN are extremely energetic and compact regions at the centers of

galaxies, powered by accretion onto supermassive black holes, exhibiting intense emission across the electromagnetic spectrum.

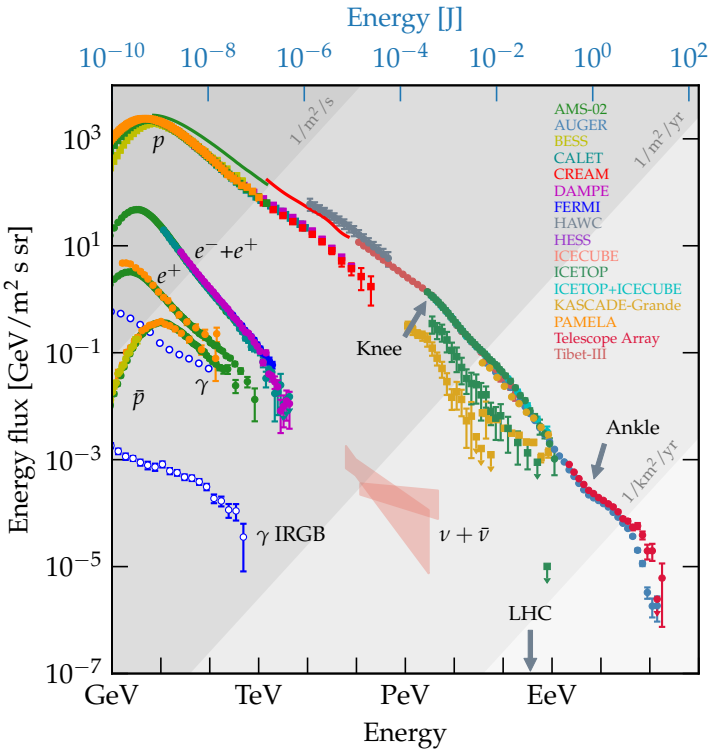

Figure 1.2: The figure shows the cosmic ray spectrum built with observational points from several facilities. The distribution follows a twice-broken power law. The first break-point is the *knee* around 10^{16} eV and the second, the *ankle*, is around 10^{18} eV. The plot also shows the distribution of gamma-ray photons in the GeV regime and the neutrinos flux. The grey diagonal areas represent the detection rates of particles in each energy range: at low energies, the rate is 1 particle $m^{-2}s^{-1}$, at intermediate energies, 1 particle $m^{-2}yr^{-1}$ and at high energies, 1 particle $km^{-2}yr^{-1}$. From Evoli (2020).

1.3 Neutrinos

Neutrinos are extremely elusive particles. Electrically neutral and with an extremely small mass, they are generally emitted as byproducts of nuclear interactions. In particular, high-energy neutrinos can be produced following interactions of cosmic rays with radiation (photo-meson interactions) or matter (proton-proton or proton-nucleus interactions).

Photo-meson interactions occur in astrophysical environments. Here the relativistic protons interact with the ambient photon field. This can originate intrinsically within the emission region of gamma rays or externally to the gamma-ray production zone. The protons-photons interaction leads to the generation charged (π^+, π^-) and neutral (π^0) pions. Neutral pions then decay giving rise to two gamma-ray photons. This process is described with:

$$p(\bar{p}) + \gamma \rightarrow \Delta^+ \rightarrow \begin{cases} p + \pi^0 \\ n + \pi^{\pm} \end{cases} \tag{1.2}$$

$$\pi^0 \rightarrow \gamma + \gamma$$

In parallel, charged pions and muons ($\mu^{\pm}$) from photo-meson interactions decay in neutrinos and anti-neutrinos of different flavours:

$$\begin{aligned}
\pi^+ &\rightarrow \mu^+ + \nu_\mu \\
\pi^- &\rightarrow \mu^- + \overline{\nu_\mu} \\
\mu^+ &\rightarrow e^+ + \nu_e + \overline{\nu_\mu} \\
\mu^- &\rightarrow e^- + \overline{\nu_e} + \nu_\mu
\end{aligned} \tag{1.3}$$

Consequently, in scenarios involving hadronic emission, the emission of gamma rays through the decay of neutral pions (π^0) is always accompanied by the production of neutrinos.

In proton-proton interactions, inelastic proton-proton collisions give rise to radiation and secondary particles, among which neutrinos. The matter interacting with relativistic protons can be provided by the accelerating region or the interstellar medium. Similar to the photo-meson interaction scenario, proton-proton interactions also generate neutrinos through charged pion decay, along with gamma rays produced from the decay of neutral pions.

Neutrino production processes are then intrinsically connected with the presence of hadronic particles. Opposite to photons that are absorbed or scattered during their paths to the Earth, neutrinos are very weakly interacting with matter so they can easily traverse dense environments. Moreover, in contrast to cosmic rays that are deflected by magnetic fields, the lack of charge of neutrinos and non-interaction with cosmic magnetic fields allow them to be traced back to their sources, providing a direct way to identify sites of hadronic interactions and possibly the origin of cosmic rays. For these reasons, neutrinos are often referred to as the smoking gun for pinpointing the particle acceleration sites.

1.3.1 Neutrino detectors

Neutrino interactions with matter are characterized by very small cross-sections, which significantly challenge their detection. In addition, the predicted high-energy neutrino fluxes from astrophysical sources are very low. To face these difficulties, large volumes filled with transparent materials, such as water or ice, are used as detectors. The vast ice platforms available in Antarctica and water bodies covering a large part of the Earth's surface can accommodate these requirements.

Neutrino detectors exploit the Cherenkov light detection technique. They identify neutrinos indirectly, by employing secondary particles generated via the interaction of neutrinos with the medium – ice or water. Secondary particles moving with a speed higher than the speed of light in the medium produce Cherenkov photons that are measured at the optical modules constituting the detectors. Exploiting the Cherenkov photons for measuring the energy and arrival direction of primary particles is also the basic principle for the Imaging Atmospheric Cherenkov Telescope (IACT) functioning. This technique will be described in detail in Chapter 1.

Among the most important neutrino detectors, the Baikal neutrino telescope, located in Lake Baikal in Siberia and operational since 1993, is the first successful project using natural water resources for neutrino detection. Other detectors exploiting water bodies are Neutrino Ettore Majorana Observatory (NEMO), Neutrino Extended Submarine Telescope with Oceanographic Research (NESTOR) and Astronomy with a Neutrino Telescope and Abyss environmental RESearch project (ANTARES), in the Mediterranean Sea. Here, soon, it will be fully operative the cutting-edge water-based neutrino telescope, the Cubic Kilometre Neutrino Telescope (KM3NeT)[3]. This instrument under construction will be a one-cubic-kilometre neutrino detector that aims to leverage the experience gained from operating existing detectors.

An example of an ice-based detector is Antarctic Muon And Neutrino Detector Array-II (AMANDA-II), which consists of multiple strings containing optical modules which convert

[3]https://www.km3net.org/

Cherenkov photons into electric pulses. The improved version of the AMANDA technology is represented by the IceCube neutrino detector, the largest neutrino telescope now existent on Earth. Located near the Amundsen-Scott South Pole Station, IceCube is a revolutionary particle detector constructed in the Antarctic ice. The Cherenkov light produced by the interaction of neutrinos with the ice atoms is detected by the over 5 thousand optical modules located down to 2500 meters under the ice surface. The optical modules and the associated electronics are located in vertical strings, frozen into 86 boreholes. The whole observatory occupies a volume of one cubic kilometre (Fig. 1.3).

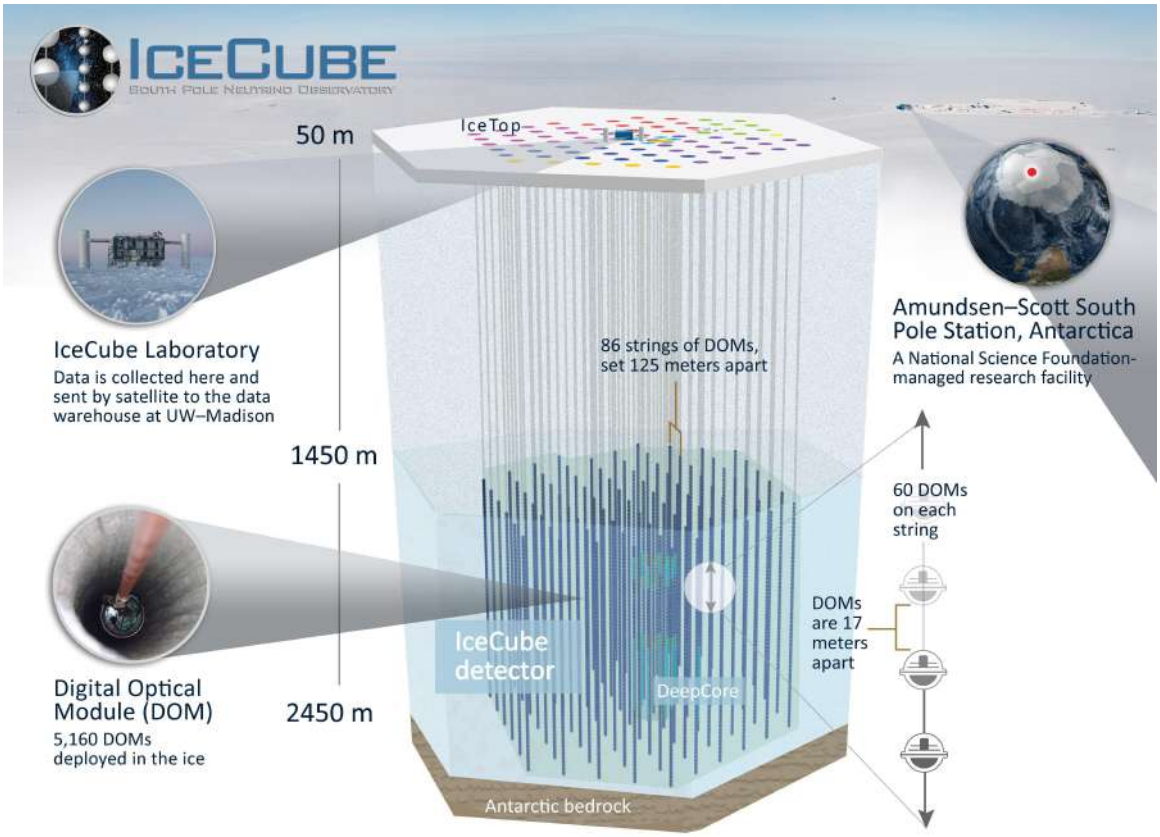

Figure 1.3: The IceCube neutrino detector, installed in the ice of Antarctica is part of the Amundsen-Scott South Pole Station. Covering a volume of one cubic kilometre, this observatory captures neutrino imprints from the sky by using the Antarctic ice. The array of optical modules is placed within the ice down to 2500 meters. The laboratory is on top of the ice sheet. More details can be found in the IceCube website from which this image has been taken.

The IceCube sensors capture the Cherenkov light, which is then digitized and transmitted to computers in the IceCube Lab on the surface, where it is transformed into light patterns, revealing the direction and energy of muons and neutrinos. IceCube offers improved angular resolution, better than 1 degree, and innovative analysis techniques have extended its field of view (FoV) to include the southern hemisphere from declination $-50°$ to $+85°$ in the PeV to EeV energy range.

IceCube's sensitivity detection depends not only on neutrino energy but also on declination. The location of the observatory in Antarctica leads to a decrease in the IceCube sensitivity above $\sim$ 100 TeV, due to the Earth's opacity to neutrinos with these energies. Indeed, the northern hemisphere is restricted to the detection of neutrinos in the TeV/sub-PeV energy range, with higher-energy neutrinos preferentially detected close to the celestial horizon. Conversely,

neutrinos originating from the southern sky can be detected without traversing the Earth. As a result, in the southern hemisphere, IceCube is sensitive to extremely high energies, achieving its greatest sensitivity at the celestial horizon (e.g., Bustamante & Connolly 2019). The drawback in the latter case is the contribution from muons and atmospheric neutrinos which is higher than the case of the northern sky. The University of Wisconsin–Madison leads the IceCube project, overseeing data collection, while the international IceCube Collaboration, comprising over 40 institutions worldwide, drives the scientific research program.

1.3.2 Neutrino sources

The Sun and supernovae were the first celestial bodies which astrophysical neutrinos have been associated with. The neutrinos from these sources are in the MeV energy range. In the 1960s, neutrinos from solar nuclear reactions were detected by Raymond Davis who was awarded the Nobel Prize in Physics in 2002 for this discovery. Neutrinos from the core-collapse supernova SN 1987A were detected by underground experiments, Kamiokande, Baksan, and Irvine-Michigan-Brookhaven (Burrows & Lattimer 1987), preceding the optical brightening of the supernova by two hours.

In 2013, the IceCube experiment reported the measurement of a diffuse flux of astrophysical neutrinos in the TeV-PeV range, with a power law-shaped energy spectrum (Aartsen et al. 2013). Despite over 275 high energy events[4] detected from 2011 to 2020 (Abbasi et al. 2023), only very few associations with known astrophysical sources or the Galactic plane were established.

Potential extragalactic neutrino sources include AGN (e.g., Kalashev et al. 2015) and AGN outflows (Padovani et al. 2018), star-forming and starburst galaxies (e.g., Tamborra et al. 2014), propagating cosmic rays protons emitted by distant AGN (e.g., Essey et al. 2010), galaxy clusters (e.g., Zandanel & Ando 2014), GRB (e.g., Petropoulou et al. 2014), tidal disruption events (e.g., Mohan et al. 2022).

1.4 Main results and open questions of the multi-messenger astronomy

Several works have shown that cosmic ray, gamma-ray, and neutrino backgrounds are interconnected (e.g., Halzen 2021; Halzen & Kheirandish 2019; Fang & Murase 2018). The quest for a unified origin of neutrinos, cosmic rays, and photons has led to the exploration of models that disentangle the interactions between the three messengers. After about two years of data collection, which started in 2010, milestone discoveries for neutrino astronomy were announced by the IceCube Collaboration. Evidence of PeV neutrinos has been reported for the first time in 2013 (Aartsen et al. 2013), followed, a few months later, by the finding of a total of 28 neutrinos with energies ranging from 30 to 1200 TeV (IceCube Collaboration 2013). Given the isotropic distribution of this neutrino flux across the sky, extragalactic sources emerge as the primary natural candidates for electromagnetic counterparts.

Among various hypotheses, blazars, a subset of AGN – that will be extensively presented in the next Chapter–, stand out as cosmic laboratories for neutrino production. Their powerful jets launched from the vicinity of the supermassive black holes are expected to be efficient particle accelerators and thus ideal sites for high energy cosmic ray protons and neutrino production (e.g., Mannheim 1993; Halzen & Hooper 2002). As we have seen in previous sections, the hadronic processes leading to neutrino emission also produce gamma rays. The extragalactic GeV-TeV sky is predominantly composed of blazar objects (e.g., Ackermann et al. 2015, and see next

[4]Throughout the Thesis, we will use the terms *neutrino events* and *events* interchangeably when discussing the detection of neutrinos.

Chapter), then they have been looked at as potential major contributors to the astrophysical neutrino flux.

The first confirmed association between a high-energy neutrino and an astrophysical source occurred in 2017 when the IceCube Collaboration reported the detection of a 290 TeV neutrino, IC 170922A, associated with the flare from the gamma-ray blazar TXS 0506+056 with a statistical significance of 3σ (IceCube Collaboration et al. 2018a). TXS 0506+056 was detected within the event error region, of about 1°, in a MWL flaring state by follow-up observations. The association was further corroborated by neutrino excess from the position of this source before the IC 170922A event (IceCube Collaboration et al. 2018b). This discovery established blazars as potential IceCube neutrino sources, confirming the theoretical expectation and providing a unique opportunity to investigate neutrino emission mechanisms in these systems through MWL observational data (e.g., Keivani et al. 2018).

Recently, the analysis of IceCube archival data from 2011 to 2020 using enhanced neutrino reconstruction techniques and refined data calibration procedures, provided a new noteworthy outcome. Individual examination of 110 pre-selected gamma-ray sources identified an excess of about 79 neutrinos spatially coincident with the starburst galaxy NGC 1068 at a significance level of 4.2σ (IceCube Collaboration et al. 2022). This association was previously hinted at in similar statistical studies with less refined analysis techniques, the significance of the association was found to be below the 3σ level. The new observed evidence aligns with phenomenological predictions of this source as a probable neutrino emitter (e.g., Inoue et al. 2020; Murase et al. 2020a). This signature of hadronic particle acceleration in NGC 1068 reveals the presence of a population of neutrino sources characterized by obscured gamma-ray emission.

Thus, both TXS 0506+056 and the active galaxy NGC 1068 emerge as convincing sources of high-energy neutrinos, each potentially with distinct emission mechanisms. However, despite these remarkable results, the low neutrino detection rate, the high atmospheric background contamination, and the limited angular resolution of current gamma-ray and neutrino detectors, typically at the sub-degree or degree scale, do not allow for frequent and unequivocal identification of neutrino gamma-ray counterparts. The number of neutrino alerts from IceCube varies over time depending on various factors. No more than tens of alerts per year are circulated and not all of them are well spatially constrained and/or have a high chance of astrophysical origin[5]. The number of alerts, however, increases by improving the sensitivity of the instrument, extending the observation time, and improving data analysis capabilities. Nevertheless, with a MWL approach based on follow-up observations and identification of best neutrino sources, it will be possible to shed light on the origin of astrophysical neutrino despite the observational complexities.

Most of the difficulties of the neutrino-electromagnetic connection are shared by another branch of MM astronomy that has been developing with a similar process: the one based on gravitational waves. According to the General Relativity Theory, accelerated motion of gravitating masses generates gravitational waves, ripples in space-time propagating at the speed of light. These waves are detected using Michelson interferometers, measuring the distance between masses with laser beams. As gravitational waves pass through Earth, they distort space-time, altering observed distances. Detection relies on the matched filtering technique, using a template to identify signals in data drowned in noise. Current interferometer limitations and theoretical uncertainties constrain detection rates. Detected waves mostly come from mergers of two compact objects in binary systems. The chirp signal, increasing in frequency and strength as objects approach, depends on binary properties. Parameters include intrinsic factors like initial masses and extrinsic factors like wave event location and orientation. Almost 100 years after

[5]The IceCube event classification based on the likelihood of the event of being astrophysical origin will be discussed in Chapter 2.

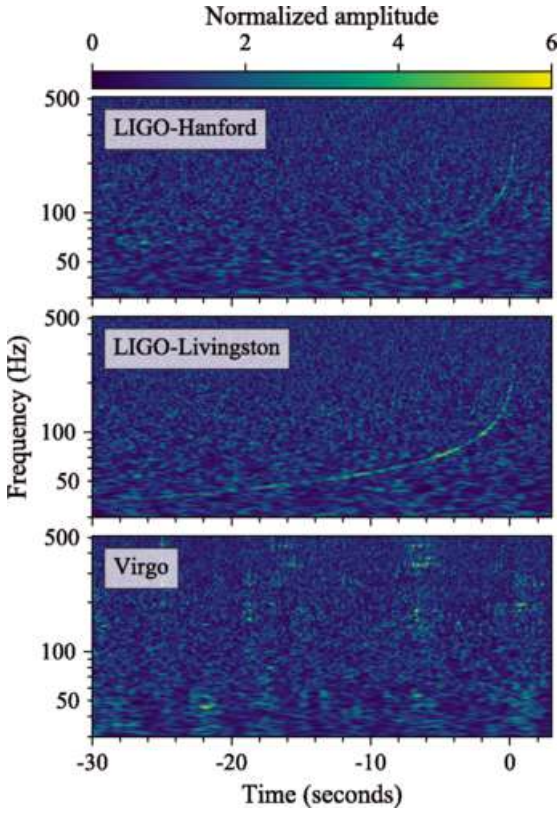

Figure 1.4: Time vs frequency representations of the gravitational wave signal from GW 170817, observed by the LIGO-Hanford (top), LIGO-Livingston (middle), and Virgo (bottom) detectors. Times are shown relative to 2017 August 17, 12:41:04 UTC. The chirp signal is visible in LIGO-Hanford and LIGO-Livingston data. Figure taken from Abbott et al. (2017c).

Einstein's prediction, in 2015, the gravitational wave signal from the coalescence of a binary black hole pair was reported, initially with the Laser Interferometer Gravitational-Wave Observatory (LIGO Abbott et al. (2016a)) and later using the combined LIGO-Virgo global 3-detector network (Abbott et al. 2017b). These milestones opened the era of gravitational wave astronomy. In 2017, a gravitational wave signal from a neutron star binary coalescence was detected by Advanced LIGO and Advanced Virgo (Figure 1.4; Abbott et al. (2017c) and Abbott et al. (2017a)). Less than 2 seconds later, a short GRB was detected by *Fermi* satellite (Goldstein et al. 2017). Soon after the optical counterpart was found (Coulter et al. 2017), while the X-ray and radio emissions were detected 9 (Troja et al. 2017) and 16 days post burst (Hallinan et al. 2017), respectively. The extensive MWL campaign that followed provided the most detailed light curves and spectra for a short GRB to date (see e.g., Margutti & Chornock 2021). The event, known as GW 170817 / GRB 170817A, was also associated with the first spectroscopically confirmed kilonova, AT 2017gfo, i.e. the radioactive decay of neutron-rich merger ejecta. High-resolution radio observations of the counterpart showed a structured jet generated from the merger of the two neutron stars in the binary system (Ghirlanda et al. 2019). Interestingly, this impressive discovery arrived just one month before the IC 170922A–TXS 0506+056 association, marking a golden year for the MM astronomy.

Combining electromagnetic and gravitational wave data provided unprecedented insights into the progenitors, geometry, and structure of GRB. Derived parameters from the gravitational wave signal included primary, secondary, and total mass. Spin angular momenta were less constrained, and the system was found to be inclined roughly 150 degrees to the observer's line of sight.

Despite the breakthrough of the GW 170817/GRB 170817A event, it remains the sole MWL event with gravitational waves to date, despite almost a decade of efforts. To explore the population of gravitational wave sources, increased sensitivities in both gravitational wave and electromagnetic facilities are essential. The ongoing fourth observing run of the LIGO, Virgo, and KAGRA network aims to extend the accessible horizon, with expected detection rates for specific mergers. Future ground-based interferometers and space-based interferometers like the Einstein Telescope, Cosmic Explorer, and LISA will offer new opportunities for MM studies of various astrophysical sources, providing a new observational window to the Universe.

The questions about the origin, formation, and evolution of binary stellar black holes, as well as the spins of black holes, need exploration and future gravitational wave observations could provide answers. Statistically significant measurements of correlations between UHECRs, high-energy neutrinos, gravitational waves, and electromagnetic messengers are the main goal of the MM for the next years.

Chapter 2

Blazars

2.1 Introduction

There is wide consensus on the fact that almost every galaxy, including the Milky Way, hosts a massive black hole at its centre. In about 1% of galaxies, the luminosity from the central regions outshines the galaxy itself, leading to their classification as AGN. The energy released from AGN cannot be attributed to a stellar population alone; instead, it arises from the accretion of matter onto the central supermassive black holes, with masses ranging from 10^6 to 10^{10} solar masses. AGN bolometric luminosities can reach up to $\sim 10^{48}$ erg s^{-1}, making them the most powerful sources of electromagnetic radiation in the Universe (Padovani et al. 2017). The radiation emitted by AGN spans a wide range of frequencies, from radio up to High Energy (HE) and even Very High Energy (VHE) gamma-rays (see Part II).

AGN can vary greatly regarding their temporal variability, luminosity, and MWL spectral features. The unified scheme of AGN attempts to explain this diversity by a limited set of physical parameters, primarily the inclination of the obscuring torus to the line of sight and the source luminosity (Antonucci 1993; Urry & Padovani 1995). Under this scheme, sources such as blazars and radio galaxies, which exhibit distinct observational characteristics, are essentially intrinsically similar objects. Any observed dissimilarities are attributed to the orientation of these objects relative to the observer.

The common structure, shared by all AGN, consists of a central black hole surrounded by an accretion disk, clumpy regions and a dusty torus located about 1-10 pc away from the centre. Clumpy regions are categorized based on the broadness of their observed optical lines, which can be either broad or narrow, termed *Broad Line Region (BLR)* and *Narrow Line Regions (NLR)*, respectively. BLRs are close to the accretion disk, within about 0.1-1 pc from the centre. Typical density of BLRs is about 10^{10} cm^{-3} (Netzer 2013). The fast rotational speed of the BLR due to its vicinity to the black hole leads to the observed Doppler-broadened lines. NLRs consist of lower density ($10^3 - 10^5$ cm^{-3}, Netzer (2013)) clouds that are farther from the central regions, at a distance of about 100 pc. Due to their slower motion for the larger distance from the central engine, the emitted lines are not affected by broadening. In about 10% of AGN, the supermassive black hole launches a collimated plasma jet perpendicular to the accretion disk. Jets extend for kpc or even Mpc from the central region (e.g., Ghisellini 2011, for a review). A schematic representation of the AGN unified scheme is shown in Fig. 2.1.

A historically significant parameter in AGN classification is the radio-loudness. The criteria for subdivision in *radio-loud* and *radio-quiet* AGN involve radio-to-optical flux ratios exceeding a specific threshold (Kellermann et al. 1989). This parameter distinguishes sources emitting a significant fraction of energy as non-thermal radiation in the radio band from those primarily emitting thermal radiation associated with the accretion disk. Among radio-loud AGN, those with a resolved host galaxy are called *radio galaxies*, while those without are known as *radio*

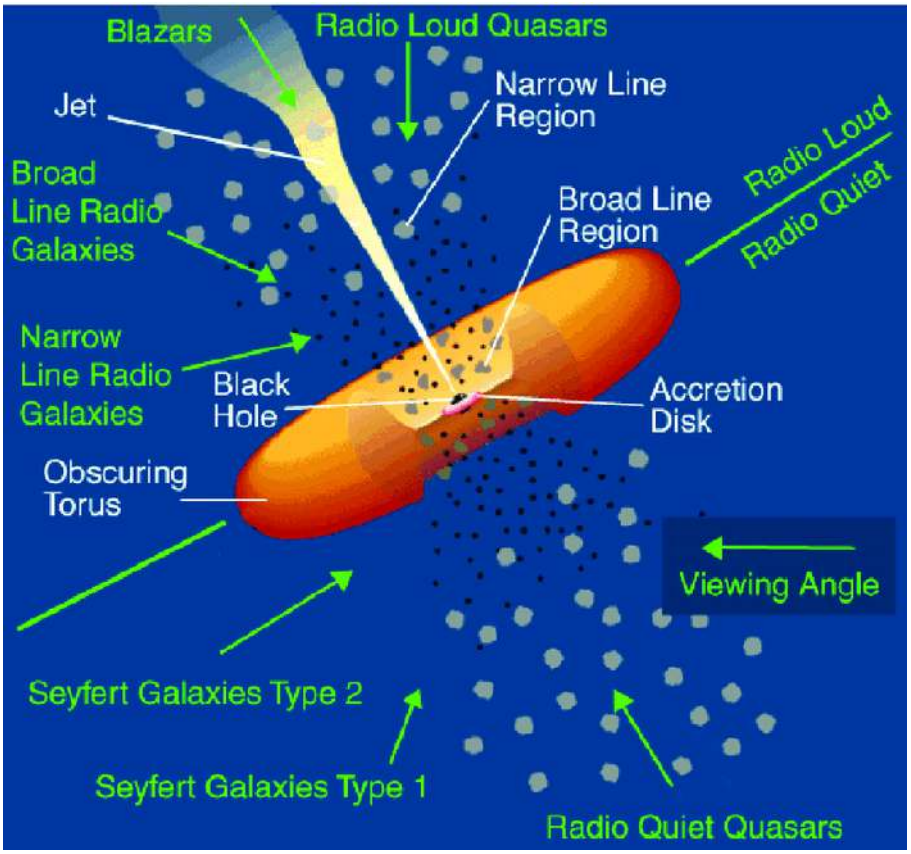

Figure 2.1: Classification of AGN based on the unified scheme framework. The figure illustrates the AGN structure, involving the central supermassive black hole, accretion disk, dusty torus, BLR and NLR. The image highlights the role of the observing angle in shaping the AGN view and subsequent classification. Image from Urry & Padovani (1995).

quasars. Radio-loud galaxies with narrow line features are categorized as Fanaroff-Riley (FR)-Type I and FR-Type II based on their radio luminosity and morphology. FR-Type I are *core dominated*, i.e., the brightest radio emission is found near the position of the central optical galaxy while FR-Type II are *lobes dominated*, with the brightest radio emission occurring in correspondence with the lobes. Subcategories within radio-quiet AGN include *Seyfert galaxies*, with Type-I exhibiting thick optical emission lines and Type-II showing narrow lines.

Radio-loud and radio-quiet galaxies exhibit striking similarities across the electromagnetic spectrum, yet they diverge in their jet properties. Whether the jet is produced or not, it seems to be connected with factors such as the accretion rate, black hole spin and/or mass, and the environment (e.g., Soares & Nemmen 2020). Padovani (2017) suggested that the differences between radio-loud and radio-quiet AGN extend beyond the radio band, reflecting intrinsic distinctions. The author rather proposes a more accurate classification which includes *jetted* and *non-jetted* classes of AGN. The defining characteristic of jetted AGN is the presence of a strong, relativistic jet. A prominent dissimilarity between jetted and non-jetted sources arises in the gamma-ray observations. Radio-loud sources emit up to GeV and sometimes TeV energies, while radio quiet AGN have a cutoff around 1 MeV. This distinction aligns with the presence or absence of a strong relativistic jet. Non-jetted AGN may have weak jets, but these are not strong enough to produce the high-energy emission observed in jetted AGN.

As anticipated before, another principal discriminator in AGN classification is the observer's viewing configuration (Urry & Padovani 1995). Depending on the source's orientation, certain

regions may be dimmed, while others dominate the galaxy's emission. Specifically, the dusty torus co-planar with the accretion disk can hide the central region depending on the viewing angle. The presence of broad or narrow optical emission lines is linked to the interception of the dusty torus with the line of sight, classifying AGN into Type-I and Type-II galaxies. In Type-I sources, the dusty tours hides the BLRs resulting in the detection of NLRs only. In contrast, Type-II sources are observed from an intermediate viewing angle from which both regions are visible. Jetted sources with the jet pointing directly toward the observer are called *blazars*. In these sources, the jet often (but not always) outshines the host galaxy and the accretion disk emission due to the high Doppler factor, which in turn is due to the small observation angle.

For an in-depth exploration of the diverse and intricate taxonomy of AGN, readers can refer to Padovani et al. (2017). This Thesis primarily focuses on the physics of the blazar class. As mentioned above, blazars set themselves apart from other radio-loud/jetted AGN classes due to a specific configuration where the jet axis closely aligns with the observer's line of sight, at an angle of fewer than ten degrees. Charged particles accelerated within the jet move at relativistic velocities, emitting non-thermal radiation across the entire electromagnetic spectrum and often outshining the host galaxy. The rest of this Chapter is dedicated to describing the characteristics of blazars.

2.2 Blazar classification

Blazars are categorized into Flat Spectrum Radio Quasar (FSRQ) and BL Lac objects based on the strength of their optical emission lines. BL Lacs exhibit almost featureless optical spectra, with optical emission lines characterized by rest-frame Equivalent Width (EW) $< 5\mathring{A}$, while FSRQ lines have larger EW.

This distinction arises from the differing configurations of the two classes. An FSRQ hosts an obscuring torus of dust around a thin, hot accretion disk, accompanied by a hot thermal corona. Evidence of NLRs and BLRs is also found. In contrast, in BL Lacs, the presence of BLRs is excluded. The absence of broad emission lines and thermal emission from the accretion disk suggests that accretion in BL Lacs occurs in a radiatively inefficient regime.

The SED of FSRQs generally exhibit a complex shape with contributions from the jet emission and the torus and hot corona, mainly at low energies. BL Lac SEDs are primarily characterized by non-thermal jet emission, with possible contributions from the host galaxy in some cases.

Blazars are further classified based on their broadband spectral features. Their SEDs exhibit two humps. The low-energy hump is attributed to the synchrotron radiation from a population of electrons, the low-energy peak is then usually referred to as *synchrotron peak*. One of the most popular hypotheses to interpret the high-energy hump involves Inverse Compton (IC) interactions between electrons in the jet with a low-energy photon field, then the high-energy peak is commonly referred to as *IC peak*. However, the origin of the high-energy component is still debated.

The synchrotron peak frequency, $\nu_{\rm peak,sync}$ determines the classification into High-Frequency Synchrotron Peaked (HSP), Intermediate-Frequency Synchrotron Peaked (ISP), and Low-Frequency Synchrotron Peaked (LSP) blazars. When applied to BL Lacs, these classes translate to High-Frequency Peaked BL Lac (HBL), Intermediate-Frequency Peaked BL Lac (ISP), and Low-Frequency Peaked BL Lac (LSP), respectively. HSP, ISP, and LSP exhibit synchrotron peaks at $\nu_{\rm peak,sync} > 10^{15}$ Hz, in the range 10^{14}Hz $< \nu_{\rm peak,sync} < 10^{15}$Hz, $\nu_{\rm peak,sync} < 10^{14}$Hz, respectively. Prototypes of HBL are the most studied blazars, Markarian 421 and Markarian 501 (hereafter Mrk 421 and Mrk 501).

The class of Extreme-High-Frequency Synchrotron Peaked (EHSP) objects or Extreme-High-

Frequency Peaked BL Lac (EHBL), showing a synchrotron peak $\nu_{\rm peak,sync} > 10^{17}$ Hz, has been introduced later (Costamante et al. 2001). Due to the synchrotron peak shifting towards higher energies, the UV/optical radiation from the host galaxy becomes detectable. EHBLs exhibit the high-energy peak in the VHE regime, therefore they are ideal targets for VHE studies. Moreover, these sources are characterized by a distinctive hard TeV spectrum (Costamante et al. 2018).

HBL and EHBL are particularly interesting sources as they provide indirect insights for Extragalactic Background Light (EBL) studies. VHE photons produced in these sources interact with the EBL field through pair production processes. This yields absorption of the TeV photons and then softer HBL and EHBL observed spectra. This method offers a means to gain information on EBL density and contributes to the understanding of various astrophysical phenomena (Mazin & Raue 2007).

In addition, TeV γ-rays from blazars can be employed to probe the Inter Galactic Magnetic Field (IGMF) by studying the deflection of positrons and electrons created through the pair production process and their subsequent IC scattering of CMB and EBL photons. In the absence of any IGMF, the reprocessed flux equals the absorbed one. However, if a magnetic field is present, the received reprocessed flux decreases. Therefore, knowledge of the absorbed TeV and GeV flux provides a method to set a lower limit on the IGMF (e.g., Neronov & Vovk 2010; Tavecchio et al. 2010b).

Non-thermal properties

Non-thermal emission from the jets dominates the radiative output of blazars, making them ideal targets for radio and gamma-ray observations (see Chapter 1). Blazars, as a class, dominate the GeV to TeV sky (Ackermann et al. 2015), with BL Lacs being the most frequently detected sources in the TeV regime. This prevalence is primarily due to the extension of HBL and EHBL SEDs up to these high energies. According to the catalogue for TeV Astronomy, TeVCat 2.0[1], at the time of writing, a total of 274 sources have been detected up to the TeV band, with 84 of them identified as blazars, including 57 belonging to the HBL class (see Fig. 2.2 and Fig. 2.3).

As previously discussed in Section 1, opposite to the thermal spectra described by Planck's law, the spectra of sources emitting radiation through non-thermal processes are characterized by a power-law function. This reflects the energy distribution of the emitting particles accelerated via Fermi acceleration processes (Fermi 1949; Matthews et al. 2020). In the fields of high-energy astrophysics and astroparticle physics, the differential energy spectrum is commonly used for determining the number of events, $\mathrm{d}N$, within an infinitesimal energy interval, $\mathrm{d}E$. Specifically, in high-energy astrophysics, the differential photon energy spectrum is given by $\mathrm{d}N_{\rm photon}/\mathrm{d}E \propto E^{-\Gamma_\gamma}$, where Γ_γ is the gamma-ray spectral index. In the gamma-ray band, FSRQ usually exhibit steep spectra with a spectral index of $\Gamma_\gamma > 2$, while harder spectra are observed in BL Lacs ($\Gamma_\gamma < 2$).

The radio flux density, S_ν, represents the energy released per unit area, time, and at a specific frequency due to synchrotron radiation. This quantity is measured in Jansky (Jy), where 1 Jy is $\sim 10^{26}\mathrm{WHz}^{-1}\mathrm{m}^{-2}$. An electron population spiralling around magnetic field lines emits synchrotron radiation following a power-law relationship of the form $S_\nu \propto \nu^{-\alpha}$ across the radio domain. The spectral index α is connected to the spectral index defining the electron energy distribution, p, by $\alpha = (p-1)/2$ (see e.g., Rybicki & Lightman 1986). The radio spectrum of blazars exhibits a flat nature, characterized by spectral indices α close to zero, especially at high frequencies, ranging from GHz to the millimetre regime (e.g., Massaro et al. 2013). These values of the spectral index are not due to the electron energy distribution having slope p=1, which would not be in agreement with acceleration mechanisms, but it is due to the

[1] http://tevcat2.uchicago.edu/

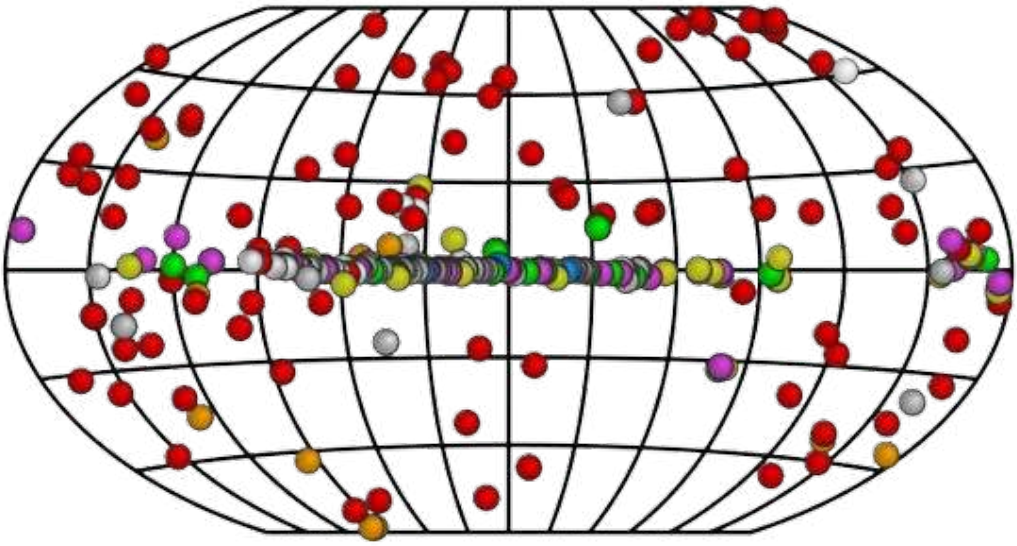

Figure 2.2: Sky map in galactic coordinates of TeV sources, where various TeV objects are distinguished by different colours. Blazars are denoted by red points. The distribution percentage of each class in the TeV catalogue is illustrated in Fig. 2.3. Image from the TeVCat 2.0 website.

superposition of regions with different self-absorption frequencies. In regions of high electron number density and intense magnetic fields, the synchrotron radiation emitted can indeed be absorbed by the particle population before exiting the region. In simpler terms, the presence of high-density particles can render the medium opaque to synchrotron radiation itself, creating the phenomenon known as *synchrotron self-absorption*. This leads to the observation of inverted spectra, where the intensity of radiation increases with frequency. At the highest frequencies, the superposition of emission from different jet regions, each undergoing synchrotron self-absorption to a different degree, leads to observing these inverted spectra.

Blazar sequence

In investigating the overall features of the BL Lacs and FSRQ, Fossati et al. (1998) identified an empirical trend in the observed SEDs. This trend, known as the *blazar sequence*, was established based on a sample of 126 blazars which show a smooth transition in the $\nu L(\nu) - \nu$ plane (Fig. 2.4). The analysis explored the correlation between $\nu_{\rm peak,sync}$ and various parameters, including luminosity in different bands and optical/radio and X-ray/radio flux ratios. Key findings revealed a strong anti-correlation between luminosity and $\nu_{\rm peak,sync}$, as well as between $\nu_{\rm peak,sync}$ and the *Compton dominance* – which is defined as the ratio between luminosity at the synchrotron peak and the luminosity at the Compton peak. In summary, sources displaying the synchrotron peak at lower frequencies tend to exhibit higher gamma-ray and radio luminosity and higher Compton dominance.

The original formulation of the blazar sequence was based on data collected during the Energetic Gamma Ray Experiment Telescope (EGRET) era and was possibly affected by significant selection biases. Following the advent of the *Fermi*–Large Area Telescope (LAT)[2], a revised version of this analysis expanded the blazar sample to 747 sources using more uniform selection

[2]This instrument will be briefly described in Section 1

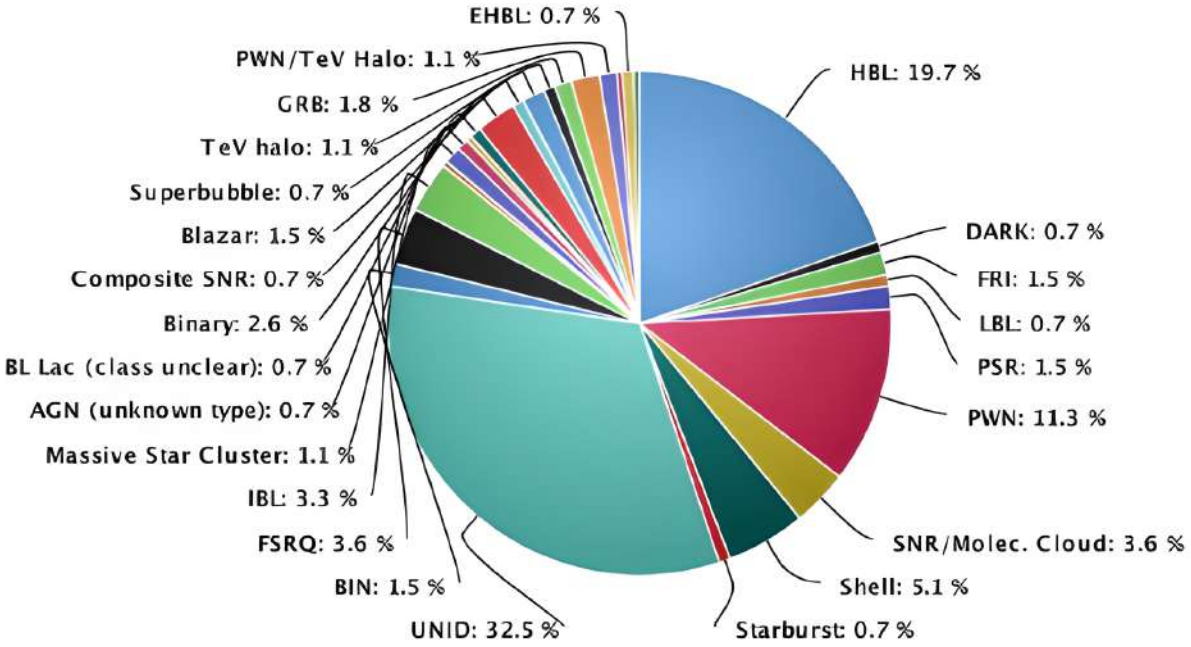

Figure 2.3: Percentage distribution of each class in the TeV catalogue, with the HBL class (light blue) dominating the largest portion. The EHBL class, while expected to emit primarily at high energy, poses challenges in detection due to its low luminosity. Image from the TeVCat 2.0 website.

criteria, resulting in a refined blazar sequence (Fig. 2.5, Ghisellini et al. (2017)). In this new sequence, the shift to higher frequencies of synchrotron and IC peak frequencies correlates with decreasing luminosity, impacting BL Lac objects more significantly than FSRQs. Conversely, an increase in Compton dominance correlates with higher luminosity within the FSRQs sub-sample.

The significance of the blazar sequence lies in its implication that a classification based on synchrotron peak position must have a physical foundation, given the seamless progression between blazar classes. The physical explanation could be that, in the case where seed photons for external Compton scattering are provided by a radiatively efficient disk in the presence of a BLR, and the strength of the BLR is correlated with the power injected into electrons in the jet, more luminous jets exhibit stronger broad emission lines. This results in efficient Compton cooling, leading to an increase in the luminosity of the high-energy peak and rapid cooling of the most energetic particles via IC, causing the peak frequencies to decrease. Conversely, as the power injected into electrons diminishes, in case of low synchrotron luminosity, inefficient disk or absence of BLRs, the low number of seed photons available for IC scattering means that the most energetic particles undergo less efficient cooling. This causes the synchrotron peak to be located at higher frequencies and the luminosity of the Compton component to be lower than in the previous case. According to this interpretation, objects with low luminosity and low-frequency peaks or objects with high luminosity and high-frequency peaks should not exist Ghisellini et al. (1998).

The revised sequence in particular unveils a more intricate scenario compared to the original one, potentially linked to a broad spectrum of black hole masses hosted in the larger sample of blazars used for the updated study. A review of the history, development and physical interpretation of the blazar sequence has recently been published by Prandini & Ghisellini (2022).

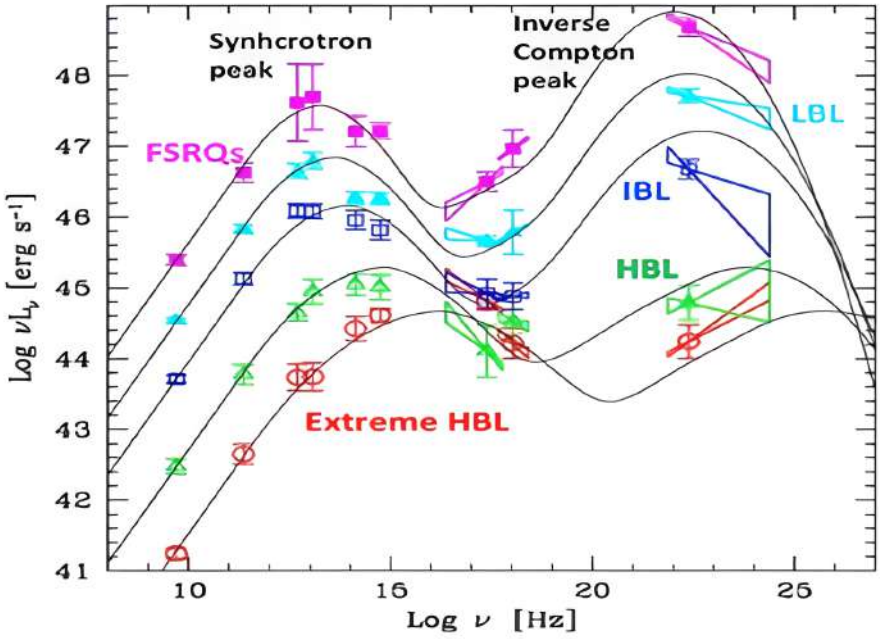

Figure 2.4: Blazar sequence from Fossati et al. (1998). Observed SEDs for 126 blazars have been averaged and modelled using analytical models (represented by black lines). The image illustrates which SED represents each blazar subclass, highlighting that FSRQs are the most luminous with the lowest $\nu_{\rm peak,sync}$, while EHBLs are the least luminous objects with the highest $\nu_{\rm peak,sync}$. Credits: Falomo et al. (2014), adapted from Fossati et al. (1998).

2.3 Blazar emission mechanisms

As mentioned in the previous Section, the typical SED of a blazar can extend from radio to TeV energies, exhibiting a double-humped structure. The low energy part of the SED spans from the radio to the X-ray band, with its peak falling in the sub-millimetre to the X-ray range. The high energy component peaks above MeV energies, extending up to TeV energies. In some cases, thermal emission from other components of blazars can significantly impact the broadband SED, leading to more complex shapes. In particular, the lower energy hump may sometimes include contributions from the host galaxy.

2.3.1 One-zone models

In one-zone models, the non-thermal continuum is described in terms of emission from a uniform spherical region, often referred to as *blob*, typically a few light days ($\sim 10^{15}$ cm) in size or smaller. This propagates along the jet, and due to its relativistic bulk motion, the radiation in the jet's frame undergoes a boost in the observer's frame influenced by the effects of relativistic Doppler shift (discussed in the next Section).

The blob is filled with a distribution of relativistic electrons and a randomly oriented magnetic field. The interaction between the magnetic field and the relativistic particles leads to synchrotron radiation (Rybicki & Lightman 1986), which constitutes the lower-energy component of the blazar SED (e.g., Ghisellini et al. 1985).

The electron energy distribution producing the jet emission is typically described as a broken power law, with the discontinuity attributed to the radiative cooling of the electrons. In the case the electrons undergo simple radiative cooling, the spectral index is usually assumed to change by 1. The mechanism behind such a discontinuity is not clear yet and might hint at

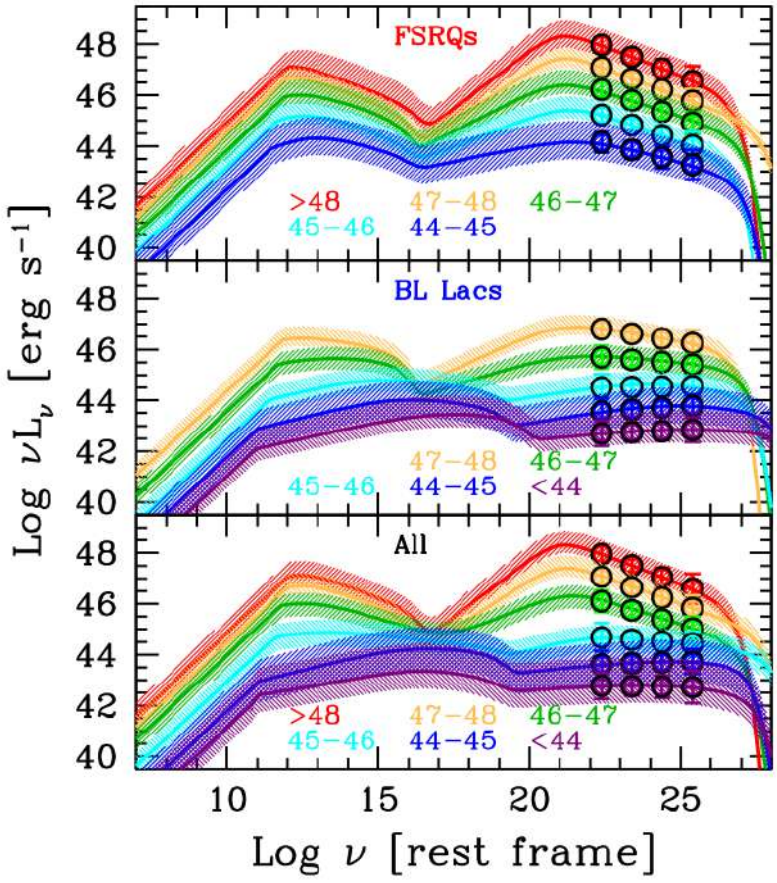

Figure 2.5: Revised blazar sequence from Ghisellini et al. (2017). Contrary to the historical version, this was built using different gamma-ray luminosity bins instead of radio luminosity bins. FSRQs and BL Lacs have been analysed separately. The results of the two analyses are shown on top for FSRQs and in the middle panel for BL Lacs. Results including all sources are reported in the bottom panel. From Ghisellini et al. (2017)

supplementary injections and cooling factors.

While the interpretation as synchrotron radiation of the low energy part of the blazar SEDs is universally accepted, two primary families of models, leptonic and hadronic, have been proposed to explain the high energy emission (for a recent review, refer to Cerruti 2020). Additionally, hybrid lepto-hadronic scenarios have also been suggested (e.g., Cerruti et al. 2015)).

Leptonic models According to leptonic models, the higher-energy component of the SED is primarily attributed to the IC scattering of low-energy photon field by high-energy electrons (Rybicki & Lightman 1986). In the case of BL Lacs, the target radiation is provided by the low-energy synchrotron photons, giving rise to the lower-energy hump itself. Therefore, in this framework, the two peaks are produced by the same electron population and for this reason the model is known as synchrotron-self Compton (SSC) scenario.

SSC can typically describe well the SEDs of HBLs. Fitting these models to LSPs' and FSRQs' SEDs is instead more challenging. In FSRQs and LSPs, due to the presence of different components, such as the accretion disk, the dusty torus and the BLR, the low-energy target photons for IC processes more probably come from a site external to the jet. For example, they may be emitted by the accretion disk and reprocessed by the BLR (e.g., Sikora et al. 1994). Also, the photon field may vary along the jet's length. Models in which the photon field is not

coincident with the jet itself are referred to as External Compton scenarios.

One-zone leptonic models are well suited for explaining the SEDs of blazars during stationary phases. However, observation of minute-scale gamma-ray variability challenges them (e.g., Begelman et al. 2008). Such variability implies extremely large bulk Lorentz factors, above 50, much larger than the Doppler factors inferred from superluminal motion speeds (see next Section), which are typically of the order of 10. The discrepancy between the estimation of the Doppler factor from gamma-ray observations and the subluminal motions observed from radio observations is referred to as *Doppler factor crisis* (Henri & Saugé 2006). Models invoking different emitting regions have been proposed to solve the crisis. These will be addressed in Section 2.3.2.

Hadronic models According to hadronic models, a population of relativistic protons coexists with the population of electrons within the emission region, contributing to the observed SEDs. In particular, proton–synchrotron mechanism and/or proton–proton collisions or, more likely, photo-hadronic interactions, generate the high-energy component of blazar SEDs. As mentioned in Chapter 1, the hadronic processes as proton–proton and photo-hadronic interactions, are connected to neutrino production.

Emitting regions filled with extremely strong magnetic fields, with strengths ranging between 30 and 100 G, and relativistic protons, with energies above 10^{19} eV, can produce synchrotron radiation analogous to that emitted by the population of electrons (Aharonian 2000). The proton synchrotron emission can account for the observed high energy emission.

In the case of BL Lacs, aside from direct proton synchrotron radiation, the relativistic protons also interact with the low-energy synchrotron photon field via photo-meson interactions (Mannheim 1993). As described in Section 1.3, photo-meson interactions generate gamma-ray photons through neutral pion decay (Eq. 1.2) or via pair cascades. The decay of charged pions generates electron-positron pairs which emit synchrotron photons leading to further pair production, thereby initiating an electromagnetic cascade. This cascade evolves until the optical depth of the emitting region allows the high-energy photons to escape without further interaction. The escaping photons are the ones contributing to the high energy part of the SEDs. Similar to the External Compton scenario in leptonic models, hadronic models also consider regions external to the jet providing the seed photon fields for the photo-meson interactions.

In principle, proton-proton interactions (also described in Section 1.3) could also be responsible for the high-energy emission in blazars. However, the density of photon fields typically surpasses the particle density within the jets, disfavoring the proton-proton process. Alternative scenarios, for example, the one involving the interaction of a cloud or star with the jet (Barkov et al. 2012), predict that proton-proton interactions can account for the ultra-fast variability observed in blazars through hadronic emission mechanisms.

An important characteristic of hadronic models is the fact that the processes involved in the high energy emission of the SED also inevitably come with the production of high-energy neutrinos (see Section 1.3). Criticisms of hadronic models include the necessity for optically thin emitting regions and higher magnetic field strength compared to the leptonic scenarios (Mücke et al. 2003). In addition, by adding a second population of particles, hadronic emission models essentially double the number of independent model parameters related to the primary particle distribution when compared to traditional leptonic models.

Extreme blazars in the SSC versus hadronic scenario The SEDs of EHBL are characterized by a synchrotron peak around 1 to 10 keV, a high-energy peak reaching 10 TeV and a hard spectrum in the VHE gamma-ray band. These features challenge the conventional SSC models. Such hard TeV spectra cannot be explained assuming a simple SSC scenario since

extreme model parameters are required to reproduce the energies reached by the synchrotron component (Tavecchio et al. 2009). Some of the extreme model parameters arising in the modelling of EHBL include high values of the minimum energy in the electron energy distribution, unrealistically large Doppler factors, slopes of the electron energy distribution in contrast with the prediction from the Fermi acceleration mechanisms, very low magnetic field values (Sol & Zech 2022).

High values of the minimum electron energy may occur under specific conditions, such as when electrons experience inefficient cooling or in cases of stochastic turbulence driving electron acceleration. The requirement for large Doppler factors would imply an extremely fast jet motion or an extremely small viewing angle, which, as mentioned previously, contradicts radio observations but can be addressed by assuming more complex models, involving multiple emitting zones (Sol & Zech 2022). An alternative scenario within the leptonic models invokes external photon fields for the IC processes to account for the extremely hard VHE spectra, although this is typically associated with FSRQs rather than HBLs.

EHBLs variability in the gamma-ray band is characterized by slower flux variability and with minor flux variations compared to other blazars (see Section 2.4.3), as observed in the VHE long-term light curve of 1ES 0229+200, the prototype of EHBLs (Cologna 2016). This low variability may be attributed to the relatively low flux of the sources, particularly at TeV energies, and the still limited sensitivity of VHE telescopes.

Given that leptonic models typically admit substantial flux variations on short timescales these are not favoured for describing the emission mechanism of EHBLs. Instead, hadronic and lepto-hadronic emission models are more likely suitable to interpret the hard spectra at high energies and the absence of rapid flux variability (see next Section). Due to the intrinsic lower luminosity of EHBLs compared to other blazar subclasses, these are particularly suitable for hadronic models. Moreover, the absence of fast flares from EHBLs aligns with the cooling time scales of protons in the jet.

2.3.2 Multi-zone models

So far, we have examined the simplest scenario of a single zone, the blob, emitting the entire radiation. However, as mentioned earlier, in some cases, it is necessary to assume the presence of multiple emitting regions to interpret observational features, as in the case of the Doppler factor crisis. Multi-zone models, whether leptonic or hadronic, propose that particles undergo acceleration and emit radiation in different sites along the jet.

Spine-shear model An example of a multi-zone approach is represented by the spine-shear model (Tavecchio & Ghisellini 2008). According to this model, the jet is structured featuring a fast spine surrounded by a slower shear layer. This velocity structure would lead to a boost of the emission from each layer as seen from the other because of the relative relativistic speeds involved – that is a consequence of the phenomenon described in the next section, the Doppler boosting.

A structured jet offers a good opportunity to reproduce rapid TeV variability states without invoking high values of Doppler factors across the entire jet. Such values of Doppler factors (above 50, as mentioned earlier) are only required within the fast spine, which is assumed to be a very compact region inside the jet. The external layer would be responsible for the emission observed in the radio band indicating lower values of Doppler factors.

A transverse velocity structure is also suggested by the limb brightening observed directly in VLBI images[3], such as in the TeV blazar Mrk 501 (Giroletti et al. 2004) or the radio galaxy

[3]However, transverse velocity structure is not the only possible cause of limb brightening.

M 87 (Kovalev et al. 2007). Due to the presence of a beamed jet in FR-I radio galaxies, these are often assumed as the BL Lacs parent population with the jet misaligned from the line of sight (e.g., Urry et al. 1991). Velocity structures with different Lorentz factors (and therefore Doppler factors) in different regions of the jet are proposed for the unification scheme of FR-I and BL Lac objects (Chiaberge et al. 2000). The target source analysed by Tavecchio & Ghisellini (2008) to verify the applicability of the spine-shear model, the FR-I radio galaxy M 87, has also been considered as a test source for a different interpretation by Georganopoulos et al. (2005). The latter discussed a model in which the jet experiences strong deceleration within the sub-parsec scale region. They assume the high-energy emission comes from the innermost and faster portion of the jet, while the slower external portions mainly contribute to low-energy emission. However, in this case, due to different beaming patterns for the synchrotron and IC components, the resulting spectrum would be characterized by strong Compton dominance, contrary to what is typically observed in known TeV emitting BL Lacs.

The spine-shear model implies that a strict correlation between low-energy and TeV emission is not required since the emission in the different bands is produced in distinct locations.

2.3.3 Modelling blazars SED

Fitting observed MWL SEDs of AGN is a powerful tool for testing and investigating assumed physical scenarios. In blazars, the SED modelling procedure enables us to deduce parameters governing particle energy losses, as these losses contribute to the observed SEDs. Consequently, this process provides insights into the acceleration processes occurring in blazar jets.

Various tools are available for modelling radiation mechanisms in AGN. A recent comprehensive review by Nigro & Tramacere (2022) highlights open-source software options for the community.

Among these tools, `agnpy` (Nigro et al. 2022) is employed for computing SED analyses in this work. This Python package[4] integrate specialized modules designed for computing leptonic radiative processes in jetted AGN. `agnpy`'s primary aim is to compute SED models employing a numerical approach under the assumption of arbitrary combinations of emission regions and radiative processes. However, it is coded in a way that allows also the fitting of observational data by interacting with other software, in particular, `Gammapy` (Deil et al. 2017), and `Sherpa` (Doe et al. 2007).

For the SED modelling with `agnpy`, a one-zone model is assumed. The support for multiple or complex emission regions is not implemented in the software yet. The emission comes from a sphere of plasma, the blob, having radius R_b, and filled with a tangled uniform magnetic field, B, and an electron population. The electron energy density in the blob reference frame, n_e, is parametrized as a function of the Lorentz factor γ, $n_e(\gamma)\mathrm{d}\gamma = \mathrm{d}n/\mathrm{d}\gamma\mathrm{d}\gamma$. The available functions include broken power law, simple power law, exponential cutoff power law, and log parabola. The blob moves along the jet with a constant relativistic velocity v, which is expressed as a function of the speed of light, c, $\beta = v/c$, and bulk Lorentz factor $\Gamma = (1-\beta^2)^{-\frac{1}{2}}$. The jet is oriented at an angle θ to the observer's line of sight. The Doppler factor, δ, is given by $\delta = [\Gamma(1-\beta\cos\theta)]^{-1}$. The viewing angle of the observer to the jet axis is a parameter for all implemented physical processes making the code versatile for describing different radio-loud AGN, not only blazars. External Compton scenarios in which the blob is homogeneously exposed to radiation from thermal emitters can also be assumed. The radiative processes implemented

[4]The calculations are grounded in established definitions from references such as Blumenthal & Gould (1970), Rybicki & Lightman (1986), and Dermer & Menon (2009). `agnpy` utilizes the `numPy` package (Harris et al. 2020) for multidimensional integrations to compute emissions from electron distributions and photon fields. The `astropy` package (Astropy Collaboration et al. 2018) manages physical constants and unit transformations. Input quantities and computation results in `agnpy` are presented as `astropy` quantities

in `agnpy` are described in detail in Nigro et al. (2022).

The SED characterisation provided by `agnpy` depends on all the model parameters as the ones described above and on the frequency. Best-fit parameters are obtained via minimization of the χ^2 statistic. In the fitting procedure, some of the parameters can be frozen depending on a priori knowledge. Different algorithms for the minimization are utilized, e.g., the `iminuit` package (Dembinski et al. 2020) for `Gammapy` and Levenberg (1944) and Marquardt (1963) for `Sherpa`.

As an example, assuming an SSC model with the electron energy density distribution described by a broken power law over an energy interval $[\gamma_{\rm min}, \gamma_{\rm max}]$:

$$n(\gamma) = n_0 \cdot \begin{cases} \left(\frac{\gamma}{\gamma_{\rm break}}\right)^{-p_1} & \gamma_{\rm min} < \gamma < \gamma_{\rm break} \\ \left(\frac{\gamma}{\gamma_{\rm break}}\right)^{-p_2} & \gamma_{\rm break} < \gamma < \gamma_{\rm max} \end{cases} . \tag{2.1}$$

the parameters involved are nine: n_0, p_1, p_2, $\gamma_{\rm break}$, $\gamma_{\rm max}$, $\gamma_{\rm min}$, δ, R_b, and B. n_0 is the normalization parameter; p_1, p_2, are the two spectral indices before and after the $\gamma_{\rm break}$. The blob is described by δ (which depends on Γ and θ), R_b, and B. The blob's radius, R_b, can be fixed by observing the variability time scale (as described in Section 2.4.3) with the Doppler factor retrieved by apparent superluminal motion (as described in Section 2.4.2).

The challenge for SED modelling software as `agnpy` is the parameter degeneracy. Similar satisfactory SED descriptions can be obtained with different sets of parameters, it is then crucial to reduce the number of free parameters. In this context, VLBI observations provide independent constraints (e.g. on the viewing angle or the magnetic field intensity) that can be used to set the SED models (MAGIC Collaboration et al. 2019; MAGIC Collaboration et al. 2020c; MAGIC Collaboration et al. 2020b).

2.4 Blazar observational features

Blazars exhibit features such as rapid flux variability, high bolometric luminosity, and apparent superluminal motions of the jet components. These can be explained by the Doppler boosting effect due to the relativistic speeds of the jets. Additional key observational characteristics of blazars include the presence of the compact radio core with a flat or inverted spectrum and high optical and radio polarization.

2.4.1 Doppler boosting

Sources in motion relative to the observer's frame undergo the Doppler effect. For blazar jets moving with relativistic velocities, this leads to the phenomena known as *Doppler boosting* and *relativistic beaming*.

Values of certain physical parameters are amplified or attenuated depending on whether the source is approaching or receding from the observer. For an approaching source, the radiation's intensity appears boosted. Conversely, a receding source could be so attenuated that it becomes undetectable. Consequently, a jet oriented toward the observer is detected with an apparent luminosity higher than its rest frame while for a receding jet, the intensity is reduced in the observer's frame.

A jet moving towards the observer's direction with a velocity, β, a bulk Lorentz factor Γ and forming an angle θ to the line of sight undergoes an amplification or reduction of the measurable quantities depending on the *relativistic Doppler factor*, δ. The frequency of the radiation emitted as seen in the jet's reference frame is denoted as $\nu_{\rm em}$. In the observer's frame, the radiation frequency corrected for the relativistic Doppler effect is $\nu_{\rm obs} = \delta \nu_{\rm em}$, that is:

$$\nu_{\rm obs} = \frac{\nu_{\rm em}}{\Gamma(1-\beta\cos\theta)} \tag{2.2}$$

The source approaching the observer, i.e., moving with $\beta > 0$, implying $1-\beta\cos\theta < 1$, is detected with an observed frequency $\nu_{\rm obs}$ higher than $\nu_{\rm em}$: the radiation is *blueshifted*. Conversely, for $\beta < 0$, the opposite effect is observed: the radiation is *redshifted*.

The time measurement in the observer frame is affected by the relativistic Doppler effect too. The path traversed by the source approaching the observer in the time interval $\mathrm{d}t_{\rm em}$ is $\Gamma v \mathrm{d}t_{\rm em}\cos\theta$. The observer measures the first and the last photon arriving from the source in a time interval:

$$textdt_{\rm obs} = \Gamma \mathrm{d}t_{\rm em} - \frac{\Gamma v \mathrm{d}t_{\rm em}\cos\theta}{c} = \Gamma \mathrm{d}t_{\rm em}(1-\beta\cos\theta) = \frac{\mathrm{d}t_{\rm em}}{\delta} \tag{2.3}$$

The time interval $\mathrm{d}t_{\rm obs}$ appears then shorter than that measured in the source frame $\mathrm{d}t_{\rm em}$, $\mathrm{d}t_{\rm obs} = \mathrm{d}t_{\rm em}\ \delta^{-1}$. The solid angle $\mathrm{d}\Omega_{\rm obs}$ under which the observer receives the radiation is related to the solid angle in the source frame, $\mathrm{d}\Omega_{\rm em}$, by:

$$\mathrm{d}\Omega_{\rm obs} = \frac{\mathrm{d}\Omega_{\rm em}}{\delta^2} \tag{2.4}$$

The observer sees the incoming radiation as concentrated in a solid angle δ^2 times smaller than the solid angle within which the radiation is emitted.

The frequency and time corrections due to the relativistic Doppler effect bring a δ factor each to the correction of the observed luminosity, $L_{\rm obs}$, with respect to the intrinsic one, $L_{\rm em}$. Assuming isotropic emission, the solid angle correction implies a variation by a further δ^2 factor for $L_{\rm obs}$. Therefore, the observed bolometric luminosity is related to the intrinsic luminosity emitted by the source with:

$$L_{\rm obs} \propto \delta^4 \cdot L_{\rm em} \tag{2.5}$$

Considering monochromatic luminosity $L_{\rm obs}(\nu_{\rm obs})$, $L_{\rm obs}(\nu_{\rm obs}) = L_{\rm em}(\nu_{\rm em}) \cdot \delta^3$. For a synchrotron spectrum ($L(\nu) \propto \nu^{-\alpha}$), the equation becomes $L_{\rm obs}(\nu_{\rm obs}) = L_{\rm em}(\nu_{\rm obs}) \cdot \delta^{3+\alpha}$.

The Doppler factor plays a crucial role in jet physics as it governs the degree of flux enhancement and timescale compression observed in the observer frame. An important consequence of the Doppler boosting effect is the so-called Doppler favouritism, a selection effect where faint sources are included in flux-density limited catalogues even if their intrinsic flux density would be too faint to reach the catalogue threshold.

Supporting the beaming effect affecting jet emission and the relativistic speeds of jets, several observation indications have been identified, such as the apparent superluminal motion of knots in jets, the rapid variability at high energy, the higher polarization and the core dominance. However, the Doppler factor cannot be directly measured due to the non-observable nature of both β and θ and can only be inferred indirectly.

2.4.2 Apparent superluminal motion

A consequence of the Doppler boosting is the apparent superluminal motion of the jet components. This phenomenon can be explained through basic geometry, and a schematic representation aiding in comprehension is illustrated in Fig. 2.6.

The blazar core (usually identified as the base of the jet) is at a fixed position, resulting in its radiation consistently taking the same time to reach the observer. On the contrary, a jet component (blue dot in Fig. 2.6) moves with speed $v \sim c$, while emitting light towards the observer at a speed c. Moving from position A to position B (see Fig. 2.6), the jet component forms an angle θ with the line of sight of the observer.

After a time interval Δt measured in the source frame, the component reaches position B. Meanwhile, the photons emitted from the source when it was in position A have already travelled to position D (small red dot in Fig. 2.6) covering the distance $AD = c\Delta t$.

The *apparent* time interval ($\Delta t_{\rm app}$) between the arrival of the photon emitted at position A and the one at position B in the observer frame is given by:

$$\Delta t_{\rm app} = \frac{AD - AB'}{c} = \frac{c\Delta t - v\Delta t\cos\theta}{c} = \Delta t(1-\beta\cos\theta) \tag{2.6}$$

The last substitution comes from the definition of $\beta = v/c$. The apparent transverse speed, $v_{\rm app}$, is determined by the transverse distance travelled by the component divided by the elapsed time between the two measurements:

$$v_{\rm app} = \frac{BB'}{\Delta t_{\rm app}} = \frac{v\Delta t\sin\theta}{\Delta t(1-\beta\cos\theta)} = \frac{v\sin\theta}{1-\beta\cos\theta} \tag{2.7}$$

Hence, we have:

$$\beta_{\rm app} = \frac{v_{\rm app}}{c} = \frac{\beta\sin\theta}{1-\beta\cos\theta} \tag{2.8}$$

From this equation, it becomes clear that $v_{\rm app}$ can appear superluminal, that is $\beta_{\rm app} > 1$, if the source is moving at a relativistic speed in a direction close to the line of sight. In particular, $v_{\rm app}$ reaches its maximum value ($v_{\rm max}$) for $\cos\theta = \beta$ and $\sin\theta = \Gamma^{-1}$. Substituting these values in Eq. 2.7 we obtain $v_{\rm max} = \Gamma v$.

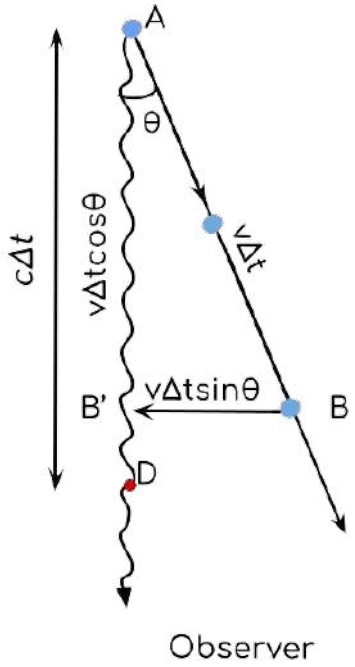

Figure 2.6: Scheme to explain the effect of apparent superluminal motion, the details are reported in the text. The jet component emitted in position A and moving towards position B is represented with the blue circle.

The milliarcsecond resolution resolution of VLBI observations is the unique tool capable of distinguishing individual components. Fig. 2.7 shows an example of the jet component analysis with VLBI of the radio galaxy 3C 111. Measurements of the component position over appropriate time intervals provide their transverse angular speed. One can then obtain the apparent velocity of the jet component by multiplying the transverse angular speed by the distance to the source, accounting for the time dilation caused by the galactic recession. Measurement of proper motions is nowadays widely used on large samples of objects to determine population properties (e.g., Lister et al. 2019).

Furthermore, the analysis of the jet components over time enables us to characterize whether the structure of the jet is conical or parabolic, which implies distinct jet collimation mechanisms (Boccardi et al. 2021) and it provides insights into the magnetic field strength. Part II describes the method for modelling jet components and its applications for the study of jet kinematics and morphology.

Despite their low radio luminosity, the parsec-scale structures of HBL can still be directly imaged with VLBI. Kinematic analyses have consistently revealed an absence of superluminal and slow-moving features within HBL jets, most of the time consistent with being stationary. This discrepancy contributes to the Doppler factor crisis discussed in the previous section. The explanation for this discrepancy may lie in the possibility that radio and gamma-ray emissions originate from distinct regions characterized by different Lorentz factors. The proposed theoretical frameworks include multi-component configurations, such as spine-layer structures (described before in this Chapter), mini-jets within the main jet, or deceleration occurring in the jet.

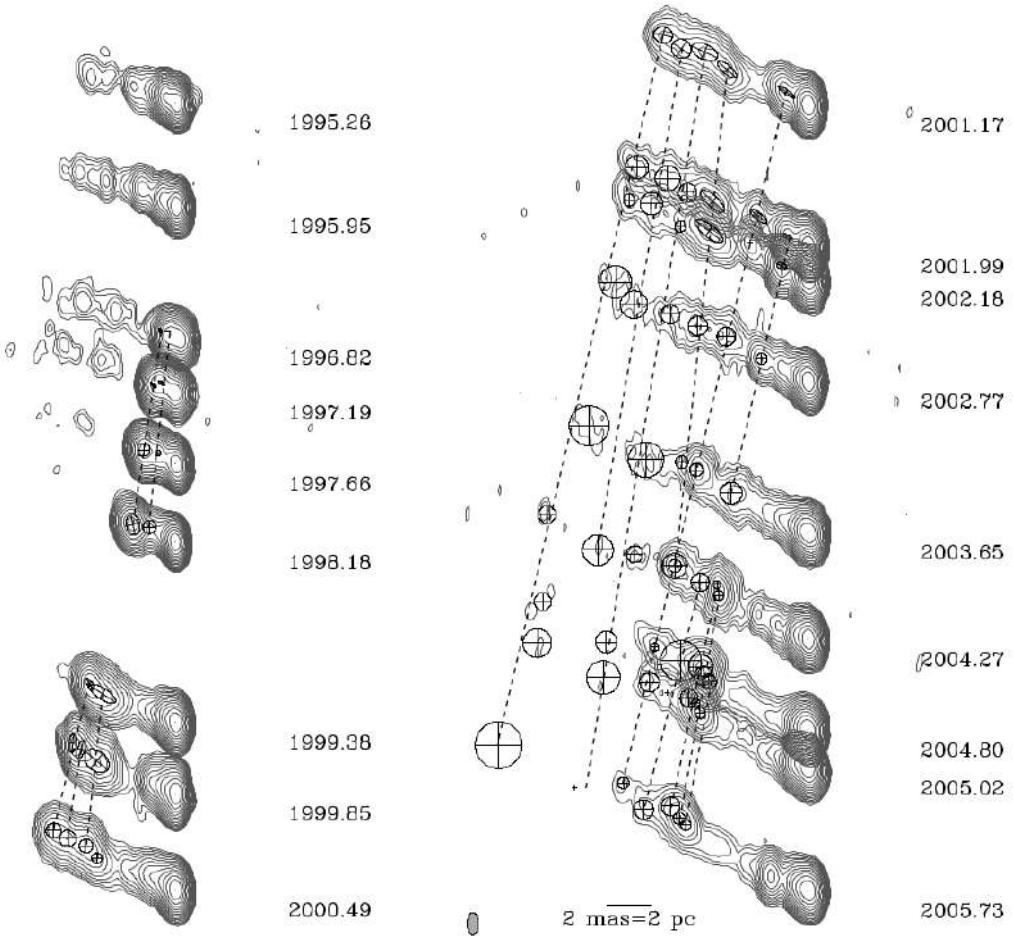

Figure 2.7: VLBI contour levels and jet components of the parsec-scale jet of 3C 111. The images trace the evolution of the jet components' motion over a decade. From Kadler et al. (2008).

2.4.3 Variability

Blazars are persistent objects across all wavelengths, however, they usually exhibit flux and spectral variability (e.g., Singh & Meintjes 2020). The terms *intra-day* variability, *short-term* variability, and *long-term* variability refer to variations in emission recorded over timescales of minutes or hours, days, and months to years, respectively (Geng et al. 2022). During these periods, the source can reach flux levels several times higher than the baseline value.

The analysis of the variability behaviours at the different wavelengths, including durations, intensities, and time delays between different bands, provides crucial constraints on the characteristics of the emitting regions.

The fastest variability timescale, often measured in the X-ray and gamma-ray band (e.g., Singh et al. 2018; Albert et al. 2007), provides an approximation of the linear size of the region emitting in that band. In the VHE band, doubling timescales[5] are observed down to 2–3 minutes and at HE down to hours (about 10 hours). Supported by causality arguments, such timescales require compact emitting regions, of sizes of the order of $\Delta r \lesssim \delta c \Delta t_{\rm obs}/(1+z)$, with δ being the Doppler factor. Assuming a typical value of $\delta \sim 10$ and a timescale $\Delta t_{\rm obs}$ of hours, the retrieved upper limit for the size of the emitting region is $\sim 10^{15}$ cm (Tavecchio et al. 2010a).

[5]The doubling or halving time are used in variability studies to estimate the minimum timescale over which the flux changes by a factor of two, particularly during flaring episodes (Zhang et al. 1999).

Such limited sizes constrain the location of the emitting region close to the central black hole, within a few hundred Schwarzschild radii ($R_s = 2GM_{BH}/c^2$, where M_{BH} is the black hole mass and G the gravitational constant) (e.g., Tavecchio et al. 2010a; Marscher et al. 2010). Among the blazar classes, HBL objects display rapid TeV variability on timescales of a few minutes (e.g., Aharonian et al. 2007). In alignment with the previous arguments, it follows that the X-ray band, characterized by some of the most rapid (hours-minutes) and high-amplitude flux variations, is believed to originate in the innermost regions of the accretion flow, such as the corona and inner disk.

The delays in flux variations occurring at different wavelengths suggest the high-energy emitting region might be located in the innermost part of the blazar jet where the opacity leads to attenuation in other frequency bands. The simultaneous detection of flares at different bands suggests photon production at the same sites along the jet. This can be verified by observing strong intra-band correlations between flux points of MWL light curves.

In addition to the timescales and delay analysis, hysteresis loops provide important information about blazar physics. Hysteresis patterns occur when the spectral behaviour of the source changes asymmetrically with variations in flux. In the framework of the synchrotron mechanism, this signature is connected to acceleration and cooling processes. It underlines the relationship between acceleration and spectral response becoming evident as the flux changes. For instance, a counter-clockwise hysteresis pattern in the spectral index-flux diagram may manifest when the system is near the peak of its acceleration capacity. In such cases, higher-energy photons exhibit a lag behind their lower-energy counterparts, resulting in a softer spectrum during flux increase. Conversely, a clockwise hysteresis pattern may occur when the acceleration timescale decreases, leading to a more rapid emission of higher-energy photons during flux increase, resulting in a harder spectrum. These loops are observed in HBLs (e.g., Abeysekara et al. (2017), see Fig. 2.8).

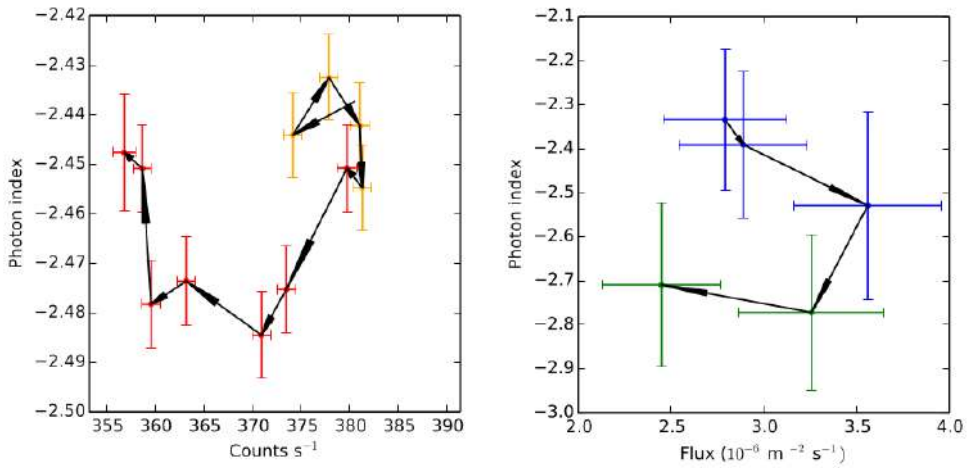

Figure 2.8: Examples of spectral hysteresis observed in Markarian 421 on May 3, 2014 (Abeysekara et al. 2017). The figure presents flux (in counts) vs. photon index diagrams for X-ray (left panel) and TeV (right panel) observations. Time progression is indicated by black arrows, while various states of the source are distinguished by different colours for data point groups.

While binary systems of supermassive black holes at the cores of active galaxies have the potential to introduce periodic variability, blazar light curves show no consistent patterns of periodicity in timescales or flux variations, as observed thus far (Ulrich et al. 1997). In cases where periodicity might arise, it could manifest at different wavelengths and timescales and be due to helical motion of the jet itself, aligned with the orbital motion of the binary system (Rieger 2004).

Quantifying the level of variability and identifying flaring episodes in blazar light curves is crucial for constraining physical mechanisms causing the variability and studying the statistical properties of the phenomenon. Uncertainties introduced during observations and data analysis also play a role in determining the state of a source. In this work, the blazar variability is quantified with parameters such as the variability index (Aller et al. (1992), see Chapter 1.3), and the fractional variability amplitude (Vaughan et al. (2003), see Chapter 4). A summary of the classical approaches employed to determine the variability in blazars can be found in Singh & Meintjes (2020), a new one is being developed (Heckmann et al. 2023).

Various physical scenarios were proposed to explain the observed variability in blazars, with hypotheses accounting for alterations in the geometrical orientation of the jets (Raiteri et al. 2017), time-dependent particle acceleration (Sinha et al. 2018), jets-in-jet models (Biteau & Giebels 2012), turbulence (Narayan & Piran 2012), shocks (Marscher & Gear 1985). VLBI observations can reveal jet components – in some cases superluminal – ejected close in time to strong gamma-ray flares supporting the latter hypothesis (Marscher & Gear 1985).

2.5 Blazars as neutrino emitters

As introduced in Chapter 1, in addition to the proposal that a fraction of the neutrino population emitting at $\sim$ TeV$-$PeV energies originate in our galaxy (Ahlers & Murase 2014), the isotropic distribution of neutrino flux across the sky suggests that sources emitting neutrinos are likely extragalactic. Blazar jets were proposed as sites of particle acceleration (e.g., Biermann & Strittmatter 1987; Neronov & Semikoz 2002; Kotera & Olinto 2011; Biteau et al. 2020) even before the first detection of the diffuse flux from astrophysical neutrinos announced in 2013 (IceCube Collaboration 2013).

As described in Section 1.3, the coexistence of energetic protons with dense photon fields results in photo-meson interactions that produce both neutrinos and gamma rays. The simultaneous occurrence of gamma rays and neutrinos from these interactions reinforces the expectation for an observational correlation between sources emitting gamma rays and those emitting neutrinos. Blazars, in particular, represent the predominant contributors to extragalactic gamma-ray emission, making them the favoured candidates for such a correlation. However, gamma-ray stacking analysis has established that the contribution from gamma-ray blazars to the diffuse neutrino flux should be less than 27% (Aartsen et al. 2017). The theoretical expectation on blazars as neutrino sources was supported by the association of the blazar TXS 0506+056 with the 290 TeV neutrino event (IceCube Collaboration et al. 2018a) (see Chapter 1). Following this relevant discovery, numerous follow-up studies focused on investigating TXS 0506+056 as a potential neutrino emitter. Simultaneously, interest in testing the connection between neutrino events and the blazar class has grown significantly, leading to the exploration of correlations between blazar populations and neutrino samples (e.g., Buson et al. 2022; Buson et al. 2023b).

In Liodakis et al. (2022), the authors discuss the strategy to identify a statistically significant correlation between neutrino emission and samples of jetted AGN. They focus on population studies, confirming that the spatial association is not enough for undoubted associations. Long monitoring (at least 5 years) of a well-defined sample of candidate counterparts would allow us to get the correlation at a 3σ confidence level (assuming, for simplicity, that only jetted AGN produce the observed high energy neutrinos). In particular, according to their findings, the ideal sample of sources is composed of radio bright jetted AGN that must be regularly monitored, particularly by radio facilities.

2.5.1 VLBI search for blazars as neutrino emitters

VLBI observations have provided fundamental information on the morphology and kinematics of the TXS 0506+056 jet, establishing connections with neutrino detection (Li et al. 2020; Ros et al. 2020; Kun et al. 2019; Britzen et al. 2019). Examining brightness temperature, core-shift, and kinematics of jet components, VLBI studies can constrain key parameters such as the apparent β of moving knots, bulk Lorentz factors Γ, viewing angles θ, Doppler factors δ, and magnetic field strength B (see Chapter 1). These parameters describe the acceleration processes, and their study enables the interpretation of neutrino production in blazar jets.

The parsecs and sub-parsec VLBI imaging of blazar jets frequently exhibit limb-brightening transverse structure, providing observational support for the spine-shear hypothesis (e.g., Giroletti et al. 2004). Such a feature can indeed be linked to efficient particle acceleration and, in turn, as a signature for neutrino production site (Tavecchio et al. 2014). The limb brightening has been detected in the inner parsec scale of TXS 0506+056 after the neutrino detection (Ros et al. 2020).

Moreover, VLBI-bright blazars have been shown to correlate with the position of neutrinos and to be in a high state, on average, during neutrino detections (Plavin et al. 2020; Plavin et al. 2021; Plavin et al. 2023). The authors explain the correlations between radio emission and neutrino production in the SSC framework. In this interpretation, the synchrotron emission serves as the target field for proton–photon interaction leading to neutrino production. The observed temporal correlation between radio flares and neutrino arrival further supports the physical connection between synchrotron and neutrino emission processes. In addition, a temporal coincidence between flares in blazars and neutrino arrival time has been found by analysing single-dish data (Hovatta et al. 2021), providing further evidence for the hypothesis on the connection between radio properties and neutrino emission. These associations are based on statistical analysis rather than source-by-source analysis. Consequently, although complete samples of sources are included in the studies, the vast majority of them are not directly associated with individual IceCube events. A source-by-source study is therefore crucial to support the neutrino-radio emission connection. Confirming this hypothesis represents one of the main purposes of this Thesis and its future development (see Section 1.3).

Although VLBI observations proved to be crucial to resolving parsecs and sub-parsec scale regions in jets and investigating the neutrino-blazar connection, VLBI studies are currently hampered by the limited angular resolution of IceCube. Typical IceCube performance allows highly probable astrophysical neutrinos to be detected within 90% localization regions of the order of several square degrees, up to 20 square degrees (see Fig. 2.9).

The largest, full-sky collection of VLBI-detected source – not limited to blazars –, namely the Radio Fundamental Catalogue (RFC)[6], comprises 21906 objects. Assuming, for simplicity, that this sample is uniformly distributed over the sky plane, ~ 0.5 sources lie in a square degree, suggesting that tens of them may be uncovered across the boundaries of the neutrino detection area. Therefore, to select the most promising candidates among these sources, MWL information becomes crucial. Prompt MWL follow-up observations of potential candidates allow us to pinpoint recurring observational properties, such as the ones identified in TXS 0506+056 which might signpost particle acceleration mechanisms and neutrino emission.

2.5.2 Gamma-ray-neutrino connection and SED modelling

Gamma-ray emission follows neutrino production (see Chapter 1), therefore, the detection of new gamma-ray sources or flares from known sources in time and spatial coincidence with neutrino events is, in principle, an ideal way to select the most promising candidate counterparts.

[6] Radio Fundamental Catalog website

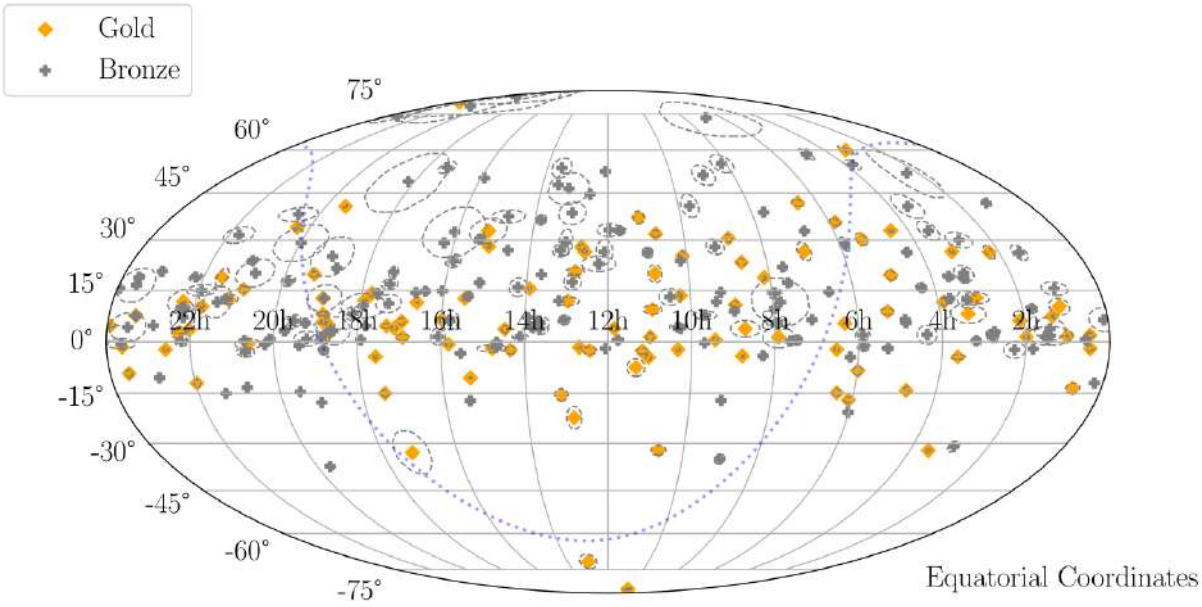

Figure 2.9: Distribution of IceCube neutrino events across the sky (in equatorial coordinates). The IceCube collaborations classify neutrino alerts based on the probability of astrophysical origin: Gold alerts, represented by orange diamonds, are likely to be astrophysical at 50%, while Bronze alerts, indicated by grey crosses, at 30% (Abbasi et al. 2023). Dashed ellipses delineate the 90% error regions at the respective locations of each alert. From (Abbasi et al. 2023).

In this context, the *Fermi*-LAT instrument, observing between approximately 20 MeV to 300 GeV, plays a major role. As a striking example, the MWL follow-up campaign which led to the association between TXS 0506+056 and IC 170922A was triggered by the *Fermi* Collaboration which reported the flaring state at HE of TXS 0506+056 soon after the neutrino detection (Tanaka et al. 2017). The almost real-time information was possible because *Fermi*-LAT operates in all-sky mode, providing us with an updated view of the gamma-ray sky every few hours. The *Fermi*-LAT follow-up program of neutrino events is described in Garrappa et al. (2024). In addition to the prompt notice on the state of candidate neutrino sources, over almost 15 years, the *Fermi*-LAT collected an extremely large amount of observations for thousands of sources, a large fraction of which are blazars. This allows us to identify sources of interest for MWL and specifically VLBI follow-up campaigns as well as select samples for the statistical study of the properties of candidate neutrino counterparts.

The detection of gamma-ray photons from photo-meson interactions (see Chapter 1) is constrained by the opacity of the gamma-ray radiation, i.e., the probability of gamma-ray photons being absorbed within the emitting region, thereby inhibiting their propagation. In blazars, dense photon regions are thought to be involved in neutrino production processes. However, due to these absorption interactions (the opacity), gamma-ray photons might get trapped or absorbed before leaving the emitting region. Consequently, this could limit the possibility of observing a direct connection between HE/VHE gamma-ray activity and neutrino production. In particular, gamma rays produced via photo-meson interactions undergo further interactions with the ambient medium, generating electron–positron pairs and initiating electromagnetic cascades. Background photons in blazar jets are enough for efficiently fueling the electromagnetic cascading. Gamma rays could then be reprocessed in electromagnetic cascades and not be observable directly.

Several works, such as Boettcher et al. (2022), propose an association between neutrino production and X-ray to soft gamma-ray activity rather than GeV-TeV radiation. Moreover,

they suggest neutrino emission and the gamma-ray radiation observed in blazars could originate in different zones of the central regions. This explains the lack of gamma rays-IceCube neutrinos association. Similar conclusions were drawn by Reimer et al. (2019), Rodrigues et al. (2019), and Petropoulou et al. (2020) by modelling the SED of TXS 0506+056 during the 2014-2015 neutrino flare, when the source was in a low state in the HE band. For the broadband SED interpretation, they took into account the processes needed for the production of the observed neutrino flux and spectrum and found the most probable scenario for the neutrino production from TXS 0506+056 involves a soft X-ray photon field as targets for photo-meson interaction. According to their model, the associated pair cascade produces a GeV flux that is too low to explain the GeV observations in 2014–2015. They conclude that the HE spectrum of TXS 0506+056 observed during that period cannot be associated with the mechanism generating neutrinos. Instead, they propose that the GeV flux is produced in a zone which is different from the neutrino production site. Keivani et al. (2018) presents a single-zone interpretation of the TXS 0506+056 SED during the flaring state and the neutrino event.

Beyond the specific findings, within the context of the neutrino-blazar connection, SED modelling emerges as a fundamental tool for comprehending the processes of acceleration and emission mechanisms, for both source-by-source and for population analyses (e.g., Tavecchio et al. 2010c; Böttcher et al. 2013; Petropoulou et al. 2015; Cerruti et al. 2015; Oikonomou et al. 2019; Liodakis & Petropoulou 2020; Capel et al. 2022; Rodrigues et al. 2023).

Part I

Blazars at high angular resolution

Chapter 1

Radio astronomy

The dawn of radio astronomy was marked in 1932 by the serendipitous discovery of radio waves emanating from our galaxy, made by the American physicist and radio engineer, Karl Guthe Jansky (Jansky 1933). In 1940, the radio amateur Grote Reber played a crucial role in mapping the sky at 160 MHz, utilizing a 10-meter parabolic antenna in his garden during his spare time. The success of radio astronomy was further boosted during World War II when the development of antennas and receiving systems for radar provided a mature technology for this observing technique. The theoretical basis of radio astronomy was then built through the successful interpretation by Karl-Otto Kiepenheuer, in 1950, who suggested that electrons and magnetic fields were diffuse in the interstellar medium, the former as a component of cosmic rays (Kiepenheuer 1950). In the same year, the idea that the radio emission observed by Karl Guthe Jansky in 1932 was produced by relativistic electrons in motion in the magnetic fields of stars was debated and largely accepted by the community.

Nowadays, radio sky samples a large number of celestial objects. Radio observations are fundamental in the study of many objects and phenomena such as the Milky Way, the interstellar medium, radio galaxies and quasars, pulsars, dark matter distribution through the 21 cm line of neutral hydrogen, as well as large-scale structures as radio halos and relics in galaxy clusters. Among the most important contributions of radio astronomy is the study of the CMB radiation, which manifests predominantly in the radio band.

As introduced in Chapter 1 and Chapter 2, below approximately 10 GHz, i.e. at radio frequencies, the synchrotron emission from relativistic electrons surpasses thermal emission. Synchrotron emission is closely tied to particle acceleration, produced by the interplay of magnetic fields and relativistic electrons, either directly accelerated or produced as secondary particles. The first non-thermal view of the universe was indeed provided by radio observations. The unique capability of reaching milliarcsec angular resolution (through VLBI) and the ability to conduct observations even during daylight made the radio band an exceptional window to the Universe, in particular, in observing the cosmic acceleration sites (see, e.g., Chapter 2). Simultaneous observations across different observatories, including radio facilities, provide the tool for exploring non-thermal signatures across a broad spectrum and interpreting the SED and variability behaviours of objects emitting non-thermal radiation. This is particularly key for transient objects and high-variable sources.

The Earth's atmosphere and ionosphere are transparent to wavelengths from 1 cm to 10 m, corresponding to a frequency range between 30 MHz to 30 GHz. This constitutes the radio window. Water vapour absorption in the atmosphere affects the incoming radiation with shorter wavelengths. Photons with longer wavelengths are instead reflected by the ionosphere. The Earth's atmosphere in the radio window is highly stable, then, the resolving power[1] for radio

[1]In the context of astronomical observations, the resolving power is generally referred to the ability of a telescope or telescope array, to distinguish between closely spaced objects or details in a celestial objects. It is a

imaging is not degraded by atmospheric turbulence, which is instead responsible for the seeing limitation in optical observations. The resolution in radio imaging is only dictated by diffraction, this limit is reached in the optical band only by launching satellites as the Hubble Space Telescope (HST).

The angular resolution, θ, is defined by:

$$\theta \propto \lambda/D \tag{1.1}$$

where λ is the observing wavelength and D is the single-dish diameter[2]. At radio wavelengths – the longest wavelengths of the electromagnetic spectrum – angular resolution of the order of arcminutes cannot be achieved with a single mirror, as in optical telescopes. Still, the so-called single-dish observations, i.e., employing a single radio antenna, are useful for some scientific topics. However, utilizing arrays of radio telescopes, distributed over very large areas, highly enhances the achievable angular resolution. The idea of exploiting multiple elements was introduced in the 1950s opening the way to the *interferometry* technique. For an interferometer, the diameter in Eq. 1.1, is measured as the distances of two (the farthest) radio telescopes of the array, this distance is called baseline. In principle, two antennas can be located arbitrarily far away from each other. The maximum expression of this technique is the VLBI, introduced in previous Chapters, and described in detail in the next Section.

By the second half of the 1960s, VLBI extended to baselines comparable to the Earth's diameter with the Global VLBI, reaching μarcsecond angular resolutions. To achieve even sharper resolution, the concept of at least one element of the interferometer to be placed in space marked the beginning of Space VLBI (Gurvits 2023).

Following this Chapter, a few basic principles of interferometry, with a focus on VLBI, and data analysis will be described. For a comprehensive theoretical background, in particular on VLBI, readers can refer to, e.g., Thompson et al. (2017).

1.1 Basic concepts of interferometry

Radio astronomy is based on fundamental principles of electromagnetism, optics, and wave theory applied to the analysis of radio waves from celestial objects. One of the primary tools used in radio astronomy is the interferometer. The specific use of the Fourier transform and the theory of Fraunhofer diffraction in radio interferometry enables the analysis and interpretation of radio signals that we observe.

The interferometer consists of several antennas working together simultaneously. Although each antenna may see the source as point-like, the combined observation provides a detailed view of the source's brightness distribution in the sky.

The signal reaching the antennas, placed at a certain distance from each other, can be either intensified or diminished when summing all contributions to the detection. Constructive interference occurs when the in-phase signal is amplified by the contribution of all antennas in use, while destructive interference occurs when the signal is diminished by the sum of out-of-phase wavefronts.

measure of the instrument's capacity to reveal fine spatial features and provide clear distinctions between adjacent celestial bodies or structures. The resolving power is determined by factors such as the instrument's aperture size, the wavelength of observation, and the quality of its optics. The term can be referred to spatial resolving power that is the angular resolution for astronomical observations. More details will be given in the rest of this Chapter.

[2]The terms radio telescope, radio antenna and single-dish will be used interchangeably, to mean the reflector for radio observations.

Fraunhofer diffraction theory It describes how radio waves propagate and interact when passing through apertures or slits, such as the antennas of an interferometer. This theory is crucial for understanding how radio waves are detected and interpreted. An interferometer with two antennas can be indeed ideally seen as two point-like apertures through which radiation penetrates. With this approximation, Fraunhofer diffraction theory provides a mathematical model for the behaviour of plane wavefronts passing through a double slit. The resulting diffraction pattern (maxima and minima of intensity) is then displayed on a screen/detector placed at a high distance from the slits.

The electric field passing through the slit as a function of the position on the slit x is described by the equation:

$$g(x) = f(x)e^{-i\phi(x)}e^{-i\omega t} \tag{1.2}$$

where $f(x)$ represents the amplitude of the wave, $e^{-i\phi(x)}$ the phase, and $e^{-i\omega t}$ the temporal component. The wave arrives at a certain point P on the screen with an additional phase contribution dependent on the position from which it originated. Integrating over the entire aperture yields the overall electric field at point P.

The electric field on the screen, $E(\phi)$ expressed in terms of the angular distance from the screen axis, ϕ, is:

$$E(\phi) \approx \int_{-\infty}^{\infty} g(u)e^{2\pi iu\phi}du \tag{1.3}$$

where $u = x/\lambda$, and the term $2\pi iu\phi$ defines the phase. It can be demonstrated that the electric field at a generic point P on the screen is given by the Fourier transform of the Eq. 1.3.

The intensity of the signal received by an antenna, containing both the contribution of resolved sources and a confusion component due to unresolved background sources, is measured in *antenna temperature*, i.e., the temperature that a resistor dissipating the signal power input would have due to Joule effect.

However, the instrument simultaneously records the sum of contributions to noise from the electronics, resulting in a system temperature, $T_{\rm sys}$, which is the sum of antenna temperature, T_A, and electronic temperature, T_R:

$$T_{\rm sys(K)} = T_A + T_R\cdot \tag{1.4}$$

Fourier transform The signal of very distant sources is seen in two dimensions, we then measure the so-called brightness distribution. The third dimension (depth) cannot be resolved. Therefore, we can consider the source surface to be projected to a sphere of a very large radius (the sky). The Fourier transform is employed to convert the temporal signal measured by different antennas into a spectral representation, allowing for information recovery about the brightness distribution of radio sources as a function of frequency. In other words, the Fourier transform enables the analysis of the various frequency components of the radio signal.

The voltages produced in each antenna of a radio interferometer by the incident radio waves converge at the correlator centre, where these signals are synthesised and adjusted for time delays arising from the varying arrival times at distinct antenna locations. Analytically, the output of the correlation processes is the function:

$$V(u,v) = V_0e^{-i\phi} \propto \int_{-\infty}^{\infty}\int_{-\infty}^{\infty} B(x,y)e^{2\pi i(ux+vy)}\,dx\,dy, \tag{1.5}$$

where V_0 and ϕ represent the amplitude and the phase terms of this complex function, known as *fringe visibility* or simply *visibility*. It represents the Fourier transform of the sky brightness

$B(x, y)$ at the (x, y) position. The sky-brightness distribution is recorded for each antenna pair at a specific time, marked by a separation vector (u, v) in the (u, v) plane. This plane is perpendicular to the line of sight and tangent to the sky at the source position, it represents the spatial distribution of baselines as seen in the source frame.

The Fourier transform of a delta function results in constant amplitudes for all baselines in the (u, v)-plane. For a resolved source, the amplitude decreases as a Gaussian for larger (u, v)-distances, assuming a Gaussian distribution of the brightness (Fig. 1.1).

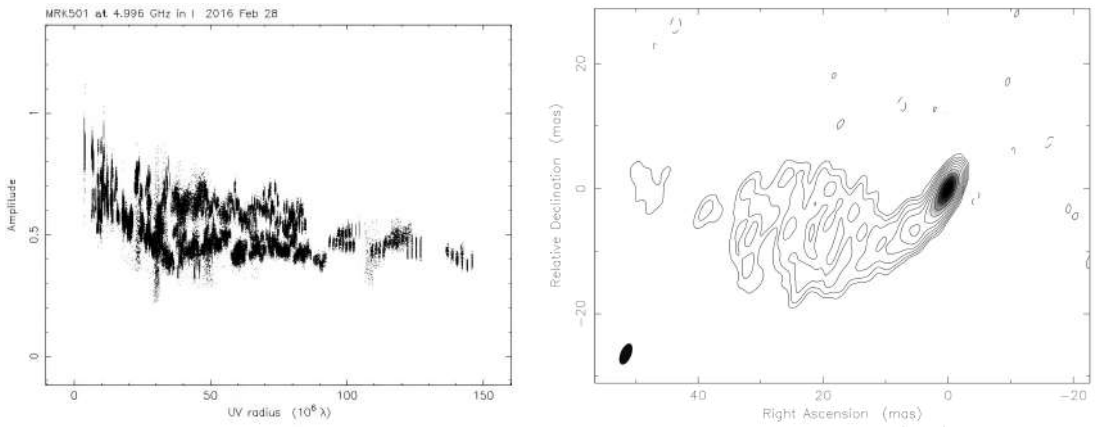

Figure 1.1: In the left panel an example of visibility amplitude (introduced in the next Section), in Jy, versus the (u, v)-distance, expressed in units of $10^6\lambda$, of the BL Lac Markarian 501 is shown. In the right panel, the contour image derived from this observation is represented. The left figure shows the differences in amplitudes sampled by the longer and the shorter baselines, underlying the presence of both large-scale emissions (i.e., the elongated jet) and compact-scale emissions (i.e., the core of the structure). The observation is carried out at 5 GHz ($\lambda = 6$ cm). Project code: S8214.

The amplitude term of visibility provides information about the source flux density, while the phase term gives information about the source structure and position in the sky.

Aperture Synthesis and uv-coverage By correlating the signal from N antennas, $N(N-1)$ baselines are available. For successful radio interferometry, varying baselines are needed to measure different Fourier components since one baseline covers one Fourier component. This is why the antennas of interferometer arrays are placed in specific configurations. However, the sparse nature of antennas results in significant gaps in the Fourier coefficients (poor uv-coverage), a good uv-coverage is crucial for obtaining high-fidelity images of the radio sources. Increasing the integration time of observations allows exploiting the Earth's rotation to improve this sampling. The apparent rotation of the sky causes a change in the position of each baseline on the (u, v), effectively enhancing the observation sampling. This is called Aperture Synthesis. Two examples of plane (u, v) samplings are represented in Fig 1.2. Fringe visibilities are acquired as a function of the baseline, acquisition time interval, frequency channel, and polarization.

1.1.1 Signal correlation

There are two primary types of astronomical interferometers: connected-element interferometers and VLBI networks. In connected-element interferometers, telescopes are linked over short distances to a central correlator sharing a common time and frequency set-up. The short distances allow the use of wide bandwidth – currently up to 64 GHz – from numerous antennas to be transferred and processed at the array correlator in real-time. VLBI networks, instead, comprise a relatively small number of telescopes, of the order of tens, and unlike connected-element arrays,

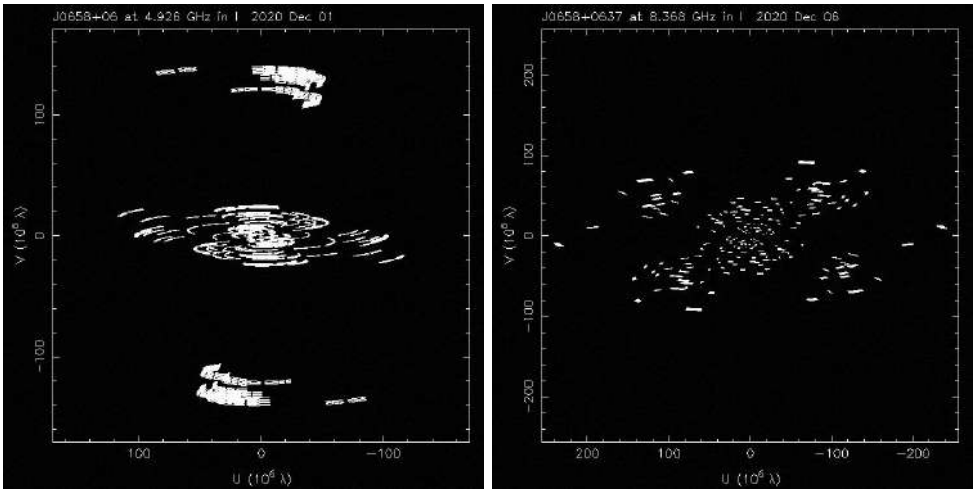

Figure 1.2: (u, v)-plane relative to two different observations. The target source in both the observations is NVSS J065844+063711, these observations are analyzed in Chapter 2. The different uv-coverege is obtained as a result of the different observation set-up and duration. The left panel represents the coverage of the VLBA observation (Project code: BG264A) at 8 GHz which lasted about two hours. The right panel shows the (u, v)-plane of the EVN observation (Project code: EG108) at 5 GHz, which lasted 7 hours allowing for denser coverage. In this case, the distribution of the EVN antennas is however less uniform than the VLBA network leading to larger gaps in the (u, v)-plane.

antennas are frequently heterogeneous with varying performance parameters, such as sensitivity, data formats and they do not share time and frequency set-up. The distances between telescopes on Earth pose challenges for real-time data transfer.

One of the most important connected-element interferometers presently is the Karl G. Jansky Very Large Array (JVLA) in Socorro (New Mexico). It consists of 27 radio antennas, each with a diameter of 25 m, spread out along three 21 km arms of a Y-shaped track. The frequency domain of JVLA ranges from $\sim 1 - 2$ GHz to $\sim 40 - 50$ GHz. The JVLA angular resolution capabilities reach the order of 0.05 arcsec at 43 GHz.

1.2 VLBI arrays

The VLBA is a VLBI array situated in the USA, consisting of 10 identical 25 m-diameter radio antennas (Fig. 1.3). The baseline lengths range from $\sim$ 200 km, between Los Alamos and Pie Town, both situated in New Mexico, up to $\sim$ 8600 km, between Mauna Kea, Hawaii and St. Croix, Virgin Islands. The VLBA operates in a frequency range from 1.2 GHz to 86 GHz, reaching an angular resolution of the order of 0.12 milliarcsec at 86 GHz. Among the huge number of high-level scientific results, VLBA is employed in the long-term monitoring of blazars which is of extreme importance for this work and the study of blazars in general. As discussed in the last Section of this Chapter and anticipated in the previous Chapter, the high angular resolution of VLBI observation is crucial for investigating parsec scale regions of blazars. The VLBI monitoring of these allows us to determine crucial information, for example, the proper motions and kinematic parameters such as the Doppler and Lorentz factors. Two very long-term monitoring are performed with VLBA: the Monitoring Of Jets in Active Galactic Nuclei with VLBA Experiments (MOJAVE, Lister et al. (2018)), conducted mainly at 15 GHz, and the Large VLBA Project BEAM-ME (Jorstad & Marscher 2016), focused on 43 GHz and, in some cases, 86 GHz observations. The latter monitors 34 blazar and 3 radio galaxies while the first observes a sample of hundreds of AGN, most of which show jet emission. Both programs perform

total intensity and polarization information. Over the last tens of years of observation, the two programs allowed important statistical population and single-source studies (e.g., Pushkarev et al. 2009; Lister et al. 2009b; Lister et al. 2009a; Weaver et al. 2022; Jorstad et al. 2017).

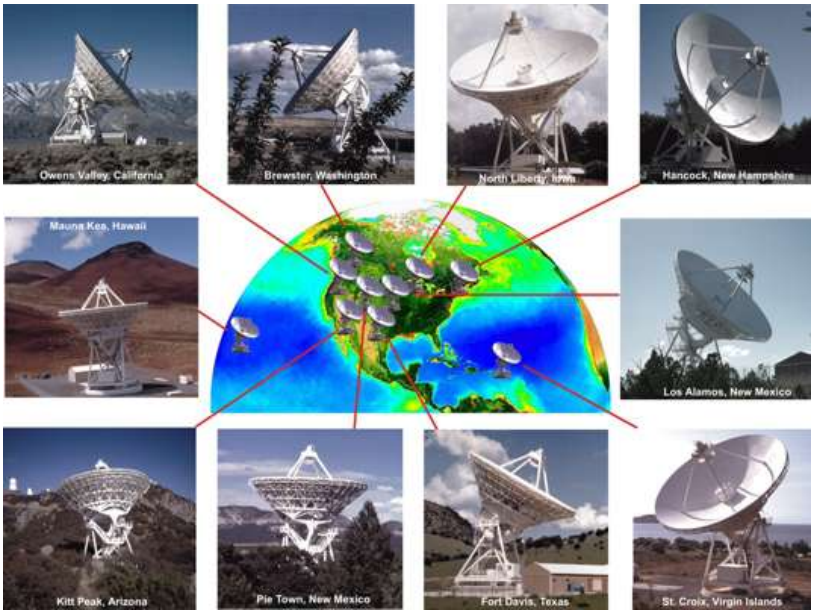

Figure 1.3: VLBA antennas sites and the pictures of the antennas. Credit: Image courtesy of NRAO/AUI and Earth image courtesy of the SeaWiFS Project NASA/GSFC and ORBIMAGE.

The EVN (Fig. 1.4) exploits radio single dishes and arrays spread mainly around Europe in a unique VLBI network. Asian and South Africa radio observatories are also strongly involved in the EVN operations. In addition, the EVN works also in collaboration with the Australian Long Baseline Array (LBA) and the American VLBA. The longest baseline reached by EVN, if only European antennas are involved, is above 7000 km (between Badary, Tunkinsky, Buryatia, in Russia and Robledo de Chavela, in Spain), if African antennas are involved is 9833 km (between Hartebeesthoek, South Africa and Badary, Tunkinsky, Buryatia, in Russia), with Asian is 9294 km (between Tamna, in Korea and Robledo de Chavela, in Spain), while if American VLBA is involved it is 12733 (between Hartebeesthoek, South Africa and Mauna Kea, Hawaii). With these baselines, the angular resolutions at 7 mm are 0.25, 0.19, 0.18, and 0.14 milliarcsec, respectively (from https://www.evlbi.org/capabilities). Due to the heterogeneous nature of the EVN, the antennas participating in the network have receivers working at different frequencies. The main overlap is in a range between 1.2 cm to 21 cm. The biggest single dish of the array is the Effelsberg single dish, with a diameter of 100 m. This and other large single dishes provide enhanced sensitivities than VLBA. Another advantage of EVN is the fast response capability which is crucial for transit objects observations.

Seven antennas distributed over the UK compose the enhanced Multi-Element Radio Linked Interferometer Network (*e*-MERLIN). The largest antenna is Lovell, located at Cheshire in North West England. With a diameter of 76 m, it is the third largest orientable dish on Earth. The other *e*-MERLIN telescopes have diameters from 25 to 32 m. The longest baselines is above 200 km. Due to these baseline lengths, the *e*-MERLIN can be considered a cross between a compact array and a small VLBI network. Also, the *e*-MERLIN is often used as a core element during EVN observations. The *e*-MERLIN observing frequency ranges from 1.2 GHz to 25 GHz, allowing for angular resolutions from 0.2 to 0.02 arcsec at 1.5 and 22 GHz, respectively.

Radio observatories located in China, Japan, and Korea are associated in the EAVN (Fig. 1.5). China contributes with 4 stations, Japan with 12 stations, and Korea with 3 stations, bringing

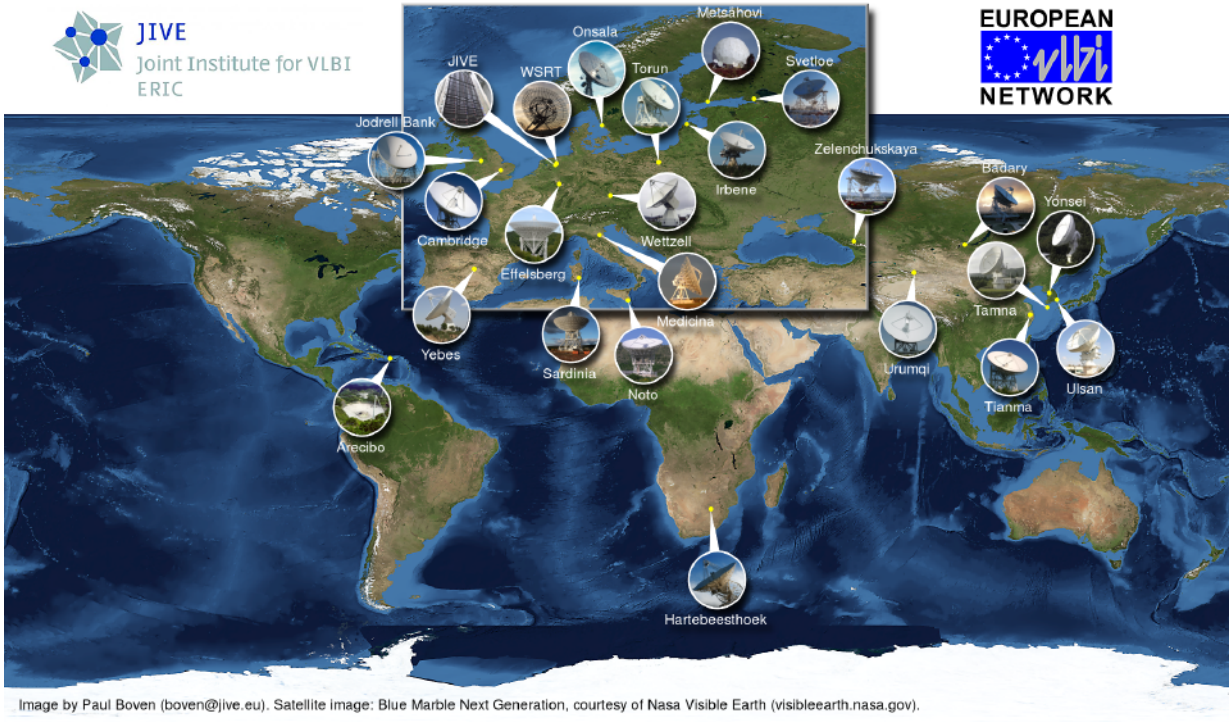

Figure 1.4: Map world with highlighted the EVN antennas location sites and the pictures of the antennas. Unfortunately, the Arecibo antenna shown here has no longer been in operation for a few years. Picture credits: Paul Boven.

the total number of EAVN stations to 19. As for EVN, the telescopes within the network show different characteristics. The frequency domain is similar to the EVN range.

The Korean VLBI Network (KVN) operates as a VLBI network even outside the EAVN. A very important characteristic of the KVN's antennas is the unique receiver system that allows simultaneous observation at four different frequencies: 22, 43, 86, and 129 GHz. Among the antennas involved in the Japanese VLBI Network, four stations compose the VLBI Exploration of Radio Astrometry (VERA), employing specific instruments for high-accurate VLBI astrometry. Particularly important for the EAVN development is the collaboration between KVN and VERA arrays which form the KaVA network.

As mentioned at the beginning of the Chapter, to achieve even higher angular resolution, a radio telescope in Earth orbit can be used, providing greatly extended baselines. The Russian satellite RadioAstron has orbited Earth between 2011 and 2018 and, together with some of the largest ground-based radio telescopes, forms baselines extending up to 350000 km.

1.2.1 SKAO

The groundbreaking advancement in aperture synthesis radio telescopes is represented by SKAO. This array will be made of an extensive network of antennas spread across a vast distance exceeding 3000 km providing a wide collecting surface, reaching up to one square km. SKAO will operate in a frequency range from 50 MHz to 25 GHz, divided into SKAO-Low, operating between 50 MHz and 350 MHz, and SKAO-Mid, operating between 350 MHz and 15 GHz (to arrive to 25 GHz). The headquarters are situated at the University of Manchester's Jodrell Bank Observatory in Cheshire, England, while the antennas will be built in the Southern hemisphere. The antennas will be deployed in unpopulated areas selected to ensure low levels of human-made interference. The SKAO-Low will be located in Australia, precisely at the Murchison Radio-

Figure 1.5: EAVN antennas sites and the pictures of the antennas.

astronomy Observatory on Mileura Station, in the Western Australia region. The SKAO-Mid will be located in South Africa, in particular, in the Karoo region of the Northern Cape Province.

The countries involved in the project so far are 16: Australia, Canada, China, France, Germany, India, Japan, Italy, the Netherlands, Portugal, South Africa, South Korea, Spain, Sweden, Switzerland, and the United Kingdom. Collaboration with many organizations in about 20 more countries is ongoing for the scientific and technical development of the project.

The SKAO-Low configuration will include 31072 antennas, organised in a central core of antennas surrounded by three spiral arms. The same core-three spiral arms configuration is planned for SKAO-Mid but this array will include 197 dishes. According to the project, the maximum baseline reached by SKAO-Low is of the order of 65 km while for SKAO-Mid is 150 km. Both arrays will provide a sub-arcsecond angular resolution.

The large number of antennas will produce a collecting area of 400.000 square meters for SKAO-Low and 33.000 square meters for SKAO-Low. These huge collecting areas, in turn, will extend the sensitivity of the array down the µJy level, allowing the detection of the faintest objects.

The large number of antennas is also designed to achieve a larger FoV that will reach several tens of square degrees at frequencies below 1 GHz. This feature is accomplished by an innovative beamforming technique with which the signal from a chosen set of antennas within the array is combined. In this way, it is possible to simultaneously observe multiple sky regions using multiple independent beams, thereby increasing the survey speed.

Integrating SKAO into the VLBI network is an ambitious initiative within the SKAO projects. The heightened sensitivity of SKAO and the angular resolution achievable by incorporating the array into the VLBI network promise extraordinary scientific outcomes (Paragi et al. 2015). Faint radio sources will be investigated with unprecedented detail. For example, gravitationally lensed radio-quiet quasars are targeted as SKAO-VLBI source of interest. The lensed structure observed in these objects suggests a dark matter configuration within the

lensing galaxy, evidenced by astrometric perturbations in relation to a smooth galaxy model.

Moreover, sensitivity and broad instantaneous bandwidths of SKAO make it an ideal instrument for measuring circular polarization (Agudo et al. 2015). This is typically weak and highly variable in AGN. Detection of transverse circular polarization gradients and Faraday rotation measurements can yield fundamental properties of the jet, such as the strength of the toroidal component of the magnetic field and the magnitude of the jet current. Polarization studies of relativistic jets in AGN then hold promises about the measurement of magnetic field properties and jet composition and electron energy distribution. SKAO-VLBI is crucial for follow-up observations to resolve polarization emission regions and extract key jet physical parameters.

1.3 Calibration of interferometric data

During an observation, the incoming signal is altered by the properties of the individual antennas of the array: the instrument records the convolution between the actual surface brightness and the response of the instrument itself. Moreover, factors such as electronic temperature fluctuations, different path lengths due to varying antenna cables, atmospheric conditions, inaccurate pointing of antennas, ionospheric delays, etc., further contaminate the signal. The calibration of amplitude and phase visibility is then required to prevent the production of artefacts and to correct the phase from the effects of temporal fluctuations and variations within the observing waveband. In this Section the idea of the interferometric calibration is explained while the calibration steps specifically for VLBI data are described.

An interferometer collects visibilities, $V_{\rm obs}$, while the true value of visibilities is given by the following relationship:

$$V_{\rm true} = G_i^{-1} G_j^{-1} V_{\rm obs} \tag{1.6}$$

with i and j indicating the i-th and j-th antenna. The gains, G_i, are complex numbers defined by different contributing factors:

$$G_i = K_i B_i J_i D_i E_i P_i T_i F_i \cdot \tag{1.7}$$

In particular, the components that make up the gains include:

- K_i: Geometrical corrections due to the telescope positions;
- B_i: Bandpass, representing the frequency response of the instrument;
- J_i: Electronic effects, accounting for contributions from the telescope's electronics;
- D_i: Polarization response of the telescope;
- E_i: Optical effects, describing how the telescope dish deforms;
- P_i: Parallactic angle, circular polarization phase difference;
- T_i and F_i: Delay introduced by the troposphere and ionosphere.

Gains in time and frequency are considered independent from each other. Frequency corrections are related to the intrinsic response of the instrument, while time corrections mainly depend on atmospheric variations. Therefore, it is possible to assume that $G_i(\nu, t) = B_i(\nu) J_i(t)$.

Calibration is then the process of applying calibration factors (gains) to the raw data, producing calibrated datasets, and assessing the impact of calibration choices on the final scientific results. The calibration is also important for uniforming the data so that averaging and

consequent enhancement of the signal-to-noise is achievable. Regular monitoring and quality assessment of data are fundamental during each calibration step. This includes flagging – i.e., marks as defective and excluded from further analysis – any data points affected by instrumental anomalies, environmental conditions, or other external factors that cannot be corrected by the calibration.

1.3.1 Calibrators

The gain solutions are retrieved by the observations of the calibrators, known sources for which the radio signal has been previously investigated. These are observed during the science target observations for specific time intervals and at specific times according to their function. Properly selecting calibrators during the observation scheduling phase is crucial for the subsequent data reduction. The calibrators are:

- *Fringe finder* Fringe finder sources have to possess high flux density levels (around 1 Jy) and ideally exhibit compactness to facilitate the calibration of phases and delays for each baseline during an observation. Typically, the fringe finder is observed for about 2 minutes at each observing band for every 3 to 4 hours of observation. They are usually observed around the midpoint and/or conclusion of the observation to ensure the visibility of the fringe finder at all stations.

- *Phase reference calibrator* Phase calibrator has to be a source as close to the science target as possible to be affected by almost the same Earth atmosphere condition. The closeness with the target also reduces the time for moving from one pointing direction to the other. It has to be bright enough, i.e., reach a signal-to-noise ratio above 5, have a well-known position, and be selected from astrometric catalogues. Scans dedicated to the phase calibrator are alternated with the ones dedicated to the target. This is crucial to ensure that the midpoints of each phase reference calibrator scan are separated by no more than the coherence time at the observing frequency. The coherence time is the time interval during which the radio signal remains coherent, meaning it retains its phase constant. The choice of the phase reference calibrator depends on the observing frequency.

- *Bandpass calibrator* The bandpass calibrator is used for characterizing the bandpass response. It is observed for about 2-minute and it has to be a bright source. The fringe finder also serves as the bandpass calibrator.

- *Check sources* In some cases, an additional bright source can be observed to check the calibration quality. Check sources should be calibrated similarly to the science target.

- *Amplitude calibrator* Element-connected interferometers observe amplitude calibrators with known absolute amplitude to perform the conversion between the instrument units to physical units. Since sources may lack point-like characteristics and can be variable, in VLBI observations amplitude calibrators are not observed. The amplitude is calibrated using the system temperature $T_{\rm sys}$.

An important corruption factor in radio astronomy is represented by the Radio Frequency Interference (RFI). This refers to any unwanted and artificial signals originating from various human-made sources that can interfere with the detection of astrophysical signals. In particular, radio, television, communication, and radar transmissions can produce strong signals on a frequency range potentially overlapping with frequencies of radioastronomy. Moreover, signals from satellites, including communication satellites and Global Positioning System (GPS) satellites, and devices using wireless communication technologies, such as Wi-Fi, Bluetooth, and

cellular networks, can introduce interference in the radio spectrum. RFI can manifest as narrowband spikes, broadband noise, or even periodic signals across the radio spectrum and must be corrected for.

1.3.2 Interfermeter fundamental quantities

Before describing the steps of interferometric data calibration, it is important to define some fundamental quantities which parameterize the interferometer performance.

- *Angular Resolution*: As seen in the previous Section, the angular resolution of an interferometry is approximately $\theta \sim \lambda/B_{\max}$, with $B_{\max}$ representing the maximum baseline. For a single antenna, the baseline term is replaced by the diameter of the dish (Eq. 1.1. The angular resolution of an interferometer is always greater than that of a single dish, improving proportionally with the increase in the maximum baseline.

- *FoV*: The FoV of an interferometer is defined by the largest individual antenna diameter, D, and it is $\propto \lambda/D$. To cover sky regions larger than the interferometer's FoV, mosaic pointing techniques become necessary. Due to the very high angular resolution, the FoV of VLBI observations are of the order of less than tens arcseconds. The uncertainties on the target source position provide a way to estimate the optimal FoV for an observation – precise astrometry is crucial in the scheduling of VLBI observations. The FoV has indeed to be as large as the accuracy of the target source position to ensure that it is detected within the FoV.

- *Sensitivity*: represents the depth limit of the observation and, therefore, the ability to distinguish a source from the background. Its theoretical definition is:

$$\sigma \propto [\eta\sqrt{N(N-1)A\Delta t\Delta\nu}]^{-1} \tag{1.8}$$

  where η is the correlator's efficiency, N is the number of antennas in the array, A is the geometric area of the antennas, Δt is the data acquisition time, and $\Delta\nu$ is the observation frequency interval (defined by the total bandwidth for the continuum observations or the amplitude of a single channel for the spectral line observations).

- *Maximum Recoverable Scale*: represents the maximum angular scale that an interferometer can observe and is defined as $\theta_{\rm MRS} \sim \lambda/B_{\min}$. For a single antenna, the parameter $B_{\min}$ is again replaced by the diameter of the dish itself, providing a $\theta_{\rm MRS} \sim \lambda/D$. To observe extended sources, it is always preferable to use a compact array configuration or, if necessary, a single dish.

- *Power Pattern*: also known as the beam or point spread function (PSF), it is calculated as the square modulus of the electric field as expressed in Eq. 1.3: $I(\phi) = |E(\phi)|$. In the optical wavelengths, the PSF characterizes the antenna's response to observing a point source at the field centre. An interferometer detects how the electromagnetic waves interact with each other as they are collected by different antennas. This interaction produces a power pattern that describes how the sensitivity of the interferometer varies in different directions in the sky. The power pattern is influenced by the configuration of the antennas in the interferometer, the spacing between them, and the orientation of the system. In simpler terms, it represents the interferometer's response to signals from various directions in the sky. This information is crucial for properly interpreting the collected data and reconstructing the final images. The power pattern is composed of one main lobe and a few secondary lobes. The full width half maximum (FWHM) of the primary lobe offers an estimate of the instrument's resolution.

A priori calibration

Calibration begins with accounting for the properties of the antennas. During observations, gravitational effects lead each antenna dish to be deformed as it adjusts its position to follow the target sources. These effects depend on antenna elevation and source position in the sky, this information is tabulated in the so-called gain curve table. At this stage also the $T_{\rm sys}$ table is employed for accounting for system temperature measurements correlated with weather conditions and receiver performance. These are employed in amplitude calibration, which rescales visibility function amplitudes into physical units (Janskys). The system temperatures are measured at the stations during observations.

Applying solution for $T_{\rm sys}$ and antenna altitude not only converts the amplitude units but it acts on the phases by homogenizing them considering the parallactic angle of each antenna, which changes over time with source tracking.

The standard format for VLBI data is the Flexible Image Transport System - Interferometry Data Interchange (FITS-IDI) file. Correlated data from the correlation centres are provided as FITS-IDI files. These contain calibration data such as tables of flagged data, in which the visibilities or baselines are marked as problematic, and tables containing information related to antenna-based calibration and $T_{\rm sys}$.

The historical software for radioastronomy data analysis is Astronomical Image Processing System (AIPS). In the last few years, the Common Astronomy Software Applications (CASA) Python-based package has been developed and is now being widely used also for VLBI data reduction. This operates with a different data format called Measurement Set (MS). A conversion process is also required to transform the FITS-IDI data into the MS format. These include converting a priori calibration data and flagging information into a format suitable for CASA.

1.3.3 Time and Frequency Calibration

Before discussing the next step of the data calibration, we introduce the *fringe-fitting* concept. The *fringe pattern* represents the variation in phase and amplitude over time of the interferometric signal. This pattern is caused by the difference in the distance travelled by radio waves from different antennas until they converge. In the ideal scenario, when the antennas are perfectly aligned, a regular fringe pattern will be observed. The fringe fitting procedure aims to determine the parameters of the fringe model so that it better fits the observed interferometric signal. These parameters include the source's position in the sky, the structure of the source, and its brightness. The goal is to minimize the differences between the fringe model and the actual signal.

In VLBI observations, the signal is affected by *delays* and *rates*. The delay refers to the additional time a signal takes to travel from a source through the Earth's atmosphere and the instrumental system to reach the receiving antenna. This delay can be caused by various factors, including the Earth's atmosphere, the electronics of the receiving system, and differences in path lengths between antennas in an array. In delay correction, efforts are made to determine and correct this time quantity so that antennas can combine signals in a synchronized way. The rate refers to the change over time of the delay. It indicates how the signal delay changes with time. This variation can be caused by dynamic effects, such as the motion of the source, the motion of the antennas, or other factors influencing signal propagation over time. Rate correction (or *fringe fitting*) aims to determine and correct these variations to obtain a precise correction of the delay throughout the observation.

Therefore, while delay represents the additional time the signal takes to reach the antenna, rates reflect the variation of this delay over time. During fringe fitting, both the delay and the rate are taken into account to obtain accurate solutions for specific time intervals during the

observation.

The actual time and frequency calibration starts with instrumental delay corrections. Contrary to geometrical delays, these are not taken into account during the signal correlation. Instrumental delays are caused by combined noise contribution from the antenna, receivers, and amplifiers used in the signal path. These delays are typically on the order of nanoseconds and they result in jumps in phase between spectral windows (that are the frequency intervals in which the total bandwidth is split). In this step of the calibration procedure, the gain solutions are computed by taking as reference the fringe finder source since it is essential to have a high signal-to-noise ratio within each spectral window independently to eliminate instrumental delay for each of them. The calibration for instrumental delay aims to remove differences in signal paths between individual antennas' spectral windows. So, at this stage, it is assumed that these differences remain constant throughout the experiment, and thus, the calibration is uniformly applied to the entire duration of the experiment.

Once the phase of the phase calibrator has been corrected for the instrumental delays (i.e., jumps in slope in the phase have been corrected as a function of the spectral window), the signal in each spectral window can be averaged to increase the signal-to-noise ratio.

Therefore, delay and rate correction over the whole observation can be computed using the phase reference calibrator. Solutions are found in a time interval adequate to closely monitor the delay across the entire range of the calibrator, that is the coherence time. The integration time is crucial for the success of the procedure because a balance between achieving a favourable signal-to-noise ratio and avoiding coherence loss in the signal due to ionospheric and troposphere variations is needed. An example of the effects of the fringe fitting procedure on the phase of the fringe finder calibrator is shown in Fig. 1.6. Note that the solutions on delay and rate found for the phase reference calibrator during this step are not the ones applied to the fringe finder.

Subsequently, delay and rate solutions are applied to the target source. The rationale behind this approach is that the phase calibrator is both bright and close to the target source in the sky. Calculating atmospheric delays on the calibrator, where there is a substantial signal, allows us to transfer these corrections to the target source, where the signal may be less robust. For sufficiently bright sources fringe fitting can be directly applied to the source. However, in the case of weak sources, a phase calibrator is necessary.

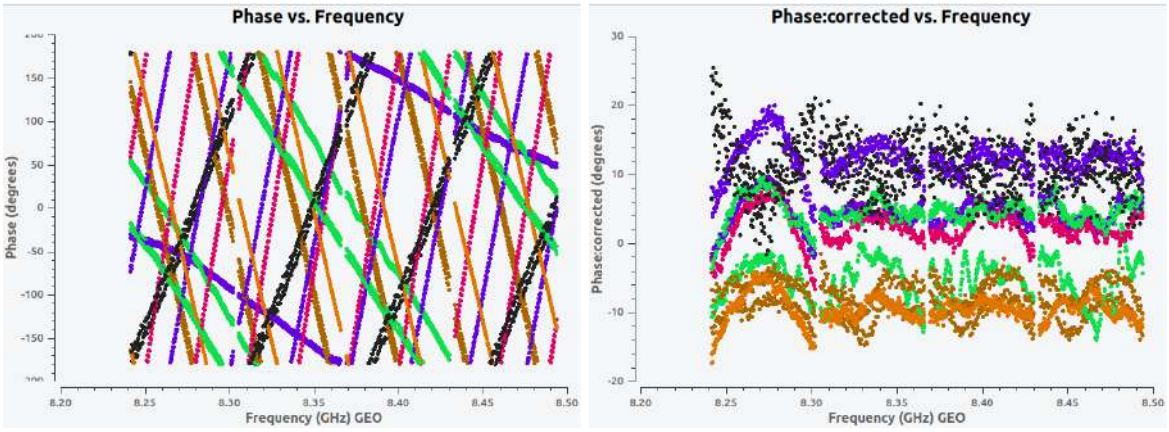

Figure 1.6: Example of a phase calibration. On the left, the phase of the fringe calibrator before the calibration is plotted against the frequency. The plot reveals slopes which correspond to delays that have not been corrected by the geometric model in the signal correlation phase. On the right, the phase of the fringe finder calibrator has been corrected with the gain solutions explained in the text. The example is taken by the observation with project code BG264A, carried out at 8 GHz. The data shown here are averaged in time and the plots are produced with the `plotms` tool in CASA.

Bandpass Bandpass calibration is applied using a bright source to ensure a flat amplitude response across frequency bands. The non-flat bandpass response is another instrumental effect, similar to the instrumental delay previously calibrated. At this stage of the calibration, a complex correction (both amplitude and phase) is computed. A complex bandpass can eliminate non-linear instrumental phase effects, contributing to flattening the phase across the band and improving the signal-to-noise ratio during averaging (Fig. 1.7). Similar to instrumental delay, this correction does not vary significantly over time.

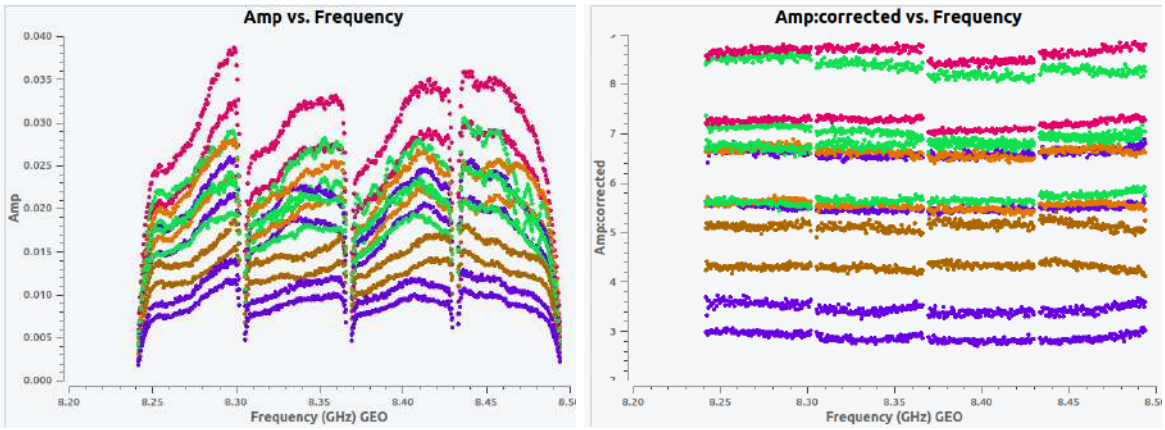

Figure 1.7: Example of a bandpass calibration. On the left, the amplitude of the fringe calibrator is plotted against the frequency. These data are raw data, before the a priori calibration, so they are still in T_{sys} units. On the right, the amplitude (now in Jy) of the fringe finder calibrator has been corrected for the bandpass. The resulted amplitude is flat with respect to the frequency and the instrumental shapes that are visible in the left panel have been corrected. The example is taken by the observation with project code BG264B, carried out at 8 GHz. The data shown here are averaged in time and the plots are produced with the `plotms` tool in CASA.

Once also the bandpass is corrected, the calibration is transferred from the calibrators (fringe finder, phase calibrator, bandpass calibrator) to the target. Subsequently, the calibrated data of the target are averaged across frequencies. Nevertheless, transferring the calibration solutions to the target introduces residual inaccuracies, as these solutions were not originally derived from the target itself. For example, the gain solutions on the phase calibrator are interpolated to find solutions for the target, however, the target phase can change faster than the time interval in which the phase calibrator is observed. Therefore, the target source visibilities can be still affected by minor errors in the amplitudes and phases. These, combined with secondary lobes (resulting from the beam) and the holes in the uv coverage, can lead to post-calibration images affected by artefacts and inaccuracies.

These residual errors cannot be corrected with an external calibrator but require calibration from the target itself. With a good signal-to-noise ratio (bright source), it is possible to perform the *self-calibration*[3], which means refining the calibration using the target itself as a calibrator for the solutions finding.

1.3.4 Imaging and Self-Calibration

imaging The calibrated fringe visibility is the product of the real visibilities and the sampling function, the sampling $S(u, v)$ is the function that describes how the interferometer catches a point-like source with amplitude 1.

[3]The term *self* refers to the fact that the process primarily relies on the data itself, without requiring external calibrators.

$$V_{\text{obs}}(u,v) = S(u,v) \cdot V_{\text{true}}(u,v) \tag{1.9}$$

In the Fourier plane, the product in the second term of this equation translates into the convolution of the real image with the dirty beam, B_{dirty}, which is the Fourier transform of the sampling function. It gives the dirty image, $I_{\text{D}}(x,y)$, i.e., the Fourier transform of the observed visibilities, $V_{\text{obs}}(u,v)$. The above equation, rewritten in the Fourier plane, becomes:

$$I_{\text{D}}(x,y) = B_{\text{dirty}}(x,y) \otimes I(x,y) \tag{1.10}$$

The imaging procedure consists of deconvolving the dirty image with the dirty beam. Various methods exist for image reconstruction, with one of the most commonly used being the CLEAN algorithm (Högbom 1974), explained in the following.

The main assumption is that the image can be divided into a sample of point-like sources, that can be represented by delta functions. In the dirty image (also called residual map), the maximum brightness values, represented by delta functions, and their positions are identified and stored. These are called clean components. They are then multiplied by the dirty beam to transition from ideal delta functions to more complex functions representative of the instrument's response. A certain percentage of the newly created map is subtracted from the initial residual map and then new maximum brightness values are searched in the resulting map. The process continues until the maximum value of the residual map is smaller than the estimated noise of the image. At the end of the process, the residual map is uniform across the entire image plane while clean components are stored. Subsequently, the final image is reconstructed by adding the last (uniform) residual map to the clean components found. This addition is done after convolving the components with a cleaned beam, typically a bidimensional Gaussian function with the same FWHM as the dirty beam. This step is crucial for maintaining the proper resolution of the observation.

The deconvolution process requires providing some parameters:

- *Cellsize* Defines the pixel size in arcseconds. It must be chosen to sample the interferometer's synthesized beam adequately, i.e., the instrument's resolution. To achieve good sampling, the pixel size should be at least 1/3 of the synthesized beam.

- *Image Size* Corresponds to the image square or rectangular sizes expressed in pixels. In the case of a single pointing, it must be at least two times the primary beam of the interferometer, as demonstrated by Nyquist's sampling theorem. For mosaic pointings, it must be at least the size of the sky region to be observed.

- *Weighting* Defines the statistical weight of the visibilities by dividing the (u,v) plane into a grid. Due to geometrical effects, the permutation of antenna pairs always provides a greater number of short baselines than long baselines, causing the outer cells of the grid to have lower density than the central cells. Therefore, the (u,v) plane is better sampled in the central part than in the outer part. By managing the statistical weights of the visibilities obtained from different baselines, the effects of this phenomenon can be adjusted. Setting the parameter as *natural* maintains statistical relevance as the array configuration produces it. The result is greater sensitivity but lower resolution. Another option is to use the *uniform* option, which, on the contrary, smooths out the statistical weight: data acquired from long baselines will have a greater statistical weight than in the natural case, and short baselines will have a lower weight. This improves image resolution but reduces sensitivity. Hybrid alternatives between the two previous options can be chosen by selecting the so-called robust parameter.

- *Threshold* Establishes the threshold at which the iteration of the cleaning process should be terminated. Typically, a value 1.5 times greater than the theoretically expected sensitivity for the observation is used to determine it. In some cases such as long observing time to detect even the faintest components of the sources, the high dynamic range can cause issues. The high dynamic range implies the presence of channels where emission and consequently noise are very strong. For this reason, during the deconvolution operation, it is challenging to reach the threshold. Interactive cleaning can be performed to solve the issue. In the interactive cleaning, boxes where brightness peaks are searched during the deconvolution operation are defined manually. The procedure can be stopped when the residual map is sufficiently uniform.

Self-calibration Self-calibration is employed to refine the model of the observed source, correcting for residual calibration errors mentioned above. Corrections are made to the preliminary model, and the data are then recalibrated. This process is repeated iteratively until the corrections converge to stable values, and the model approaches the real radio emission of the target source. Once self-calibration is completed, the corrected data are used to generate high-resolution images of the source of interest. Errors in the model or low signal-to-noise ratio can make self-calibration dangerous as it modifies the image based on assumptions about its structure. If there are errors in the model or a low signal-to-noise ratio, inaccuracies can propagate. With self-calibration, amplitude and phase fluctuations in time are calibrated.

The standard calibration is performed under the assumption of a point-like source model. However, the target has usually a much more complex structure. A more accurate model of the target is then necessary to obtain more suitable solutions. The self-calibration iterative process generates models that progressively better align with the visibility function. A satisfactory self-calibration is obtained when the differences between the model and the visibility data are no longer significant, that is, in practice, when dividing self-calibrated amplitude by the model and plotting as a function of the *uv* distance the unity is reached. (fig)

The self-calibration starts with the creation of a source model by imaging the source for the first time. The source can exhibit a complex structure. In addition, even if it does not show a complex structure, it can be offset from the centre of the field, and in this case, even if the source is point-like, some structure can be retrieved from this first image.

After creating the model, the gain solutions are found and applied to the visibilities. A new improved image is produced. To check the improvement one can measure the noise level of the image and compare it with the previous image. The improved model is further refined by building a new source model and computing the gain solutions again. The model is improved iteratively by refining the model and recalibrating the data each time.

The self-calibration process begins with phase-only self-calibration first. The time interval for the solution is progressively decreased at each iteration while improvements are monitored. Once satisfied for phase calibration also the amplitude undergoes the same process. Applying self-calibration for amplitudes involves solving for time-dependent gain residuals but not for flux scale, which is fixed by the main calibration. Although CASA is becoming widely used not only for the calibration but also for the imaging, the most suitable software specifically for VLBI imaging and self-calibration is Difmap (Shepherd et al. 1994).

1.3.5 `MODELFIT`

To quantitatively analyze alterations in the position and flux of specific features over time, a small number of components, often a mix of a few delta functions, and circular or elliptical Gaussian functions are used to model the visibilities. The modelling process starts with a single circular Gaussian component approximating the core brightness distribution. The process

follows by iteratively adding components selected to model any residual bright features identified in the residual map. The most commonly used tool for this process is the `MODELFIT` tool of Difmap.

At each `MODELFIT` iteration, the best-fit parameters of the components are determined. These are the flux density, distance from the core, relative position angle, angular sizes, and axial ratio – that determine the point-like, circular or elliptical shape of the components. The best agreement between the model and visibility data is evaluated by a χ^2 test. The selection of the precise number and type (delta function, elliptical or circular) of components is also driven by a χ^2 minimization. To minimize the reduced χ^2, various model parameters can be adjusted and, to reduce the number of free parameters, they can be kept constant. Opting for fewer components, and focusing on the strongest ones also reduces the risk of model-fitting a component that may not be genuinely present. The iterative process of adding components continues until the addition of a new one no longer significantly improves the χ^2 value of the model. Once an accurate model is established, the residual map should mimic noise, as for the CLEAN process.

The model fitting technique is particularly important for the kinematic analysis of blazars, described in Section 2. The model of an earlier epoch can be used as the starting model for the next epoch, assuming that the jet structure does not undergo drastic changes between roughly monthly observations. In this way, individual feature properties are monitored over time and the presence of new components is easily recognised.

1.3.6 Radio image analysis

The final target images are examined to retrieve the scientific results. The flux density of a source is usually determined within a region delimited by $3\sigma_{rms}$ contours. The σ_{rms} represents the noise of the image, which is the signal measured from a source-free region in the image. The radio power at a certain frequency ν is given by:

$$L = 4\pi S_\nu D_L^2 (1+z)^{\alpha-1} \tag{1.11}$$

where D_L is the luminosity distance of the source, calculated according to the adopted cosmology, and α is the spectral index.

1.4 Kinematic and morphological study of blazar jets with VLBI

Powerful and largely employed tools provided by VLBI observations for the study of the blazar jets are briefly introduced below. All provide important insights on the physical condition of the jet system allowing to investigate the acceleration processes. Some of them have been exploited for the study of blazar jets possibly connected with neutrino events in this work (see Chapter 2) while the others are planned to be employed in future development of that study as multi-epoch observations are being carried out. In addition, these approaches provide measurements of physical parameters crucial to model the blazar SEDs.

Apparent velocities The parsec-scale jet morphology of blazars typically exhibits a stationary feature located at the upstream end of the jet observed in milliarcsec resolution of VLBI images. This is always referred to as *core*, which is also often the brightest feature in the jet. However, in some cases, a component downstream from the core may be the brightest. The core identifies the region closest to the black hole, where the jet becomes optically thick at a given frequency. The core location relative to the central black hole indeed depends on the observing frequency. Higher frequency observations allow imaging closer to the black hole.

The jet morphology usually extends a few parsec/kiloparsec – depending on the observing frequency – from the core. The radio emission of the jet can be modelled with one or more components downstream of the core applying the model fit procedure explained in the previous section. The term *knot* is often used to refer to these Gaussian components, corresponding to compact features of enhanced brightness in the jet. These knots can be quasi-stationary or move along the jet, in some cases at apparent superluminal speeds. By measuring the position of the components as a function of the time, the apparent velocities, $\beta_{\rm app} = v_{\rm app}/c$, can be inferred.

Insight from brightness temperature measurements In general, the brightness temperature represents the temperature at which an ideal black body would need to be brought to emit the same radiation as an astronomical object observed at a certain frequency. It is an important concept in radio astronomy for characterizing the brightness of radio sources. The formula for calculating brightness temperature is derived from the Rayleigh-Jeans law, which describes the emission spectrum of a black body.

In radio observations, the temperature is often expressed in units of kelvin and serves as a relative measure of the radio signal intensity coming from a specific source. The brightness temperature, $T_b^{\rm obs}$, of an elliptical Gaussian component in the rest frame of the source can be calculated using the formula (Shen et al. 1997):

$$T_b^{\rm obs} = 1.22 \times 10^{12} \frac{S_\nu}{\nu^2 \theta_{\rm max} \theta_{\rm min}} (1+z) \tag{1.12}$$

where z is the redshift, S_ν is the observed peak flux density at the observed frequency ν, and $\theta_{\rm min}$ and $\theta_{\rm max}$ are the major and minor axes in milliarcseconds.

The brightness temperature is particularly important because it is linked to Doppler boosting. The intrinsic brightness temperature, $T_b^{\rm int}$, is influenced by the Doppler factor δ following $T_b^{\rm int} = T_b^{\rm obs}/\delta$. The observed values of brightness temperature often surpass physical limits, like the equipartition limit, i.e., the condition in which the radiation energy density is equal to the magnetic energy density, or even the threshold of the phenomenon known as Compton catastrophe. The maximum brightness temperature sustainable in the rest frame of the emitting plasma in equipartition is approximately 10^{12} K (Kellermann & Pauliny-Toth 1969) and this can be used to constrain δ by assuming $T_b^{\rm int} < 10^{12}$ K.

The Doppler factor can undergo temporal variations, which are correlated with changes in the total flux density of the source. In addition, the core may have higher Doppler factors at higher frequencies compared to lower frequencies. The monitoring of $T_b^{\rm obs}$ provides information on the Doppler factor behaviour which is lined with the physical condition of the source.

Insight from apparent velocities measurements A key challenge in unified models is to find a way to determine the viewing angles for various AGN types because, as seen in Section, θ is not directly measurable. Measurable quantities related to θ and the Lorentz factor Γ include the apparent superluminal speed and the Doppler factor.

Assuming a relativistic boosting model, the apparent velocity depends on the true velocity $v = \beta c$ and the angle to the line of sight, θ, as expressed by the equation:

$$\beta_{\rm app} = \frac{\beta \sin\theta}{1 - \beta\cos\theta} \tag{1.13}$$

As seen in Chapter 2, the Doppler factor is defined as $\delta = \gamma^{-1}/(1-\beta\cos\theta)^{-1}$
where $\gamma = \frac{1}{\sqrt{1-\beta^2}}$ is the Lorentz factor.

Following Ghisellini et al. (1993), the Lorentz factor and the viewing angle can be computed by observing $\beta_{\rm app}$ using the following relations:

$$\gamma = \frac{\beta_{\rm app}^2 + \delta^2 + 1}{2\delta} \tag{1.14}$$

$$\tan\theta = \frac{2\beta_{\rm app}}{\beta_{\rm app}^2 + \delta^2 - 1} \tag{1.15}$$

Core-shift The core shift refers to a positional change in the radio core when observed at different frequencies, resulting from the frequency-dependent optical depth of synchrotron self-absorption (Blandford & Königl 1979). The core position is identified with the surface at which the optical depth is equal to unity. The optical depth determining the synchrotron self-absorption depends on the electron number density, magnetic field strength, and observing frequency. Assuming a certain profile of electron number density and magnetic field strength as a function of the radial distance from the core (usually a power law), the frequency-dependent core position function can be retrieved and it is in the form $r(\nu) \propto \nu^{-\alpha}$ with α positive spectral index and depending on the electron number density and magnetic field strength trend. According to this relationship, as frequencies increase, the cores progressively shift towards the upper stream and converge toward the central black hole's location. The latter can be estimated by fitting the observed core-shift measurements with the frequency-dependent core position function assumed.

For core-shift measurements, multi-frequency observations are needed. The core position for each jet image can be identified through circular Gaussian model fittings using `MODELFIT` in Difmap. The core offset must be accurately measured (e.g., Croke & Gabuzda 2008). A successful application of the core-shift method is shown in Fig. 1.8

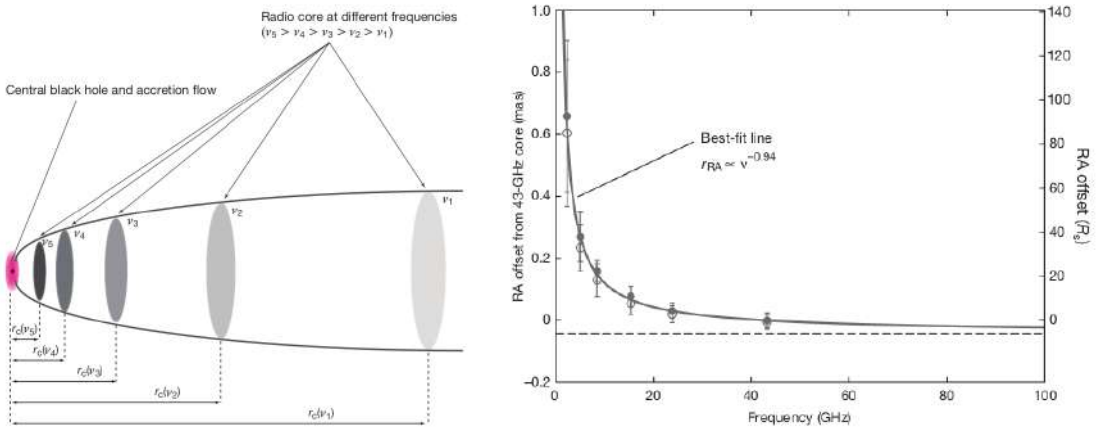

Figure 1.8: On the left, the radio core-shift explanation with a scheme. The central black hole is indicated by the black dot and the surrounded accretion disk by the red ellipse. The distances from the black hole are indicated with vertical ellipses within the jet. In addition, the frequencies of VLBI observation are indicated in correspondence with the radial distance they can penetrate. The core positions are detected in the outer regions as the frequency decreases. On the right, an example of core-shift measurements for M 87 radio galaxy (Hada et al. 2011). The plot has the core offset in right ascension in the y-axis and the observing frequency in the x-axis. The filled and open circle data points refer to two different epochs of observation. The VLBI measurements have been conducted at 2.3, 5.0, 8.4, 15.4, 23.8, and 43.2 GHz. The best-fit solution is shown with the solid line. Both the plots are from Hada et al. (2011)

.

Helical structure The evolution of the orientation of the jet components from the milliarcsecond to arcsecond scales (parsec to kiloparsec) provides insights into the jet geometrical pattern. In particular, the variations in the position angle of the jet components over time and the periodicity of these variations have suggested jet helical motions in many sources (e.g., Lobanov &

Zensus 2001). A graphical representation of the helical model is shown in Fig. 1.9 (left panel). Helical jets can result from precession jet base (Begelman et al. 1980; Linfield 1981) and/or hydrodynamic instabilities at the interface between the jet and the surrounding medium (Hardee 1987). In hydrodynamic instability models, the helix might be triggered by small perturbations in the accretion flow or random perturbations, such as jet-cloud collisions at the onset of the jet. Initial perturbations can be amplified by Kelvin-Helmholtz hydrodynamic instability. Precession could be caused by the disturbance of the jet axis by a secondary black hole in a binary black hole system or from interactions between the wobbling accretion disk and the spinning black hole (Liu & Melia 2002). The investigation of helical patterns in the blazar jets can indeed test the hypothesis on binary black holes at the centre of these sources, as the case of the BL Lac OJ 287 (Valtonen & Pihajoki 2013).

A simple approach to derive the helical pattern is to fit a sinusoidal function to the position angle of the jet components as a function of time. A more accurate helical model description can be found in, e.g., Steffen et al. (1995) in which four different cases with different physical conditions are discussed and the helical model parameters are estimated. An example of a detailed study of the helical pattern of the quasar 3C 345 is shown in the right panel of Fig. 1.9.

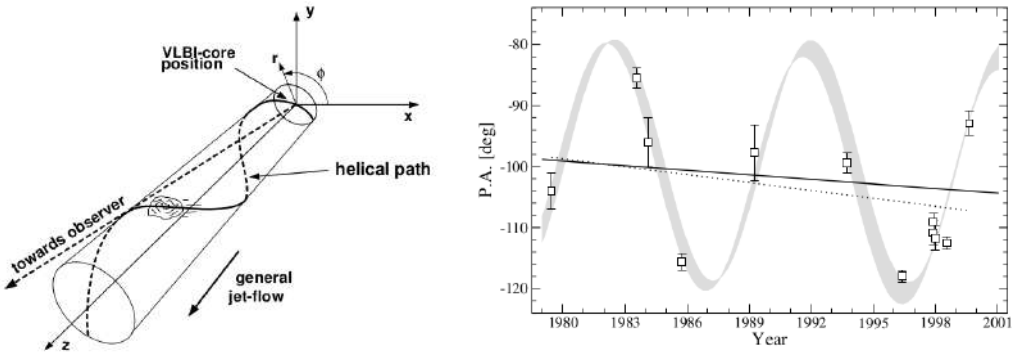

Figure 1.9: On the left, a schematic representation of the helical structure in the blazar jets from Steffen et al. (1995) is shown. On the right, the position angle of various jet components of the quasar 3C 345 is plotted as a function of time (Lobanov & Roland 2005). The authors measured periodic short-term variations, with a period of about 9.5 years and a long-term trend, with a period of about 1600 years, indicated by the dotted line which is retrieved by fitting a linear regression. The similar-sinusoidal shaded area indicates the best fit resulting from the combination of two periodic trends.

Chapter 2

Candidate neutrino-emitting blazars

2.1 Introduction

As seen in Chapter 1 and Chapter 2, relativistic jets of blazars represent ideal particle accelerators in which high-energy neutrinos can be produced (e.g., Mannheim 1995). This theoretical expectation was successfully confirmed in 2017 when the first significant evidence for a blazar-neutrino association was identified. The IceCube-170922A (IC 170922A) event, detected with an energy of 290 TeV and a high probability of being of astrophysical origin, was found in spatial coincidence with the blazar TXS 0506+056 and in temporal coincidence with a gamma-ray flare from this source (IceCube Collaboration et al. 2018a). The MWL campaign, which began after the discovery of the neutrino and the gamma-ray flare, showed that TXS 0506+056 emission increased at almost all bands of the electromagnetic spectrum. The radio observations showed a long-term activity which was delayed with respect to the gamma-ray flare (Acciari et al. 2022).

VLBI observations played a crucial role in investigating the neutrino production mechanism in TXS 0506+056. Using VLBI archival and post-event data of TXS 0506+056, Ros et al. (2020) showed that a rapid expansion of the radio core occurred after the neutrino detection. They also interpreted the limb brightening in the jet of TXS 0506+056 as a sign of transverse velocity structure. This reinforced the idea of a connection with neutrino production given the considerations from previous theoretical studies (e.g. Tavecchio et al. 2014). Li et al. (2020) highlighted a decrease of the magnetic field strength in the VLBI core of TXS 0506+056, inferred from the core shift and variability analysis. They suggested that the lower value of magnetic field strength after the neutrino detection could be linked to the conversion of magnetic energy density to particle energy density. All these features observed in the parsec-scale region of TXS 0506+056 can be framed in the scenario of this source as the emitter of IC 170922A.

Moreover, population studies carried out with VLBI data by Plavin et al. (2020) and Plavin et al. (2021) suggested a correlation between bright VLBI sources and IceCube neutrino events. In particular, they stressed the fact that the region of neutrino production lies at the base of the jet, which is only reachable by the high-resolution VLBI observations. Plavin et al. (2020) and Plavin et al. (2021) performed the same statistical analysis with low-resolution radio data of a sample of non-VLBI-selected sources, finding no evidence of a connection between radio emission and neutrino events.

To explore the association between blazars and neutrinos, we investigated candidate blazar-like neutrino counterparts. In this work, we present high-resolution multi-frequency VLBI follow-ups dedicated to four high-energy neutrino events among those occurring between 2019 and 2020. In particular, due to the considerations in favour of a connection between neutrino events and gamma-ray emission, as in the case of TXS 0506+056, we focused on radio counterparts of gamma-ray blazars close to the neutrino event, most of them lying within the 90% event error region. Adopting this approach, we attempted to determine if recurring morphological

and evolution radio properties, such as those observed in TXS 0506+056, emerge in gamma-ray blazars in spatial coincidence with neutrino emission.

In the following, we first introduce the four neutrino events and the candidate counterparts in Section 2.2. The VLBI observations are presented in Section 2.3, and the results and analysis of the observations are given in Section 2.4. We discuss our findings in Section 2.5 and conclude in Section 2.6. In Appendix 2.7.1, we briefly present results on observed sources, which are less favoured neutrino candidates according to our discussion.

Table 2.1: Properties of IceCube neutrino events analysed in this work.

IC event	Date	Alert type	RA(J2000)	DEC(J2000)	Loc. region (90%) (deg^2)	Energy (TeV)	γ-ray sources (inside 90%)	γ-ray sources (outside 90%)
(1)	(2)	(3)	(4)	(5)	(6)	(7)	(8)	(9)
190704A	04 Jul 2019	Bronze	10h47m24.00s	27°06′36″	20.1	155	2	–
200109A	09 Jan 2020	Gold	10h57m57.60s	11°52′12″	26.6	375	2	1
201021A	21 Jan 2020	Bronze	17h23m16.80s	14°33′00″	5.98	105	1	1
201114A	14 Nov 2020	Gold	07h01m00.00s	06°03′00″	3.66	214	1	–

Notes: (1) IceCube event name; (2) date of the detection; (3) IceCube event classification; (4) and (5) neutrino best-fit position (RA and DEC); (6) localisation area (90% PSF containment); (7) neutrino energy; (8) number of gamma-ray counterparts inside the 90% localisation region; (9) number of gamma-ray counterparts outside the 90% localisation region but taken into account as candidate counterparts.

2.2 IceCube neutrino events

In 2016, the IceCube Neutrino Observatory started a real-time alert programme that releases public notifications on high-energy neutrino detections. These are collected in the GCN Circulars Archive[1]. The aim is to inform the astronomical community in a timely fashion to obtain multi-wavelength data coincident in time and position with the neutrino arrival. We performed VLBI follow-up observations of four IceCube neutrino alerts detected between July 2019 and November 2020.

Considering still poor knowledge about associations between neutrinos and astrophysical sources and the limited sample of neutrino events collected by the IceCube detector every year, we decided to not apply too strict criteria on which events (and relative candidate counterparts) to follow. The intent of our study is rather to present new VLBI results on blazars as possible neutrino counterparts. We devoted follow-up observations to neutrino events that have piqued interest in the MM astronomy community. Most of the events have indeed been investigated with MWL follow-ups. In this context, the VLBI results presented in this work also have the aim of being complementary to other wavelength studies (e.g., Menezes et al. 2021).

In Table 2.1, we report the basic properties of the neutrino events. According to the most recent IceCube classification, neutrino detections are divided into gold or bronze class. Gold alerts are announced for high-energy neutrino track events that are at least 50% (on average) likely to be of astrophysical origin, while bronze alerts have a 30% probability[2]. We targeted two gold and two bronze events. Bronze events still belong to a sample of well-reconstructed neutrino events with an average likelihood of being of cosmic origin only 20% lower compared to the Gold sample. The two Bronze events presented in this work have indeed drawn attention based on the possible connection with astrophysical sources, as was the case in literature with previous detections showing similar likelihoods of astrophysical origin (e.g., the IC 141209A – GB6 J1040+0617 coincidence in Garrappa et al. 2019b).

The energies of the neutrino events vary between ∼100 TeV and 375 TeV and the arrival localisation area spans from ∼4 to 27 square degrees (90% error region). Plavin et al. (2020)

[1]The archive can be consulted at https://gcn.gsfc.nasa.gov/gcn/gcn3_archive.html.
[2]https://gcn.gsfc.nasa.gov/doc/IceCube_High_Energy _Neutrino_Track_Alerts_v2.pdf

pointed out that the 90% error regions around the neutrinos' best-fit positions published in the IceCube notifications do not take into account all the systematic errors, including, for example, the ones due to the non-trivial characterisation of the ice inside which the IceCube detector operates. We did not include an estimation of these systematic errors in the published error regions as Plavin et al. (2020) and other authors did.

The neutrino candidate counterparts targeted by our VLBI follow-ups are the ones that have been notified in the GCN circulars and in the ATels[3] dedicated to the four events. This second network collects notices about follow-up observations (usually quickly triggered after the GCN alerts) of transient objects. In these follow-up campaigns, the selection criteria were not uniquely established but rather defined on a one-by-one case. Our final sample partly reflects this all-encompassing approach and is admittedly formed by a heterogeneous collection, both in neutrino events and candidate counterparts. Also, in light of the possible underestimation of the localisation area, we observed sources outside the 90% error region when these are indicated as possible counterparts in the ATels.

Based on the scenario of a connection between neutrinos and gamma-ray emission in blazars (e.g., IceCube Collaboration et al. 2018a; Kadler et al. 2016), among the candidates reported in the ATels that we observed, we primarily analysed those sources with a gamma-ray association. For this reason, we gave priority to ATels published by the *Fermi* collaboration. The only exception was the case of the last event, IC 201114A, for which we also observed two non-gamma-ray-associated sources as they are reported in the dedicated ATels.

Each neutrino event has between 1 and 3 associated gamma-ray sources, already catalogued or detected after the neutrino event with a dedicated analysis. Most of these are indeed part of the *Fermi*-LAT Fourth Source Catalogue (4FGL Abdollahi et al. 2020) or its incremental version (4FGL-Data Release 2 (DR2), Ballet et al. 2020a). The properties of the gamma-ray candidate counterparts are summarised in Table 2.2. The two gamma-ray sources, 4FGL J1114.6+1225 and 4FGL J1728.0+1216, lie outside the 90% error region of the IC 200109A and IC 201021A events, respectively. The first one, 4FGL J1114.6+1225, was initially identified as the possible counterpart of the neutrino event by Garrappa et al. (2020). The spatial coincidence of 4FGL J1728.0+1216 with IC 201021A was reported in the GCN 28715, sent by the IceCube Collaboration.

In Table 2.3, we report the MWL properties of the sources associated with the gamma-ray ones. In the majority of the cases we used the association reported in the ATels and GCN circulars. For gamma-ray sources already present in the *Fermi* catalogue, we verified that the counterparts proposed in the circulars coincide with the ones in the catalogue. Only in the case of 4FGL J1114.6+1225 the association is not reported in the ATel; in this instance, we consulted the NASA/IPAC Extragalactic Database (NED), according to which the nearest source is the infrared object WISEA J111439.67+122503.7. We identified the possible radio counterpart of this in the Very Large Array (VLA) surveys (see the next section). In these surveys, we found a detection located at a distance of about 2 arcmin from the infrared position reported in the NED.

The classification of the associated sources listed in column 8 of Table 2.3 is retrieved from the *Fermi* catalogue. When this information is not present in the *Fermi* catalogue (in the case of new, non-catalogued, or without associated sources), it is taken from the NED. In the context of blazars as neutrino-emitters, among the gamma-ray-associated sources, we only analysed objects classified as BL Lac or FSRQ. Sources that are not confirmed blazars (although they display some blazar-like features) are presented in Appendix 2.7.1. In Table 2.3 we also present the two non-gamma-ray-associated sources (WISEA J065633.43+053922.7 and NVSS J065916+055252) that have been identified as possible neutrino counterparts in the ATels dedicated to the IC 201021A

[3]https://www.astronomerstelegram.org/

event (see Section 2.3 and Appendix 2.7.1). Taking into account our focus on gamma-ray-associated sources, we consider WISEA J065633.43+053922.7 and NVSS J065916+055252 as less favoured candidates because they are not associated with any gamma-ray source. However, other studies (e.g.,, Plavin et al. 2020; Plavin et al. 2021) argue for a direct connection between neutrinos and VLBI cores, independently of the gamma-ray emission. Therefore, we analyse and briefly discuss these two sources in Appendix 2.7.1.

Throughout the paper, we refer to the radio counterpart of the sources listed in Table 2.3 with the name reported in that table.

Table 2.2: Properties of the candidate gamma-ray counterparts for the neutrino events.

IC event	4FGL or 4FGL-DR2 or Id.	RA(J2000)	DEC(J2000)	neutrino sep. (deg)	$F_{100\,\mathrm{MeV}-100\,\mathrm{GeV}}$ $\times10^{-10}$ph cm^{-2} s^{-1}	Γ	Ref.
(1)	(2)	(3)	(4)	(5)	(6)	(7)	(8)
190704A	J1045.3+2751	10h45m22.32s	27°50′52.80″	0.80	9.8±4.6	1.88±0.16	(a)
	J1049.8+2741	10h49m50.40s	27°40′48.00″	0.79	19.8±8.4	2.13±0.17	(b)
200109A	J1103.0+1157	11h03m05.33s	11°57′55.44″	1.26	270±19	2.41± 0.03	(b)
	J1114.6+1225[a]	11h14m39.36s	12°25′06.24″	4.12	20.2±1.1	2.27±0.22	(b)
	J1055.8+1034	10h55m52.80s	10°34′48.0″	1.38	16±8	2.06±0.18	(c)
201021A	J1728.0+1216[a]	17h28m04.85s	12°16′32.20″	2.56	238±26	2.45±0.05	(b)
	J1725.5+1312	17h23m02.40s	14°23′24.00″	0.16	18±5	2.2±0.2	(d)
201114A	J0658.6+0636	06h58m33.60s	06°36′00.00″	0.81	3.2±1.1	1.97±0.11	(b)

Notes: (1) IceCube event name; (2) 4FGL or 4FGL-DR2 or identification (in case of new sources) of a candidate gamma-ray counterpart; (3) and (4) gamma-ray counterpart coordinates (RA, DEC); (5) angular separation between gamma-ray counterpart and the best-fit position of the event; (6) integral photon flux from 100 MeV to 100 GeV; (7) gamma-ray photon index. Columns (2), (3), (4), and (7) are taken from the LAT 10-year Source Catalog 4FGL/4FGL-DR2. (8) *Fermi* catalogue reference: (a) = 4FGL-DR2 and (b) = 4FGL or 4FGL-DR2; ATels reference: (c) = Garrappa et al. (2020), (d) = Buson et al. (2020b). The sources marked with [a] lie outside the 90% neutrino localisation region.

Table 2.3: Information on other-wavelength associations with the candidate counterparts of neutrino events.

IC event	4FGL/4FGL-DR2 or Id.	Name	Counterpart RA(J2000)	Counterpart DEC(J2000)	d from ν	d from gamma [arcmin]	Class [arcmin]	z
(1)	(2)	(3)	(4)	(5)	(6)	(7)	(8)	(9)
190704A	J1045.3+2751	1WHSP J104516.2+275133	10h45m16.30s	27°51′33.46″	53	1.5	BLL	1.914
	J1049.8+2741	NVSS J104938+274212[b]	10h49m38.80s	27°42′13.00″	47	2.9	G	0.144
200109A	J1103.0+1157	TXS 1100+122	11h03m03.53s	11°58′16.62″	75	0.6	FSRQ	0.91
	J1114.6+1225	WISEA J111439.67+122503.7[b]-A	11h14m37.02s	12°27′13.12″	247	2.2	IrS	-
		WISEA J111439.67+122503.7[b]-B	11h14m29.76s	12°28′03.40″	245	3.8		-
	J1055.8+1034	WISEA J105553.74+103446.5[b]	10h56m47.79s	10°30′28.10″	84	14.2	IrS	-
201021A	J1728.0+1216	PKS 1725+123	17h28m07.05s	12°15′39.49″	154	1.0	FSRQ	0.568
	J1725.5+1312	1RXS J172314.4+142103[b]	17h23m14.12s	14°21′00.62″	12	3.7	XrayS	-
201114A	J0658.6+0636	NVSS J065844+063711	06h58m45.02s	06°37′11.49″	48	3.0	BCU	-
	-	WISEA J065633.43+053922.7	06h56m33.43s	05°39′22.87″	70	-	BC	-
	-	NVSS J065916+055252	06h59m18.00s	08°13′30.95″	132	-	BC	-

Notes: (1) IceCube event name; (2) 4FGL or 4FGL-DR2 or identification (in case of new sources) of candidate gamma-ray counterpart; (3) name of the source associated with the gamma-ray candidate neutrino counterpart and of the candidate neutrino counterparts without a gamma-ray association; (4) and (5) radio coordinates (RA, DEC, inferred from the VLBI observations analysed in this work) of the radio sources associated with the objects indicated in (3). There are two possible radio counterparts associated with WISEA J111439.67+122503.7, which are indicated with A and B. (6) Angular separation of the associated radio source from the neutrino (ν) best-fit position and (7) from the gamma-ray source best-fit position; (8) classification of the associated source from the *Fermi* catalogue or from the NED. The latter catalogue is consulted when the gamma-ray sources are non-associated in the *Fermi* catalogue. These sources are marked with [b]. (9) Spectroscopic redshift of the associated source. WISEA J065633.43+053922.7 and NVSS J065916+055252 have no gamma-ray counterpart reported. (BLL = BL Lac; G = galaxy object; FSRQ = Flat spectrum radio quasar; IrS = infrared source; XrayS = X-ray source; BCU = blazar candidate or unknown in the 4FGL classification; BC = blazar candidate according to the VOU_Blazar tool (the tool is described in Chang et al. 2020), and the BC classification is reported in (Giommi et al. 2020b).

2.3 Observations and data reduction

To investigate the radio structures and variability of the candidates, I analysed both new VLBI observations carried out after the neutrino detection and archival data. Since our new multi-frequency VLBI observations have been performed over longer integration times and at different observing frequencies, these allowed us to produce higher quality and higher fidelity images compared with the available archival data of the targets. Moreover, some of them have never been observed at VLBI resolution before.

2.3.1 New VLBI data

The VLBI follow-up observations of the four events have been performed with the VLBA, EVN (see Chapter 1), and the *e*-MERLIN array. Details about the observations are listed in Table 2.4. Blazar sources are expected to experience variability in the radio emission at the GHz regime on timescales of several weeks (e.g., Orienti et al. 2013b). Therefore, our VLBI observations were carried out with time gaps from the neutrino detection in the range of a few days to one month. The observation frequencies, from 1.5 GHz to 23.5 GHz, were selected to optimise the balance between sensitivity and resolution of the jet structure on different mas-scales. The total bandwidth ranges between 32 MHz, 64 MHz, and 128 MHz (up to 512 MHz for the *e*-MERLIN array; see below). All the sources have been observed at least at two observing frequencies. Only in the cases of PKS 1725+123 and 1RXS J172314.4+142103 we obtained a single-frequency observation. The sensitivity levels of the images are between 20 μJy beam^{-1} and 100 μJy beam^{-1}. The restoring beam sizes range from 0.8 mas to 12 mas in VLBA and EVN images and from 35 mas to 84 mas in *e*-MERLIN images. Antennas participating in the observations are reported in Table 2.4.

In processing all the raw VLBI data, we applied the standard approach of VLBI data reduction described in the AIPS cookbook[4] (Greisen 2003), which includes visibility amplitude calibration, bandpass calibration, and phase calibration (see Chapter 1 for details on the data analysis procedure). This calibration procedure was carried out either with the AIPS software package or with CASA (McMullin et al. 2007). After these steps, we exported the single-source visibilities from AIPS or CASA and imported them into the Difmap software (Shepherd et al. 1994) for self-calibration and imaging. For imaging, the Difmap software follows the CLEAN approach (Högbom 1974) (see Section 1.3.4).

IC 190704A The follow-up observations of the event were focused on the two candidates listed in Table 2.3: the radio galaxy NVSS J104938+274212 and the BL Lac object 1WHSP J104516.2+275133.. The candidates were observed less than one month after the neutrino detection, on 2019 July 18 and 22, for a total of 3 hours of observation at 1.5 GHz, 4.4 GHz, 7.6 GHz, and 8.4 GHz. We separately calibrated the datasets of the two days and then concatenated them into one. After a first inspection of the observation, we decided to dedicate a second, deeper observation (4 hours) only to the blazar-like source, 1WHSP J104516.2+275133 (see Section 2.4). This second observation was performed on 17 January 2020 using the wide C band with two intermediate frequency bands (IF; i.e. sub-bands) centred at 4.7 GHz and two IFs centred at 7.7 GHz. The calibrated data were split into two halves with one half containing the first two IFs and the other half containing the last two IFs. Due to the faintness of the targets and the uncertainties on their coordinates, the observations were performed adopting the phase-referencing mode. The phase-calibrator is a nearby bright FSRQ: J1037+2834 (B1034+2551, taken from the VLBA Calibrator Survey, VCS[5]). It is outside the 90% neutrino error region and

[4] http://www.aips.nrao.edu/cook.html
[5] http://astrogeo.org/vcs/

it is not associated with gamma-ray sources.

IC 200109A The VLBA and EVN follow-up observations of the event included the four targets reported in Table 2.3: one confirmed FSRQ (TXS 1100+122 associated with 4FGL 1103.0+1157) and three unclassified radio sources associated with two gamma-ray objects. In particular, in spatial coincidence with 4FGL J1114.6+1225 (associated with the infrared source WISEA J111439.67+122503.7), there are two possible radio counterparts. Throughout the Chapter, we refer to them using the name WISEA J111439.67+122503.7 followed by the suffixes A and B. The observation was carried out at 8.4 GHz and 23.5 GHz with the VLBA and 4.9 GHz with the EVN. The position of the candidate TXS 1100+122 is constrained with a precision of the order of 0.1 mas (Kovalev et al. 2020a, coordinates from VCS). Also, it is bright enough to allow for fringe fitting in the calibration procedures. Both EVN and VLBA data of the other two candidates, WISEA J111439.67+122503.7 and WISEA J105553.74+103446.5, were calibrated using TXS 1100+122.

IC 201021A About 14 hours of *e*-MERLIN observing time was spent on the two possible IC 201021A counterparts: 1RXS J172314.4+142103 (a radio and X-ray blazar candidate) and the $z = 0.568$ FSRQ PKS 1725+123. The *e*-MERLIN interferometer provides different total bandwidth and angular resolution than VLBA and EVN. The *e*-MERLIN observations were carried out at 5.1 GHz with a bandwidth of 512 MHz. The angular resolution of *e*-MERLIN, of the order of 30–80 mas, corresponds to larger linear scales when compared to the VLBA and EVN ones. Being a bright source, PKS 1725+123 was used as the phase-reference calibrator. The *e*-MERLIN data reduction was performed using the *e*-MERLIN CASA Pipeline v1.1.19 (Moldon 2021).

IC 201114A The VLBA and EVN observations of IC 201114A candidate counterparts are described in Table 2.3. Since the most favoured candidate (see Section 2.4), NVSS J065844+063711, was known to be a faint radio source from the RFC data, both VLBA and EVN observations were carried out in phase-referencing mode. NVSS J065916+055252, also identified as a possible radio counterpart of the neutrino event (Giommi et al. 2020b), is the phase calibrator for NVSS J065844+063711, with an offset of 1.6 degrees. The other candidate reported in Giommi et al. (2020b), WISEA J065633.43+053922.7, was included in the observation schedule as the check source. In some cases, the check-source is added to the VLBA observation schedule to test the goodness of the phase solutions derived from the phase calibration[6].

2.3.2 Archival data

In addition to the proprietary data, we analysed archival VLBI data and publicly available surveys of larger-scale data to have a more complete picture of the characteristics of the sources. Most of the archival VLBI data are retrieved from the RFC, which contains raw and calibrated data and images for thousands of sources. The RFC collects datasets of observations devoted to calibrator monitoring or astrometry experiments. Archival data of PKS 1725+123 used in this work are taken from the MOJAVE (Lister et al. 2018) archive. Therefore, we explicitly refer to MOJAVE data in the case of PKS 1725+123. To describe the extended sources with Gaussian components, we re-imaged the available calibrated data from the RFC and MOJAVE with the Difmap software. The properties of the RFC and MOJAVE images are summarised in Table 2.5. Generally, the short observing duration of archival observations (of the order of minutes) results in a poorly sampled (u, v) plane.

[6]See https://science.nrao.edu/facilities/vlba/docs/manuals/obsvlba/referencemanual-all-pages and Chapter 1.

Table 2.4: Summary of VLBI observations.

IC event	Target	Date	Code	Array	ν (GHz)	$t_{\rm obs}$ (min)	n antennas
(1)	(2)	(3)	(4)	(5)	(6)	(7)	(8)
190704A	1WHSP J104516.2+275133	18+22 Jul 2019	BG261	VLBA	1.5	14+13	9 (−Sc)
					4.4	9+8	
					7.6	9+8	
					8.4	17+18	
		17 Jan 2020	BA133	VLBA	4.7	175	9 (−Kp)
					7.6	175	
	NVSS J104938+274212	18+22 Jul 2019	BG261	VLBA	1.5	13+14	
					4.4	8+9	
					7.6	9+9	
200109A	TXS 1100+122	29 Feb 2020	RG011	EVN	4.9	525	13
		04 Feb 2020	BG263	VLBA	8.4	60	10
					23.5	270	
	WISEA J111439.67+122503.7-A	29 Feb 2020	RG011	EVN	4.9	34	
	WISEA J111439.67+122503.7-B				4.9	34	
	WISEA J111439.67+122503.7	04 Feb 2020	BG263	VLBA	8.4	14	
					23.5	36	
	WISEA J105553.74+103446.5	29 Feb 2020	RG011	EVN	4.9	33	
		04 Feb 2020	BG263	VLBA	8.4	14	
					23.5	36	
201021A	1RXS J172314.4+142103	05 Nov 2020	DD10006	*e*-MERLIN	5.1	486	6
	PKS 1725+123					155	
201114A	NVSS J065844+063711	01+02 Dec 2020	EG108	EVN	4.9	328	16
		06 Dec 2020	BG264A	VLBA	8.4	72	9 (−Hn)
					23.5	198	
	WISEA J065633.43+053922.7	01+02 Dec 2020	EG108	EVN	4.9	20	
		06 Dec 2020	BG264A	VLBA	8.4	18	
					23.5	46	
	NVSS J065916+055252	01+02 Dec 2020	EG108	EVN	4.9	252	
		06 Dec 2020	BG264A	VLBA	8.4	43	
					23.5	139	

Notes: (1) IceCube event name; (2) candidate neutrino counterpart; (3) date of observation; (4) project code; (5) instrument; (6) observation frequency in GHz; (7) on-source time in minutes; (8) number of antennas used in the observations. We report in brackets which antenna was not operating during VLBA experiments. VLBA telescopes are Saint Croix (Sc), Kitt Peak (Kp), Hancock (Hn), Mauna Kea, Brewster, Owens Valley, Pie Town, Los Alamos, Fort Davis, and North Liberty. The EVN telescopes partecipating in the observations are Jodrell Bank (Jb), Onsala (O8), Tianma (T6), Nanshan (Ur), Torun (Tr), Yebes (Ys), Svetloe (Sv), Zelenchukskaya (Zc), Badary (Bd), Irbene (Ir), Westerbork (Wb), Effelsberg (Ef), Medicina (Mc), Noto (Nt), and Hartebeesthoek (Hn). In particular, the RG011 project is performed with Jb, O8, T6, Ur, Tr, Ys, Sv, Zc, Bd, Ir, Wb, Ef, and Hh; the EG108 project is performed with Jb, Wb, Ef, Mc, Nt, O8, T6, Tr, Ys, Hn, Sv, Zc, Bd, Ir, and the *e*-MERLIN stations Cambridge (Cm), Darnhall (Da), Defford (De), Knockin (Kn) and Pickmere (Pi).

The arcsecond-scale extended emission of the sources was studied using VLA survey observations. A comparison between our VLBI data and information taken from VLA surveys helps to determine the nature of the targets, from mas- to arcsecond-scales. In particular, we retrieved the images of the targets from the NRAO VLA Sky Survey (NVSS; Condon et al. 1998), the Faint Images of the Radio Sky at Twenty-cm (FIRST; Becker et al. 1994) survey, and the VLA Sky Survey (VLASS; Lacy et al. 2020). The VLASS images are taken from the Canadian Initiative for Radio Astronomy Data Analysis (CIRADA) catalogue[7] (Gordon et al. 2020). The VLASS is an ongoing project and the final catalogue had not been released yet at the time of the analysis presented here. The VLASS images taken from the CIRADA catalogue were produced using a simple imaging algorithm and no self-calibration was applied. This limits the accuracy of the results that we inferred from these images. The surveys are carried out at 1.4 GHz (NVSS and FIRST) and 3 GHz (VLASS). NVSS and FIRST images are characterised by a beam of $45'' \times 45''$ and $5.4'' \times 5.4''$, respectively, while the VLASS has a resolution of about

[7] www.cirada.ca/catalogues

$3'' \times 2''$. For some sources, the VLASS has two runs, denoted as 1.1 and 1.2 in Table 2.6. This table reports the properties of all the archival images.

Table 2.5: Properties of RFC and MOJAVE observations.

Source	Date	ν (GHz)	$S_{\rm peak}$ (mJy beam^{-1})	$S_{\rm int}$ (mJy)	RMS (mJy beam^{-1})	Beam (mas×mas,°)
(1)	(2)	(3)	(4)	(5)	(6)	(7)
200109A						
TXS 1100+122	30 Apr 2004	2.3	268±27	310±31	0.6	7.4×3.2, −0.1
	30 Apr 2004	8.6	279±28	311±31	0.7	2.0×0.9, 1.1
	01 Aug 2007	8.4	353±35	403±41	0.4	2.2×1.2, 35.1
	20 Feb 2012	8.4	105±11	150±15	0.3	2.0×0.9, 8.0
201021A						
PKS 1725+123	06 Oct 2018	15.3	579±58	622±62	0.10	1.2×0.6, 6.7
	19 Jul 2019	15.3	495±50	509±51	0.10	1.8×0.6, −18.1
	25 May 2020	15.3	460±46	470±47	0.10	1.8×0.7, −21.6
	21 Jan 2020	15.3	530±53	555±56	0.09	1.1×0.5, −4.6
	01 Dec 2020	15.3	638±64	657±66	0.08	1.2×0.6, −4.8
201114A						
NVSS J065844+063711	08+09 Apr 2013*	4.3	18.8±1.8	22.5±2.3	0.2	4.6×1.9, −7.3
	08+09 Apr 2013*	7.6	17.9±1.8	22.7±2.3	0.2	2.8×1.1, −12.2
	19 Oct 2013	7.6	10.7±1.1	15.2±1.5	0.09	2.2×1.3, −3.3

Notes: (1) Candidate neutrino counterpart; (2) date of the observation; (3) observation frequency in GHz; (4) peak brightness in mJy beam^{-1}; (5) integrated flux density in mJy; (6) 1-σ noise level of the image in mJy beam^{-1}; (7) major axis (in mas), minor axis (in mas), and position angle (in degrees, measured from north to east) of the restoring beam. The parameters refer to natural weighting images. Observations marked with * were originally separate datasets that we concatenated into one as these observations were made over a short time interval of a few days.

Table 2.6: Properties of NVSS, FIRST, and VLASS observations.

Source	Survey	ν (GHz)	Date	$S_{\rm peak}$ (mJy beam^{-1})	$S_{\rm int}$ (mJy)
(1)	(2)	(3)	(4)	(5)	(6)
190704A					
1WHSP J104516.2+275133	NVSS	1.4	11 Jan 1994	2.7±0.3	2.7±0.4
	FIRST	1.4	04 Nov 1995	3.5±0.4	3.5±0.4
	VLASS 1.2	3	08 June 2019	2.5±0.4	2.5±0.4
NVSS J104938+274212	NVSS	1.4	11 Jan 1994	18.0±2.0	20.0±2.2
	FIRST	1.4	04 Nov 1995	9.0±1.0	15.6±1.6
	VLASS 1.2	3	08 June 2019	7.1±1.1	11.6±1.7
200109A					
TXS 1100+122	NVSS	1.4	27 Feb 1995	251±25	264±27
	FIRST	1.4	15 Jan 2000	274±27	300±30
	VLASS 1.1	3	22 Nov 2017	282±28	308±31
	VLASS 1.2	3	21 Jul 2020	314±31	344±35
WISEA J111439.67+122503.7-A	NVSS	1.4	27 Feb 1995	2.5±0.2	3.1±0.3
	FIRST	1.4	15 Dec 1995	3.5±0.2	2.9±0.2
	VLASS 1.1	3	28 Dec 2017	3.9±0.6	4.1±0.5
	VLASS 1.2	3	18 Aug 2020	4.0±0.4	3.8±0.4
WISEA J111439.67+122503.7-B	NVSS	1.4	27 Feb 1995	2.7±0.2	3.6±0.3
	FIRST	1.4	15 Dec 1995	2.7±0.2	3.1±0.3
	VLASS 1.1	3	28 Dec 2017	2.5±0.3	2.8±0.3
	VLASS 1.2	3	18 Aug 2020	2.6±0.3	2.9±0.4
WISEA J105553.74+103446.5	NVSS	1.4	27 Feb 1995	343±17	356±18
	FIRST	1.4	15 Jan 2000	333±17	347±18
	VLASS 1.1	3	21 Nov 2017	208±21	204±20
	VLASS 1.2	3	21 Jul 2020	193±19	192±19
201021A					
1RXS J172314.4+142103	NVSS	1.4	27 Feb 1995	$< 0.6^{*}$	
	VLASS 1.2	3	30 Mar 2019	1.2±0.3	0.9±0.1
PKS 1725+123	NVSS	1.4	27 Feb 1995	335±34	348±35
	VLASS 1.2	3	30 Mar 2019	353±35	360±36
201114A					
NVSS J065844+063711	NVSS	1.4	15 Nov 1993	24.3±2.5	23.8±2.5
	VLASS 1.1	3	15 Sept 2017	19.1±1.9	19.7±2.1
	VLASS 1.2	3	09 Aug 2020	14.6±1.5	17.6±1.8
WISEA J065633.43+053922.7-A	NVSS	1.4	15 Nov 1993	53.7±2.7	61.5±3.2
	VLASS 1.1	3	15 Sept 2017	29.2±3.0	36.0±3.6
	VLASS 1.2	3	09 Aug 2020	31.2±3.2	31.0±3.1
WISEA J065633.43+053922.7-B	NVSS	1.4	15 Nov 1993	140.4±7.0	160.3±8.1
	VLASS 1.1	3	15 Sept 2017	47.5±4.8	78.0±7.8
	VLASS 1.2	3	09 Aug 2020	46.2±4.6	61.8±6.2
NVSS J065916+055252	NVSS	1.4	15 Nov 1993	896±90	935±94
	VLASS 1.1	3	15 Sept 2017	723±73	823±83
	VLASS 1.2	3	21 Sept 2020	829±83	910±91

Notes: (1) Candidate neutrino counterpart; (2) survey; (3) observation frequency in GHz; (4) date of observation; (5) peak brightness in mJy beam^{-1}; (6) integrated flux density in mJy. * RMS=0.2 mJy beam^{-1}.

2.4 Analysis and results

2.4.1 Analysis methods

In Table 2.7, we list image parameters of the new VLBI data, using natural weighting. We measured the peak brightness, $S_{\rm peak}$, and the integrated flux density, $S_{\rm int}$, of each target at each frequency. The latter was extracted from a polygonal area on the target images using the `viewer` tool of the CASA software. The area of extraction is the one above three times the RMS contour levels of the images. The RMS was measured within an off-source region on the image plane. The uncertainties on $S_{\rm int}$ are given by

$$\sigma_{S_{\rm int}} = \sqrt{({\rm RMS} \times \sqrt{N_{\rm beam}})^2 + \sigma_{\rm cal}^2}, \tag{2.1}$$

where $N_{\rm beam}$ is the number of beams of the area in which $S_{\rm int}$ is extracted. The error in the calibration procedure, $\sigma_{\rm cal}$, is defined as $\sigma_{\rm cal} = \xi \times S_{\rm int}$, in which we assumed ξ of the order of 10% for VLBA, EVN, and VLASS data and of the order of 5% for *e*-MERLIN, NVSS, and FIRST data. When the source is unresolved, we fitted the emission with a two-dimensional Gaussian function with the `imfit` task in CASA. In this case, the uncertainties on the flux densities were estimated with the sum of squares of the fit error plus the calibration error. At the time of writing, we are aware of an issue with VLBA data taken starting from the first half of the 2019[8]. Our VLBA data at 23.5 GHz could be affected by this issue. However, our images passed the test suggested by the NRAO helpdesk consisting of producing the left and right circular polarization images and checking the differences in the flux measurements. In this section and Section 2.5 we briefly discuss the presence and the implications of additional errors in the flux density scales used.

The compactness of the sources can result in synchrotron self-absorption affecting the lower frequencies. Assuming $S \propto \nu^{\alpha}$, with α being the spectral index, we fitted two power laws for couples of adjacent frequencies to calculate the spectral index pattern over the sampled frequencies. The uncertainty of α is calculated based on the error propagation equation:

$$\alpha \pm \Delta\alpha = \frac{\ln\left(\frac{S_1}{S_2}\right)}{\ln\left(\frac{\nu_1}{\nu_2}\right)} \pm \left|\frac{1}{\ln\left(\frac{\nu_2}{\nu_1}\right)}\right| \sqrt{\left(\frac{\sigma_{S_1}}{S_1}\right)^2 + \left(\frac{\sigma_{S_2}}{S_2}\right)^2}. \tag{2.2}$$

Before calculating the spectral index, both images at each frequency couple had been restored with the same *uv*-range, pixel size and restoring beam size and shape. We used the portion of *uv*-range covered by the observations at the two frequencies. Measurements of the spectral index are reported in Table 2.8.

Following the case of TXS 0506+056 which significantly increased its radio emission during the neutrino event (Kun et al. 2019; Ros et al. 2020; Li et al. 2020), we searched for similar behaviour in our sources. To quantitatively estimate the flux density variability for sources for which archival VLBI observations are available, we adopted the method used by Aller et al. (1992). This consists of calculating the variability index, V, with:

$$V = \frac{(S_{\rm max} - \sigma_{S_{\rm max}}) - (S_{\rm min} + \sigma_{S_{\rm min}})}{(S_{\rm max} - \sigma_{S_{\rm max}}) + (S_{\rm min} + \sigma_{S_{\rm min}})}, \tag{2.3}$$

where $S_{\rm max}$ and $S_{\rm min}$ are the integrated flux densities of the higher and lower state and $\sigma_{S_{\rm max}}$ and $\sigma_{S_{\rm min}}$ are the associated uncertainties. According to Aller et al. (1992), a variability of the

[8] https://science.nrao.edu/enews/14.4/ see "The VLBA Flux Density Scale at 2cm"

order of 10%, which corresponds to $V \geq 0.1$, indicates a significant change in the flux density of the source. From the flux density data reported in Ros et al. (2020), $V \sim 0.1$ in TXS 0506+056 over six months.

For those sources with a known redshift, z, we computed a radio luminosity based on the following formula:

$$L_\nu = 4\pi S_\nu D_L^2 (1+z)^{\alpha-1}, \tag{2.4}$$

where D_L is the luminosity distance of the source. The luminosities reported in Table 2.9 were measured at around 1.4 GHz and about 5 GHz. The spectral index α, adopted for the luminosity computation, is estimated between 1.4 GHz and 3 GHz data from the not simultaneous (separated by ∼20-25 years) NVSS and VLASS.

We characterised the jet emission of extended sources with the `MODELFIT` routine in the Difmap software (see also Section 1.3.5). In this procedure, we fitted the visibility data with elliptical Gaussian functions, referred to as model components. A good fit is achieved when $\sigma_{\rm res} = (1 \pm 0.1)\sigma_{\rm cln}$, where $\sigma_{\rm res}$ and $\sigma_{\rm cln}$ are, respectively, the RMS noise level of the residual and the cleaned image. This ensures that the model components include all the signal from the sources and the model satisfactorily describes the data. We set the uncertainty associated with each component's flux density as 10% of the flux density of the component itself. The precision associated with the polar coordinates of the components, that is the radius and the position angle (PA), depends on the dimensions and the orientation of the image-restoring beam. We assumed that the component centre lies within an ellipse oriented as the beam, and with the major and minor axis equal to the 10% of the beam ones. In some cases, it was necessary to fix the axis ratio or the position of the components (or both) to obtain a reliable fit (see, e.g., Table 2.14 in Appendix 2.7.2).

Table 2.7: Imaging parameters of VLBI observations.

Source	Date	Code	ν (GHz)	$S_{\rm peak}$ (mJy beam^{-1})	$S_{\rm int}$ (mJy)	RMS (μJy beam^{-1})	Beam (mas×mas,°)
(1)	(2)	(3)	(4)	(5)	(6)	(7)	(8)
190704A							
1WHSP J104516.2+275133	18+22 Jul 2019	BG261	1.5	3.5±0.3	3.8±0.4	95	11.6×6.1, −18.4
			4.4	3.3±0.4	3.7±0.5	90	4.3×2.2, −24.5
			7.6	3.8±0.4	3.7±0.5	138	2.4×1.3, −20.7
			8.4	3.4±0.3	3.5±0.4	47	2.1×1.1, −22.8
	17 Jan 2020	BA133	4.7	2.5±0.2	2.7±0.3	27	3.5×1.4, −3.7
			7.6	2.5±0.3	2.7±0.3	21	2.0×0.8, −3.0
200109A							
TXS 1100+122	29 Feb 2020	RG011	4.9	307±31	332±33	68	3.6×2.6, 7.8
	04 Feb 2020	BG263	8.4	380±38	409±41	106	2.2×1.0, −6.3
			23.5	360±36	392±39	118	0.8×0.3, −9.6
201021A							
1RXS J172314.4+142103	05 Nov 2020	DD10006	5.1	0.83±0.03	0.91±0.07	15	34.5×34.5*
PKS 1725+123	05 Nov 2020	DD10006	5.1	323±16	334±17	49	82.4×38.7, 23.9
201114A							
NVSS J065844+063711	01+02 Dec 2020	EG108	4.9	8.4±0.8	12.9±1.3	33	1.8×1.1, 82.4
	06 Dec 2020	BG264A	8.4	9.4±0.9	14.7±1.6	32	2.0×1.0, 2.2
			23.5	8.5±0.9	12.5±1.5	79	1.0×0.4, −13.5

Notes: (1) Candidate neutrino counterpart; (2) date of observation; (3) project code; (4) observation frequency in GHz; (5) peak brightness in mJy beam^{-1}; (6) integrated flux density in mJy; (7) 1-σ noise level of the image in μJy beam^{-1}; (8) major axis (mas), minor axis (mas), and PA (in degrees, measured from north to east) of the restoring beam. The parameters refer to natural weighting images. * this image was produced using a circular restoring beam.

Table 2.8: Spectral index measured with VLBI data.

IC event	Source	Date	ν (GHz)	$S_{\rm peak}$ (mJy beam^{-1})	uv-range Mλ	Beam mas×mas,°	α
(1)	(2)	(3)	(4)	(5)	(6)	(7)	(8)
190704A	1WHSP J104516.2+275133	18+22 Jul 2019	1.5	3.1±0.3	2-40	5.6×4.9, 69.9	0.2±0.1
			4.4	3.7±0.4			
			4.4	3.4±0.4	5-105	2.8×2.1 -57.8	0.2±0.3
			7.6	3.8±0.4			
		17 Jan 2020	4.7	2.3±0.2	5-140	2.2×1.1, −2.0	0.2±0.3
			7.6	2.5±0.3			
200109A	TXS 1100+122	29 Feb 2020	4.9	302±30	4-180	2.2×1.1, −6.3	0.4±0.3
		04 Feb 2020	8.4	378±38			
			8.4	374±37	13-250	1.0×0.7, −10.4	−0.05±0.15
			23.5	355 ±36			
201114A	NVSS J065844+063711	01+02 Dec 2020	4.9	7.7±0.8	4-165	2.0×1.0, 2.2	0.4±0.3
		06 Dec 2020	8.4	9.4±0.9			
			8.4	9.1±0.9	12-250	1.5×0.9, −7.43	−0.02±0.14
			23.5	8.9±0.9			

Notes: (1) IceCube event name; (2) candidate neutrino counterpart; (3) date of observation; (4) frequency in GHz; (5) peak intensity in mJy beam^{-1}; (7) selected uv-range (in Mλ) for the spectral index computation; (8) major axis (mas), minor axis (mas), and PA (in degrees, measured from north to east) of the restoring beam; (9) spectral index.

Table 2.9: Radio luminosity of the sources.

IC event	Source	z	d_L (Mpc)	ν (GHz)	$\alpha_{\rm NVSS}^{\rm VLASS}$	L_ν (WHz^{-1})	νL_ν (erg s^{-1})
(1)	(2)	(3)	(4)	(5)	(6)	(7)	(8)
190704A	1WHSP J104516.2+275133	1.914	14722.8	1.5	−0.2±0.3	$(5.4\pm1.0)\times10^{25}$	$(8.0\pm1.7)\times10^{41}$
				4.4		$(4.2\pm1.1)\times10^{25}$	$(2.3\pm0.5)\times10^{42}$
				4.7		$(3.8\pm0.7)\times10^{25}$	$(1.7\pm1.2)\times10^{42}$
200109A	TXS 1100+122	0.91	5880.5	4.9	0.08±0.19	$(6.4\pm1.2)\times10^{26}$	$(2.8\pm0.5)\times10^{43}$
201021A	PKS 1725+123	0.586	3430.4	5.1	0.06±0.19	$(2.7\pm0.3)\times10^{26}$	$(1.2\pm0.1)\times10^{43}$

Notes: (1) IceCube event name; (2) candidate neutrino counterpart; (3) redshift of the source; (4) luminosity distance in Mpc; (5) frequency in GHz; (6) spectral index measured between 1.4 GHz and 3 GHz (from NVSS and VLASS data); radio luminosity resulting from our observations, expressed in WHz^{-1} in (7) and in ergs^{-1} in (8).

2.4.2 Notes on individual neutrino events

IC 190704A There are two possible gamma-ray counterparts, J1049.8+2741 and J1045.3+2751, that are spatially coincident with IC 190704A. The former is a 4FGL gamma-ray source without any associated low-energy counterpart (Table 2.2). The only radio source within its error ellipse is NVSS J104938+274212. Taking into account the unremarkable radio and optical properties of this source, we only observe it with a few scans. The resulting characteristics of this source are described in Appendix 2.7.1.

The other gamma-ray source, J1045.3+2751, was a new detection at the time of the follow-up campaign (Garrappa et al. 2019a) and was later included in the 4FGL-DR2 catalogue (Table 2.2). The possible counterpart is 1WHSP J104516.2+275133, classified as HBL (Arsioli et al. 2015; Chang et al. 2017). It is located at a redshift of 1.914 which is extremely high for the class of blazars. A possible connection between HBL sources and archival IceCube neutrino events has been suggested by Giommi et al. (2020a) and Padovani et al. (2022b).

1WHSP J104516.2+275133 is unambiguously detected as a compact single component at all the frequency bands in the two epochs. Details of the radio images are listed in Table 2.7, and the total flux density at each frequency in the two epochs is shown in Fig. 2.1. To determine if the

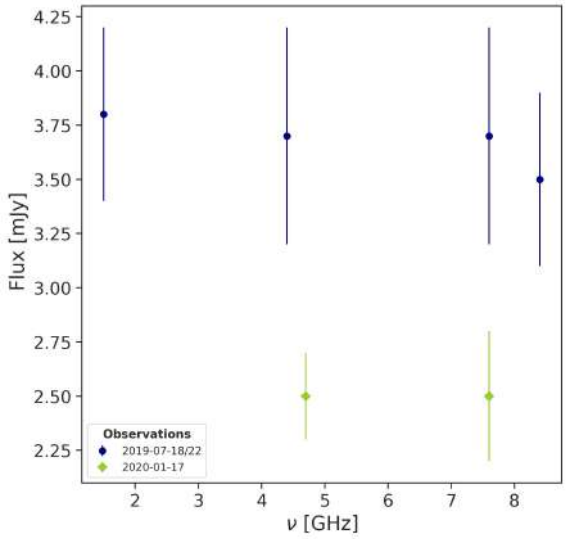

Figure 2.1: 1WHSP J104516.2+275133 total radio flux density at different frequencies and epochs.

source underwent an increase of flux, we compared the VLBA integrated flux densities in the two epochs, measured at around 4 GHz and 7.6 GHz using Eq. 2.3. The resulting variability index, $V \sim 0.03$, between the epochs at both frequencies implies that the source did not experience an increased radio activity after the neutrino detection. It was not possible to check the source's long-term activity level because there were no archival RFC data available. The peak intensity and the total flux density are consistent with each other in both our observations, indicating that 1WHSP J104516.2+275133 is a compact source at VLBA scales. By fitting the emission observed in the second epoch with an elliptical component using the `imfit` task, the major axis (deconvolved from the beam) turns out to be about 6 pc at 4.7 GHz and 7.6 GHz. In the first epoch, the dimensions of the source were not retrieved because it appears as point-like when deconvolved from the beam. From the 4.4 GHz `imfit` analysis we obtained an upper limit for the major axis ≤ 14 pc.

The survey data at 1.4 GHz indicate that the source remains compact on arcsecond scales (Table 2.6). The comparison of arcsecond and mas-scales (even if not simultaneous) does not suggest the presence of any emission on intermediate scales. Carried out a month before the neutrino event, the VLASS observation recorded flux densities in agreement with the NVSS measurements, which were slightly lower than FIRST ones, though consistent within the uncertainties.

From our multi-frequency data, we were able to compute the synchrotron spectral indices of 1WHSP J104516.2+275133 which is ∼0.2 both between 1.5 GHz and 4.4 GHz and between 4.4 GHz and 7.6 GHz (Table 2.8). The compact structure of the source remains self-absorbed, at least until 7.6 GHz, in both epochs. Accounting for the source redshift, the radio luminosity is $\sim 4.2 \times 10^{25}$ W/Hz at 4.4 GHz in the first epoch and $\sim 3.8 \times 10^{25}$ W/Hz at 4.7 GHz in the second one (Table 2.9). For comparison, the radio luminosity of TXS 0506+056 is of the order of 1.8×10^{26} W/Hz at 1.4 GHz (Padovani et al. 2019).

IC 200109A Among the three candidate gamma-ray counterparts of the gold event IC 200109A, the 4FGL catalogue reports highly statistically significant association for only one of them, J11103.0+1157, which is associated with the FSRQ TXS 1100+122. The other two gamma-ray candidates, J1114.6+1225 and J1055.8+1034, can be spatially associated with WISEA J111439.67+122503.7 and WISEA J105553.74+103446.5, respectively. However, these associa-

tions are not confirmed by statistical arguments such as the likelihood ratio method adopted for source associations in the 4FGL (Abdollahi et al. 2020). WISEA J111439.67+122503.7 is located at about four degrees from the neutrino's best-fit position, making its connection with the event less likely compared to the other two candidates. Moreover, both WISEA J111439.67+122503.7 and WISEA J105553.74+103446.5 are not classified as blazars or blazar candidates; thus, we present the VLBI analysis of those two targets in Appendix 2.7.1, while in this section we focus on TXS 1100+122 which was immediately pointed out as potential neutrino source by Kovalev et al. (2020a). The final images for the VLBA and EVN observations of this source are shown in Fig. 2.2. The image parameters are listed in Table 2.7. The total flux density measured from our data with respect to the total flux density from RFC data can be seen in Fig. 2.3.

An elongated structure extending towards the southeast is recognisable at all the observing frequencies. We modelled the source structure with Gaussian components with the `MODELFIT` procedure in Difmap for the new and archival VLBI observations. The properties of the components are reported in Table 2.14 in Appendix 2.7.2. At each frequency, we fitted an elliptical or circular component representing the compact core emission. In addition to the core, five, six, and three other Gaussian models describe the 4.9 GHz, 8.4 GHz, and 23.5 GHz jet structures, respectively. The maximum elongation measured as the distance between the centre of the core component and the centre of the outermost component is about 255 pc, 150 pc, and 22 pc, at 4.9 GHz, 8.4 GHz, and 23.5 GHz, respectively (7.8 pc/mas). The properties of the RFC observations are summarised in Table 2.5. The best-fit parameters of the components are reported in Table 2.14. The model components identified in our observation are not cross-identified in the RFC data. This can be due to either more than 10 years elapsed between the observations or to the absence of intrinsically distinct compact regions in the jet or the different data quality. The absence of well-defined, compact components or stationary components (i.e. found at the same radius in different epochs) indicates that we are sampling a smooth, featureless, and quite homogeneous jet emission. The jet lies at a PA between $\sim$ 140 and 165 degrees (measured from north to east with respect to the image's central pixel) and it does not show any bending. Only the last component identified in our 8.4 GHz data seems to be misaligned with respect to the others, detected at a PA of 170 degrees. It might represent a curved structure undetected in the other observations.

In Table 2.8, we report the spectral index of TXS 1100+122 measured from VLBI data. The source shows an inverted spectrum with a peak around 8.4 GHz. In the 8.4−23.5 GHz frequency range, the spectrum is flat. A flatter spectrum at lower frequencies (between 2.3 GHz and 8.4 GHz) results from the archival RFC data (Table 2.10). Our spectral index measurements disagree with the spectral behaviour observed with the RATAN-600 telescope, as reported by Kovalev et al. (2020b). The synchrotron spectrum derived from the RATAN-600 observation is inverted up to 22 GHz. They measured the highest flux density, 552±39 mJy, at 22 GHz. Around this frequency, we observed a flux density of ∼390 mJy. A RATAN-600 observation was performed on 11 and 14 January 2020, only a few days after the neutrino detection, while our follow-up was carried out more than one month after the detection. The different flux density measurements around 22 GHz and 23.5 GHz could suggest that the radio flare from TXS 1100+122 occurred before or simultaneously to the neutrino emission and that we observed the source once the flare was already extinguished. As reported in the NRAO notice mentioned at the beginning of this section, because the BG263 observation was carried out in DDC mode, the flux density of TXS 1100+122 at 23.5 GHz could be 12% lower than the one that we measured. By adding a factor of 12% to Eq. 2.1 (squaring sum), we obtain a flux density of 392±61, so the upper limit would be 453 mJy. The 22 GHz RATAN-600 lower limit is 513 mJy, which results in a non-negligible difference of about 60 mJy between our and RATAN-600 estimation. Part of this discrepancy may arise from the difference in spatial scales to which RATAN-600 and VLBA are sensitive. Diffuse emission contributes to the total flux density measured by RATAN-600 while

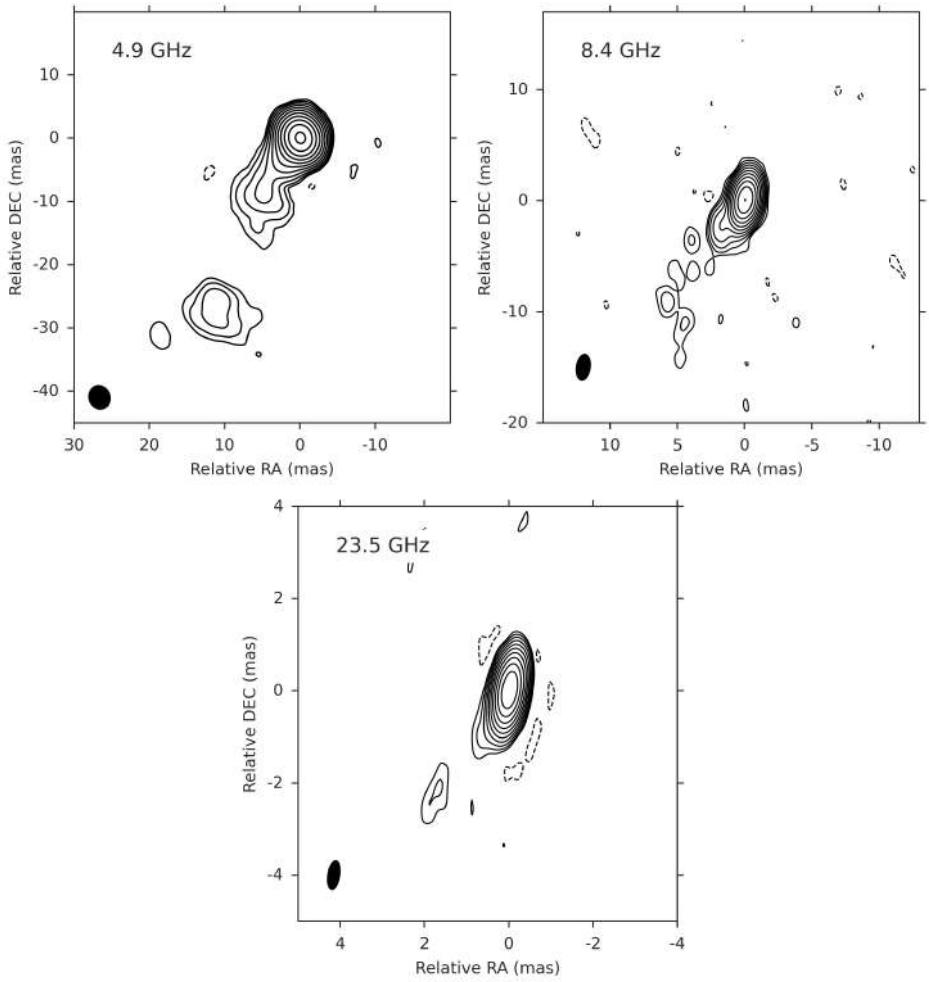

Figure 2.2: EVN-4.9 GHz and VLBA-8.4 GHz and VLBA-23.5 GHz contour images of TXS 1100+122. The contour levels are drawn from 3 × the RMS noise of the images. Contours increase by a factor of 2. The noise level and the beam size of each image are reported in columns (7) and (8) of Table 2.7. The black ellipse in the bottom left corner represents the restoring beam.

it is filtered out by VLBA. For this reason, the flux densities measured by the two instruments must always obey the following relation: $S_{\mathrm{RATAN-600}} \geq S_{\mathrm{VLBA}}$. However, it is not possible to determine if the discrepancy of 60 mJy is entirely attributable to this effect or if it indicates an actual decrease of the flux density of the source in the time range between the RATAN-600 and VLBA observations.

We evaluated the variability of the source with respect to the RFC data taken at 8.6 GHz, which is the frequency closest to our observation frequency. We obtained $V = 0.38$ between 2012 and 2020 (Table 2.11). From NVSS and FIRST data, TXS 1100+122 flux densities at 1.4 GHz are consistent to each other and lower than our observations (Table 2.6 and Table 2.7). Although the different resolution and observing frequency do not allow for a rigorous comparison between the NVSS and FIRST results and the VLBI measurements, a simple explanation for the discrepancy in the flux density is offered by the inverted spectrum in the low frequencies regime (see Table 2.8), which implies low flux density at that frequency. Adopting the spectral index measured from our data, the flux density extrapolated at 1.4 GHz results in agreement with the one inferred from the survey data. The presence of emission on intermediate angular scales seems unlikely. Carried out two years prior to the neutrino detection, the first epoch VLASS observation of TXS 1100+122 reveals flux density measurement in agreement with the NVSS

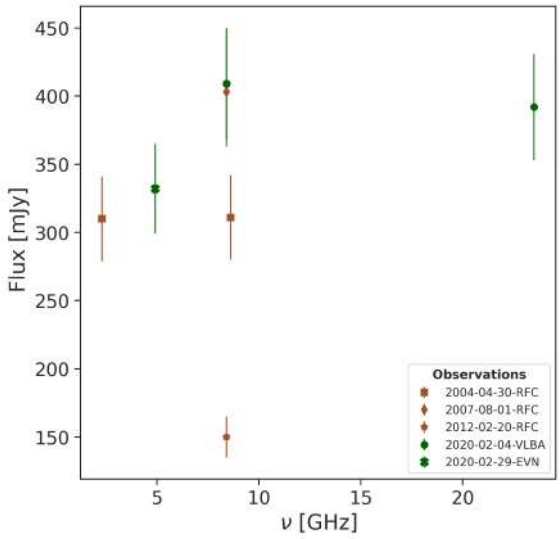

Figure 2.3: TXS 1100+122 total radio flux density at different frequencies and epochs.

and FIRST results. In the second VLASS epoch (a few months after the neutrino detection and after our observations) the source shows higher flux density compared to the first VLASS epoch. The two measurements are, however, consistent with each other within the uncertainties ($V = -0.05$). This suggests there is no significant variability on arcsecond scales, but we also remark that the VLASS data are still preliminary and should not be over-interpreted.

Table 2.10: RFC Spectral index.

IC event	Source	Date	ν (GHz)	$S_{\rm peFak}$ (mJy beam^{-1})	uv-range Mλ	beam mas×mas,°	α
(1)	(2)	(3)	(4)	(5)	(6)	(7)	(8)
200109A	TXS 1100+122	30 Apr 2004	2.3	254±26	6-70	3.1×2.5, 0.5	0.1±0.1
			8.4	302±30			
201114A	NVSS J065844+063711	08+09 Apr 2013	4.3	18±2	4-110	2.9×1.6, 5.5	0.05±0.25
			7.6	19±2			

Notes: (1) IceCube event name; (2) candidate neutrino counterpart; (3) date of observation; (4) frequency in GHz; (5) peak intensity in mJy beam^{-1}; (6) selected uv-range (in Mλ) for the spectral index computation; (7) major axis (mas), minor axis (mas), and PA (in degrees, measured from north to east) of the restoring beam; (8) spectral index.

IC 201021A Two gamma-ray sources have been detected as possible IC 201021A counterparts. We performed the *e*-MERLIN follow-up of this event and the resulting image parameters are reported in Table 2.7.

PKS 1725+123 This source lies about 70 arcmin outside the 90% localisation region of the event. However, being a bright FSRQ experiencing a temporal coincident high state at 15.3 GHz (from the MOJAVE data, described below), it would represent a good candidate for the neutrino association. Our *e*-MERLIN observation shows a jet structure pointing northwest (Fig. 2.4, left). The emission extends for about 700 mas from the core, which corresponds to a distance of ∼4.6 kpc (6.6 pc/mas). The jet remains collimated along this distance. From the 5.1 GHz *e*-MERLIN observation, it results that the emission from the core region dominates over the total flux density of the source. The same emerges from survey observations that sample arcsecond scales (Table 2.6). In addition, our 5.1 GHz flux density and the survey's 1.4 GHz and 3 GHz flux densities are comparable to each other within the errors, indicating the

Table 2.11: Variability index calculated between our VLBI observations and RFC observations.

Source	Obs.	Date	ν (GHz)	beam mas×mas,°	$S_{\rm int}$ (mJy)	V
(1)	(2)	(3)	(4)	(5)	(6)	(7)
200109A						
TXS 1100+122	RFC	30 Apr 2004	8.6	2.0×0.9, 1.1	311±31	
	VLBA	04 Feb 2020	8.4	2.2×1.0, −6.3	409±41	0.04
	RFC	01 Aug 2007	8.6	2.2×1.2, 35.1	403±41	
	VLBA	04 Feb 2020	8.4	2.2×1.0, −6.3	409±41	−0.09
	RFC	20 Feb 2012	8.6	2.0×0.9, 8.0	150±15	
	VLBA	04 Feb 2020	8.4	2.2×1.0, −6.3	409±41	0.38
201114A						
NVSS J065844+063711	RFC	08+09 Apr 2013	4.3	4.6×1.9, −7.3	22.5±2.4	
	EVN	01+02 Dec 2020	4.9	1.8×1.1, 82.4	12.9±1.3	0.17
	RFC	08+09 Apr 2013	7.6	2.8×1.1, −12.2	23.2±2.6	
	VLBA	06 Dec 2020	8.4	2.0×1.0, 2.2	14.7±1.6	0.12
	RFC	19 Oct 2013	7.6	2.2×1.3, −3.3	15.2±1.6	
	VLBA	06 Dec 2020	8.4	2.0×1.0, 2.2	14.7±1.6	−0.09

Notes: (1) Candidate neutrino counterpart; (2) origin of the VLBI observation: RFC or our VLBA or EVN observations; (3) date of observation; (4) frequency in GHz; (5) major axis (mas), minor axis (mas), and PA (in degrees, measured from north to east) of the restoring beam; (6) integrated flux density in mJy; (7) variability index. Negative values of V mean that the source does not show variability (Aller et al. 1992).

dominance of the core emission holds from the smaller scales over larger ones. The `MODELFIT` analysis of the *e*-MERLIN visibility data indicates that the jet contributes less than 5% to the total emission, while the largest contribution is given by the compact core component. Best-fit model parameters are reported in Table 2.15 of Appendix 2.7.2.

With PKS 1725+123 being a bright VLBI calibrator, it has frequently been monitored with VLBI observations over the years. We reported the last five 15.3 GHz-MOJAVE observations taken in epochs close to the neutrino detection, with one precisely conducted on the day of the detection (Table 2.5). The `MODELFIT` analysis that we performed on the MOJAVE data (Table 2.15) does not highlight long-standing features in the jet between 2018 and 2020.

The 15.3 GHz flux density is higher than our almost simultaneous 5.1 GHz observation due to the inverted shape of the self-absorbed synchrotron spectrum of the core. As a consequence of the different scales sampled by the *e*-MERLIN and VLBI data, we could not calculate the spectral index between 5.1 GHz and 15.3 GHz properly, despite the data being taken almost simultaneously. The *uv* range of the two datasets does not overlap. To set an upper limit to the core spectral index using the available data, we first identified the core emission region in the *e*-MERLIN data. To do this, we fitted the visibility points with a delta function and an extended elliptical component representing the jet contribution. The jet component extends on angular scales, which are filtered out by the VLBI observations; then, the *e*-MERLIN delta function alone can be considered as the core emission region. The flux density of this component is 323±16 mJy. We then interpolated the 15.3 GHz-MOJAVE data assuming a linear growth with time between the last MOJAVE epochs and retrieved the 15.3 GHz flux density value at the date of our *e*-MERLIN observation. This results to be 572±57 mJy. Finally, the calculated 5.1 GHz to 15.3 GHz spectral index is 0.5±0.1.

The variability index of the source at 15.3 GHz turns out to be ~ 0.1 in the time range close to the neutrino event (25 May 2020 vs. 01 December 2020), showing that increased activity is

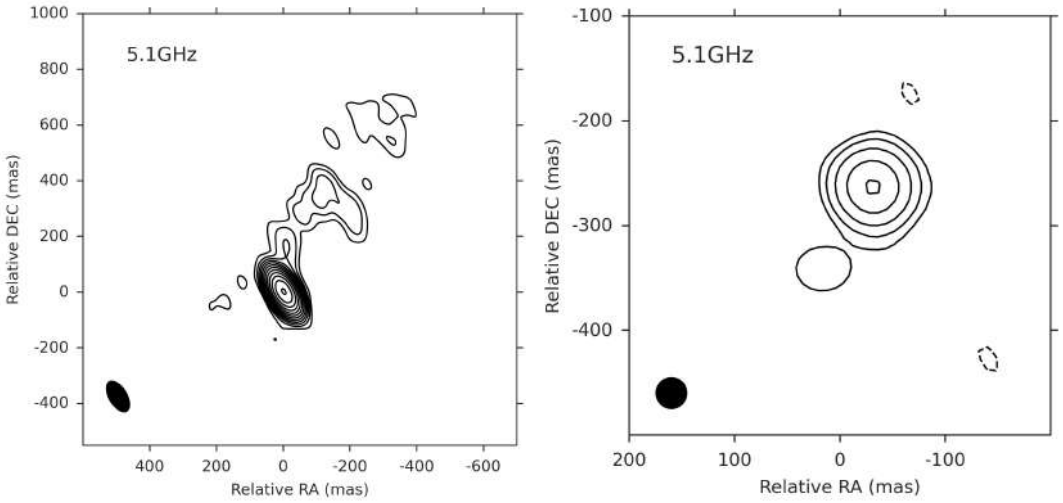

Figure 2.4: *e*-MERLIN contour images of PKS 1725+123 on the left and 1RXS J172314.4+142103 on the right. The contour levels are drawn from 3 × the RMS noise of the images and increase by a factor of 2. The noise level and the beam size of the images are reported in columns (7) and (8) of Table 2.7. The black ellipses in the bottom left corner represent the restoring beams.

detected at least in the nuclear region.

1RXS J172314.4+142103 This is the possible counterpart for the newly detected gamma-ray source, J1725.5+1312, reported in Buson et al. (2020b). This gamma-ray source was significantly detected in the gamma-ray band when only performing the integration of the *Fermi* data taken over ten years of observations (Buson et al. 2020b). This suggests that J1725.5+1312 is a faint source in the gamma-ray band. The association with a radio (although weak) counterpart identified in the VLASS data indicates that it represents a good blazar candidate.

1RXS J172314.4+142103 is detected in our *e*-MERLIN images (Fig. 2.4, right). Its radio structure consists of a main component with a flux density of about 0.96 mJy and a blob component 90 mas southeast of the core with a flux density of about 160 μJy. The source is not detected in the NVSS, allowing us to set an upper limit of about 0.6 mJy (i.e. 3 times the noise measured on the image plane). No FIRST data are available for 1RXS J172314.4+142103, as the source is slightly outside the region covered by the survey. In the VLASS image, 1RXS J172314.4+142103 appears as a compact source with a flux of 0.9±0.1 mJy (Table 2.6), consistently with our result. No indication about the 1RXS J172314.4+142103 variability can be deduced from the available data.

IC 201114A The IC 201114A gold event was found in spatial coincidence with three possible counterparts, two of them are known blazars without an associated gamma-ray source (Table 2.3). Here, we focused on the only candidate with a gamma-ray association: NVSS J065844+063711, which has also been targeted by a multi-wavelength campaign started after the neutrino detection (Menezes et al. 2021). A low-significance excess of archival low-energy neutrinos observed by IceCube and spatially consistent with the source is reported in Hooper et al. (2019). Moreover, a 155 GeV photon from the gamma-ray counterpart of NVSS J065844+063711 has been detected by the *fermi*-LAT on 28 January 2018 (Buson et al. 2020a). The gamma-ray source is also included in the The Third Catalog of Hard *Fermi*-LAT Sources (3FHL; Ajello et al. 2017), suggesting it as a potential very-high-energy-emitting blazar. We present the analysis on the two other candidates in Appendix 2.7.1.

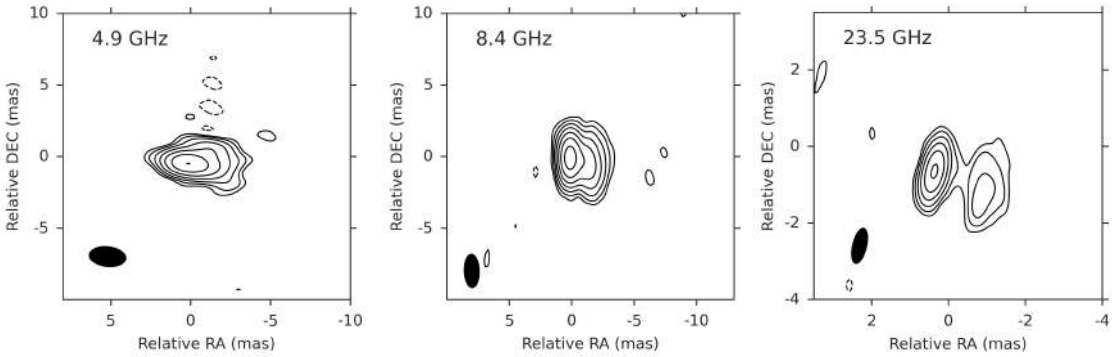

Figure 2.5: EVN-4.9 GHz and VLBA-8.4 and -23.5 GHz contour images of NVSS J065844+063711. The contour levels are drawn starting from 3 × the RMS and are spaced by a power of two. The noise level and the beam size of each image are reported in columns (7) and (8) of Table 2.7. The black ellipse in the bottom left corner represents the restoring beam.

In Fig. 2.5, we show the NVSS J065844+063711 images produced at 4.9 GHz, 8.4 GHz, and 23.5 GHz. The parameters of the images are reported in Table 2.7. The source slightly extends towards the west. With the VLBI data, we were able to partially resolve the jet structure. To represent the morphology of this emission by means of discrete Gaussian components, we performed the `MODELFIT` analysis with the Difmap routine. In the 4.9 GHz image, the best-fit representation of NVSS J065844+063711 is obtained with a point-like core component and two additional components for the jet. We also carried out the `MODELFIT` analysis in the RFC data, finding no evidence of standing shocks as bright knots present at the different epochs. The `MODELFIT`, best-fit parameters are reported in Table 2.16 in Appendix 2.7.2.

NVSS J065844+063711 is compact at arcsecond scales, as deduced from the consistency between the peak brightness (i.e. the core emission) and the total flux density in the NVSS and VLASS observations (Table 2.6). Moreover, the TELAMON[9] program targeted NVSS J065844+063711 after the IC 201114A event. By comparing our results to the TELAMON ones (Kadler et al. 2021), the VLBI total flux density of NVSS J065844+063711 at 4.9 GHz seems to be consistent with the flux density recorded around the same frequency by the Effelsberg single dish, suggesting that the extended emission from this source is negligible and confirming its compact nature.

Table 2.8 reports the spectral indices of the core measured with the VLBI data. The spectrum is self-absorbed between lower frequencies and flat between high frequencies. The same behaviour was observed from the archival RFC data (Table 2.10).

Both NVSS and 2017- VLASS data of NVSS J065844+063711 show a higher flux density compared to our VLBI results. Slightly lower flux density values with respect to the first VLASS epoch are also derived in the second VLASS epoch, taken four months before the neutrino event and three years after the first epoch. Therefore, archival data also seem to suggest that in the time range just before and soon after the neutrino detection, NVSS J065844+063711 was experiencing a low activity state in the radio band (Fig. 2.6). The decrease of the radio flux density on mas scales was up to $V \simeq 0.17$ at around 4.3 GHz between 2013 and 2020 (Table 2.11). On the other hand, the TELAMON monitoring of NVSS J065844+063711 (Kadler et al. 2021) suggests the presence of variability on potentially much smaller timescales.

[9]The monitoring program is described in Kadler et al. (2022).

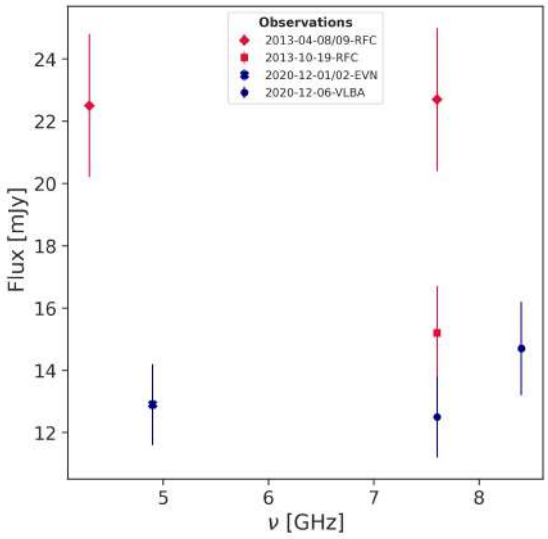

Figure 2.6: NVSS J065844+063711 total radio flux density at different frequencies and epochs.

2.5 Discussion

We conducted VLBI follow-ups of cosmic neutrino events to analyse the status of the radio emission of the blazar sources spatially consistent with these events. We present a total of five sources potentially associated with four IceCube events. We identified one favoured candidate (on the basis of its blazar-like nature and its association with a gamma-ray source) for each event. Just in the case of IC 201021A we investigated two sources; one is the only out-of-90%-neutrino-error-region object studied in detail in this work. It was included in the analysis on the basis of its potentially interesting variability and multi-wavelength characteristics (see Section 2.4). In our search for possible blazar neutrino emitters, we found a heterogeneous sample of objects. In this section, we discuss our results on the properties of these candidate counterparts in comparison with the current knowledge about the neutrino-blazar connection.

The typical radio properties of the blazars, such as the core-dominated jet structures and the inverted and flat spectra, drove our candidate selection among the radio sources spatially coincident with the neutrino events that we observed. These properties are confirmed with our VLBI data. Also in the gamma-ray regime, we found expected values of gamma-ray photon index (Table 2.2); harder gamma-ray photon indices are observed in HSP-like sources, while softer ones are found for FSRQ sources.

2.5.1 Jet morphology and kinematics

Theoretical arguments indicate that compact parsec-scale regions of blazars are sites of efficient neutrino production. As anticipated in Section 2.1 analyses on TXS 0506+056 suggest a connection between this blazar and the neutrino emission. In particular, the increase of the core size of TXS 0506+056 and the opening angle of its jet was identified after the neutrino detection. These were addressed as observational key features indicating the neutrino production (Ros et al. 2020). Moreover, from the evolution of the PA, (Li et al. 2020) inferred a helical structure in the TXS 0506+056 jet. They pointed out the link between this configuration and the occurrence of instabilities at the base of the jet. These mechanisms, in turn, likely drive efficient particle acceleration and the neutrino production in these sites.

All five candidates presented in this work are found to be compact and core dominated from mas to arcsecond scales. We were able to resolve a faint one-sided jet for three of the candi-

dates: the two FSRQ sources, TXS 1100+122 (associated with IC 200109A) and PKS 1725+123 (associated with IC 201021A), and the blazar candidate NVSS J065844+063711 (associated with IC 201114A). In the *e*-MERLIN image of the faintest source of our sample, 1RXS J172314.4+142103 (associated with IC 201021A), we observed only a small blob southeast of the core, while in the HBL object, 1WHSP J104516.2+275133 (associated with IC 190704A), no jet structure was detected in our observations. Performing the `MODELFIT` analysis on the jetted sources for which we have multi-frequency observations, TXS 1100+122 and NVSS J065844+063711, we did not reveal distinct bright knots present in their jets at different frequencies. Also, we did not identify components that can be clearly recognised in the archival RFC data at the same frequencies in our data. From the analysis of two epochs of 2016-MOJAVE data, Lister et al. (2019) highlighted the presence of a discrete component in the jet of PKS 1725+123. They measured an apparent speed of this component of (12 ± 8) μas yr^{-1}; that is, (0.40±0.28)c. A similar value was found by Li et al. (2020) for the closest-to-the-core component of the TXS 0506+056 jet. Testing the kinematics and the evolution of this component with future high resolution VLBI data could become relevant in order to compare the PKS 1725+123 and TXS 0506+056 cases and infer a possible relation with the neutrino production.

The trend of the PA of the TXS 1100+122, PKS 1725+123 and NVSS J065844+063711 jets seems to remain unchanged over the period between the observations (see Table 2.14 for TXS 1100+122, Table 2.15 for PKS 1725+123 and Table 2.16 for NVSS J065844+063711). The analysis of the PA variation with time performed by Li et al. (2020) is not fully compatible with the cases studied here, because we could not identify the comparable jet components in each epoch and because the data are poorly sampled in time.

As far as the relation between neutrino production and blazar core size is concerned, in the case of TXS 0506+056, the source increased its core size from 68 μas to 158 μas in the six months after the neutrino detection (Ros et al. 2020). The apparent expansion occurred at about twice the speed of light at the redshift of TXS 0506+056 ($z = 0.34$, Paiano et al. 2018). As suggested by Ros et al. (2020), this behaviour should test the presence of ongoing hadronic processes of which high-energy neutrinos are very likely products. In the case of TXS 1100+122, the 8.4 GHz core is smaller in our observations than in the 2007 and 2012 RFC observations at the same frequency (see Table 2.14). However, the core linear size is much larger in TXS 1100+122 (about 1.2 pc) than in TXS 0506+056, both before (∼0.33 pc) and after (∼0.76 pc) the apparent superluminal expansion; this is due to TXS 1100+122 being located at redshift 0.91, while TXS 0506+056 is at redshfit 0.34. Based on the RFC and our data, we can speculate that TXS 1100+122 is in its initial compact phase, which could be followed by an expansion phase in the future.

In the case of PKS 1725+123 throughout the 2020-MOJAVE observations (15.3 GHz), the core size did not change significantly within the uncertainties (see Table 2.15). Also in this case, however, the source is more distant than TXS 0506+056 and therefore our angular resolution does not allow us to probe the scales of the expansion discussed by Ros et al. (2020). An important caveat in this context is that Ros et al. (2020) deduced the superluminal expansion of the core from 43 GHz VLBA observations. Due to the small beam size, mm-VLBI observations are a desirable approach for future core size expansion measurements.

We derived the observed core brightness temperatures, $T_b^{\rm obs}$ using Eq 1.12 (see Section 1.4). For TXS 1100+122, we found $T_b^{\rm obs} = 4.1 \times 10^{11}$ K in the 2007 RFC data, $T_b^{\rm obs} = 8.6 \times 10^{11}$ K in the 2012 RFC data, and $T_b^{\rm obs} = 7.7 \times 10^{12}$ K in our 2020 data, all at 8.4 GHz. The brightness temperature depends not only on the core geometric factors but also on its flux density. Differences in brightness temperature values reflect different physical conditions in the core. The observed variation might be a result of a larger Doppler boosting factor in the 2020 data compared to the past data (e.g., Kardashev 2000; Kellermann 2002). In general, such values of $T_b^{\rm obs}$ suggest the presence of a highly relativistic flow. The core brightness temperature of

PKS 1725+123 at 15.3 GHz is $T_b^{\rm obs} = 20.2 \times 10^{12}$ K based on the May 2020 data, $T_b^{\rm obs} = 6.0 \times 10^{12}$ K in the October 2020 data, and $T_b^{\rm obs} = 20.3 \times 10^{12}$ K in the December 2020 data. At 15.3 GHz, Li et al. (2020) observed values of $T_b^{\rm obs}$ in TXS 0506+056 core that are significantly higher in the observing epochs following the IC 170922A event with respect to the previous observations. However, it must be noted that a rigorous comparison between the `MODELFIT` results from our and RFC data is not possible because of the difference between the *uv* sampling of our and RFC data. For this reason, the core components of both TXS 1100+122 and PKS 1725+123 are not unambiguously and uniformly identified in each epoch.

Limb-brightening and transverse structure features are invoked to explain the high-energy neutrino emission when an external (to the jet) seed photon field is lacking. This is the case of BL Lac objects for which a two-layer spine-sheath jet has been proposed (Tavecchio et al. 2014). The two layers of the jet, moving with different Doppler factors (highly relativistic spine and slower external sheath) are thought to provide an energetic enough photon field owing to their relative motion. In this context, limb-brightening and transverse structure are then expected to be observed in possible neutrino counterparts and, indeed, these have been found by Ros et al. (2020) in TXS 0506+056. Interestingly, PKS B1424−418 jet (proposed as counterpart of HESE-35; Kadler et al. 2016) also exhibits hints of transverse structures in its tapered image (Ojha et al. 2010). Based on a simple, by-eye inspection of the flux density contour levels of the images, the limb-brightening configuration is not visible in any of the jetted sources. In the case of NVSS J065844+063711, if the spine-sheath layer structure is present, the low flux density of the source combined with the observing limitations could have prevented the detection of such features.

2.5.2 Flux density variability

A temporal connection between an increased flux density around 22 GHz and the neutrino arrival is deduced in VLBI observations by Plavin et al. (2020) and confirmed with single-dish observations at 15 GHz by Hovatta et al. (2021) for a sample of blazars. Single-source works also support this idea (e.g., Kadler et al. 2016; Ros et al. 2020). According to Plavin et al. (2020), the simultaneity between the neutrino event and the radio flare could be due to an energetic radio outflow arising from particle injection mechanisms near the central black hole. Based on the energetic requirements and the synchrotron opacity constraints, Plavin et al. (2020) and Plavin et al. (2021) were also able to confine the region of the neutrinos' origin in the core of blazars to within a few parsecs at the jet base. The increased radio activity in TXS 0506+056 can be noted in the light curves reported by IceCube Collaboration et al. (2018a), and it results in a significant (according to Aller et al. 1992) variability of $V \sim 0.1$ from the VLBI data referring to the time range between November 2017 and May 2018 (these values of flux density are taken from Ros et al. 2020). We highlight that the variability index defined in Eq. 2.3 is mostly useful to compare the flux density variations in objects which show large differences in flux density levels. In this way, the V-index allows us to quantitatively verify if the emission of a source has significantly varied. However, it could not be sufficient to catch the magnitude of radio flares, as can be seen in the low value of V measured even for the case of TXS 0506+056. The same consideration holds with other variability indicators. Hovatta et al. (2021) applied an activity index to the OVRO light curve data of a sample of blazars to detect the presence of high states. They also claim that their approach could fail to reflect notable flaring states of the sources properly. Plavin et al. (2020) pointed out that the self-absorption in the more compact (and then variable) central regions, together with the contribution of the unresolved diffuse emission, could lead to the underestimating of the variability in the radio activity of the sources.

In April 2021, a 224 TeV-neutrino event with 97% probability of astrophysical origin was detected in the vicinity of TXS 0506+056 by the Baikal-GVD neutrino detector (GVD210418CA,

Allakhverdyan et al. 2024). In particular, TXS 0506+056 falls within the 6.2-degree opening angle of the event's reconstructed direction. Despite the less accurate localization region of this event – that is a *cascade* event, characterized by poorer localization compared to *track* events as IC 190704A –, it provides further evidence of the connection between the radio activity in TXS 0506+056 and neutrino production. Indeed, the GVD210418CA event preceded a 2022 source flare in the 11 GHz radio band detected by the RATAN600 telescope (see Allakhverdyan et al. 2024, for details).

In our sample, one of the five sources, PKS 1725+123, shows a high state of activity in the radio band. We revealed an increased activity ($V \sim 0.1$) from this source's 15.3 GHz MOJAVE data. The neutrino was detected on 21 January 2020 while the 15.3 GHz flux density grew from May 2020 (Table 2.5).

The preliminary results from the RATAN-600 observations, reported by Kovalev et al. (2020b), suggest an increase of the TXS 1100+122 emission soon after the neutrino detection and before our observations (carried out one month after the neutrino arrival). At the same RATAN-600 frequency, we observed a lower value of flux density. As discussed in Section 2.4, the discrepancy between our and the RATAN-600 flux density also holds if we account for the VLBA calibration issues described in the NRAO notice. The discrepancy can be due to either the different sensitivity of RATAN-600 and VLBA to the diffuse emission, or to the variability of the source itself.

An extraordinarily low activity level of TXS 1100+122 was observed in the 2012-RFC data (Table 2.5). If we compare our flux density measurement to this observation, we could speculate, in line with RATAN-600 results, that the source is also, in fact, in a significantly higher state in our observation (Table 2.11). However, with this RFC flux density measurement being from a single isolated epoch, separated by several years from our observation, the indication of an increased flux density does not lead to firm conclusions. In our VLBI data, TXS 1100+122 was in a state of activity compatible with the 2004- and 2007- RFC observations.

While 1WHSP J104516.2+275133 does not seem to exhibit an enhanced flux density and no VLBI archival data of 1RXS J172314.4+142103 are available to check its variability, the last of the five sources, NVSS J065844+063711, is clearly in a low state of activity in the radio band at the neutrino arrival, as deduced by the comparison of our results with the archival RFC observations (Table 2.11). The largest change in the flux density follows by comparing the 2013-RFC data with our EVN observation, both carried out at ∼4.3 GHz. As noted above and reported in several works, the low frequencies are less affected by the activity occurring within the jet base and core (i.e. the region in which the neutrino production is thought to happen). Since we lack archival data of NVSS J065844+063711 at high frequencies, we could not determine the state of activity at these frequencies. However, the lack of an enhanced state of activity is not in contrast to what was found in the case of TXS 0506+056. Indeed, after the IC 170922A event, the inspection of archival IceCube and multi-wavelength data from the direction of TXS 0506+056 resulted in evidence of a neutrino flux excess from that position. In coincidence with this archival neutrino detection, no radio flares have been detected along with other-wavelength flares.

2.5.3 High-energy neutrino production

The origin of neutrinos in blazars can be associated with regions enabling the acceleration of relativistic protons and cosmic rays (e.g., Matthews et al. 2020). These sites can be hosted by the accretion disc and relativistic jet, which offer a favourable environment for hadronic and photo-hadronic interactions that produce neutrinos (e.g., Mannheim 1995; Matthews et al. 2020; Righi et al. 2019; Murase et al. 2020b). The shock acceleration of protons in a turbulent environment must occur over timescales shorter than those involving synchrotron energy loss or

the diffusion of protons away from the acceleration zone (e.g., Zhang et al. 2017).

The shock itself may originate from a diversity of physical processes in the central nuclear region. Jet scenarios include propagating or re-confinement shocks at varying distances from the supermassive black hole (e.g., Ghisellini et al. 2002; Matthews et al. 2020; Zech & Lemoine 2021), magnetic re-connections (e.g., Shukla & Mannheim 2020; Matthews et al. 2020), interaction with transiting gravitationally bound clouds or clumps (e.g., Araudo et al. 2010), or an interaction with the external radiation field (e.g.,, Hoerbe et al. 2020; Winter & Lunardini 2021).

The physical characteristics of the production region can be probed by comparing the acceleration timescale for protons $t_{\rm acc}$ with the dynamical timescale over which any changes are propagated, $t_{\rm dyn}$. Assuming a second-order Fermi acceleration of the protons (e.g., Kimura et al. 2015; Hayasaki & Yamazaki 2019),

$$t_{\rm acc} \approx 10 \frac{r}{c} \left(\frac{v_A}{c}\right)^{-2} \left(\frac{r_L}{r}\right)^{2-s} \gamma^{2-s}, \tag{2.5}$$

where r is the radial distance to the acceleration location, $v_A = B/(4\pi\rho)^{1/2}$ is the Alfvén velocity expressed in terms of the magnetic field strength B and local density ρ, $r_L \sim m_p c^2/(eB)$ and γ are the Larmor radius and the Lorentz factor of the protons, and $s = 1.5 - 2$ is the spectral index of the turbulence scale length distribution.

For the jet scenario, the dynamical timescale $t_{\rm dyn}$ is the typical time for the propagation of a signal in a region of size $\varpi = r/\Gamma$ projected along the observer line of sight (assuming a jet bulk Lorentz factor Γ) and is

$$t_{\rm dyn} = \frac{r}{v_j} = \frac{\tilde{r} R_S}{v_j}, \tag{2.6}$$

where $v_j/c = (1 - \Gamma^{-2})^{1/2}$ is the jet bulk velocity scaled in units of c, $R_S = 2GM_\bullet/c^2$ is the Schwarzschild radius around a black hole of mass $M_\bullet$, and $\tilde{r} = r/R_S$ is a scaled radial distance. The density of plasma in the jet can be evaluated using

$$\rho = \frac{L_{\rm j,kin}}{\frac{\pi r^2}{2} v_j^3 c^3 \Gamma^2}, \tag{2.7}$$

where $L_{\rm j,kin}$ is the kinetic energy in the jet. Assuming that the energy equipartition holds in the jet, the magnetic field strength is

$$B = \left(\frac{8\pi}{3\beta}\right)^{1/2} (\rho v_j^2)^{1/2} = \frac{4}{r\Gamma} \left(\frac{L_{\rm j,kin}}{3\beta v_j}\right)^{1/2}, \tag{2.8}$$

where β is the plasma beta (ratio between the plasma pressure and the magnetic field pressure). With the condition $t_{\rm acc} \leqslant t_{\rm dyn}$, assuming $\beta = 1$, $s = 1.5$, $v_j/c \approx 1$,

$$E_p = \gamma m_p c^2 \leqslant (7.11 \times 10^{16}\ {\rm eV}) \left(\frac{L_{\rm j,kin}}{10^{46}\ {\rm erg\ s^{-1}}}\right)^{1/2} \left(\frac{\Gamma}{5}\right)^{-2}. \tag{2.9}$$

The above rough estimates indicate that protons can certainly be accelerated to PeV or greater energies. Individual neutrinos up to PeV energies can be produced with the availability of suitable cross sections for the hadronic and photo-hadronic interactions as they are expected to have energies of $E_\nu \approx E_p/20$ (e.g., Hayasaki & Yamazaki 2019). This toy model then offers strong support of jets as hosts of energetic protons and neutrinos. Distinguishing between this and other scenarios, such as the one involving mechanisms occurring at the accretion disc site, is beyond the scope of the current work.

2.5.4 Searching for neutrino-emitting sources

Other neutrino-emitter candidates are currently taken into account. One of the most intriguing phenomena is the case of the tidal disruption event (TDE) AT2019dsg, which is highly likely to be associated with the IC 191001A detection (Stein et al. 2021). TDEs take place when a star orbits too close to the central supermassive black hole in a galaxy and it is destroyed under the action of the tidal force (see e.g., Komossa 2013, for a review). The star destruction releases energetic outflows able to produce high-energy cosmic particles and high-energy neutrinos. Other studies mostly focus on the connection between the X-ray emission from blazar and the neutrino events (e.g., Stathopoulos et al. 2021), while others investigate specific classes of AGN (e.g., Maggi et al. 2017) or all radio-loud AGN (Larson et al. 2021). According to Giommi et al. (2020a), ISPs and HBLs are promising counterparts of neutrinos. Recently, the combined activities of AGN and star formation phenomena in starburst galaxies are raising attention to these objects as ideal neutrino sources. Both AGN and star formation phenomena have the potential to serve as cosmic ray accelerators, accompanied by gamma-ray and neutrino emissions. This hypothesis has been confirmed with the evidence of high-energy neutrinos from the starburst galaxy NGC 1068 (IceCube Collaboration et al. 2022).

The growing number of astrophysical objects showing hints of a connection with neutrino emission suggests we should keep the door open to all kinds of possible neutrino event-related sources. In this context, we also observed non-blazar-like sources (reported in Appendix 2.7.1) and sources slightly out of the neutrino error region to leave an observational reference for further studies on the astrophysical neutrino counterparts. The sources analysed in this work have not previously been studied in detail, and for some of them, we also provide VLBI observations for the first time. We stress the fact that our VLBI observations are crucial, not only for the improved quality of the data in comparison with the archival VLBI data of the targets but, above all, for their temporal coincidence with the neutrino arrivals. Then, these data provide a unique opportunity to investigate the evolution of the possible electromagnetic counterparts after the neutrino detection.

In particular, dense monitoring of the sources is required to efficiently estimate proper motions of the components of the jet (e.g., Blasi et al. 2013). Proper motion studies will allow us to infer the physical and geometrical parameters of the jets. As shown in the previous section, some of these parameters, such as, for example, the magnetic field strength or the jet bulk Lorentz factor, could provide a test for the theoretical expectations.

Due to the limited sensitivity of IceCube at high energies, the collected detections are considered to be the tip of the iceberg of larger low-energy neutrino flux. In this regard, retrieving the IceCube archival data of the neutrinos observed at lower energies could be worthwhile to confirm the presence of low-energy neutrino excess from the positions of the sources analysed here.

So far, except for the cases of TXS 0506+056 and NGC 1068, no source is statistically significantly associated with neutrinos. These kinds of searches are often penalised by a large number of trial factors, and it would be important to have a limited number of source positions tested based on their potential association with neutrino events. A dedicated analysis of IceCube archival data at those positions could lead to findings similar to the 2014–2015 neutrino excess from the direction of TXS 0506+056.

2.6 Summary and conclusions

We presented VLBI follow-up observing results of four IceCube neutrino events, both with high and moderate (gold and bronze) probabilities of being associated with a cosmic origin. We analysed data from a total of ten radio sources in spatial coincidence with the neutrino

events. Following previous results reported for the case of TXS 0506+056, and the ones based on statistical approaches using VLBI data, we aimed to identify the possible neutrino emitters by testing the presence of radio properties connected to the neutrino production processes. We used our follow-up data in comparison to VLA (NVSS, FIRST, VLASS) surveys and archival VLBI (RFC) data. The candidate neutrino counterparts have a heterogeneous optical classification, ranging from BL Lac to FSRQ and including a few sources of uncertain classification. Among the ten candidates, we selected five blazar-like sources (based on their radio properties) with a gamma-ray counterpart. A description of the other candidate counterparts is provided in Appendix 2.7.1. The main outcomes about the five principal candidates can be summarised as follows:

- The core spectral behaviour of all the sources is well represented by a self-absorbed spectrum at low radio frequencies and a flat spectrum at high radio frequencies. When the objects are bright and the image noise allows it, we can recognise a core-jet morphology. These appear in three of the sources. All sources are core dominated from mas VLBI resolutions to arcsecond VLA survey resolutions.

- From a morphological point of view, we did not identify parsec-scale radio properties in our sample that could be linked to the neutrino emission, as was previously studied in the case of TXS 0506+056 and expected from theoretical arguments. This can be mostly due to the lower quality of archival data compared to our new data and the lack of frequent observations of these sources in the past at VLBI resolution.

- One of the five candidates, FSRQ PKS 1725+123 exhibits hints of an enhanced activity state in our data. However, it is found outside the 90% localisation region around the neutrino position. Another source, NVSS J065844+063711, is found in a low radio activity state. The case of TXS 1100+122 remains ambiguous since in only one archival RFC observation does this source show a lower flux density compared with our results, while previous RFC flux density measurements are in agreement with our results. On the other hand, Kovalev et al. (2020b) confirmed a high state of TXS 1100+122 at the neutrino arrival.

- None of the sources show exceptionally outstanding properties, in terms of their radio luminosity, variability, and kinematics. However, while we can derive the radio luminosity values from our observations, the variability and the kinematics parameters are much less constrained.

- We present a toy model for proton acceleration in jets that supports the jet scenario for neutrino production in these sites. The model requires kinetic parameters that can be inferred by well-time-sampled VLBI jet monitoring. As mentioned above, a study of the kinetic parameters of the jet motion will require a longer dedicated VLBI monitoring campaign that we are undertaking as a development of this project.

In conclusion, based on the analysis of the morphological evolution, we cannot exclude or support the hypothesis of the sources analysed as a potential neutrino counterpart. However, the results, which suggest significant variability in the radio band in PKS 1725+123 at the neutrino arrival are consistent with the evidence of radio flares in blazars in temporal coincidence with neutrino emission (Plavin et al. 2020; Hovatta et al. 2021).

VLBI results provide us with important pieces of information on the neutrino candidates. In addition, a complete characterisation of these candidate neutrino-associated sources could hopefully come from the combined efforts of multi-wavelength campaigns, triggered almost simultaneously to our follow-up (e.g., Menezes et al. 2021), together with the VLBI follow-up

observations that we will present in future works. In the last years, we performed new VLBA, EVN and *e*-MERLIN follow-up observations of candidate counterparts. Some preliminary results on these new observations are reported in Nanci et al. (2023). The sources are monitored with multi-epoch and multi-frequency observations that characterise variability and probe the presence of superluminal motions. The latter, in turn, provide constraints on velocity and viewing angles. The candidate counterparts for which we are collecting observations are listed in the following.

- The **ISP PKS 0735+17** as candidate counterpart of **IC 211208A** (GCN 31190): it was found in high state at different wavelengths at the neutrino detection (Sahakyan et al. 2023). An estimation of the redshift locates the source at $z \sim 0.45$ (Nilsson et al. 2012).

- The **blazar and candidate lensed object PKS 1413+135** as a possible counterpart of **IC 220205A** (GCN 31551): it was found in a high state in gamma-ray at the neutrino arrival time (Garrappa et al. 2022). This source is a peculiar object. It shows blazar-like features (compactness, core-dominated emission, flat spectrum), however, the detection of a counter-jet and the low degree of polarization led to questioning its blazar nature for many years. Only recently, new detailed studies provide strong evidence of PKS 1413+135 belonging to the BL Lac object class (Readhead et al. 2021). In addition, its location has been a matter of debate for a long time. It was initially located as the host of a Seyfert-II galaxy at a redshift $z = 0.247$ (Wiklind & Combes 1997). Subsequently, it was re-located between $0.247 < z < 0.5$ (Readhead et al. 2021), and then proposed to be beyond the Seyfert-II galaxy, hence possibly gravitationally lensed by it. The milli-lensing hypothesis is strongly supported by the detection of an extremely rare variability behaviour in the light curve (Vedantham et al. 2017). The source indeed seems to periodically experience a perfectly symmetric decrease and increase of the flux density, independent of the observing frequency. About four of these so-called Symmetric Achromatic Variability have been identified in the PKS 1413+135 light curves, from about 15 to 350 GHz observations (Peirson et al. 2022).

- The **blazar PKS 1741-03** (z=1.05, from NED) as candidate counterpart of **IC 220205B** (GCN 31554): it was identified as one of the most probable neutrino counterparts by Plavin et al. (2020) and further discussed recently as probable neutrino emitter in by (Plavin et al. 2023).

- The **blazar TXS 1742-078** ($z = 1.054$ White et al. (1988)), found in a high state at the optical band at the neutrino arrival time (Zhirkov et al. 2022), and the radio source **TXS 1749-101** possibly associated with past neutrino IC 181023A (GCN 23375), both candidate counterparts of **IC 220425A** (GCN 31944).

- The **very bright LSP BL Lac OT 081** ($z = 0.322$ (Stickel et al. 1988)) as a possible counterpart of **IC230708A** (GCN 34170).

- The **FSRQ B3 1746+470** ($z = 1.484$, from NED) as a possible counterpart of **IC 231027A** (GCN 34891): it was found in a high state in gamma-ray at the neutrino arrival time (Buson et al. 2023a).

- **the blazar PKS 0446+11** ($z = 2.153$ (Stickel et al. 1988)) as a possible counterpart of **IC 240105A** (GCN 35485): it has been recently observed in a high state both in gamma-ray (Sinapius et al. 2024) and the radio band (Shaw et al. 2012) simultaneously with the neutrino detection.

Further investigation into the candidates presented in this work and, most importantly, the identification of a large number of new ones, will shed light on the open question of the nature of extragalactic neutrinos and of blazars as the best candidate neutrino counterparts.

2.7 Appendices

2.7.1 Appendix A: Other candidates

NVSS J104938+274212 Lying within the 50% uncertainty region, 4FGL J1049.8+2741 was the first identified candidate source associated with the IC 190704A neutrino event. Its possible radio counterpart is NVSS J104938+274212 (SDSS J104938.80+274213.0, a galaxy at $z = 0.144$, (Alam et al. 2015)). Parameters of VLBI observation are reported in Table 2.12 and spectral indices deduced from these data are in Table 2.13. The FIRST 1.4 GHz peak flux density is 9.2 mJy, and the integrated flux density is 15.6 mJy, suggesting that NVSS J104938+274212 contains a resolved radio structure on arcsecond scales (see Table 2.6). Our VLBI observations reveal a compact component on parsec scales, with a lower flux density than what is observed in the VLA surveys. The luminosity of the source at 1.5 GHz is $(2.1\pm0.2)\times10^{23}$ WHz^{-1}, assuming a spectral index $\alpha_{\rm NVSS}^{\rm VLASS} = -0.3 \pm 0.2$.

WISEA J111439.67+122503.7 One of the candidate gamma-ray counterparts associated with IC 200109A is 4FGL J1114.6+1225 (Table 2.2). A possible counterpart of this source is WISEA J111439.67+122503.7, the properties of which are reported in Table 2.3. Among all the candidate counterparts associated with the events of our sample, this is the source located farthest from the position of the relative neutrino (about four degrees away from IC 200109A). This first leads us to disfavour it as the most promising candidate. Moreover, it is not catalogued as a blazar. We identified two radio counterparts in spatial coincidence with WISEA J111439.67+122503.7. In the following, we refer to them with WISEA J111439.67+122503.7-A and WISEA J111439.67+122503.7-B. Information about their arcsecond-scale, low-frequency properties are provided in Table 2.6.

WISEA J111439.67+122503.7-A Inspecting the highest resolution image of this source produced at 23.5 GHz, we resolved two components separated by about 8.4 mas. The second component was also detected in the 8.4 GHz images, while it is not detected in the 4.9 GHz image. In Table 2.12, the properties of the VLBI observations of these components are reported. We use the suffix A1 for the brightest and A2 for the least bright detection. The spectral index between 8.4 GHz and 23.5 GHz of the A1 component is 1.4±0.1, while that of the A2 component is −1.4±0.4. From these results, we can speculate that we are looking at a self-absorbed core component (A1) and a contribution from a steep spectrum jet (A2). However, it must be noted that with these data we were not able to measure the spectral index adequately, that is, by adopting the same *uv*-range, pixel size, and restoring beam in the two frequency images. Then, the resulting spectral indices could be biased by the differences in the observation setups.

WISEA J111439.67+122503.7-B This source was not detected in our 8.4 GHz and 23.5 GHz observations. The upper limits set as three-times the RMS noise levels of the images are 2.3 mJy and 80 μJy at 8.4 GHz and 23.5 GHz, respectively. At 4.9 GHz, the source is composed of two components (B1 and B2), located at a distance of around 7 mas from each other. The properties of these components are reported in Table 2.12. Comparing these results to the low-frequency ones (Table 2.6), the source seems to be characterised by a steep spectrum.

WISEA J105553.74+103446.5 The other source within the error region of the IC 200109A event is WISEA J105553.74+103446.5 (Table 2.3). The possible radio counterpart observed by the VLBI shows a significant emission outside the core, as deduced by comparing the integrated

flux density and the peak intensity at 4.9 GHz and 8.4 GHz (Table 2.12). In our 23.5 GHz data, WISEA J105553.74+103446.5 lies under the RMS noise level of the image, that is 0.9 mJy beam^{-1}. The corresponding upper limit for the surface brightness of the source is 2.7 mJy beam^{-1}. The NVSS, FIRST, and VLASS data reveal that a large fraction of the source emission is spread over arcsecond scales (Table 2.6). This is also confirmed by the steep spectral index obtained from our 4.9 GHz and 8.4 GHz data (Table 2.13).

WISEA J065633.43+053922.7 The blazar-like source WISEA J065633.43+053922.7 is one of the possible IC 201114A counterparts (Giommi et al. 2020b). However, both the absence of a gamma-ray association with this source and its position outside the 90% error region of the neutrino event (see Table 2.1) lead us to disfavour WISEA J065633.43+053922.7 as the best candidate. In the VLBI observations (Table 2.12), the source shows a partially resolved structure with a core and a shallow emission extended towards the southwest. Due to the large beam size of the NVSS data, it results that the source emission is embedded with a close ($\sim$44″) source in the field. In the VLASS, these two objects are separated. We measured the two contributions in NVSS data by fitting the object's emission with two Gaussian components using the `imfit` tool of CASA. For completeness, we report the parameters of both the sources, labelled WISEA J065633.43+053922.7-A and WISEA J065633.43+053922.7-B, in Table 2.6. The target of our observation is WISEA J065633.43+053922.7-A. The contribution of WISEA J065633.43+053922.7-B is not detected in our VLBI data. Table 2.13 reports the VLBI spectral indices of the main target source. We confirm the blazar nature of this source, based on the large core prominence (as indicated by the comparison of the VLBI and NVSS/ VLASS flux densities) and the behaviour of the spectral index, which is inverted at low frequencies and flat at higher frequencies.

NVSS J065916+055252 The second blazar candidate associated with IC 201114A is NVSS J065916+055252 (Giommi et al. 2020b). This source is not associated with any gamma-ray detection either (Table 2.3). In our VLBI observations, NVSS J065916+055252 is composed of a bright core and an elongated jet that extends in the northwest. In Table 2.12, we report VLBI properties of this source. Survey data show that this source is core-dominated at arcsecond scales (Table 2.6). The VLASS flux densities in the two epochs (2017 and 2020, two months before the neutrino detection) are consistent within the errors, implying the absence of variability at VLASS scales in that time range. In Table 2.13, we report the spectral index measurements.

Table 2.12: Images parameters of VLBI observations.

Source	ν (GHz)	$S_{\rm peak}$ (mJy beam^{-1})	$S_{\rm int}$ (mJy)	RMS (μJy beam^{-1})	Beam (mas×mas,°)
(1)	(2)	(3)	(4)	(5)	(6)
190704A					
NVSS J104938+274212	1.5	3.0±0.3	4.9±0.5	83	11.6×6.2, −24.5
	4.4	5.7±0.6	6.3±0.6	136	5.7×5.3, 23.1
	7.6	3.3±0.5	4.8±0.6	143	2.4×1.3, −20.1
200109A					
WISEA J111439.67+122503.7-A	4.9	1.0±0.1	1.7±0.3	57	1.8×1.5, 45.0
A1	8.4	1.8±0.2	2.2±0.2	66	2.2×1.0, −5.5
	23.5	0.30±0.03	0.55±0.07	95	1.2×0.8, −8.1
A2	8.4	0.25±0.05	0.14±0.05	66	2.2×1.0, −5.5
	23.5	0.42±0.05	0.64±0.08	95	1.2×0.8, −8.1
WISEA J111439.67+122503.7-B1	4.9	0.39±0.05	0.52±0.08	34	1.8×1.5, 30.6
B2		0.22±0.03	0.41±0.07		
WISEA J105553.74+103446.5	4.9	17.2±1.8	34.1±4.1	476	2.6×2.2, 79.0
	8.4	8.4±0.9	24.4±4.2	452	2.8×2.0, 0.8
201114A					
WISEA J065633.43+053922.7	4.9	25.3±2.7	38.6±4.3	58	3.5×1.7, 74.5
	8.4	68.7±6.9	76.0±7.6	95	2.1×1.1, 1.1
	23.5	47.4±4.7	49.3±4.9	96	0.9×0.4, −9.9
NVSS J065916+055252	4.9	521±52	734±74	262	2.8×2.0 73.2
	8.4	421±42	568±57	254	2.3×1.1, −7.1
	23.5	129±13	192±21	766	1.1×0.4, −14.4

Notes: (1) Candidate neutrino counterpart; (2) observation frequency in GHz; (3) peak brightness in mJy beam^{-1}; (4) integrated flux density in mJy; (5) 1-σ noise level of the image in μJy beam^{-1}; (6) major axis (in mas), minor axis (in mas), and PA (in degrees, measured from north to east) of the restoring beam. Parameters refer to natural weighting images.

Table 2.13: Spectral index measured with VLBI data.

IC name	Source	ν (GHz)	$S_{\rm peak}$ (mJy beam^{-1})	uv-range Mλ	Beam mas×mas,°	α
(1)	(2)	(3)	(4)	(5)	(6)	(7)
190704A	NVSS J104938+274212	1.5	2.9±0.3	2-40	6.6×5.6, 67.0	0.7±0.1
		4.4	5.9±0.6			
		4.4	3.8±0.4	5-100	2.8×1.7, −5.3	0.0±0.3
		7.6	3.8±0.4			
200109A	WISEA J105553.74+103446.5	4.9	16.3±1.7	4-155	2.6×1.9, 0.8	−1.4±0.3
		8.4	7.8±0.9			
201114A	WISEA J065633.43+053922.7	4.9	25.1±2.5	13-144	1.5×1.1, 6.4	1.8±0.3
		8.4	67.6±6.8			
		8.4	66.6±6.6	13-244	1.4×0.9, 0.9	−0.3±0.1
		23.5	49.1±4.9			
	NVSS J065916+055252	4.9	421±42	8-165	2.2×1.2, −7.5	−0.4±0.3
		8.4	520±52			
		8.4	385±39	12-245	1.6×0.9, −15.0	−0.9±0.1
		23.5	154±15			

Notes: (1) IceCube event name; (2) candidate neutrino counterpart; (3) observation frequency in GHz; (4) peak intensity in mJy beam^{-1}; (5) uv-range in Mλ; (6) beam sizes; (7) spectral index.

2.7.2 Appendix B: MODELFIT parameters

In this section, we report the MODELFIT parameters of the three jetted sources, TXS 1100+122, PKS 1725+123 and NVSS J065844+063711. These results are presented in Section 2.4 and discussed in Section 2.5.

Table 2.14: Model fit component parameters of **TXS 1100+122**.

Date	Obs.	ν (GHz)	Comp.	Flux (mJy)	Radius (mas)	PA (deg)	Maj. Axis (mas)	Ax. ratio	10% beam (mas × mas)	$\theta_{\rm beam}$ (deg)
(1)	(2)	(3)	(4)	(5)	(6)	(7)	(8)	(9)	(10)	(11)
30 Apr 2004	RFC	2.3 GHz	1	280±28	0.05	21	1.4	0.4	0.4×0.3	−0.1
			2	2.4±0.2	4.0	128	4.7	0.7		
			3	10±1	10.0	149	2.4	0.5		
			4	1.8±0.2	15.2	141	11.0	0.5		
			5	12±1	28.5	157	8.9	0.5		
30 Apr 2004	RFC	8.6 GHz	1	287±29	0.1	105	0.4	0.6	0.1×0.2	1.1
			2	21±2	0.7	157	0.8	0.5*		
			3	9.3±0.9	2.7	145	2.9	1.0*		
01 Aug 2007	RFC	8.4 GHz	1	384±38	0.006	62	0.5	1.0*	0.2×0.1	35.1
			2	22±2	1.2	159	1.0	1.0*		
20 Feb 2012	RFC	8.4 GHz	1	100±10	0.09	−28	0.3	0.5	0.3×0.1	8.0
			2	4.7±0.5	1.0	148	0.5	0.98		
			3	0.57±0.06	4.6	150	5.0	0.3		
29 Feb 2020	EVN	4.9 GHz	1	306±31	0.05	166	0.2	1.0*	0.4×0.3	7.8
			2	10.8±1.1	3.0	142	0.5	1.0*		
			3	2.9±0.3	7.0	152	0.5	1.0*		
			4	4.8±0.5	10.7	151	3.5	1.0*		
			5	4.8± 0.5	29.4	158	4.4	1.0*		
			6	0.23±0.02	32.7	165	9.1	1.0*		
04 Feb 2020	VLBA	8.4 GHz	1	318±32	0.07	−19	0.15	0.5*	0.2×0.1	−6.3
			2	73.8±7.4	0.45	158	0.2	0.9		
			3	7.6±0.8	1.6	156	0.6	0.5		
			4	5.9±0.6	3.1	143	1.1	0.2		
			5	1.2±0.1	7.0	147	1.6	1.0*		
			6	3.9±0.4	10.2	157	5.2	1.0*		
			7	1.8±0.2	18.8	170	2.9	1.0*		
04 Feb 2020	VLBA	23.5 GHz	1	338±34	0.01	−22	0.15	0.5*	0.08×0.03	−9.6
			2	50±5	0.2	159	0.2*	0.9*		
			3	3.0±0.3	0.9	153	0.6*	0.5*		
			4	1.8±0.2	2.8	142	1.1*	0.2*		

Notes: (1) Date of observation; (2) origin of the observation: RFC or MOJAVE or our VLBA or EVN or *e*-MERLIN observations; (3) observation frequency in GHz; (4) component numbering. We assign numbers to components as a guide to help visualise them. However, the same numbers at different epochs and frequencies do not refer to the same components in the jet because the components are not identified at all epochs and frequencies. Then, in the case in which this numbering is taken as a reference, it must be interpreted according to each dataset independently. (5) Flux density in mJy; polar coordinates: (6) radius in mas and (7) PA in degrees, measured from north through east of the component's centre with respect to the image central pixel; (8) FWHM of the component's major axis in mas; (9) axial ratio between FWHM major and minor axes of the component; (10) 10% of the image restoring beam (major and minor axis in mas) and (11) restoring beam orientation (from north through east, in degrees) indicated as a reference for the component's position uncertainty. Parameters marked with an asterisk were fixed during the fitting procedure.

Table 2.15: Model-fit component parameters of **PKS 1725+123**.

Date	Obs.	ν (GHz)	Comp.	Flux (mJy)	Radius (mas)	PA (deg)	Maj. Axis (mas)	Ax. ratio	10% beam (mas × mas)	$\theta_{\rm beam}$ (deg)
(1)	(2)	(3)	(4)	(5)	(6)	(7)	(8)	(9)	(10)	(11)
06 Oct 2018	MOJAVE	15.3	1	485±25	0.04	143	-	-	0.2×0.06	6.7
			2	128±7	0.2	−38	-	-		
			3	7.4±0.4	1.1	−27	0.4	1.0*		
			4	0.70±0.04	3.3	−26	0.17	1.0*		
19 Jul 2019	MOJAVE	15.3	1	491±25	0.05	−18	0.04	1.0*	0.2×0.06	−18.1
			2	17±1	1.0	−33	0.3	1.0*		
			3	1.18±0.05	2.7	−24	0.9	1.0*		
25 May 2020	MOJAVE	15.3	1	455±46	0.006	−32	0.17	0.09	0.2×0.07	−21.6
			2	13.1±0.1	0.7	−31	0.15	1.0*		
			3	2.6±0.2	2.8	−31	3.9	0.10		
21 Jan 2020	MOJAVE	15.3	1	532±53	0.01	−2.9	0.17	0.4	0.11×0.05	−4.6
			2	20±2	0.5	−26	0.5	0.4		
			3	2.9±0.3	1.4	−31	0.5	1.0*		
			4	2.1±0.2	4.2	−24	1.5	1.0*		
01 Dec 2020	MOJAVE	15.3	1	635±64	0.004	20	0.14	0.2	0.12×0.06	−4.8
			2	13.5±1.4	0.5	−29	0.2	0.3		
			3	4.73±0.5	1.3	−32	0.7	0.3		
			4	0.9±0.09	2.6	−30	0.7	1.0*		
			5	1.3±0.1	4.5	−24	1.4	1.0*		
05 Nov 2020	*e*-MERLIN	5.1	1	333±17	0.2	−176	4.3	0.1	8.2×3.9	23.9
			2	6.7±0.4	285	−15	291	0.4		
			3	2.8±0.2	703	−29	186	1.0*		

Notes: Same as Table 2.14.

Table 2.16: Model-fit component parameters of **NVSS J065844+063711**.

Date	Obs.	ν (GHz)	Comp.	Flux (mJy)	Radius (mas)	PA (deg)	Maj. Axis (mas)	Ax. ratio	10% beam (mas × mas)	$\theta_{\rm beam}$ (deg)
(1)	(2)	(3)	(4)	(5)	(6)	(7)	(8)	(9)	(10)	(11)
08+09 Apr 2013	RFC	4.3	1	18.7±1.2	0.17	82	0.4	1.0*	0.5×0.2	−7.3
			2	6.2±0.6	1.1	−102	1.0	1.0*		
08+09 Apr 2013	RFC	7.6	1	22.3±2.2	0.03	−59	0.4	1.0*	0.3×0.11	−12.2
			2	3.5±0.4	1.6	−116	1.0	1.0*		
19 Oct 2013	RFC	7.6	1	11.9±1.2	0.01	145	0.5	1.0*	0.2×0.13	−3.3
			2	3.0±0.3	1.4	−114	0.9	1.0*		
			3	1.1±0.1	2.7	−119	1.4	1.0*		
01+02 Dec 2020	EVN	4.9	1	7.3±0.7	0.7	146	-	-	0.2×0.11	82.4
			2	5.5±0.6	1.2	−115	1.3	1.0*		
			3	0.5±0.1	5.1	−79	6.9	1.0*		
06 Dec 2020	VLBA	8.4	1	11±1	0.3	124	0.9	0.7	0.2×0.1	2.2
			2	3.7±0.4	1.5	−118	1.3	0.7		
			3	0.17±0.02	2.7	−94	0.9	1.0*		
06 Dec 2020	VLBA	23.5	1	9.3±0.9	0.8	150	0.2	0.6	0.1×0.04	−13.5
			2	4.5±0.4	1.5*	−143	1.3	0.7*		

Notes: Same as Table 2.14.

Part II

Blazars at very high energy

Chapter 1

Gamma-ray astronomy

The domain of gamma-ray astronomy spans energies ranging from 0.5 MeV[1] (equivalent to the electron mass) to 10^{20} eV. The field can be split into sub-bands mainly based on the different emission mechanisms occurring at each energy range and techniques used to acquire signals.

The High Energy (HE) domain covers the energy range from approximately tens MeV to 300 GeV. Observations are conducted using space-based instruments, such as satellites' detectors or atmospheric balloons. Examples of instruments operating in this energy range are the Astroriv-elatore Gamma ad Immagini LEggero (AGILE), and the LAT, mounted on the *Fermi* satellite, both successors of the EGRET on board of Compton Gamma Ray Observatory (CGRO).

The Very High Energy (VHE) domain extends from energies of about hundreds GeV up to hundreds TeV. Beyond 100 GeV, gamma-ray flux significantly decreases. Space-based instruments become less efficient at detecting gamma rays in this range due to their limited dimensions. These limitations can be overcome by ground-based facilities which have collection areas an order of magnitude larger. VHE observations are then performed using these ground-based instruments.

However, the Earth's atmosphere is opaque to high-energy gamma rays, preventing their direct detection. Nevertheless, when VHE gamma rays interact with the atmosphere, they initiate cascades of charged particles and secondary photons. These particles move faster than the speed of light in the surrounding medium, producing Cherenkov light flashes. Analyzing this radiation allows us to indirectly determine the energy and incoming direction of the primary gamma-ray photons. This is the fundamental principle behind Imaging Atmospheric Cherenkov Telescopes (IACTs), sometimes also referred to as Cherenkov telescopes, operating in the VHE regime. Moreover, the IACT technique allows the discrimination of the gamma-ray-induced cascades from the background noise. This is due to particle showers initiated by charged particles.

For over three decades, two main generations of IACTs have enabled the exploration of the VHE gamma-ray window. The pioneering experiments such as the Whipple 10-meter Telescope, High Energy Gamma Ray Astronomy (HEGRA), CANGAROO (Collaboration between Australia and Nippon for a Gamma Ray Observatory in the Outback), and others, were followed by the current three main experiments, High Energy Stereoscopic System (HESS), Major Atmospheric Gamma-ray Imaging Cherenkov (MAGIC), and Very Energetic Radiation Imaging Telescope Array System (VERITAS).

The next milestone will be reached with the construction of the Cherenkov Telescope Array Observatory (CTAO), which will not only significantly improve performance but also lead to a massive development in the field of VHE astronomy. Unlike the current instruments indeed, the CTAO will be run as an astronomical observatory for the entire scientific community.

[1]For reference: the MeV energy range corresponds to frequencies around $\nu \sim 10^{20}$ Hz, the GeV one corresponds to around 10^{24} Hz, the TeV one corresponds to frequencies in the range $\nu \sim 10^{26}$ Hz

At even higher energies, Ultra High Energy (UHE, 100TeV $< E <$ 100PeV) and Extreme High Energy (EHE, $E >$ 100PeV) observations are performed by Air Shower Particle Arrays. These instruments are designed to detect the secondary particles in the cascades initiated by gamma rays or cosmic rays, as opposed to Cherenkov Telescopes, which detect the Cherenkov light produced by those cascades. At lower energies, in the VHE regime, the development of showers is not extensive enough to detect a significant number of secondary particles, primarily due to atmospheric absorption.

In the next Section, the methods utilized for gamma-ray detection will be discussed. The description of the IACT will be prioritized due to its relevance in this Part of the Thesis. While HESS, MAGIC, and VERITAS all operate on similar principles, MAGIC telescopes will be taken as the example since MAGIC data are analysed in this Part of the Thesis.

1.1 Detection methods

Gamma-ray detection techniques vary depending on the energy range of observation. Above 10 MeV, pair conversion becomes the dominant process. HE instruments on satellites, like *Fermi*-LAT, are designed to exploit this process. These instruments consist of a converter and a tracker for electron and positron tracking, a calorimeter for energy reconstruction, and an Anti coincidence detector (ACD), to shield the detector from background caused by charged cosmic rays that also collide with the instrument.

In *Fermi*-LAT, gamma rays enter the tracker which is composed of layers of so-called *conversion foils*. The collision of the photons with the high-metallicity material of the foils generates electron-positron pairs. The trajectories of these particles are tracked by silicon strip detectors within the tracker. Finally, the charged particles traverse the calorimeter, placed beneath the layers of the tracker, where they deposit their energy. Depending on where the charged particles deposit their energy in the tracker and calorimeter, pulse-height signals are generated as the output of the *Fermi*-LAT observations. By combining the pulse heights with the coordinates of each silicon strip detector hit, it becomes possible to reconstruct the particle's trajectory and its energy losses. The *Fermi*-LAT analysis reconstructs the tracks of the particles and allows us to distinguish between events from photons and background events, determine the incident photon's direction, and estimate its energy. The reconstructed direction of the incoming gamma ray is limited by multiple scatterings of the pair components in the tracker material and the spatial resolution of the tracker itself.

In particular, the *Fermi*-LAT was designed to operate in the 20 MeV to 300 GeV energy range. It provides a wide FoV, covering approximately 20% of the sky, and reaches a few arc-minutes of angular resolution at around 10 GeV and about 3 degrees at 100 MeV.

All spaced-based gamma-ray instruments present some limitations such as a small effective area (about 1 square meter), limited sensitivity, and high cost, partly dependent on their weight. However, they offer a reasonably large FoV, and high-duty cycles, unaffected by the night and day cycle. Angular resolution is constrained by the opening angle of the electron-positron pair produced in pair production, and particularly at low energies, by multiple scattering. Energy resolution depends on the size of the calorimeter, and weight restrictions can lead to inadequate containment of the particle shower generated by the initial electron and positron, resulting in energy measurement degradation.

When VHE gamma rays interact with Earth's atmosphere, they undergo pair conversion as they interact with atmospheric particles. Then, for ground-based telescopes, the atmosphere plays the role of the calorimeter. Electrons and positrons from pairs moving in the electric field of the atmospheric nuclei dissipate their energy via bremsstrahlung radiation. Additionally, these secondary gamma rays interact with atmospheric particles, producing more electron-positron

pairs and new gamma rays. The number of particles and bremsstrahlung photons grows as they travel deeper into the atmosphere, leading to the development of the so-called *Extensive Air Shower (EAS)*. A schematic representation is reported of an EAS in Fig. 1.1.

As the shower grows, the average energy per particle decreases. A fraction of the energy is also dissipated via ionization, but this is still negligible in the high-energy regime, when the shower development starts. When energy losses due to ionization dominate over bremsstrahlung, no more secondary gamma rays are generated, and the shower ceases to grow. This happens when a critical energy level is reached. Beyond this point, the number of particles decreases with increasing atmospheric depth.

Charged particles within the EAS move at relativistic speeds as they travel the atmosphere, emitting Cherenkov light in the UV-optical band. IACTs detect this light. Reconstructing the shower's image from the analysis of Cherenkov radiation allows the determination of the direction and the energy of the primary gamma ray. A deep knowledge of the physics of the EAS is key for the IACTs operations.

1.1.1 Description of Extensive Air Showers

In Earth's atmosphere, gamma rays, high-energy electrons, and cosmic rays (primarily protons) create EAS. *Electromagnetic showers* are produced by gamma rays and high-energy electrons. Only the gamma-ray electromagnetic showers constitute the signal the Cherenkov telescopes are searching for. On the other hand, cosmic ray protons generate *hadronic showers* which, along with electromagnetic showers from electrons, introduce background noise to the gamma-ray signal. The primary goal of Cherenkov data analysis is to distinguish gamma-ray signals from the background noise caused by cosmic rays and electrons. In the following discussion, our focus will be on gamma-ray-induced electromagnetic showers. However, gamma rays and electrons produce electromagnetic showers that undergo the same processes, so the same principles can be applied to electron showers as well.

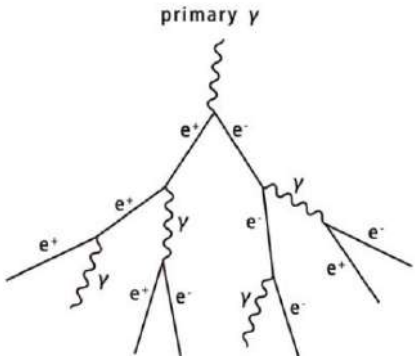

Figure 1.1: Schematic representation of the EAS generated by a gamma-ray photon entering the atmosphere. Electron and positron pairs together with secondary gamma-rays produced by the bremsstrahlung process compose the shower. From Feng et al. 2021.

As mentioned in the previous section, the main mechanisms responsible for generating electromagnetic showers are pair conversion and bremsstrahlung. The critical energy for pair conversion in the atmosphere is 20 MeV, meaning that gamma rays with energies greater than 20 MeV produce electron-positron pairs through this process.

Secondary gamma rays, which result from the interaction of charged particles with the Coulomb field of atmospheric nuclei, gradually lose their energy through bremsstrahlung radiation, as long as their energy remains above the critical energy, E_c. This is 84 MeV in the Earth's atmosphere. When gamma rays have energies higher than 84 MeV, they undergo bremsstrahlung losses. As their energy decreases to levels below 84 MeV, ionization losses become the predominant mechanism.

The energy lost by an electron through bremsstrahlung radiation over a differential path length $\mathrm{d}x$ is quantified by:

$$-\frac{\mathrm{d}E_e}{\mathrm{d}x} = \frac{E_e}{X_0} \tag{1.1}$$

Here, E_e represents the electron's energy, and X_0 denotes the characteristic *electromagnetic radiation length*. This length indicates the distance over which an electron dissipates $1/e$ (approximately 37%) of its energy via bremsstrahlung radiation. The precise value of X_0 depends on the composition of the medium and, in the case of Earth's atmosphere, is approximately 36.7 g cm^{-2}. The energy lost by an electron via pair production is characterized by the mean free path for pair creation which is equivalent to 9/7 of X_0.

The initial interaction between a gamma ray and an atmospheric nucleus typically occurs at an altitude of approximately 20 km above sea level (as shown in Fig. 1.5). Following this collision, the resulting shower of secondary products initially travels in the same direction as the primary photon. As a first approximation, within each radiation length, a single particle, gamma ray or electron, generates two additional particles that equitably share the energy. The original energy of the gamma-ray photon, E_0, is subsequently distributed among the resultant secondary products. The maximum number of particles in the cascade is determined by the ratio of E_0 to E_c.

By the approximation known as *approximation B*, postulated by Rossi & Greisen 1941, the maximum number of particles generated within the shower is directly proportional to the primary energy E_0. In addition, the maximum development of the shower in terms of particle content occurs at an atmospheric depth of:

$$x_{\max} = X_0 \log\left(\frac{E_0}{E_c}\right) \tag{1.2}$$

The growth in the number of particles within showers, initiated by gamma rays of different initial energies, is shown as a function of radiation lengths in Fig. 1.3. This representation allows for the visual identification of $x_{\max}$ for each case. Moreover, Fig. 1.3 illustrates that, as the primary gamma-ray photon possesses greater energy, it penetrates deeper into the atmosphere, resulting in a corresponding shift of $x_{\max}$ towards the right. In contrast, lower-energy photons (with energy $E_0 < 100$ MeV and below) cause the shower to terminate before reaching the Earth's surface.

In the showers, the relativistic charged particles move at speeds exceeding the speed of light in the air. This generates Cherenkov light reaching the ground as short flashes (a few ns). In particular, the air represents a transparent dielectric medium and particles moving within it interact with the local electromagnetic field, displacing electrons within the atoms and inducing their polarization. As a consequence, the excited electrons emit photons to return to their equilibrium state. The emission depends on the particle's velocity, $v = \beta c$, in comparison to the speed of light within the medium. If the particle's velocity is lower than the speed of light in the medium ($\beta < 1/n$ or $v < c/n$, where n is the refractive index of air), the emitted photons interfere destructively, resulting in no detectable radiation. When the particle's velocity overcomes the speed of light in the medium ($\beta > 1/n$, or $v > c/n$), the wave fronts can combine coherently, leading to the emission of the Cherenkov light. The two cases are shown in Fig. 1.2.

The emission angle of the Cherenkov flashes, θ_C, is related to β and n by the equation $\cos\theta_C = 1/\beta n$. At sea level, this angle is approximately 1 degree. Moreover, particles in the EAS undergo multiple Coulomb scattering events, causing the expansion of the EAS over both horizontal and vertical directions as it approaches the Earth's surface. However, the secondary particles generated in an electromagnetic shower do not scatter off too much from the shower axis. They develop following a roughly axis-symmetric profile compared with their initial direction.

The typical Cherenkov light pool originated from an EAS is characterized by a radius, on the ground, larger than 100 meters for a 100 GeV electromagnetic showers (as shown in Fig. 1.5). It may be larger for higher-energy primary gamma rays.

The Cherenkov radiation spectrum is predominantly composed of optical (blue) and UV emissions, with a peak occurring at around 340 nm. Light at shorter wavelengths is absorbed

by the atmosphere, particularly by ozone, and therefore, it does not reach the ground unless it originates at low altitudes in the atmosphere.

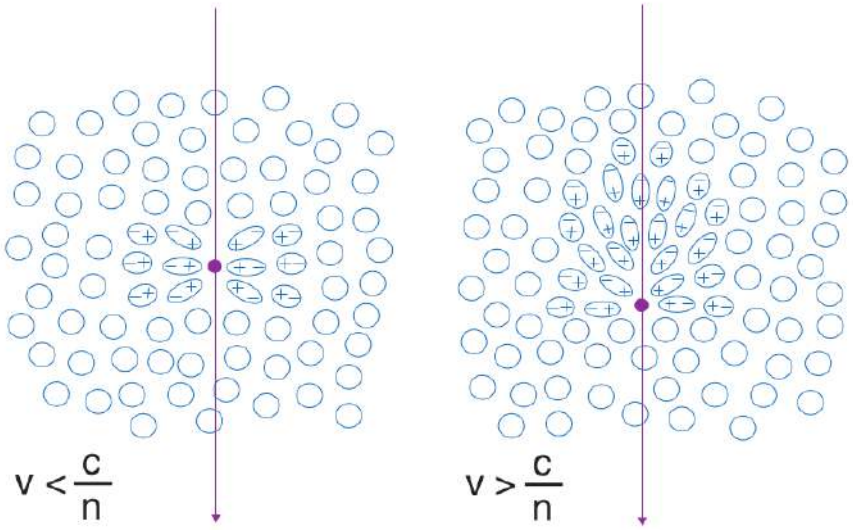

Figure 1.2: Charged particles travelling through a dielectric medium producing polarization of the atoms there. In the left panel, the particle moves with a velocity v lower than the speed of light in the medium c/n, resulting in symmetrical polarization. In the right panel, the particle's velocity exceeds the speed of light in the medium, leading to asymmetric polarization in the direction of the particle's motion and to the emission of Cherenkov light. From Wagner 2007.

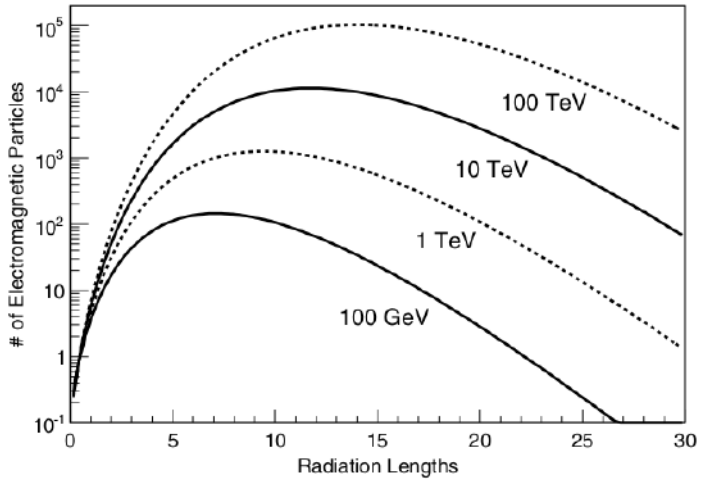

Figure 1.3: The longitudinal growth of an EAS, as described by Approximation B of Rossi & Greisen 1941, represented for different primary gamma rays energies. The x-axis represents atmospheric depth, quantified in terms of the number of radiation lengths while the y-axis represents the count of electromagnetic particles within the air shower. To provide context, sea level corresponds to approximately 28 radiation lengths of the atmosphere, 2600 meters above sea level, slightly higher the MAGIC site, is approximately 20 radiation lengths, 4300 meters above sea level is equal to roughly 16.5 radiation lengths.

As the hadrons component of cosmic rays interact with the Earth's atmosphere, secondary particles emitting Cherenkov light are generated. The mean free path in this case is roughly 80 g cm^{-2}, which is larger than the 36.7 g cm^{-2}, the one for electromagnetic showers. Thus, hadronic showers penetrate deeper into the atmosphere before the shower development starts. The interactions between hadrons and the air nuclei produce charged (π^+ and π^-) and neutral (π^0) pions. The π^0 decays into two photons and roughly one-third of the primary hadron energy develop electromagnetic cascades. Meanwhile, the charged pions decay into secondary neutrinos and muons. In turn, muons are unstable and soon decay generating electron and positron pairs. These particles follow the destiny of the electromagnetic shower losing energy via bremsstrahlung

and pair conversions. As in the case of electromagnetic showers, the particles from the hadronic ones move in a transparent dielectric medium (the atmosphere) faster than the speed of light in that medium, producing Cherenkov emission. However, the Cherenkov photons from a hadronic shower are not only produced through direct pion decay but also through the decay of secondary leptons (the latter generating electromagnetic showers). The leptonic component from hadronic showers is challenging to distinguish from pure electromagnetic showers.

The hadronic showers develop broader and more irregularly with respect to gamma-ray-initiated ones because of the larger transverse momentum. As a consequence broader is also the Cherenkov light pool. Indeed a larger amount and variety of secondary particles are produced with respect to the electromagnetic cascade. Moreover, the hadronic showers take longer (tens ns) for their development compared to electromagnetic showers (a few ns).

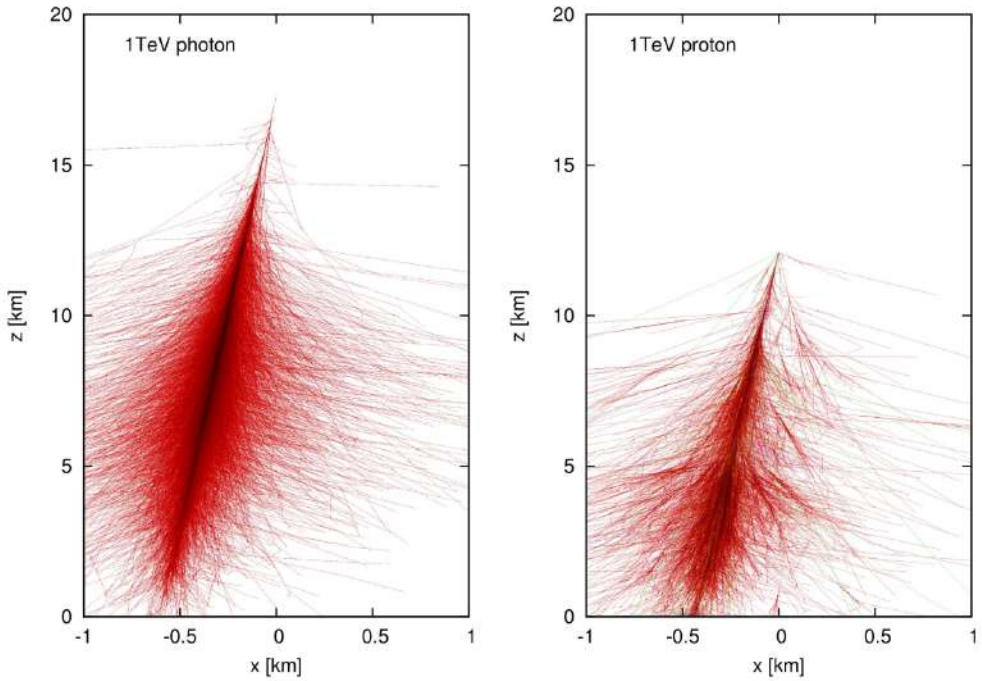

Figure 1.4: Electromagnetic (left) and hadronic (right) simulated EAS produced with COsmic Ray SImulations for Kascade (CORSIKA), a numerical code employing Monte Carlo simulations to reproduce the interactions between particles within an EAS. At each line corresponds the path of an elementary particle raised during the development of the shower. The electromagnetic shower (on the left) is generated by a photon of 1 TeV energy, while the hadronic shower (on the right) is produced by a 1-TeV proton. From Barnacka et al. 2012.

1.1.2 The IACT technique

The longitudinal and lateral development of the electromagnetic showers can be retrieved by recording images of the Cherenkov light distribution from the cascades. This, in turn, allows us to indirectly determine the arrival direction and energy of the primary gamma-ray photons. The IACT technique is very challenging because of the short duration and faintness of the Cherenkov light emitted by secondary particles in the air shower. For this reason, highly sensitive pixelized cameras, with fast sampling rates, serve to detect the high-speed signal amidst the continuous background of night-sky photons. At low energies, telescopes with large mirrors are necessary to capture enough Cherenkov photons.

The Cherenkov photons producing the light pool are collected by the telescope's reflective

surfaces and focused onto a camera. The photosensors of the cameras, typically Photomultiplier Tube (PMTs), convert the collected Cherenkov photons into electrical impulses. The PMT and the associated electronics are built to effectively operate on the short timescales as ones of the Cherenkov flashes. To ensure an optimal signal-to-noise ratio between Cherenkov light and the Night Sky Background (NSB), including starlight and scattered light, and minimize the integration time for background light, fast trigger systems and readout electronics are necessary.

Once the telescopes record the images of each shower, the second step is the offline analysis. Each event is processed individually, the image is *cleaned* to eliminate noise and influence from the NSB, and parametrized. The characteristics of the images recorded from pure electromagnetic showers initiated by gamma rays differ from those of showers initiated by hadronic cosmic rays. The parameterization of the image is then critical for the discrimination of gamma-ray events from the background created by hadronic showers or any events associated with noise or survived NSB after the initial cleaning process. In the case of a gamma-ray-initiated cascade where the emission comes from the pointing direction, photons emitted in the higher atmosphere are reflected to the center of the camera, while the tails extend toward the edges of the camera. Consequently, the electromagnetic shower is concentrated in a narrow distribution pointing to the direction of the primary incoming gamma ray. Which region in the camera is reached by photons from different parts of the shower depends on the angle between the telescope axis and the direction of incoming photons. As shown in Fig. 1.5, gamma-ray-induced showers appear as compact ellipses in the camera, and their parameters are used to extract information about the primary photon that initiated the shower.

In contrast, hadronic cascades exhibit a more irregular and broader shape due to the complex interactions of hadrons and the larger variety of particles produced.

The energy threshold of the detected photons for an IACT is directly proportional to the square root of the flux from the background, the solid angle of the mirror, and the integration time of the Cherenkov signal. These values should be kept as low as possible if the aim is to lower the energy threshold for detection. However, the threshold is also inversely related to the efficiency and the mirror's surface area. Indeed, larger collection areas allow the detection of Cherenkov light from gamma rays with lower energies.

The simultaneous observations of Cherenkov light with multiple IACTs is called stereoscopic observation mode, opposite to the monoscopic observation mode, performed by a single Cherenkov telescope. The implementation of stereo observations enhances both the efficiency in the three-dimensional reconstruction of showers and the ability to tag background signals. This improvement has notable effects on factors such as sensitivity, angular resolution, and energy reconstruction. Additionally, it allows us to reduce the energy threshold of the instrument.

The details about the telescope structures and the analysis methods introduced in this Section will be addressed in the next Chapter, using the MAGIC telescopes and relative data analysis chain as an example.

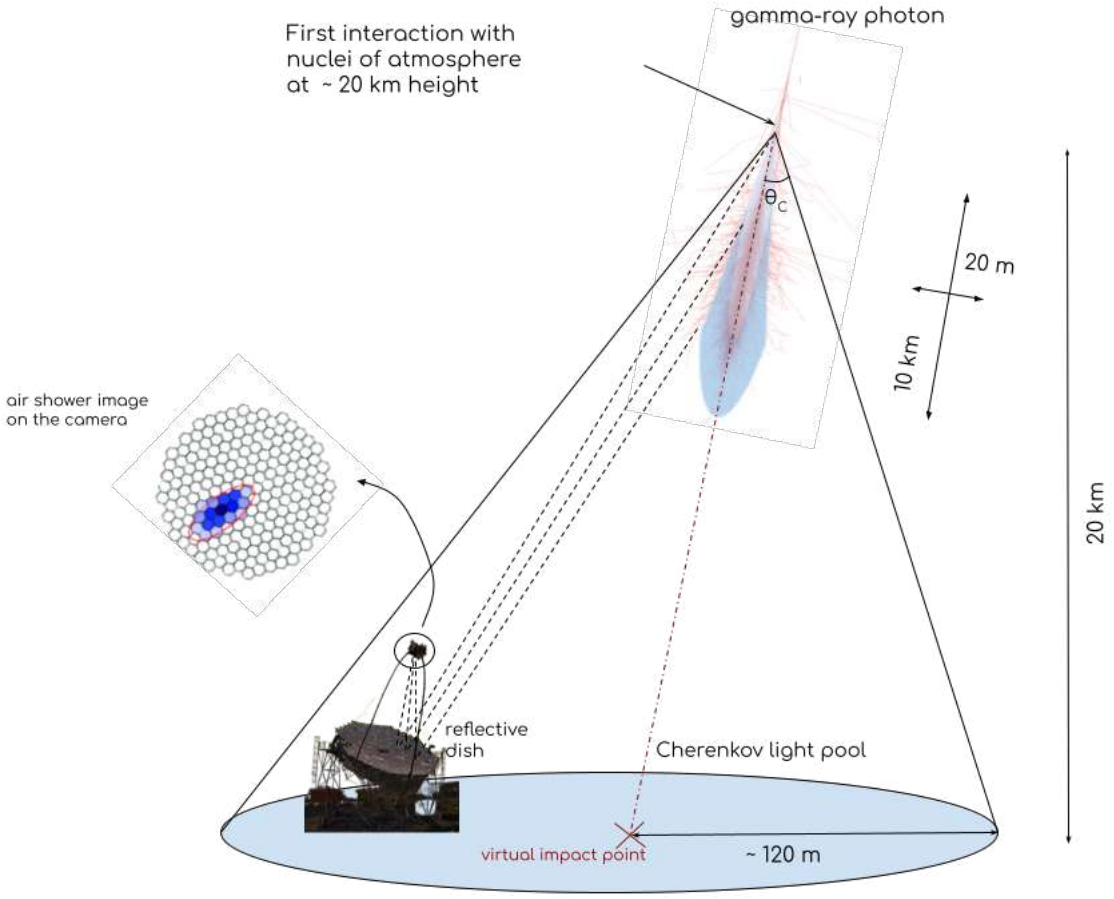

Figure 1.5: Schematic illustration of a IACT system collecting the Cherenkov light from a gamma-ray-induced shower.

Chapter 2

Current generation of IACTs: the MAGIC telescopes

2.1 The MAGIC telescopes description

Two Cherenkov telescopes compose the MAGIC stereoscopic system (Fig. 2.1). The telescopes, MAGIC-I and MAGIC-II, are located within the Roque de los Muchachos observatory of La Palma, in the Canary Islands. Due to the quality of the sky and the low light pollution there, the observatory hosts one of the largest collections of telescopes dedicated to astronomical research in the world.

Figure 2.1: A daytime view captured at the MAGIC site, where the two telescopes are in their park positions, with the cameras set atop their pillars. In the middle, the CH structure hosts the LIDAR on its roof. In the background, other telescopes and instruments that are part of the Roque de los Muchachos observatory can be seen.

The two MAGIC telescopes are situated at about 2200 metres above sea level. At this height, the atmospheric absorption of the gamma-ray signals is the optimal one for observations. MAGIC-I has been operational since 2003, while MAGIC-II started its operations in 2009. The energy range covered by the system goes from about 30 GeV to tens of TeV.

MAGIC-II was built to be as much identical as possible to MAGIC-I. They separated from a distance of 85 m and between them is located the *Counting House* (CH, shown in Fig. 2.1).

From this building, the telescopes are operated.

The fundamental parts of the telescopes are the parabolic reflective dish and the camera. The two can be seen in Fig. 2.2 using MAGIC-II as an example whereas a schematic view is provided in Fig. 1.5.

The 17-meter diameter reflector dish of the two telescopes provides a collection area of 236 m^2. In particular, each reflective area is tessellated of individual mirrors of about 1 m^2 each. The reflector has a parabolic shape in which the radius of curvature is equal to the focal length. Coma and astigmatism affect this type of reflecting surface. However, this configuration is also the most effective for focusing light isochronically. The signals reflected by the mirrors at the same angular distance from the centre arrive at the same time (isochronous). This is crucial to preserve the timing structure of the high-speed Cherenkov signals. The signal-to-noise ratio of the photon pulse in each camera pixel is optimized. Therefore, the integration windows used to search for the signal can be narrowed, thus reducing the background from spurious night skylight. The quality of the reflective performance is monitored each night by measuring the PSF. This describes the probability distribution of a point source in the sky on the camera plane. The PSF value can slightly vary depending on environmental conditions.

The structures supporting the reflector dish of the two telescopes are constructed from carbon fibre. This material is robust but lightweight, the total weight of each telescope is indeed less than 70 tons. This allows rapid movements of the telescopes, which are key for quickly repointing and observing transient sources like GRB. The telescopes can be oriented to any point in the sky in less than 20 seconds. To this purpose also the weight of the camera is reduced by locating the readout electronics in the CH. The signal is transmitted from the camera to the CH using optical fibres. The mirrors are mounted on an alt-azimuthal mount that moves along a circular rail with a 19-meter diameter. The mounts allow azimuthal and altitudinal movement through the use of three driving motors. The telescopes can point in any direction over a range from $+99°$to $-72°$in declination and from $-89°$to $+318°$in azimuth. To ensure precise pointing, a starguider camera is positioned at the centre of the telescope dish. This camera measures any potential deviations between the positions of reference stars in the FoV and the known positions of those stars stored in standard star catalogues. If any misalignment occurs, it is promptly corrected. The pointing accuracy is further refined by an Active Mirror Control (AMC) that adjusts the mirrors of the reflector dish according to the zenith angle of the target under tracking.

Since the last major upgrade in 2012, the cameras of the two MAGIC telescopes are identical and designed to provide a fast response and high sensitivity, crucial features for IACTs. They are set in the focus of the reflectors, supported in place by two metallic tubes forming an arch. When the telescopes are not observing, the cameras are laid on a tower (Fig. 2.2). Both cameras comprise 1039 UV-sensitive PMT. For easy replacement and upgrades, the PMTs are grouped into 169 clusters of hexagonal shape. Each cluster contains seven pixels. The FoV of each PMT is about $0.1°$, and the total FoV of each camera is $3.5°$. The small size of each PMT allows a good sampling of the image's showers and a reduction of the noise from the NSB light, making the detector more sensitive to lower-energy events. In the PMTs the Cherenkov photons are converted into a cascade of phe and finally into an electrical signal. The voltage applied to each PMT can be adjusted. To ensure an equal number of photons at the entrance of each PMT, a flat-fielding procedure that corrects for variations between PMT is applied. The QE of PMTs is of the order of 34% at a wavelength of 350 nm which is the peak of the Cherenkov spectrum. The electrical signal generated from PMTs is then converted into optical pulses. The optical pulses are driven to the CH via optical fibres (mentioned above). For protection from environmental conditions and sunlight, the cameras are equipped with plexiglass windows in front of the light collectors and covered by lids.

The total achievable observing time for MAGIC telescopes is approximately 2200 hours per year if considering Moon periods too. This time is allowed by the capabilities of the telescopes to

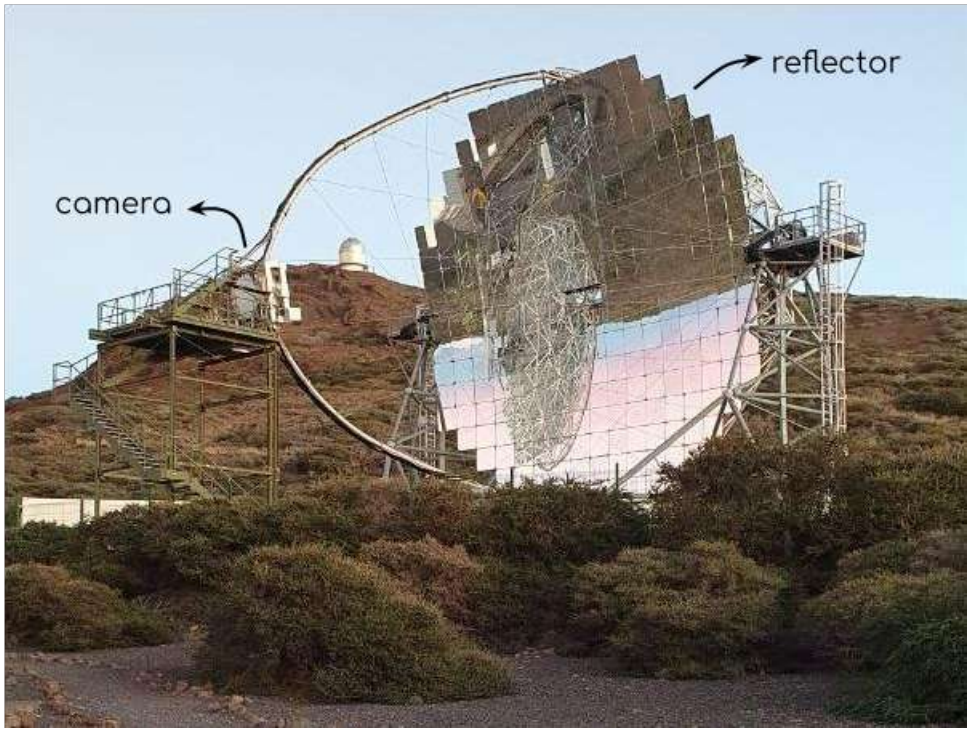

Figure 2.2: Picture of MAGIC-II in park position before the operation starting. MAGIC-I can be recognized mirrored in the reflector dish.

operate under various conditions, including during twilight, and even bright Moon conditions. About 10-15% of the total available observing time is lost due to technical problems or unfavourable weather conditions. The telescope operations are controlled by the *Super Arehucas*[1] software, designed through a LabView interface. It supervises all the subsystems which control each part of the telescope.

2.2 Data tacking procedures

A multi-level decision system part of the telescopes determines event acquisition. This trigger system consists of three levels: Level-0 (L0), Level-1 (L1), Level-3 (L3). Selected a Discriminator Threshold (DT), L0 triggers reject signals below that DT on a pixel-by-pixel basis. Once passed the L0 level, at the L1 stage, the signals encounter a coincidence trigger system, organized into overlapping hexagonal macrocells, each comprising 37 pixels. The individual telescope trigger is based on a Next-Neighbour (NN) logic, which means it searches for neighbouring pixels that exhibit a signal exceeding the DT within a tightly defined time window. For standard stereoscopic operations, the 3NN logic is the most commonly used, but from 2NN to 5NN ones are also employed in some cases. Before being transmitted to the next trigger level (L3), the survived signal is adjusted accounting for the differences in arrival times of Cherenkov light events due to the azimuth and zenith orientation of the telescopes. Finally, the L3 triggers combine the L1 information from each telescope, searching for timing coincidences. The width of the time windows for coincidence varies with the telescope's pointing directions. This is because the delay of the signals is determined by the relative orientation of the telescopes. A maximum delay of 200 ns is acceptable. If this value is exceeded, the telescopes are unable to initiate a trigger event. The values of the three trigger levels (in Hz) are strongly affected by

[1]From the name of a known rum from Gran Canaria

the observing conditions as the NSB level, the presence of clouds, etc. For example, during a standard observation with no Moon and no clouds, the L0 rate is around 800 kHz. The DT adopted at each level is selected to minimise the number of accidental events and background events in each observing condition. For example, the DT is increased during Moon observations and when pointing to the galactic plane. Moreover, bad weather conditions can lead to the potential damage to the instrumentation itself. To ensure the good quality of the data and safeguard the instruments, weather parameters are monitored. If certain safety thresholds are exceeded, the data acquisition is halted.

Two additional trigger types have been introduced to enhance the performance of the MAGIC telescopes at low energies. The *SumTrigger* sums analog signals from various macrocells and compares the sum to a given DT (acting as an L1 trigger), while the *TOPO Trigger* involves topological event discrimination to significantly reduce the rate of accidental events (acting as an L3 trigger).

Once the optical signal reaches the CH via optical fibres, it is converted to an electric signal again and split into two halves: an analog readout branch where the signal is collected waiting for the trigger decision and a trigger digital branch. The latter generates L0 individual pixel trigger signals applying the DT, the signal is then sent to L1 and L3 as described above. If L3 is triggered, the data previously collected and waiting for the trigger decision is digitized and stored to disk by the Data AcQuisition System (DAQ).

2.2.1 Calibration

Data acquisition is organized into subruns, grouped into runs of 15/20 minutes each. At each run, three types of events are recorded: pedestal events, calibration events, and data events. Pedestal events are recorded to define the electronic noise of the readout system. Calibration events come in two forms: extensive and interleaved. Extensive calibration runs occur at the beginning of each night's observation for a new source and serve to flat-field the camera using the F-factor method (Mirzoyan 1997). Interleaved calibration events are taken during data acquisition, together with pedestal events. These are used to correct for PMT performance variation due mainly to changes in temperature. Calibration runs primarily aim to provide the conversion factor between Analog-to-Digital Converter (ADC) counts and the number of phes. The calibration electronics are contained in *calibration boxes* located at the centre of the reflectors.

2.2.2 Observing mode

Currently, the most commonly adopted observing mode for MAGIC observations is the so-called *wobble mode*.

This approach consists of slightly offsetting the telescope's pointing away from the exact coordinates of the source in the sky. Throughout the observation, the telescopes then rotate among a series of these offset positions, all of which are equidistant from the source's actual position (Fig. 2.3). The regions observed are referred to as "wobbles". Conventionally, an angular offset of 0.4 degrees is selected between the source coordinates and the wobble position.

During each data run, the telescopes are directed toward a wobble position. Once a data run concludes (after 15/20 minutes), the pointing position is shifted to a new wobble position. In the wobble mode approach, the background signal is estimated from a region located at the same distance from the camera's centre as the source. For instance, if two wobble positions are employed, the background is extracted from a region positioned on the opposite side of the camera's centre (Fig. 2.3).

This strategy achieves two goals: *(i)* evaluating the background signal from a camera region where the response closely resembles the part of the camera dedicated to the target (assuming symmetrical camera efficiency from centre to periphery) and *(ii)* saving observation time by collecting target and background data simultaneously, thus avoiding the need to move between target and background positions. However, the efficiency of gamma-ray detection decreases as a fraction of electromagnetic cascades lie outside the camera's trigger region due to the offset from the true source position.

The number of regions used for background estimation can range from one to five, with four being the usual choice. Utilizing multiple regions enhances the precision of background estimation by reducing systematic effects.

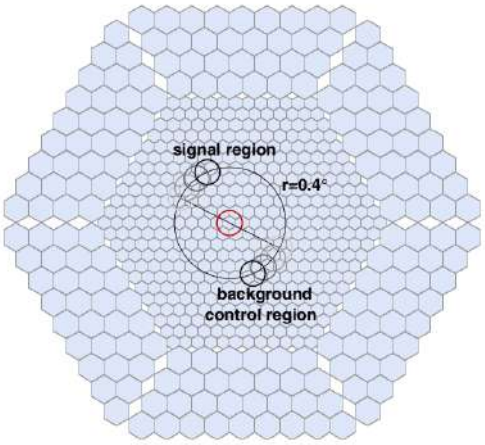

Figure 2.3: Scheme of a wobble observing mode. As the observations proceed, the two wobble positions are alternated.

The alternative observing mode, in some cases employed in MAGIC observations, is the "ON/OFF mode". In this case, the telescopes are directly pointed at the source position, keeping it at the centre of the camera. Background data are collected during a different pointing to a source-free region.

2.3 MAGIC data analysis chain

The data from the MAGIC telescopes are analysed with the proprietary software MAGIC Analysis and Reconstruction Software (MARS, Zanin et al. 2013), a ROOT-based software written in C++. It includes several executables for the reconstruction of the signal information starting from the shower's image. The data from MAGIC telescopes are organized in ROOT files, composed of ROOT trees containing all the data information stored in branches and leaves.

2.3.1 Telescope level signal extraction and calibration

Originally, MAGIC data contains waveforms of the signal per event and pixel. A waveform represents the signal binned into fifty-time slices of a duration of 0.5 ns each. The initial data processing stage involves the calculation of the signal arrival time and the transformation of the sampled waveform from each pixel into an integrated charge in phe units. To correctly obtain the signal charge, the signal baseline has to be evaluated and subtracted from the waveform. For that, the pedestal events mentioned in the previous Section are used. Knowing and subtracting the pedestal level, the signal extraction is performed using a sliding window algorithm. For each sampled waveform, the total charge is determined as the maximum sum of 5 consecutive time slices.

The charge, given in ADC counts in MAGIC raw files, is then converted to phes using the F-factor method (Mirzoyan 1997), according to which the number of phes follows a Poisson distribution. The typical conversion ratio is 1 phe to 60 integrated ADC counts. The arrival time of the signal is calculated as the weighted average of the time slices within the integrated window. This accounts for pixel-to-pixel differences due to variations in optical fibre lengths and electron transit times in the PMT.

The calibration process is managed by the `sorcerer` executable of MARS.

2.3.2 Telescope level image cleaning

Once the signal from the camera pixels is extracted and converted into phes, the next step consists of removing the pixels from which the signal does not come from the shower's image but from the NSB fluctuations. This procedure is known as *image cleaning*. The most effective method for image cleaning utilizes both the information regarding the charge content and the arrival time to distinguish between pixels containing the actual shower image and those with background noise. A pixel with a charge content exceeding a certain threshold in phes, and at least one neighbouring pixel meeting the same condition, is recognized as a *core pixel*. The concept is similar to the NN algorithm used in the L1 trigger level. All pixels with at least one core neighbour and a charge above a threshold (lower than the one for the core) are integrated into the image and identified as *boundary pixels*. In this process, it is essential to carefully select the optimal threshold values. Adjusting the cleaning levels can lead to a larger number of pixels per image and, consequently, a lower energy threshold for the analysis, as a minimum pixel count is necessary for the analysis to proceed. However, lower cleaning levels increase the risk of including noise pixels in the cleaned image. The presence of unrelated pixels in the image degrades its parameters and decreases the subsequent analysis's performance.

The arrival time value for each pixel is used to refine the selection of core and boundary pixels. Timing coincidence windows are employed to discriminate between the Cherenkov signal, collected within a few nanoseconds, and the NSB noise which follows a random time distribution. The mean arrival time of all core pixels is compared with the individual core pixel arrival time and if the time gap is larger than a selected time window, the pixel is rejected as coming from the background. Similarly, for the selection of boundary pixels, the time difference between the boundary pixel candidate and its neighbour core pixels must be smaller than a second fixed time constraint. These values have been optimized for dark night conditions, higher NSB levels are expected during moonlight or twilight observations.

This time-based image-cleaning approach method mitigates the confusion between NSB signals and actual image tails and consequently allows us to relax the cleaning threshold values and lower the energy threshold. All the discarded pixels are set to 0 phes in the ROOT files containing the cleaned images. The image cleaning is executed by the `star` package of MARS, the resulting ROOT files are indeed called `star` files and are used in the following step of the analysis.

The one described above is the most used approach for image cleaning in the MAGIC analysis, however, it must be mentioned that other approaches also exist.

2.3.3 Telescope level image characterisation and event reconstruction

After cleaning the shower image, the next step is to determine whether the event was induced by a gamma ray or a hadron based on the shower image parameters. This is accomplished using the `star` executable, soon after the cleaning procedure. The shower images then undergo the so-called *image characterisation*. This process involves the calculation of image parameters, often referred to as Hillas parameters from the name of the first scientist who introduced them (Hillas 1985). These are derived from the moments of the light distribution within the camera pixels. Due to the distinct distributions of those parameters for gamma-ray and hadron events, they will be used later on also for the background rejection. As seen in the previous Section, the gamma-ray shower image typically has an elliptical shape, and some of the parameters are related to the geometric properties of the ellipse.

Following is a list of some of the main parameters.

- *Size*: Total charge contained within the shower image, which is more or less proportional to the primary particle's energy.

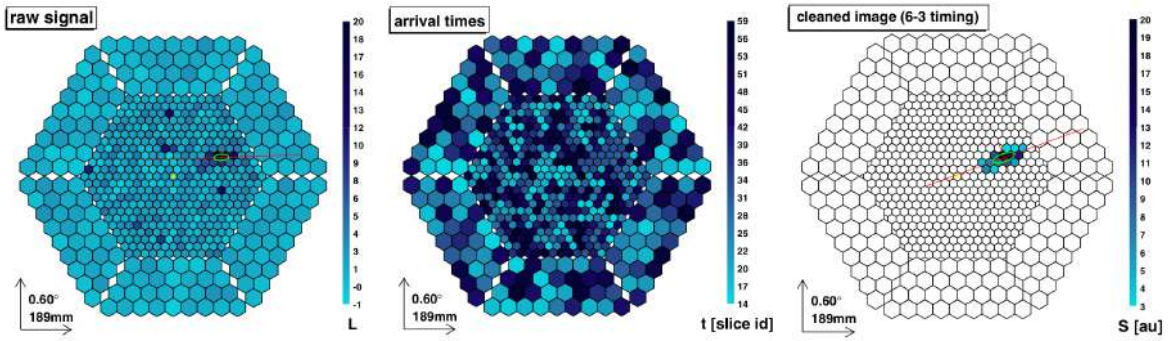

Figure 2.4: Example of a shower image from a gamma-ray photon collected by a MAGIC camera. Starting from the left: in the first panel the raw data in terms of phe content per pixel is shown, and in the second panel the raw data in terms of arrival times is represented. The third panel shows the shower image in the camera plane after the image cleaning. This is performed by adopting a charge threshold of 6 phes for core pixels and 3 phes for boundary pixels. The time windows adopted are 4.5 ns and 1.5 ns, respectively. All the pixels not coming from the shower images are set to 0 phes. The Hillas ellipse is highlighted in green. Adapted from Aliu et al. 2009.

- *Length*: The root mean square (RMS) spread along the major axis of the elliptical image. This parameter provides information about the longitudinal development of the shower. Typically, hadron-induced showers exhibit a larger Length value compared to gamma-ray-induced showers.

- *Width*: The RMS spread along the minor axis of the elliptical image. It characterizes the lateral distribution of the shower's light.

- *Center of Gravity (CoG)*: A pair of values (X and Y in the camera's reference frame) representing the centre of mass of the shower image.

- *M3long*: The third momentum of the image along the major axis of the ellipse. It provides information about the asymmetry of the shower image and where the shower is pointing.

- *Number of islands*: Indicates the count of distinct islands within the image, with an island being a group of isolated pixels surviving the cleaning process.

- *Conc-n*: For the n brightest pixels it measures the compactness of the shower maximum region. It is calculated as the ratio of the light content of the n pixels to the total light content of the shower. Typically, gamma-ray showers exhibit greater compactness.

This variety of shower shapes and characteristics presents different challenges and opportunities in the analysis of gamma-ray events.

The timing feature has a high discrimination power between gamma-ray- and hadron-induced EAS's images. The timing profile along the major axis of the shower image is influenced by the shower's impact parameter (Fig. 1.5) and it is key to recognize Cherenkov flashes. For an impact parameter smaller than ∼60 meters, the light from the upper part of the shower (shower head) arrives later than the light emitted from the lower part of the shower (shower tail). This happens because the initial photons travel at a slower speed (c/n) compared to the ultra-relativistic particles in the shower that produce photons closer to the ground. If the impact parameter is greater than 120 meters, this effect is reduced or even inverted, as the arrival time from the tail becomes the sum of the times spent in particle and photon paths, respectively. Taking this into account, two time-related image parameters are employed in MAGIC analysis (Aliu et al. 2009).

- *Time Gradient*: The rate at which the arrival time changes along the major axis of the ellipse. It is the angular coefficient of a linear function used to fit the arrival time as a function of the spatial coordinate along the major axis of the ellipse. It is positive when the arrival time increases with the pixel's distance from the source position in the camera.
- *Time RMS*: Represents the spread of the arrival time distribution of the pixels belonging to the image after the cleaning. the Time RMS distribution for hadron-induced showers typically exhibits a longer tail towards larger values.

The values of the image's parameters are stored in the ROOT `star` files which will be the input files for the successive MARS executable.

2.3.4 Stereoscopic reconstruction

At this stage, two separate datasets contain the same events observed from two different viewpoints, from MAGIC-I and from MAGIC-II. The *stereoscopic reconstruction* stage consists of merging the MAGIC-I and MAGIC-II `star` datasets into a single dataset while calculating stereoscopic parameters that provide a three-dimensional description of the events. The stereoscopic parameters that are computed at this stage are the following:

- *Shower Axis*: The shower axis gives the direction of the event coming towards the ground. It is derived taking into account the intersection of the major axes of the two images when overlaid on a common camera plane, and the impact point on the ground, determined by the intersection of the major axes of the two elliptical images originating from the telescope positions, accounting for the distance between the two telescopes.
- *Impact Parameter with respect to Each Telescope*: This parameter provides information about the position of the impact point relative to the telescope's pointing axis. It is measured as the perpendicular distance between the shower axis and the telescope's pointing axis.
- *Shower Maximum Height*: The height of the shower maximum is determined by observing the angle at which the image's CoG is viewed from each telescope. The height of the shower maximum depends on the cascade energy, with higher-energy showers penetrating deeper into the atmosphere, resulting in a lower maximum height. This parameter is particularly useful for distinguishing between gamma-ray events and low-energy background events.
- *Cherenkov Radius*: The Cherenkov radius represents the size of the Cherenkov light pool on the ground. It is calculated under the assumption that Cherenkov light is produced by a single electron of the shower at the height of the shower maximum, with an energy equivalent to the critical energy of 86 MeV.
- *Cherenkov Photon Density*: The Cherenkov photon density on the ground is evaluated under the same assumptions used for the Cherenkov radius parameter and it provides insights into the distribution of Cherenkov light and details of the atmospheric cascade.

In the MAGIC analysis chain, the stereoscopic reconstruction is performed running the `superstar` executable of MARS.

All the steps described up to this point — the signal extraction and calibration, the image cleaning, characterization and the stereoscopic reconstruction — are performed in a standard way for each dark observations. These procedures do not necessitate specific user interventions or parameter adjustments. For this reason, these steps are usually executed by a dedicated team in the MAGIC Collaboration. The final cleaned and stereoscopic-reconstructed `superstar` data are provided to the users for the subsequent analysis.

2.3.5 Data pre-selection

Unstable weather conditions significantly impact the data collection process of IACTs. The primary sources for signal corruption and obstacles in data acquisition are the presence of dust aerosols, wind, and water aerosols caused by high humidity, rain, and clouds. These phenomena can result in the attenuation of Cherenkov light through the scattering and absorption of photons, affecting the accurate energy reconstruction and subsequent measurement of shower parameters.

Positioned on top of the MAGIC counting house is a weather station that constantly monitors meteorological parameters such as temperature, humidity, pressure, and wind speed. The accurate determination of cloud presence in the direction of pointing of the MAGIC telescopes instead relies on a pyrometer. The pyrometer evaluates sky temperature and employs an empirical function to compare it against a reference sky temperature in cloud-free conditions.

On top of the CH is the Light Detection and Ranging (LIDAR) system[2] (Fig. 2.1). This operates by emitting laser pulses close to the observation coordinates and measuring the quantity of light backscattered to its detector. More specifically, as the laser light transits the atmosphere, it interacts with aerosol particles, leading to reflection and scattering. Given the isotropic nature of these processes, a portion of this scattered light is also directed back to the LIDAR detector. Then, through the analysis of backscattered light intensity and arrival time, the LIDAR system determines the aerosol transmission profile as a function of the altitude above the MAGIC site, specifically at elevations of 3 km, 6 km, 9 km, and 12 km. The aerosol transmission value provided by LIDAR is a dimensionless number that essentially quantifies the ratio between the backscattered light and the emitted light. Atmospheric extinction due to aerosol and clouds along the light path dictates this ratio. It ranges from 0 to 1, where 0 implies that numerous aerosols in the air entirely absorb or scatter the laser light, while 1 indicates that all the laser light is detected back at the LIDAR, so no absorption or scattering has corrupted the signal.

According to the conventional data quality division adopted in MAGIC analysis, high-quality data are ensured when the transmission is between 1.00 and 0.85, while data with transmission from 0.85 down to 0.70 still maintain good quality. When the transmission ranges between 0.70 and 0.55, data must be corrected by additional processing, and when the transmission is below 0.55, collected data are considered unsuitable for analysis.

Even though weather and aerosol monitoring prevents instrumentation damage and data taking during not optimal conditions, the quality of the data can still be compromised due to software and instrument malfunctions, including the unavailability of LIDAR measurements itself, and other unpredictable factors (such as light flashes from humans in the proximity of the MAGIC site, increasing the trigger rates). For this reason, a quality check of the data is essential before proceeding with the analysis. Usually, if LIDAR data are available, the selection is mainly based on the aerosol transmission, in particular at 9 km, because the average altitude at which showers manifest is around 10 km. Data with transmission below a certain transmission threshold are removed.

Other parameters can be taken into account for data selection, such as zenith and azimuth angles, event rates, and clouds. In situations where LIDAR data is unavailable (for instance, when the LIDAR is not operational), cloud cover or event rates can serve as alternatives.

All the weather parameters described are collected in the ROOT files together with the event information. In practice, the quality selection is performed by running `quate` executable of MARS, which inspects several parameters as a function of factors like the zenith angles. The output of `quate` generates a sub-dataset that exclusively contains high-quality data or, alternatively, a list of data earmarked for exclusion in subsequent stages of analysis. The threshold on

[2] A comprehensive overview of the LIDAR's performance and functionalities can be found in Fruck et al. 2022 and in the references therein

each parameter used for the selection is adjusted by the users.

For further assessments of the quality of the data-taking, the runbooks for the observing nights provide many details that can also improve the data selection. The runbooks collect notes by the telescope operators taken at each step of the observation. In addition, a series of plots reporting the instrumentation performance is generated by the subsystems at any stage of observation and are made accessible to users.

2.3.6 Event selection and background rejection

As seen in the previous Sections, the main source of background for IACT is the significant detection of hadrons: around 1 gamma-ray event over 10^4 hadron events is recorded. Then, hadron events need to be identified and filtered out.

This is done through a process called *gamma/hadron separation*. The separation is feasible because gamma-ray and hadron events follow distinct distributions of image and stereo parameters, allowing us to differentiate between them.

To accomplish the separation, a multidimensional classification algorithm, specifically the Random Forest (RF, Albert et al. 2008) algorithm, is employed. The RF is implemented in the MARS executable called `coach`.

The image and stereo parameters of each event, previously computed using the `star` and `superstar`, are collected in a multidimensional array. Each event is described by a set of N parameters, and these parameters define an N-dimensional space encompassing all the events. The algorithm starts at the root node, where one of the N parameters is randomly picked and a specific cut is applied to divide the events based on the parameter. The choice of the cut is fine-tuned to optimally separate the hadronic and gamma-ray samples based on this specific parameter. This process is iteratively repeated, with different parameters chosen at each node and optimized cuts determined. The algorithm continues until the final nodes exclusively contain gamma-ray or hadron events. The Gini index is used to optimize parameter cuts and tree building. This is a way to measure what is the rejection power of a parameter. The RF method aims to maximize this separation.

The final nodes of the decision trees provide a global parameter hadronness value for each event, indicating the likelihood of being a gamma-ray or a hadron event. All the nodes together constitute a decision tree. In `coach`, 100 trees are generated, and the cumulative hadronness value is obtained by averaging the ones across 100 trees.

The decision trees are first trained using known samples, that are simulated gamma-ray-events and a set of solely hadronic events, the "OFF" data, taken from actual observations of a dark patch in the sky. The gamma-ray events are obtained from Monte Carlo (MC) simulations. An MC dataset of events is previously split into two samples, one for the RF training and one as a test sample, utilized for computing the instrument response function (IRF).

To ensure efficient rejection of hadronic background, maintain event characterization consistency, and optimize the IRF construction (see Section 2.3.8, the selection of the MC and OFF data sample aims to closely mirror the observation conditions of the target data (the "ON" data). MC data have to be simulated assuming, for example, the same zenith range, Moon level, observation setting and so forth, as in ON observations. For this reason, various sets of MC data are provided by the team of the MAGIC Collaboration whenever the telescopes undergo any modifications, such as updates in instrumentation or software, or following particularly impactful natural events that could significantly alter the telescopes' response. In such cases, a comprehensive range of observation conditions is simulated to ensure the appropriate MC dataset for each observation.

OFF (i.e., background) data could be simulated as MC data. However, many targets have a too weak signal to be detected in one MAGIC observation. Therefore, many MAGIC datasets

only contain background noise and these can be used as OFF data. The principle of mirroring ON data is equally applicable to selecting OFF data. Initially, the OFF sample is built by the user by searching in the MAGIC database for the (background) data taken in the same time interval and with the same zenith angle as the target source. Then, the finer selection (described in Section 2.3.5) is applied to the sample, to delete bad-quality data and data not precisely matching with the ON sample.

2.3.7 Energy Estimation

At this stage of the analysis, with the `coach` executable, the energy and the arrival direction of gamma-ray events are computed. The energy is estimated with the Look-Up Tables (LUTs) (Aleksić et al. 2012) which are multi-dimensional tables divided into average energy intervals. These LUTs are generated using the MC sample used for training the RF. The sample is partitioned into bins based on combinations of image parameters that affect energy reconstruction like, as a first approximation, the image size as measured by each telescope. Finer corrections are applied to account for factors such as the shower's maximum height, zenith and azimuth angles, larger images that are only partially captured by the camera, etc. The final energy estimation is computed as the average of the energies independently reconstructed for each telescope, with assigned weights based on the inverse of their respective uncertainties. By placing the collected gamma-ray event in the LUTs bin according to the event's image parameters, the energy of the gamma-ray is estimated. The energy resolution within the range of 200 GeV to 1 TeV is approximately 15%. The resolution tends to degrade to around 25% at lower energies (around 100 GeV).

The arrival direction of gamma-ray events is measured with the $DISP$ method (Aleksić et al. 2012; Aleksić et al. 2016). A representation of the method for a stereoscopic mode is illustrated in Fig. 2.5, where image 1 and image 2 are the two images taken at each telescope camera. As mentioned earlier, the shower's image appears as an ellipse when the telescope's camera captures it. The major axis of this ellipse defines the arrival direction from which the shower reached and interacted with the camera.

The direction in the sky from which the gamma-ray event comes is aligned with this major axis, although not exactly at the centre of the ellipse, i.e., the CoG of the image. Instead, it is located at a specific distance away from it. The distances from CoG parameters are computed by applying the RF algorithm trained on the MC sample. As a first approximation, the formula describing the $DISP$ parameter is a function of the Width and Length parameters and it is defined as (Fomin et al. 1994):

$$DISP = a + b\frac{\text{Width}}{\text{Length}} \tag{2.1}$$

In the extended form, it also takes into account correction terms for the truncation of large images at the camera's edge. A distance value is measured for each event and each telescope. In a stereoscopic system, there are as many distance values as the number of telescopes. In principle, for the MAGIC telescopes, two solutions emerge for each event along the major axis of the two ellipse images.

A further ambiguity in estimating the shower's arrival direction arises due to two potential positions on either side of the image's centre. In Fig. 2.5 these are identified with the empty circles 1A and 1B for image 1, and 2A and 2B for image 2. These positions correspond to the head and tail of the shower's image on the telescope camera. Consequently, for the MAGIC two-telescope system, the $DISP$ method yields four distances from the CoG initially.

The angular distances between these four positions are calculated (in Fig. 2.5: the dotted lines connecting 1A and 2A, 1A and 2B, 1B and 2A, 1B and 2B), and the pair with the smallest distance is chosen, that is the distance between 1B and 2B in the scheme of Fig. 2.5. The final estimated source position is obtained by averaging these two positions. In Fig. 2.5, the estimated source position is marked with the black circle and the true source position with the empty diamond. The angular distance θ between the true source position and the estimated position for the gamma-ray event is drawn with the black solid line. The angular resolution of the $DISP$ method is of the order of 0.07 degrees at 300 GeV. It increases at higher energies.

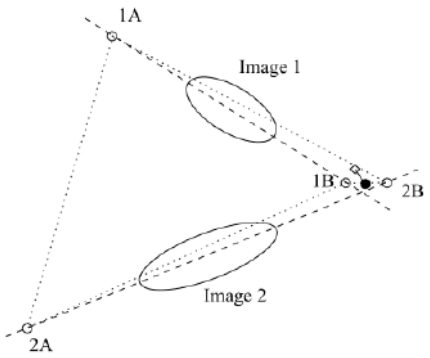

Figure 2.5: Scheme for the estimation of an event's arrival direction, known as the $DISP$ method. The details are described in the text. From Aleksić et al. 2016.

The `coach` execution, employing MC and OFF datasets, provides the trained RF algorithm and LUTs that will be used to extract gamma-ray-induced events from the hadron background and to estimate their energy and arrival direction.

Finally, the RF and LUTs are run on the target dataset (ON data) via `melibea` executable of MARS. This provides `melibea` data format, that is the source event list composed of surviving gamma-ray events with assigned hadronness, estimated energy and arrival direction. `melibea` is also run on MC test dataset – opposite to MC train dataset used up to this point. The MC `melibea` data are crucial for the next steps of the analysis.

2.3.8 The Instrument Response Function

The knowledge of the IRF is necessary to convert the estimated parameters into gamma-ray photons' true physical values and thus can be done only through MC-simulated data, taking into account all relevant observing factors. Essentially, for IACTs, the IRF depends on mathematical functions of the energy and the arrival direction of the events. The IRF computation also accounts for the cuts applied in the previous steps of the analysis.

The effective area provides how much of the total available collection area is contributing to detecting photons. The larger the effective area, the higher the telescope's sensitivity to detecting events. The effective area strongly depends on the zenith angle and the energy of the primary gamma ray. Photons arriving from high zenith angles, cross a larger portion of the atmosphere so they are more probably absorbed or reflected, mainly at low energies. This results in a smaller effective area at low energies. At low zenith angles, the light pool of the photons is smaller but the detectable photons increase due to less interference with the atmosphere, the efficiency of the collection increases at low energies too. An example of the typical effective area trend as a function of the energy is shown in Fig. 2.6.

The energy dispersion characterises how much the estimated energy (from the LUTs) might deviate from the true energy for different events. The calculation of this is based on the accuracy of energy reconstruction.

2.3.9 Signal detection

After retrieving the event list in the form of `melibea` files, the following step is to ascertain the presence of a gamma-ray signal within the considered dataset. The significance of the signal is

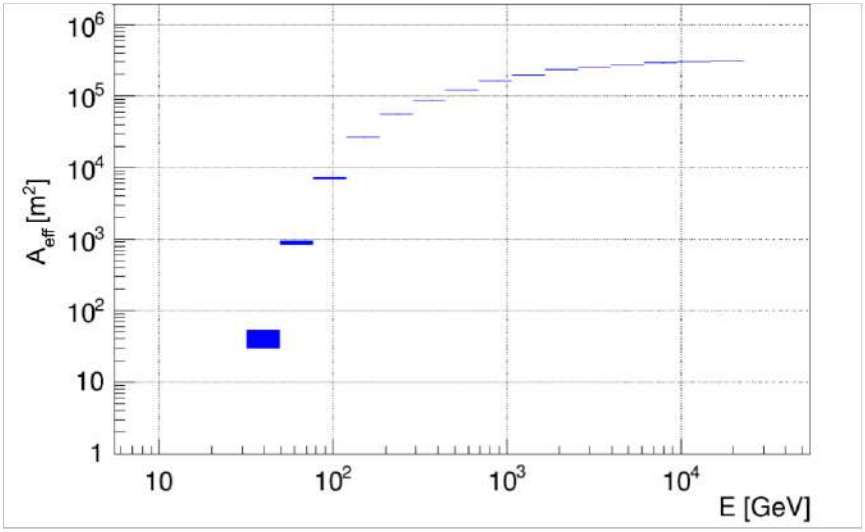

Figure 2.6: Collection area, A_{eff}, calculated from an actual observation. It is given in m^2, as a function of the energy, in GeV.

measured by comparing the signal emerging from the target source — quantified by the count of "ON" events, denoted as N_{ON} — with a background signal — comprising "OFF" events, represented as N_{OFF}. The background signal consists of electron showers, surviving hadronic events, and diffuse gamma rays.

The region of the sky containing the source is called the "ON region", while the background portion of the sky is named the "OFF region". Multiple OFF regions can be used for background estimations. MAGIC observations are usually carried out in wobble mode (described in Section 2.2.2). In most cases, three wobble positions are used. At each wobble position, the OFF region is the circular area on the camera's opposite symmetric side relative to the source location.

The count of OFF and ON events extracted from the respective ON and OFF regions is plotted versus the square of their θ parameter, in the θ^2-plot. Here, θ (introduced in Section 2.3.6) is the angular distance between the reconstructed arrival position of the (ON or OFF) event and the region's centre. The signal region is established as a circle centred around the source position, with a radius determined by the angular distance θ. Each event is located at a distance θ from the centre, within the signal region. The ON events that populate the θ^2-plot are chosen upon applying selection criteria that account for parameters such as hadroness, size, and estimated energy. These criteria are fine-tuned for optimal sensitivity in observations of the Crab Nebula which is a standard candle for gamma-ray astronomy due to its brightness and flux stability.

In the presence of a significant signal from the source, the distribution of the events from the ON region as a function of θ^2 shows the peak at low θ^2, at the true source position. This distribution then rapidly declines as θ^2 increases. In contrast, the distribution of OFF events — attributable to an isotropic background — is uniform across all θ^2 values. In Fig. 2.7 two examples of θ^2-plots are illustrated.

The excess of ON events, N_{ex}, with respect to the background of N_{OFF}, is given by $N_{\text{ex}} = N_{\text{ON}} - \alpha N_{\text{OFF}}$, where α is the number of OFF regions considered. The statistical significance

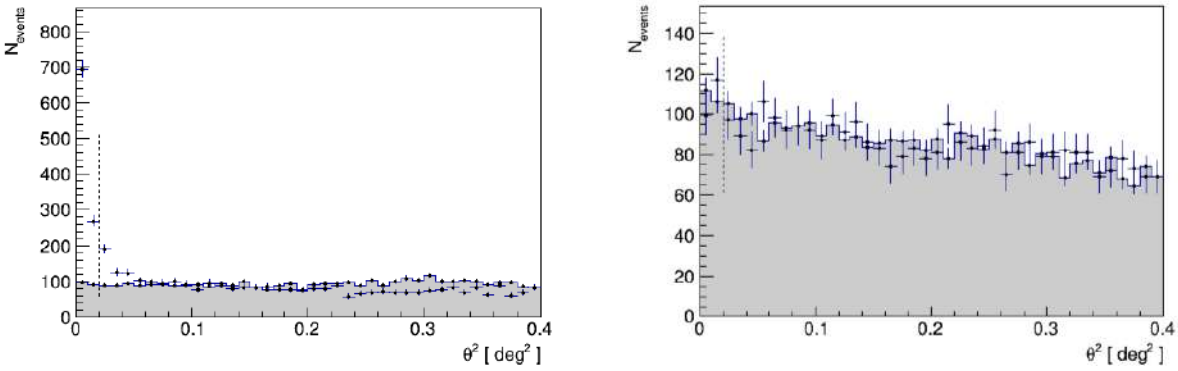

Figure 2.7: Two examples of θ^2 plots for two observations. On the left, the source is detected with a significance above 30σ (computed with Eq. 2.2), on the right the signal from the source is compatible with the background (Eq. 2.2 confirms a 0σ detection). The ON and OFF events are represented by the crosses, the grey area is taken from the background regions. When the signal from the ON region is statistically significant it can be seen that the number of ON events drastically increases at low θ^2. The dashed lines in both the plots indicate the θ^2 cuts used to calculate the significance with Eq. 2.2.

of the measured signal is calculated by the formula (Li & Ma 1983):

$$S = \sqrt{2\left\{N_{\mathrm{ON}} \ln\left[\frac{1+\alpha}{\alpha}\left(\frac{N_{\mathrm{ON}}}{N_{\mathrm{ON}}+N_{\mathrm{OFF}}}\right)\right] + N_{\mathrm{OFF}} \ln\left[(1+\alpha)\left(\frac{N_{\mathrm{OFF}}}{N_{\mathrm{ON}}+N_{\mathrm{OFF}}}\right)\right]\right\}} \tag{2.2}$$

The creation of the θ^2-plot and the application of Eq. 2.2 to obtain the significance of the signal detection is implemented in the `odie` executable of MARS.

2.3.10 Flux and light curve computation

The differential photon flux, namely the number of photons per energy, area, and time unit is estimated by:

$$\frac{\mathrm{d}N}{\mathrm{d}E}(E) = \frac{\mathrm{d}N_\gamma}{\mathrm{d}E \mathrm{d}A_{\mathrm{eff}} \mathrm{d}t_{\mathrm{eff}}} \quad \left[\mathrm{phTeV}^{-1}\ \mathrm{cm}^{-2} s^{-1}\right] \tag{2.3}$$

the quantity N_γ represents the total count of gamma rays from the source at an energy E, the effective observing time t_{eff}, and the instrument's effective area A_{eff} (described in Section 2.3.6). The effective observing time is obtained by subtracting from the overall observing time dedicated to the source the dead time of the observation, due to the electronic readout and any other interruption in the data taking. These parameters are computed by the `flute` executable in MARS, starting from `melibea` data of the target and the MC test sample. The target data contain the information on N_γ and t_{eff}, while the MC-simulated data are used to produce IRF and so the A_{eff}. Similarly to the signal estimation, the count of gamma rays N_γ with energy E is determined through the surplus of gamma events observed within each energy interval. Specific cuts on some parameters such as on the hadronness, the size and the θ^2 value for each energy bin drive the split of the events.

Spectral models The spectral points are obtained as flux points in small energy bins. These are fitted by functions describing the emitting processes. In non-thermal mechanisms, at a first approximation, the spectra can be described by a simple power law function:

$$\frac{\mathrm{d}N}{\mathrm{d}E} = N_0 \left(\frac{E}{E_0}\right)^{-\Gamma} \tag{2.4}$$

in which F_0 is the flux normalization and Γ the spectral index. In some cases, an exponential cutoff has to be introduced to describe the spectral behaviour. The function representing this model is a power law with an exponential cutoff:

$$\frac{\mathrm{d}N}{\mathrm{d}E} = N_0 \left(\frac{E}{E_0}\right)^{-\Gamma} \exp\left(-\frac{E}{E_{\mathrm{cutoff}}}\right) \tag{2.5}$$

where E_{cutoff} is the energy at which the cutoff occurs. Another spectral behaviour commonly observed is the one showing a curvature. This is represented by the logarithmic parabola function with the spectral parameter α and β describing the slope and the curvature:

$$\frac{\mathrm{d}N}{\mathrm{d}E} = N_0 \left(\frac{E}{E_0}\right)^{-\alpha-\beta[\log_{10}(E/E_0)]} \tag{2.6}$$

The last most frequently used model is the logarithmic parabola with an exponential cutoff:

$$\frac{\mathrm{d}N}{\mathrm{d}E} = N_0 \left(\frac{E}{\mathrm{E}_0}\right)^{-\alpha-\beta[\log_{10}(E/\mathrm{E}_0)]} \exp\left(-\frac{E}{E_{\mathrm{cut}}}\right) \tag{2.7}$$

The light curve provides the evolution of the integrated flux as a function of time. The integrated flux is computed above an energy threshold E_0 assuming a certain spectral distribution. When the uncertainty on a flux point is too large to be meaningful, `flute` provides an upper limit for a spectral point, both in the differential (one for each energy bin) and integral (above a certain energy) calculation. The upper limit is given if the relative error on the estimated flux is larger than 0.5.

Unfolding Estimated energies (E_{est}) are assigned to observed gamma-ray events from a gamma-ray source, while the true energies of these events (E_{true}) remain unknown. The gamma-ray events from the observed source are then grouped into bins based on their estimated energies. In the computation of the differential energy spectrum, the excess of events in bins of E_{est} energies, divided by the effective area in bins of E_{true} energies is taken into account. The fact that the effective area of the telescope is built as a function of true energy bins (involving the MC events) leads to inaccuracy. Because of the limitations in constructing in MC samples, some of these simulated gamma rays might not trigger the telescopes, resulting in the absence of an energy bin representing that particular estimated energy. Furthermore, an event with a certain E_{true} within a given interval of energies can be measured with estimated energy falling outside that energy bin.

Consequently, when comparing the number of observed events identified with an E_{est} with the effective area calculated based on E_{true}, the resulting energy estimation could be inaccurate. These effects are referred to as *spillover* or *migration* of events.

To achieve an accurate energy calculation, considering these effects alongside detector characteristics and other systematic deviations, the *unfolding* procedure is executed. This method takes migration effects between actual and estimated energies into account by calculating a *migration matrix*. This matrix links actual energies to estimated energies and is derived using the MC sample.

Given g_i, the excess events divided in i E_{est}-bins, and f_j, the excess events in j E_{true}-bins (the observable necessary for a correct estimation of the energy spectrum), the problem can be described with:

$$g_i = \sum_j M_{ij} f_j \Rightarrow \mathbf{g} = \mathbf{M} \cdot \mathbf{f} \tag{2.8}$$

where M_{ij} is the migration matrix, the noise terms are not taken into account for simplicity. It defines the likelihood that an event, originally falling within true energy bin j, is detected within estimated energy bin i due to the instrument's performance. The unfolding procedure is achieved by inverting M_{ij}, and so obtaining the f_j elements — that are the detected gamma-ray events grouped into true energy bins. However, M_{ij} is non-invertible and the elements of the matrix are correlated between them, so the solution to the problem is not univocal and different approaches are used and compared. In MAGIC analysis, the methods implemented are Tikhonov & Arsenin 1977, Schmelling 1994, and Bertero 1989. During the analysis, practice is to adopt all the methods and compare the results as a crosscheck.

2.3.11 Moon data analysis

As previously discussed, the MAGIC duty cycle has been extended by including periods with moderate moonlight. This becomes feasible through the optimization of both MAGIC's instrumentation design and its data analysis chain. As seen in the previous Sections, the presence of twilight and moonlight leads to increased NSB fluctuations at the pixel level. This translates to a higher average background of phes compared to observations conducted in dark conditions. The elevated NSB level causes a decrease in the accuracy of Hillas parameters estimation, subsequently degrading the reconstruction of the shower's images. The presence of the Moon makes the discrimination of gamma rays from the background more challenging at low energy, affecting the precision of energy and arrival direction determination. As a consequence, the energy threshold for the analysis increases.

The NSB levels are quantified by the Direct Current (DC) measurements by the pixels in the two cameras. As a reference, in dark conditions, the median DC recorded by the MAGIC-I camera ranges from 1.1 to 1.3 μA, observing the Crab Nebula at low zenith angles with a nominal High Voltage (HV) setting. However, the median DC increases as the Moon's presence intensifies during the lunar cycle. To account for these variations, observations during moonlight periods are conducted under various configurations, achieved by adjusting the pixel voltages. The nominal HV is used for standard or moderate Moon observations while reduced HV is employed in the case of a strong Moon. UV-pass filters are also introduced to enable observations during high NSB levels. During non-dark observations, the L0, L1, and L3 record lower rates. The DT is then properly selected to prevent accidental triggers. The details on the performance of MAGIC telescopes observing in Moon conditions can be found in Ahnen et al. 2017.

The data analysis chain for Moon observations follows the same steps as the dark analysis. However, to account for the higher NSB noise and the presence of a spurious signal at the pixels, it is necessary to adjust the threshold levels during the cleaning stage and apply parameter cuts (especially size and hadronness) when using the `flute` executable. Unlike standard analysis, for Moon analysis, the user starts with calibrated data (output of `sorcerer` executable) and carries out cleaning with higher thresholds based on the NSB noise level.

For the RF training, both the Monte Carlo (MC) and OFF samples should exhibit the same noise level as the target. However, standard MC data are generated with NSB levels compatible with dark conditions. Although OFF data with matching noise as the source can be available in the MAGIC database, the infrequency of Moon observations can lead to the unavailability of an appropriate OFF sample in some cases. As seen before, using MC and OFF samples not matching the target observing conditions impacts energy estimations, effective areas computation, and related parameters like flux, light curve etc. For this reason, in addition to image cleaning and parametrization, the `star` executable allows the introduction of artificial

noise into the calibrated data before the cleaning. This noise can be in the form of an artificially generated pedestal signal. To apply this noise, users need to specify RMS values for the pedestal signal. The optimal RMS values for specific NSB levels have been investigated and tabulated.

The Moon data analysis chain can be summarized as follows:

- Calibrated (dark) MC and, if necessary, OFF samples are prepared with the adequate NSB levels. This is achieved by adding noise on each sample using `star`;
- As `star` is running, also the cleaning with proper thresholds (in accordance with the NSB levels) and the image characterization are carried out;
- In parallel, calibrated data of the target are cleaned with proper thresholds running `star`;
- The MC, OFF and target datasets are affected by the same NSB noise. They have been cleaned and the image characterization has been performed. At this stage, by running `superstar` for each dataset, the events are stereoscopically reconstructed;
- Following the standard dark analysis, the RF is trained executing `coach`. The `superstar` MC and target data are subjected to the gamma/hadron separation and energy reconstruction applying the RF;
- With the `melibea` data, the signal significance and the flux and lightcurves are measured.

If the data of the target source are taken under different NSB levels, the procedure has to be performed as many times as the NSB levels. A tuned RF has to be used to perform the gamma/hadron separation in each case.

The NSB levels during the Moon phases are expressed as multiples of the NSB level during the dark condition, $\mathrm{NSB_{dark}}$. For instance, using the nominal HV setup, the NSB levels can be divided in four groups, including ranges of $\mathrm{NSB_{dark}}$ levels: $1-2\times\mathrm{NSB_{dark}}$, $2-3\times\mathrm{NSB_{dark}}$, $3-5\times\mathrm{NSB_{dark}}$ and $5-8\times\mathrm{NSB_{dark}}$. Each of these levels requires different artificial noise to be added in MC and OFF samples, distinct cleaning cuts, and specific parameter cuts.

Nevertheless, it's important to note that all the adaptations employed for Moon analysis may result in reduced sensitivity, especially under strong NSB conditions, potentially introducing additional systematic uncertainties and increasing the threshold energy.

Chapter 3

Next generation of IACTs: the CTAO era

The Cherenkov Telescope Array Observatory (CTAO) will represent the cutting-edge generation of IACTs. The project aims to significantly enhance various aspects of the VHE astronomy field. Once fully operational, CTAO will be operated as an open proposal-driven observatory. The observatory will serve a wide user community, providing data products and tools suitable for non-expert astronomers.

The CTAO will consist of two arrays located in two different geographic locations (Fig. 3.1). In the northern hemisphere, the *CTAO-North* site hosts the northern array within the Roque de los Muchachos observatory, in La Palma. This is the same site where the two MAGIC telescopes are located. In the southern hemisphere, the CTAO-South site will be hosted in the European Southern Observatory (ESO) near Paranal, in Chile. The two observatory will guarantee the maximum sky coverage. In its initial configuration, CTAO includes 64 telescopes stations. Sub-arrays can also operate independently, allowing the simultaneous observation of various targets. To achieve cost-effectiveness and broad energy coverage, the arrays will consist of three telescope designs: the Large-Sized Telescope (LST), optimized for low energy observations, the Medium-Sized Telescope (MST), for intermediate energies, and the Small-Sized Telescope (SST) optimized for energy > 10 TeV.

The design drivers of the project are multiple: *(i)* an enhancement of the sensitivity with respect to existing experiments, *(ii)* the wide energy coverage ranging from 20 GeV to 300 TeV. This will allow the study of high-redshift sources and extreme accelerator phenomena.

CTAO is expected to offer an angular resolution of sub-arcminute and an energy resolution of approximately 10% at ~ 1 TeV. These advancements, together with the wide gamma-ray FoV, of about 6-7°, will impact the imaging of extended gamma-ray sources and the detection of spectral features, low-surface brightness, and low-flux objects. The enhanced background rejection, increased collection area, and improved angular resolution will provide enhanced sensitivity to the observation of point-like sources as well.

The surveying and monitoring capabilities will be boosted thanks to the full-sky coverage and the possibility of observing in different directions simultaneously with the different sub-arrays. Supernova explosions, gravitational wave transients, and GRBs will be observable from almost anywhere in the sky. Crucially important will be the surveys of the large error boxes of gravitational wave alerts. The array's design allows for rapid response to external alerts and the issuance of its alerts. The system's telescopes are optimized for swift movement across the sky. A real-time analysis pipeline will allow the quick identification of gamma-ray activity and the distribution of alerts to other instruments.

All these innovations together, in turn, will be inevitably followed by new significant scientific outputs. CTAO science projects will focus on exploring the boundaries of the VHE gamma-ray

Figure 3.1: The two CTAO sites on a world map. The Headquarters and the Science Data Management Center locations are also displayed. The latter is hosted in the Deutsches Elektronen-Synchrotron (DESY) institute in Zeuthen, Germany. The Centre is responsible for managing data and scientific operations, maintaining software, and ensuring that the scientific outputs become accessible to the scientific community. The Headquarters are located in Bologna, Italy, and they serve as the nerve centre for the CTAO activities. It combines administrative functions, technical support, and coordination to ensure that the observatory operates effectively and efficiently, while also fostering collaboration and communication within the global scientific community. Image from the CTAO web-page.

astronomy and address a large number of still unanswered questions. The study of the origin of relativistic cosmic particles, the search for dark matter at high energies, and the investigation of extreme environments providing new knowledge about the acceleration mechanisms in astrophysical sources are a few of the key science goals.

3.1 The telescopes

3.1.1 LST

To coordinate the construction and operation of the LSTs, the LST Collaboration has been established, bringing together hundreds of scientists and engineers from various countries. A total of four LSTs[1] are planned for construction at the CTAO-North site, and they are designed to ensure maximum efficiency in observing the lowest energy range of the CTAO project, covering from 20 GeV to 150 GeV.

The first prototype of LST, known as LST-I, was installed at the CTAO-North site (Fig. 3.2) and has been under commissioning since 2018. During the commissioning phase, simultaneous observations were conducted with the nearby MAGIC telescopes, leading to enhanced sensitivity.

LST-I's performance has been assessed through observations of the Crab Nebula, the standard candle for VHE astronomy (Abe et al. 2023b). The results obtained for the Crab Nebula spectrum and light curve are compatible with measurements from other instruments (i.e., other IACTs and *Fermi*-LAT). LST-I achieves an angular resolution of 0.3 degrees at 100 GeV, and its best integral sensitivity is approximately 1.1% of the Crab Nebula's flux above 250 GeV after

[1]More technical details can be retrieved at the dedicated section in the CTAO web-page

Figure 3.2: Picture of the LST-I, the first LST built. It is mounted in the Roque de los Muchachos observatory, close to the MAGIC telescopes. The telescope is already taking data, also in stereoscopic mode in combination with the MAGIC telescopes, and producing the first scientific and technical results.

50 hours of observations.

The LSTs' reflector dish replicates the parabolic shape of MAGIC telescopes with a larger diameter, of 23 meters and a total reflective surface of the order of 400 square meters. Despite weighing about 100 tonnes, the LSTs can be repositioned within approximately 20 seconds, which is crucial for observing transient astronomical events. The optical FoV of LSTs is about 4.3 degrees.

3.1.2 MST

The design of the MSTs[2] has been optimized for the core energy range from 150 GeV to 5 TeV. It is based on a modified single mirror Davies-Cotton design. This choice was made to strike a balance between optimizing the PSF over a significant portion of the camera's FoV and ensuring uniform performance across the reflector. Each MST will consist of 86 hexagonally-shaped mirrors, forming a 12-meter-diameter reflector with a total reflective area of about 88 square meters. The telescopes will have a focal length of 16 meters and the FoV of the cameras will be 8 °. The optical PSF will be less than 0.18 °, with a source localization precision better than 5 arcseconds under precision pointing conditions. Two types of cameras will be installed on the MSTs: the NectarCAM for telescopes at the northern site and the FlashCam, for the ones at the southern site. Both cameras are designed to meet specific requirements, including precise event timing, full waveform recording for triggered events, a wide dynamic range for each pixel, low instrument dead time, and precise gain calibration.

Currently, the construction and testing of the first MST components are underway. Both cameras have undergone testing. According to the schedule, the on-site installation is set to begin mid 2026.

[2]A recent update on the MST project can be found in Bradascio 2023 and more technical details at the dedicated section in the CTAO web-page

3.1.3 SST

The SSTs is optimized for the upper edge of the energy range of CTAO, above 5 TeV. At these high energies, gamma rays give rise to a substantial amount of Cherenkov light but are also less frequent compared to lower-energy ones. To face the challenge of the low shower counts, SSTs employ small-size reflectors with wide FoV. Also, the SST type will be the most numerous within CTAO South site. 37 SSTs are planned to be distributed over a 1 squared kilometre area in the initial phase.

The design for the SST detectors is based on an innovative Schwarzschild-Couder dual-mirror configuration. This choice ensures adequate resolution across a wide FoV. The primary mirror of the SST will have a diameter of 4.3 meters and will consist of 18 hexagonal segments. The monolithic secondary mirror will have a diameter of 1.8 meters.

The design, structural development, and functionality of the SST are currently in the testing and review phases, soon to be followed by the production and on-site installation phases.

The SST concept has already been validated through the development of the Astrofisica con Specchi a Tecnologia Replicante Italiana (ASTRI)-Horn Cherenkov telescope, a prototype dual-mirror telescope. Subsequent improvements have been made to the ASTRI-Horn telescope structure with the development of the ASTRI mini-array telescopes. Nine of these telescopes are under construction.

3.2 Performance

The optimization of the telescope layout and evaluation of the performance of the observatory relay on detailed MC simulations that consider multiple parameters. It is essential to incorporate an atmospheric model and geomagnetic field values for both sites to accurately simulate the propagation of air showers in the atmosphere. Detailed simulations of the optical elements within the telescopes are conducted. These include modelling how various telescope components, such as mirrors and camera components, affect the collection of Cherenkov light.

Laboratory and on-site prototype measurements of various telescope components are crucial for validating the accuracy of the simulations and making necessary adjustments. In the simulations, trigger threshold levels are optimized to determine which events should be recorded ensuring that only relevant data are collected. Estimations of the expected night-sky background light level in each camera pixel are made. This information is vital for understanding the background noise level and ensuring it is properly accounted for during data analysis.

These steps ensure that the simulations closely replicate real-world conditions and measurements, enabling accurate assessments of the array sensitivity, angular resolution, and other performance parameters.

Among various layout options, the initial, fully founded array configuration is the *Alpha Configuration*. It includes 4 LSTs and 9 MSTs at the CTAO-North site, as well as 14 MSTs and 37 SSTs at the CTAO-South site. The *Alpha Configuration* schemes for the two sites are shown in Fig. 3.3. Differential sensitivity, which refers to the minimum flux required to detect a point-like source with a statistical significance of 5σ is the primary measure used to choose between different telescope layouts.

The performance of an array of IACTs is determined by *(i)* effective collection area, *(ii)* angular resolution, *(iii)* energy resolution, *(iv)* residual background rate, and *(v)* differential sensitivity. The expected performance for these criteria is illustrated in the CTAO web page.

The simulation results indicate that CTAO will outperform current-generation IACTs (HESS, MAGIC, VERITAS) by a factor of at least five across the entire energy range (Fig. 3.4a). At high energies, CTA's energy coverage will extend to several hundred TeV, a significant improvement over current facilities. However, at energies above 10-20 TeV, other observatories like the

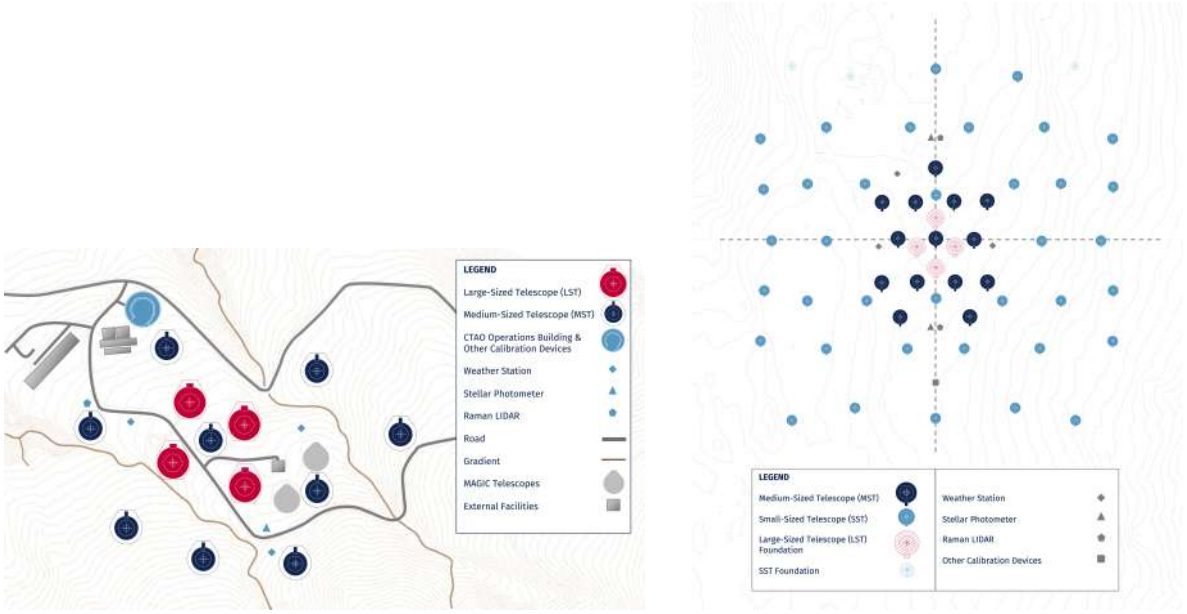

Figure 3.3: The Alpha Configuration selected for the arrangement of the telescopes at the two CTAO sites. On the left is shown the CTAO-North scheme where MSTs and LSTs will be located. The other instruments such as the LIDAR and weather station are also indicated in the map; in grey are shown the positions of the MAGIC telescopes. The northern site will cover an area of about 0.5 kilometres squares. On the right is represented the planned map for the CTAO-South site. At the southern site, the most numerous telescopes will be the SSTs. The site will occupy an area of 3 kilometres squares. Image from the CTAO web-page.

particle shower detectors High-Altitude Water Cherenkov Observatory (HAWC), Large High Altitude Air Shower Observatory (LHAASO), and the future Southern Wide-field Gamma-ray Observatory (SWGO) may exhibit higher sensitivity, albeit with lower angular resolution.

CTAO is anticipated to offer a substantial improvement in angular resolution compared to other instruments, ranging from 0.02°to 0.2°. Additionally, CTAO possesses a high potential for discovering short-term transient phenomena. The differential sensitivity as a function of observing time shows that CTAO provides orders of magnitude greater sensitivity for short observation periods compared to *Fermi*-LAT. In this context, CTAO is an optimal instrument for follow-up observations in the time domain.

Thanks to its significantly enhanced sensitivity, wider energy coverage, and superior energy resolution compared to existing instruments, CTAO will play a crucial role in distinguishing between different radiation mechanisms in blazars. An example is depicted in Fig. 3.5. The capability of CTAO to detect and precisely reconstruct high-energy photons will provide access to fast intra-night variability, spectral variability, and detailed spectral shape at VHE.

Numerical simulations, which consider the expected performance of CTAO and observational constraints, along with theoretical models of emission mechanisms in blazars, have demonstrated the potential of CTAO to significantly advance the current understanding of the astrophysical processes governing the blazar's behaviour in the TeV energy range.

3.2.1 Gammapy

The transition of CTAO to an open observatory implies the necessity for data products to be accessible and manageable for the astronomical community. To this purpose, processed and standardized data will be directly distributed from CTAO data centre to the user. Data will be provided at the Data level 3 (DL3), encompassing the list of selected gamma-like events and

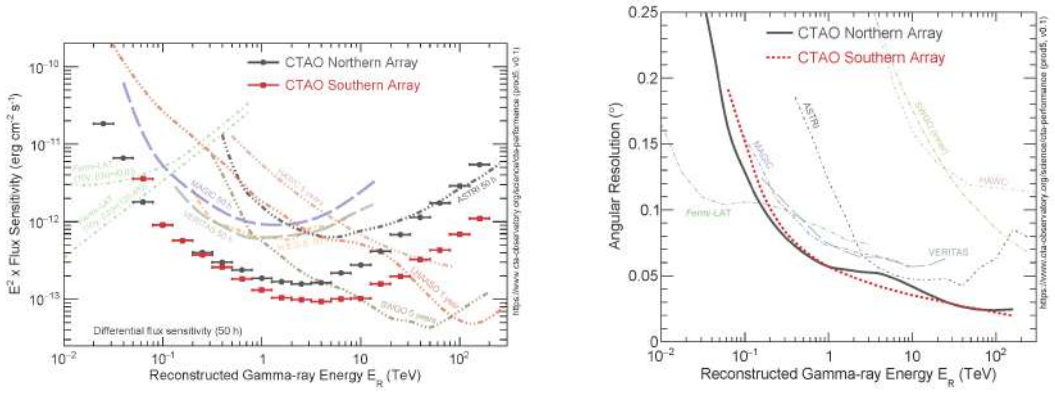

(a) (b)

Figure 3.4: *Left:* CTAO sensitivity expressed in terms of differential energy flux - which is the amount of energy emitted by gamma rays in an energy interval - compared to those of the main facilities currently operating in the field of gamma-ray astronomy. The sensitivity curves give a general idea of the relative sensitivities of each telescope. The exact sensitivities depend on many factors, such as the type of gamma-ray source being observed and the observing conditions. A considerable improvement will be provided in the central part of the energy range covered by CTAO. At the edges of the range, the observatory will provide e.g. better angular resolution, being in this way complementary to other instruments with higher sensitivity. The CTAO sensitivity is calculated assuming 50 hours of exposure. *Right:* Expected angular resolution per energy bin of CTAO compared with the angular resolution of other instruments. At high energy CTAO will provide unprecedented values for this parameter. Image from the CTAO web-page.

instrument response tables. To obtain the DL3 format, raw data from the telescope (Data level 0, DL0) are first calibrated (Data level 1, DL1) and subsequently shower parameters, including energy, direction, and particle identification are reconstructed (Data level 2, DL2) (Lamanna et al. 2015).

The science analysis of CTAO is performed using the Python package Gammapy (Deil et al. 2017). This package is built employing scientific libraries, including Numpy, Scipy, and Astropy. Gammapy offers a comprehensive suite of instruments for high-level gamma-ray data analysis, enabling tasks such as generating sky images, extracting spectra and light curves, and retrieving essential information about the positions, shapes, and spectra of gamma-ray sources. These capabilities are achieved by processing event lists and utilizing IRF specific to different facilities contained in the DL3 format.

One of the key innovations that Gammapy brings to the gamma-ray community is its versatility. Originally, it was used for analyzing data from HESS and *Fermi*-LAT. Currently, data analysis for MAGIC is also transitioning from MARS to Gammapy. Presently, the results of the MAGIC data analysis have to be validated with both tools before publication. This led to testing the functionality of Gammapy as a more consolidated data analysis software and promoting its usage within the community. Gammapy has also found application in simulating and analyzing observations conducted by CTAO.

The adoption of a common data analysis tool for all gamma-ray facilities, moving away from proprietary and dedicated software, has become a necessity in the CTAO era. A Python-based package was chosen to pave the way for advancements in the field of gamma-ray astronomy as a whole.

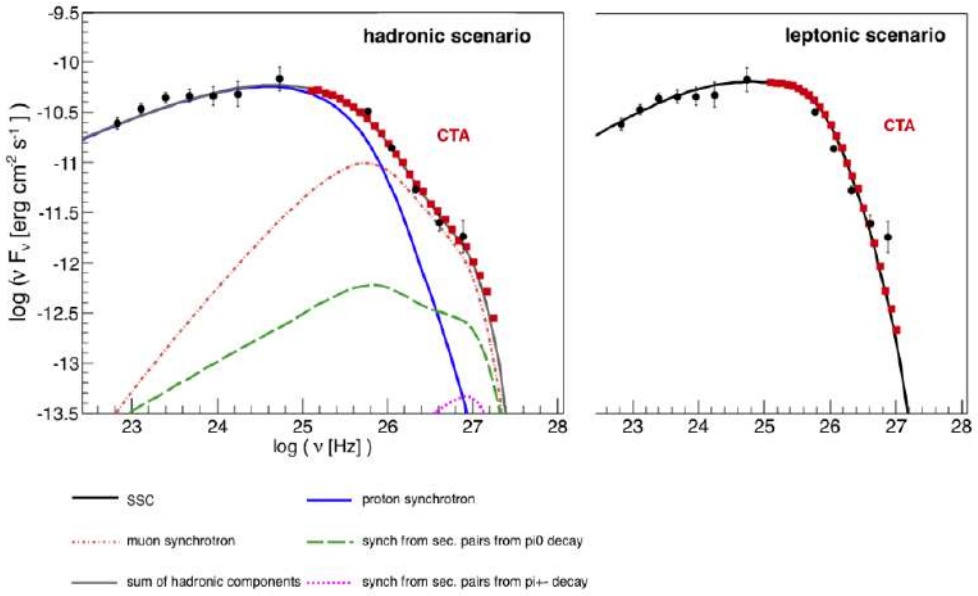

Figure 3.5: Simulated CTAO data points for the VHE spectra of the blazar PKS 2155-304. The emission models used to describe the data are a hadronic scenario (*Left*) and a SSC leptonic scenario (*Right*). The data points are obtained assuming an exposure time of 33 hours in both cases. The data points from CTAO simulations are shown in both panels. Black points are from a 33-hour HESS observation of the source. The CTAO observation significantly improves the ability to discern between the two scenarios (hadronic or leptonic) with respect to the HESS observation. From Cherenkov Telescope Array Consortium et al. 2019.

3.3 Science cases connected to AGN

As discussed in Chapter 2, gamma-ray observations of AGN are crucial for understanding extreme astrophysical environments, such as the accretion physics, jet formation, and interaction processes near supermassive black holes. Indirect evidence for cosmic-ray acceleration in AGN can be obtained through the observations of gamma rays and, possibly, neutrinos. Rapid flux variations and spectral characteristics can help constrain emission models.

The objectives of the AGN science case for CTAO are under discussion (Cherenkov Telescope Array Consortium et al. 2019). One of the key goals would be to comprehend the differences between various classes of blazars and the processes underlying their variability and to determine the origin of VHE gamma-ray emissions in radio galaxies, investigating whether the emissions occur in the jet or the core region of these sources.

A large collection of AGN data will allow us to measure the Extragalactic Background Light (EBL), originating from various extragalactic sources (Mazin et al. 2013), and characterizing the Inter Galactic Magnetic Field (IGMF) (Sol et al. 2013). The EBL spectrum can be obtained with CTAO measurements by studying deviations from the expected spectra of blazars. These measurements will be conducted on blazars located at different redshifts, allowing forLunedì 13 maggio ore 9 psicologa a more accurate characterization of the EBL spectrum. The IGMF and its origin, whether primordial or astrophysical, can be investigated by exploiting the observations of blazars. The strength of the IGMF can be evaluated indirectly by looking for phenomena like pair halos around blazars. CTAO observations of distant blazars are expected to provide insights into reduced opacity at VHE caused by Axion-Like Particles-photon oscillations.

Lorentz Invariance Violation (LIV) is a theoretical framework that suggests a violation of the fundamental principle of Lorentz invariance, which is a cornerstone of Einstein's theory of

Special Relativity. This theory can be tested through AGN observations. By examining the dispersion of gamma rays from AGN, it can be distinguished between intrinsic source physics and propagation-induced effects associated with LIV. While individual AGN light curves may not exhibit rapid features to directly measure dispersion, cumulative data from long-term monitoring can still allow for the determination of time delays through cross-power spectral analysis methods, providing a novel approach to constrain LIV parameters (de Angelis et al. 2009). It is important to note that modifying the dispersion relation for gamma rays LIV can also impact the kinematics of pair-production with the EBL, potentially changing the threshold for interaction and affecting EBL absorption of gamma rays. Deep observations of distant AGN with hard spectra can be used to test for any changes in EBL absorption, which is relevant to LIV studies.

Lastly, the projects within the AGN science case have the potential to make available catalogues of sources, flux maps, and data cubes to the AGN community.

3.4 Sinergies

The field of the VHE astronomy relies heavily on collaboration with complementary facilities working at different wavelengths to produce high-impact results. As anticipated in the previous Parts of the Thesis, MWL and MM studies are becoming increasingly vital for addressing long-standing questions about cosmic ray nature and acceleration physics. As the most advanced facility in the VHE field, CTAO aims to establish significant synergies with the next generation of observatories, such as the SKAO.

As well as the VHE field, radio astronomy is indeed proceeding through a prosperous phase. Existing radio facilities have undergone upgrades in the last years, enhancing their bandwidth and sensitivity (e.g., Jansky Very Large Array (JVLA)). Moreover, the SKAO pathfinders, Low Frequency Array (LOFAR) and MeerKaroo Array Telescope (KAT), are leading the way for unprecedented highly sensitive observations at low radio frequencies (see LOFAR2.0 White Paper and Jonas & MeerKAT Team (2016)). Alongside specific target observations, they provide monitoring of the sky daily and triggering, and cataloguing of new radio transients. In addition, the huge dimensions of LOFAR and MeerKAT datasets, make urgent the development of big data handling systems pushing towards new methods of storing and managing radio data. SKAO will inherit its pathfinder capabilities and will bring them to an even enhanced level.

The CTAO science case dealing with the transients perfectly meets with the advanced capabilities expected from SKAO. At the edge of the electromagnetic spectrum, the two facilities will provide a systematic investigation of the transient universe. A large fraction of the observing time of the two observatories will be devoted to surveying the sky during the first years of operation. This will allow a deep exploration of non-thermal sources, both from the quantity side, with many new objects, and from the quality side, with high-sensitivity observations at the two bands (Cherenkov Telescope Array Consortium et al. 2019).

SKAO will also be involved in the VLBI network providing the high angular resolution necessary to observe the parsec scale regions of astrophysical objects. In particular, the high-resolution images of AGN in the radio band will be complemented by an accurate spectral characterization at high energies from CTAO (e.g., Giroletti et al. 2015). The two pieces of information together will allow the detailed inspection of broadband SEDs and of the connection between radio and gamma-ray activities in these sources.

Strong synergies between CTAO and the current generation of IACTs instruments are already well established. HESS, MAGIC and VERITAS could serve as monitoring instruments for bright sources. This is particularly valuable when CTAO sites are at different longitudes than the current IACTs, as they can extend the monitoring of bright flaring sources before and after CTAO observations.

In the MM context, the synergy of CTAO and the IceCube neutrino detector, will be employed in the search for proof of hadronic acceleration and sources of high-energy particles. In addition, shortly, the capabilities of neutrino observatories will be remarkably improved with the operation of the Baikal-Gigaton Volume Detector (GVD) – the upgrade of the Baikal Neutrino Telescope operating since the 90s –, and the KM3NeT, built in the Baikal Lake and the Mediterranean sea, respectively, and by the expansion of the IceCube observatory (IceCube-Gen2). In particular, the first two facilities will be dedicated to the Southern neutrino sky complementing the observations of the Northern sky carried out by the IceCube observatory. Both gamma rays and neutrinos indeed point back to their sources, unlike charged cosmic rays possibly deflected by intergalactic magnetic fields. The CTAO follow-up observations of neutrino triggers can lead to the localization and identification of the hadronic accelerators responsible for the emission of high-energy neutrinos and gamma rays.

Although in the MM-MWL astronomy each messenger can bring important new information that will allow us to build a more complete global picture, to maintain brevity, this Section has focused on synergies between CTAO and the facilities relevant to the Thesis (radio and neutrino detectors).

Chapter 4

The blazar 1ES1959+650

As discussed in Chapter 2, VHE observations with current experiments are key to characterising the emission mechanism of blazars. In particular, the blazar's properties can be successfully explored in a MWL context. In this Chapter, we will examine the case of 1ES 1959+650, a longtime studied source the behaviour of which is still not completely understood.

4.1 Introduction

1ES 1959+650 is a blazar belonging to the HBL class, situated at a redshift of 0.047 (Perlman et al. 1996). The source was initially detected at 4.85 GHz using the National Radio Astronomy Observatory (NRAO) 91m Green Bank radio telescope (Gregory & Condon 1991). Soon after discovering the source in the radio band, its detection in the X-ray band was reported in the Einstein Imaging Proportional Counter (IPC) Slew Survey by Elvis et al. (1992). The name 1ES 1959+650 was subsequently adopted from the Einstein Slew Survey catalogue and has become the commonly used identifier. At VHE energies, 1ES 1959+650 was one of the early known BL Lacs, following the footsteps of Mrk421, Mrk501 and a few others. In 1998 the Utah Seven-Telescope Array Collaboration (Nishiyama 1999) measured, for the first time, a signal from 1ES 1959+650 with a 3.9σ significance, reached in 57 hours of observations. More details about the source behaviour at VHE will be given below. At HE, 1ES 1959+650 is part of the *Fermi*-LAT 3rd- and 4th- Source Catalogues (Acero et al. 2015; Ballet et al. 2020b).

In 2002 the source experienced an exceptionally heightened state in terms of VHE emissions, causing the flux to exceed the flux of the Crab Nebula by 3 times. This enhancement occurred within less than 10 hours, starting from a flux level of less than 0.5 CU above 2 TeV. The flaring activity was reported by the Whipple[1] and HEGRA Collaborations (Holder et al. 2003; Aharonian et al. 2003). In particular, the monitoring of the source unveiled two significant outbursts in the TeV range, separated by 30 days, occurring in May and June 2002, and lasting one day each. Above 2 TeV, the high-state data were fitted using a power law (Eq. 2.4) with a slope ~ 2.83 (Aharonian et al. 2003). The first flare promptly triggered an MWL campaign that extended over several months, covering the period of the second flare as well (Krawczynski et al. 2004). This campaign showed that, while the first VHE flaring event coincided with enhanced flux across various other energy bands, in particular in the X-ray band, the second one lacked any MWL counterparts. The detection of an "orphan" flare – detected solely in the VHE range, without a simultaneous high state in other energy bands – challenges the one-zone SSC scenario. According to this model, both the low and high-energy components of the SED are generated by the same population of electrons. This implies that enhanced states should be observed at nearly all wavelengths simultaneously. Remarkably close in timing to

[1]The Whipple 10m telescope and the collaboration are the predecessors of the VERITAS Collaboration

the orphan flare, the AMANDA Collaboration reported two neutrino events spatially consistent with 1ES 1959+650 (Halzen & Hooper 2005). While the statistical significance of these two neutrino detections was insufficient for confirmation, the coincidence of a TeV flare with neutrino observations carries substantial implications in the framework of hadronic scenarios for blazar emission, in particular for HBLs (e.g., Sahu et al. 2013). Indeed, as described in Section 1 and Section 2, proton-photon interactions that give rise to high-energy emissions inherently lead to neutrino production. Hadronic models also provide a plausible explanation for the orphan flare originating from 1ES 1959+650: the non-correlation between the low and high-energy segments of the broadband SED is expected, as they likely are due to distinct particle populations. Although the hadronic scenario is not the only possible explanation, as described below, a hadronic origin of the emission during the orphan flare is plausible. It is worth noticing that recent analyses of the archival data from the IceCube neutrino detector did not show any statistically significant neutrino excess from the source position (Aartsen et al. 2020; Abbasi et al. 2021).

The work by Krawczynski et al. (2004) explored several explanations for the phenomenon, still within the framework of the SSC scenario. They included the possibility of distinct emitting regions driving the first and second flares or an alignment of the magnetic field with the line of sight so that the synchrotron emission from the orphan flare could not be observed. Supporting a hadronic origin of the orphan flare, Böttcher (2005) instead proposed a reflection model. In this scenario, as the synchrotron photons from the first flare escape the flare site, they encounter a cloud that reflects them acting as a mirror. These reprocessed photons provide the target field for proton-photon interactions, which lead to π^0 decay and the subsequent orphan VHE emission. Another VHE orphan flare was announced in 2012. In contrast to the previous event, a high state in X-rays was also observed this time but with a significant temporal delay in comparison to the VHE activity. During the time of the X-ray high state, the VHE emission was at the low-state level (Aliu et al. 2014), revealing an uncorrelated pattern between the VHE and the X-ray emission from the source. A reflection model similar to the one of Böttcher (2005) was proposed in this case too (Aliu et al. 2014).

In 2015 and 2016, 1ES 1959+650 experienced a new phase of flaring activity detected across the whole electromagnetic spectrum, from the optical wavelengths to the VHE band (Buson et al. 2016; Biland & FACT Collaboration 2016a; Biland et al. 2016b; Kapanadze et al. 2016; Biland et al. 2016a; Biland & FACT Collaboration 2016b). The peak flux at VHE was reached in 2016, between June 13 and 14, a new peak was observed on July 1. The MAGIC telescopes observed 1ES 1959+650 peak fluxes, above 3 CU with 300 GeV energy threshold, on the nights of June 13 and 14, and July 1. The flux at VHE increased by a factor ~ 17 compared to the historical flux of 18% CU (Benbow 2011). The MAGIC observations located the IC peak in the 0.4–0.7 TeV range (MAGIC Collaboration et al. 2020a). The analysis of 1ES 1959+650 spectra in the 150 GeV – 1 TeV energy range on these days revealed that, while a simple power law resulted in inadequate in describing the data, spectral shapes such as cutoff power law (Eq.2.5), cutoff logarithmic parabola (Eq.2.7), and logarithmic parabola (Eq.2.6), all provided satisfactory fits. No one of these models demonstrated clear statistical superiority over the others but all indicated the presence of a spectral curvature. During the highest peak, on June 13, the VHE photon index (assuming a simple power-law) is about 2.0, which is harder than the spectrum during the orphan flare detected in 2002, when the photon index was estimated to be about 2.83, see above.

During this flaring period, spectral changes occurred. Both the synchrotron and IC peaks moved towards higher energies, reaching values of $\sim 10^{17}$ Hz for the low-energy synchrotron peak and above 0.4 TeV for the high-energy peak (MAGIC Collaboration et al. 2020a). This transition in the position of the synchrotron peak denotes a shift from a standard HBL to an EHBL-type. A similar evolution in behaviour has been observed in HBLs such as Mrk501 (Albert

et al. 2007; Ahnen et al. 2018), hinting at the possibility of a shared mechanism governing these categories of blazars during flaring episodes. Since during the EHBL phase the position of the high-energy peak of the SED falls in the VHE energy range, it is important to precisely measure the VHE spectrum to constrain the energy distribution of the emitting particles. In addition, the luminosity of 1ES 1959+650 increased significantly, reaching values $\sim$ 1 order of magnitude higher than expected from the blazar sequence. The Compton dominance parameter also changed appreciably if compared with previous observations.

Several scenarios have been explored to explain the broadband flaring emission of 1ES 1959+650 in 2016. These range from the conventional one-zone or two-zone SSC model to more complex scenarios involving hadronic and two-zone photohadronic models (MAGIC Collaboration et al. 2020a; Sahu et al. 2021).

Due to the large amount of MWL data over 20 years, several efforts have been made to shed light on the physics that govern the 1ES 1959+650 emission. However, a comprehensive interpretation of the emission mechanism during the various stages of the source is still missing. The present work aims to contribute to the understanding of the source by analysing new almost simultaneous MWL datasets. The project is part of a large observational program by the MAGIC Collaboration, that aims at a long-term monitoring of 1ES 1959+650 at VHE. The MAGIC observations are carried out in coordination with other facilities observing the sky at lower energies. An introduction to the MAGIC proposal of observations will be provided in the following.

4.1.1 1ES 1959+650 under the MAGIC monitoring

The MAGIC telescopes detected 1ES 1959+650 in 2004 while the source was in a state of relatively low activity, with a flux of the order of 0.2 CU (Albert et al. 2006). In 2015 the MAGIC Collaboration started a monitoring program dedicated to this source. Before this, the observations of 1ES 1959+650 were activated only when an enhanced flux state was observed in other energy bands. The current campaign is designed to consistently observe the source throughout the entire year (depending on the visibility).

As previously mentioned, 1ES 1959+650 exhibits distinctive features, such as complex intra-band correlation patterns, rapid variations intra-nights and over extended periods, and a shift towards higher energies in the SED peaks. These attributes often elude a comprehensive explanation from a standard one-zone SSC model. For example, it is not clear whether the EHBL behaviour can be observed every time the source experiences a high state or whether it was exceptional in 2016. The study of variability patterns on different time scales offers insights into particle acceleration and cooling mechanisms and on the size of the emission region, and its distance from the central core. Moreover, 1ES 1959+650 is a bright source in the VHE energy band. For all these reasons, it stands out as an exceptional candidate for addressing numerous blazar physics aspects. Therefore, the proposal for a monitoring program by MAGIC was a natural choice.

The systematic observations of 1ES 1959+650 by MAGIC, conducted in coordination with simultaneous MWL campaigns, aim to accumulate a comprehensive, long-term dataset across multiple energy bands. This MWL monitoring allows investigations into variability patterns, broadband SED evolution, comparisons of flux states, and the testing of emission mechanisms involving VHE neutrino production.

The monitoring of MAGIC is scheduled for one hour each night with a one-week cadence, spanning a period of eight months. This observation period corresponds to the time when the source is visible from the MAGIC site, reaching its culmination at a zenith distance of 35°. All the observations are therefore carried out mainly between 35°– 66°. Some of the MWL facilities involved in the program are the Effelsberg and Medicina radio single dishes, the Global

millimeter VLBI array (GMVA), the Institut de radioastronomie millimétrique (IRAM) 30m radio telescope dedicated to total intensity and polarization monitoring in the millimetre band, optical telescopes as Asiago and Siena, the *Swift* and XMM-*Newton* satellites in the X-ray band. Independently, *Fermi*-LAT performs sky scans every three hours, continuously monitoring the gamma-ray sources, including 1ES 1959+650, in the HE band (Atwood et al. 2009; Ackermann et al. 2012) and providing public data to the community.

4.2 The 2020-2022 MAGIC campaign

4.2.1 Observations and data analysis

In this work, we present the MAGIC observations of 1ES 1959+650 from 2020 to 2022, part of the long-term monitoring proposal above mentioned. During the three years, about 144 hours of observations have been collected. About 111 hours of good-quality observations taken during 85 nights survived the selection process. Approximately 23% of data have been discarded. The final dataset comprehends data from the 20th of June to the 23rd of December 2020, from the 10th of March to the 29th of September 2021, and from the 31st of March to the 28th of August 2022. In 2021, the monitoring was halted due to the eruption of the Cumbre Vieja volcano. From September 2022 onward, observations were exclusively conducted in monoscopic mode due to maintenance on one of the two telescopes. Monoscopic data were not used in this work. The zenith distance of the observations ranges from 35° to a maximum of 66°.

As explained in Section 2.3.5, the quality of the data strongly depends on meteorological conditions – such as cloudiness and dust presence – along with instrument performance during observations. Therefore, a selection process is carried out before analysis. The 1ES 1959+650 good-quality data used for this work were chosen using `quate` (see Section 2.3.5). An atmospheric transmission threshold of 70% was employed for the selection (see Section 2.3.5). All weather parameters used in the selection – including cloudiness, dust, humidity, and others – were kept at default settings, leading to a selection of overall good weather conditions for the MAGIC observations. Two examples of the selection based on the transmission are shown in figure Fig 4.1. This selection was cross-verified through consultation of runbooks and other informative plots, as detailed in Section 2.3.5.

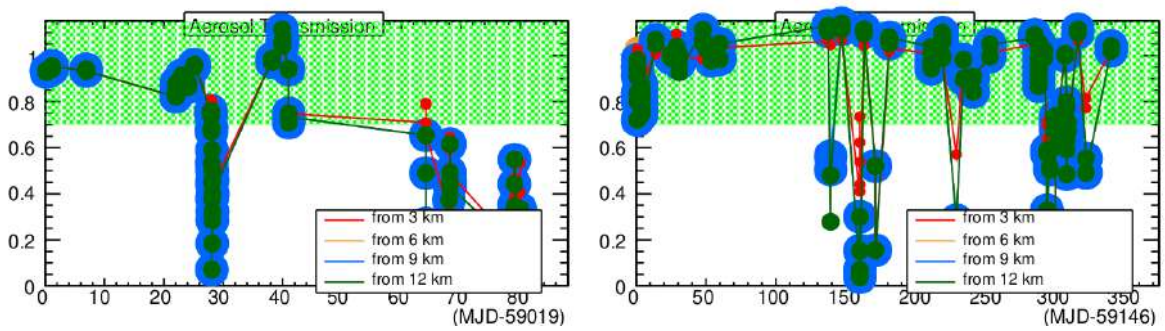

Figure 4.1: Aerosol transmission versus time (in MJD) recorded during the observing dataset 03.14 (left) and 03.16 (right). The aerosol transmission parameter is measured at different altitudes, as reported in the legend (see Section 2.3.5). For the selection, we take into account the aerosol transmission recorded at 9 km because this is close to the average altitude at which the showers manifest. The threshold for the aerosol transmission is set to be $> 70\%$. This value delimits the area highlighted in light green in the plot (indicating the data surviving the selection). The bullets indicate the observation runs: the ones falling in the green area are selected for the analysis, while the rest are discarded. These and other plots referred to other parameters considered for the selection are produced by the `quate` executable.

The data reduction was performed with the MAGIC analysis software MARS (Zanin et al. 2013; Aleksić et al. 2016). The steps of the analysis are described in Section 2.3. OFF and MC samples have been employed in training the RF algorithm for the gamma/hadron separation, energy and arrival direction estimation. The RF was then run on 1ES 1959+650 data. The samples of OFF data have been properly selected to match all the 1ES 1959+650 observing conditions. OFF data are real data from archival MAGIC observations with no gamma rays detections.

As described in Section 2.3.6, MC gamma-like simulated data are produced for distinct MAGIC observation datasets to account for the different performances of the instrument. During the 2020-2022 period, the performance of MAGIC telescopes significantly varied mainly because of the volcano eruption which caused the PSF deterioration because of the volcanic ash. For the three years of 1ES 1959+650 observations analysed in this work, I used 5 distinct performance periods, each of which corresponds to a MC production (in the following we will refer to these as *MC datasets* or simply *dataset* with their reference number according to the MC Collaboration nomenclature). Each MC dataset produces the correct IRF. The basic properties of each dataset are reported in Tab. 4.1.

Table 4.1: Summary of MAGIC observation of 1ES 1959+650

MC dataset	obs. date	zenith range [°]	total obs. time [hours]	dark	moon
(1)	(2)	(3)	(4)	(5)	(6)
03.14	19 June 2020 – 14 Sept 2020	35 – 62	41.1	20.1	21.0
03.15	15 Sept 2020 – 18 Oct 2020	35 – 62	9.1	3.8	5.3
03.16	25 Oct 2020 – 29 Oct 2021	35 – 66	40.8	20.8	20
03.17	31 Mar 2022 – 7 June 2022	45 – 60	13.3	10.9	2.4
03.18	10 June 2022 – 28 Aug 2022	35 – 50	6.9	4.3	2.6

Notes: (1) MC dataset identification, following the MAGIC Collaboration naming; (2) starting and final day of observation of 1ES 1959+650 within the corresponding MC dataset, the observations of the target are carried out in sparse days within the indicated time interval; (3) zenith range of the source in the corresponding time interval; (4) total (moon and dark) observing time, after cutting bad-quality data; (5) hours of dark observations; (6) hours of moon observations.

About 60 hours of observations out of the total 111 hours have been taken during dark time, the other $\sim$ 51 hours are affected by the presence of the moonlight. Since the moonlight affects the observations, as described in Section 2.3.11, for each dataset, dark and moon data have been analyzed independently. The three years of observations have been then further divided according to the NSB level. In particular, the first three datasets (03.14, 03.15, 03.16) have been split into 4 different NSB level datasets: the *dark* dataset, with a median DC recorded by the MAGIC-I[2] camera ranging from 1.1 to 1.3 μA (see Section 2.3.11), and three *moon* dataset, with data taken during higher NSB conditions and higher median DCs, indicated in column (2) of Tab. 4.2. For the last two datasets (03.17 and 03.18), the good-quality dataset selected for the analysis did not include observation with NSB level higher than the 3–5 NSB (see Tab. 4.2). Therefore, these have been split into three datasets (the dark dataset and the two moon datasets). For dark data, I followed the standard analysis chain, starting from calibrated and stereoscopic-reconstructed data, while for data collected under moonlight conditions, I followed the Ahnen et al. (2017) prescription (also described in Section 2.3.11).

For the moon data analysis, I had to start from calibrated-format MC, OFF and 1ES 1959+650

[2]Values for the MAGIC-I camera are taken as reference in all the MAGIC studies. A conversion factor between MAGIC-I and the MAGIC-II camera is then applied to account for the right values of median DC for each camera.

Table 4.2: Properties of moon data analysis

NSB level	Equivalent DC [μA]	$Q_{\text{core}} - Q_{\text{bound.}}$ [phe per pixel]	Added Noise ped. mean and RMS	Size Cut [phe]
(1)	(2)	(3)	(4)	(5)
1−2	1.1−2.2	6−3.5	–	50
2−3	2.2−3.3	7−4.5	3.0; 1.3	80
3−5	3.3−5.5	8−5	3.5; 1.4	110
5−8	5.5−8.8	9−5.5	4.1; 1.7	150

Notes: (1) NSB level defined as a multiple of NSB_{dark} level, which is the first level in this Table; (2) Median DC measured by MAGIC-I in each NSB level. This parameter is used to split the data into NSB level datasets. The subdivision in NSB levels according to the DC is based on the study of the Crab Nebula at a low zenith angle; (3) Cleaning thresholds for NSB levels applied during the cleaning procedure. The thresholds are defined in terms of the phes charge in core and boundary pixels; (4) Mean and RMS pedestal events added to the MC and OFF data to match with the noise level of 1ES 1959+650 observations; (5) Size cuts adopted for the flux and light curve computation. The size measures the total charge contained within the shower image, in phes.

data. To match the noise of the target data to compute the proper RFs, MC and OFF samples have been contaminated with a fake noise simulating the noise level of the target observations. This procedure consists of modifying the mean and RMS of the pedestal events of each observation run to reproduce the background noise of the observations. In the cleaning procedures of MC, OFF and target dataset, the cleaning thresholds have been adjusted to the requirements for each NSB level.

As explained in Section 2.3.2, the cleaning thresholds are set in terms of the number of phe per pixel. In the core pixels, the threshold is Q_{core} phe per pixel and in the boundary pixels the threshold is $Q_{\text{bound.}}$. The thresholds on the arrival time are included in the cleaning procedure but these are kept at their standard values in moon analysis too. Finally, during the spectral analysis to retrieve the light curve and the energy spectrum (see Section 2.3.10), the size cuts have been adjusted properly to the NSB levels.

Tab. 4.2 reports the DC, the cleaning thresholds and the noise added to each NSB dataset. As explained in Section 2.3.11, the NSB levels during various lunar phases are quantified in terms of multiples of the NSB during dark conditions, NSB_{dark}. All the observations here reported are performed with the standard HV configuration.

4.3 VHE results

4.3.1 Energy threshold for the light curve

The energy threshold of the analysis is determined as the peak of the distribution of MC events to which the RF of the analysis has been applied, plotted against true energy (deconvolved by the instrument response). To obtain this distribution, the (hadroness and size) cuts used for the target data analysis are applied to the MC events. These are also reweighted to match the spectral shape used for the target data[3], that is, in our case, a simple power law with an index of 2.15 (see next Sections).

The energy distribution of MC events is influenced by various factors, such as the spectral characteristics of the target source, the observing conditions and the instrument performance. Key contributors playing a role in the energy threshold determination are the NSB level and the

[3]The MC events are simulated assuming a power law distribution with a spectral index of 1.6.

observing zenith angle. Higher NSB levels introduce noise to the low-energy signal, necessitating a higher energy cut. Consequently, energy thresholds can vary across different MC datasets and NSB levels as shown in Fig. 4.2. As an example of how the energy distribution of the MC events can vary, we show the distributions for the four levels of the 03.14 dataset in Fig. 4.3.

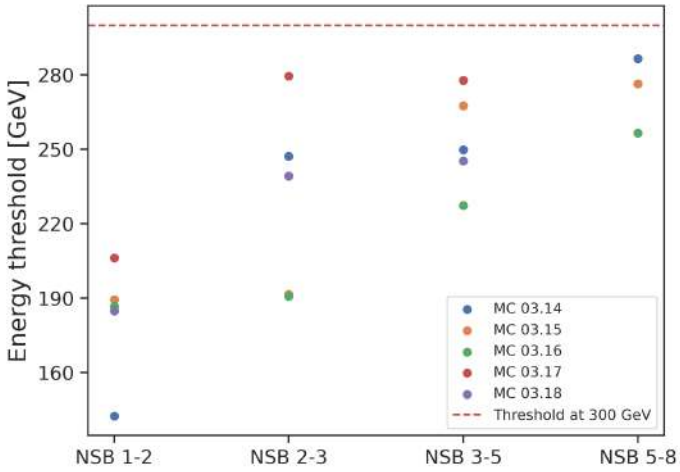

Figure 4.2: Energy thresholds as a function of the NSB levels for the 5 MC datasets.

The 1ES 1959+650 dataset for the 2020-2022 period consists of 5 MC datasets, each divided into 3 or 4 NSB levels. We then set a common energy threshold valid for each case. The thresholds for moon analyses are in the range between $\sim$ 190 and 290 GeV, and the ones for our dark analyses are all below 200 GeV. The chosen 300 GeV energy threshold for the 2020-2022 analysis is a conservative value, ensuring an adequate energy threshold for the highest NSB levels. Additionally, this conservative threshold considers the relatively high zenith angles (ranging between 35° and 66°), as higher zenith angles hamper the detection of low-energy signals (see Section 2.3.6). Moreover, the 300 GeV threshold aligns with previous works on this source, facilitating a meaningful comparison with earlier analyses (e.g., The MAGIC Collaboration et al. 2022).

4.3.2 Source detection

The signal search is performed in each of the five datasets independently, including moon and dark data. The significance was calculated with the Li & Ma (1983) formula (Eq. 2.2, see Section 2.3.9). This formula takes into account the number of events in the source and background regions. Fig. 4.4 shows the θ^2-plot for each MC dataset. The plots represent the θ^2 distribution for events over the full energy range of the MAGIC observation. Each plot manifests a significant excess of gamma-like events at low θ^2 values, largely surpassing canonical 5σ significance necessary to claim a detection. As described in Section 2.3.9, signal detection significance is calculated within the optimized signal regions delineated by the vertical dashed lines in Fig. 4.4. Table 4.3 presents the count of excess events, N_{ex} (see Section 2.3.9), and the significance, S according to Li & Ma (1983), computed in the energy range spanning approximately from 300 GeV to a few TeV for each MC dataset.

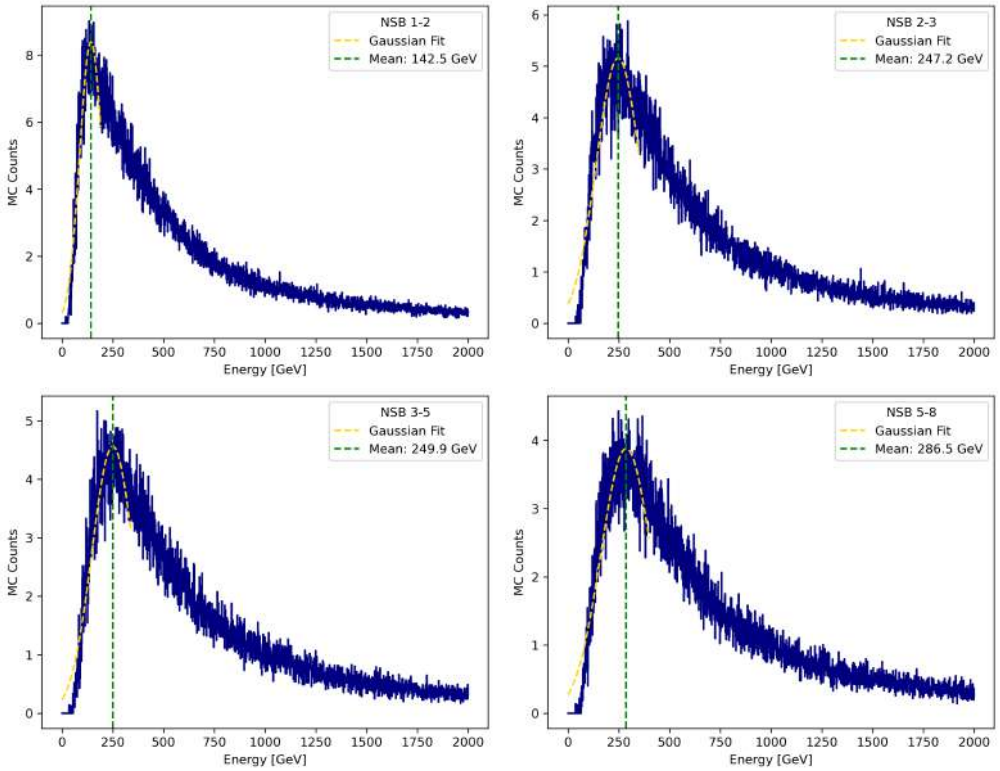

Figure 4.3: Distribution of MC events plotted against true energy for the 03.14 dataset and each NSB level. A Gaussian function is roughly fitted to the distribution's peaks to determine the energy thresholds in each case.

Table 4.3: Signal detection significance

MC dataset	observing time [hours]	S	N_{ex}
(1)	(2)	(3)	
03.14	41.1	50.0σ	1369.3 ± 39.2
03.15	9.1	15.6σ	159.3 ± 13.9
03.16	40.8	26.9σ	609.3 ± 28.9
03.17	13.3	23.1σ	298.2 ± 18.1
03.18	6.9	13.9σ	123.0 ± 12.1

Notes: (1) MC dataset; (2) Total (moon and dark) observing time; (3) Significance, S, computed with Li & Ma (1983) equation (Eq. 2.2).

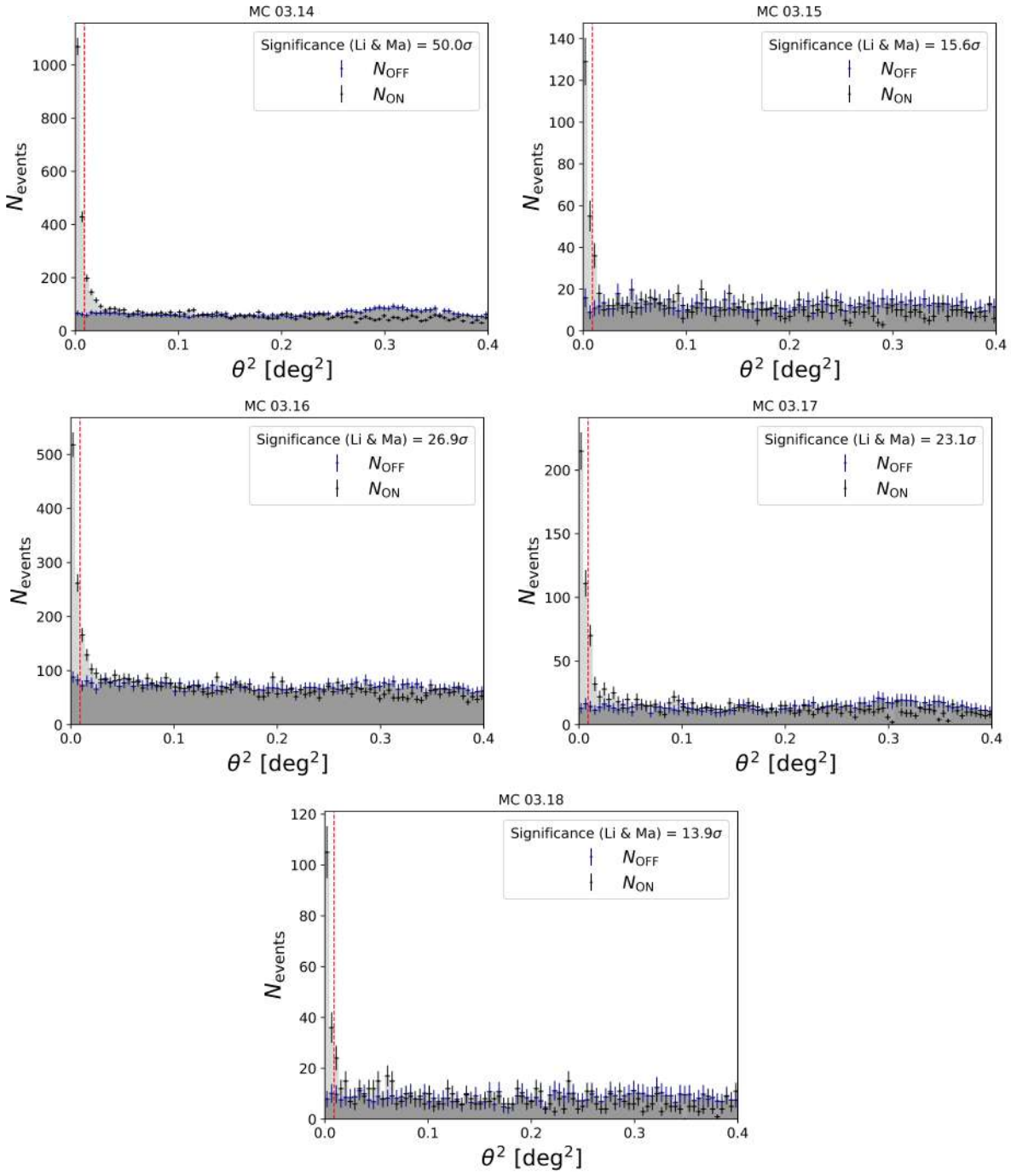

Figure 4.4: θ^2 plots for the 1ES 1959+650 observations in the energy range approximately from 300 GeV to a few TeV. The plots are refereed to each MC dataset, including moon and dark datasets. The significance of the detections is computed with Eq. 2.2 within the regions indicated by the red dashed lines. The ON and OFF events are represented by the black and blue crosses, respectively. The background regions are indicated with dark grey areas while the signal regions are defined with light grey areas.

4.3.3 Light curve

The integral flux in each time bin is calculated assuming a simple power law with a photon index $\Gamma_\gamma = 2.15$. The photon index chosen is compatible with the best-fit results derived from the unfolded spectra analysis (see next Section). The temporal binning is set at one day. Integral flux points are computed above the 300 GeV energy threshold. The 2020-2022 VHE light curve is shown in Fig. 4.5. The average flux over the 2020-2022 period is about 0.2 CU. From the comparison between the 2020-2022 low state and the long-term monitoring from 2015 to 2019 (Fig. 4.6) we observe that the time interval from 2016 to 2018, 1ES 1959+650 was in a high state characterized by a relatively intense variability with the prominent flaring state occurred between June and July 2016, as described in Section 4. During the 2016 flare, the source reached a flux above 3 CU. Since 2019, the source's flux level has consistently remained below 0.5 CU. This trend persisted until the end of the 2020-2022 period, in August 2022, except for a brief interval of approximately 100 days, spanning from MJD 59019 to MJD 59120 (from June 2020 to the end of September 2020). Being focused on the 2020-2022 time interval, this work investigates one of the periods characterized by the lowest flux levels observed for 1ES 1959+650.

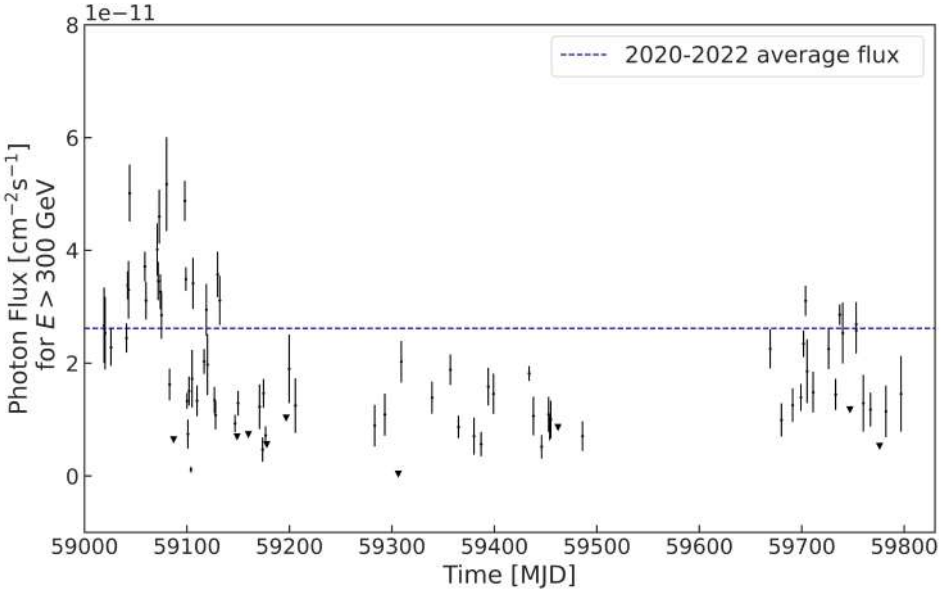

Figure 4.5: The MAGIC light curve of 1ES 1959+650, binned daily, using an energy threshold of 300 GeV. The blu dashed line represents the average flux over the 2020-2022 period.

4.3.4 Spectrum

The VHE spectra of 1ES 1959+650 have been generated using the unfolding procedure described in Section 2.3.10 to account for the IRF. Fig. 4.7 illustrates the spectra of the 2020-2022 period compared with the one of 13 June 2016, which is the day of highest flux detected at VHE during the 2016 active period. The 2016 data are from MAGIC Collaboration et al. (2020a). The two spectra shown in Fig. 4.7 are not deabsorbed for the EBL. We tested both a power law (Eq.2.4) and a log parabola (Eq.2.6) function to fit the 2020-2022 spectrum and conducted a Likelihood Ratio Test (LRT) statistic to assess the superiority of one model over the other. We found that the log parabola is preferred over a power law spectrum with a significance of about 3σ. The results of the fitting are summarized in Tab 4.4.

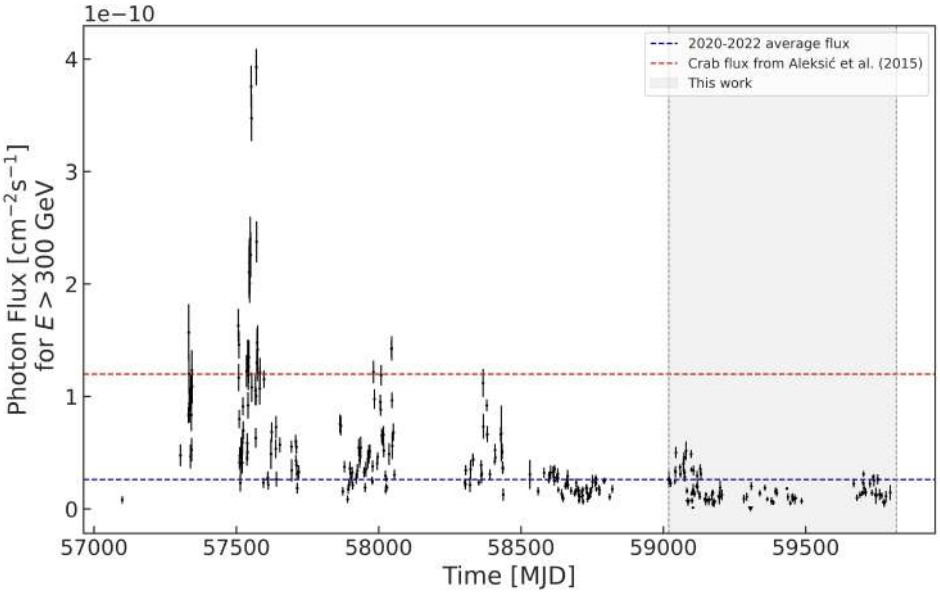

Figure 4.6: The MAGIC light curve of 1ES 1959+650 as in Fig. 4.5. For completeness, here the 2015-2019 data from The MAGIC Collaboration et al. (2022) are also plotted, starting from MJD 57099. For reference, the brown and the blu dashed lines represent the integral flux of the Crab Nebula above 300 GeV (from Aleksić et al. (2015)) and the average flux over the 2020-2022 period, respectively, as reported in the legend. The grey area highlights the data considered in this work, from MJD 59019 to MJD 59782, represented in Fig. 4.5.

Table 4.4: Best-fit spectral paramters

Date	Function	α	β	Γ_γ	χ^2/d.o.f
(1)	(2)	(3)	(4)	(5)	
2020-2022	log parabola	$2.18^{+0.04}_{-0.04}$	$0.71^{+0.05}_{-0.05}$	–	7.0/14
	power law	–	–	$2.47^{-0.02}_{+0.02}$	92.1/15

Notes: (1) Period for the spectrum computation; (2) Spectral function assumed; (3) α and β best-fit parameters in case of log-parabola function; (4) Γ_γ best-fit parameter in case of simple power law function; (5) χ^2 over degrees of freedom (d.o.f).

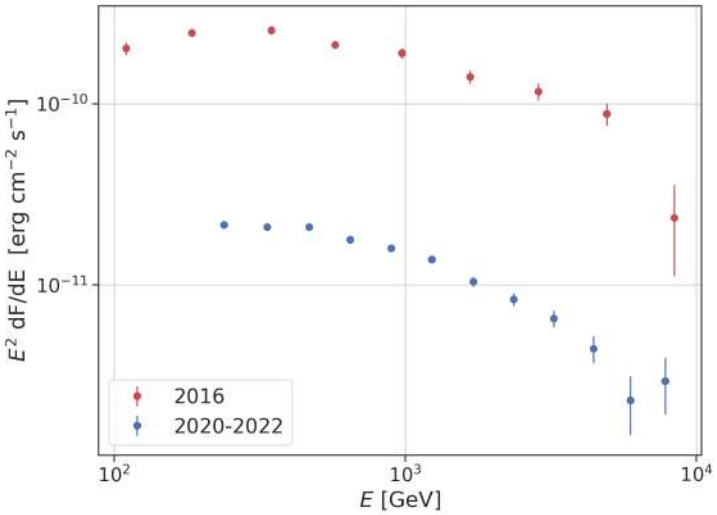

Figure 4.7: Averaged 2020-2022 observed spectrum compared with the spectrum of 13 June 2016 from MAGIC Collaboration et al. (2020a).

4.4 MWL observations

Employing MWL information is crucial for drawing a global picture of the blazars' behaviour. To interpret the broadband spectral features of 1ES 1959+650, we used MWL data over the 2020-2022 period. Excluding the MAGIC data, discussed in previous Sections, the following Section reports the list of MWL data used in this work. In particular, I performed the analysis of MAGIC and *Swift*-XRT data.

- ***Fermi*-LAT**. In the HE band, data from the 1ES 1959+650 monitoring performed by the *Fermi*-LAT satellite (described in Chapter 1) have been used. This instrument observes gamma rays with energies between 20 MeV and 300 GeV via pair conversion. The monitoring of 1ES 1959+650 has been ongoing since 2008. The *Fermi*-LAT data are analyzed and made available by the *Fermi* Collaboration. The automatic analysis is performed with the LAT `Fermitools3` (version 1.0.5) and provides light curves with different time intervals (Abdollahi et al. 2023). The public data can be downloaded from the *Fermi* LAT Light Curve Repository website[4].

  In this work, we included *Fermi*-LAT data of 1ES 1959+650 overlapping the MAGIC data time interval, from 2020 to 2022. After a first check of the public analysis, an accurate and tailored data reduction using the `Fermitools3` has been carried out specifically for this project. The energy range adopted for the HE spectra and lightcurve is 0.3-300 GeV, and the temporal binning for the light curves is 7 days to ensure enough statistics for each flux point. With this time binning, 139 flux points have been obtained from January 4th, 2020 to August 27th, 2022. The HE light curve is shown in the second panel of Fig. 4.8.

- **XMM-*Newton*** Three deep observations in coordination with MAGIC observations have been performed with the XMM-*Newton* satellite (Jansen et al. 2001), once per year: between 2020-07-16 21:28:34 and 2020-07-17 06:40:14 for a total duration of 33.1 ks, between 2021-08-07 19:23:36 and 2021-08-08 03:58:36 for a total duration of 30.9 ks, between 2022-06-06 21:33:31 and 2022-06-07 07:41:51 for a total 36.5 ks. All three EPIC cameras (pn, MOS1, and MOS2) were operated in Small Window mode with medium filter. Following standard procedures, the data were reduced using the XMM-*Newton* Science Analysis System (SAS v20.0.0). Time intervals with strong background flaring were filtered out following standard procedures using the high-energy light curves with cuts of 0.4 and 0.35 counts s^{-1} for the pn and MOS, respectively.

  Source and background spectra were extracted from circular regions of radius 34 arcsec for all three detectors. All spectra were binned to contain at least 20 counts per bin and not to oversample the intrinsic energy resolution by more than a factor of three. All the spectra suffered from a significant pile-up effect (see e.g., Jethwa et al. 2015). To remove the pile-up effect, we extracted again the source spectra from an annulus region with an internal radius of 10 or 15 arcsec, depending on the single observation, and an outer radius of 45 arcsec. Since the MOS data have a lower statistic than PN, we used only PN data. The total good exposure times after filtering for PN are 18.9, 19.4, and 19.1 ks in 2020, 2021, and 2022, respectively.

- ***Swift*-XRT** The *Neil Gehrels Swift Observatory* operates the X-Ray Telescope (*Swift*-XRT, Gehrels et al. (2004)) observing in the energy range of 0.2-10 keV. 1ES 1959+650 is regularly monitored by the *Swift* satellite since 2005 and the data are public. To match

[4]https:fermi.gsfc.nasa.gov/ssc/data/access/lat/LightCurveRepository/about.html

the MAGIC observations, the XRT dataset of 1ES 1959+650 analysed in this work consists of 111 snapshots, starting from June 1st, 2020 to September 12th, 2020. The XRT observations analysed in this work were performed with the Windowed Timing (WT) mode.

The XRT spectra were generated with the *Swift*-XRT data products generator tool at the UK *Swift* Science Data Centre[5] (for details see Evans et al. 2009). The obtained spectra are grouped using the task `grppha` to have at least 20 counts per bin. We used the spectral redistribution matrices in the Calibration database maintained by HEASARC. The X-ray spectral analysis was performed using the `XSPEC` 12.13.1 software package (Arnaud 1996).

The X-ray spectra in the 0.3–10 keV energy range are fitted by an absorbed log-parabola model using the photoelectric absorption model `tbabs` (Wilms et al. 2000) with a HI column density consistent with the Galactic value in the direction of the source, as reported in Kalberla et al. (2005), i.e. 1.01×10^{21} cm^{-2}. The flux as a function of the time of XRT data is displayed in the third panel of Fig. 4.8. The goodness of the fit between observed data and the model is evaluated with the χ^2 test.

- ***Swift*-UVOT** The *Neil Gehrels Swift Observatory* operates the Ultraviolet Optical Telescope (*Swift*-UVOT, Roming et al. (2005)) which is equipped with ultraviolet and optical band filters (UVW1, UVM2, UVW2, and U, B, V), observing at wavelengths from 170 to 650 nm. The number of UVOT flux points of 1ES 1959+650 shown in Fig. 4.8 ranges from a minimum of 111 to a maximum of 118, depending on the filter. Observations are taken almost simultaneously with the *Swift*-XRT instrument.

  The HEAsoft package v6.29 with the `uvotproduct` task was used to perform the analysis. Source counts were extracted from a circle centred on the source nominal position with a 5 arcsec radius. Background counts were obtained from a 30 arcsec radius circle around the source position, masking out the source position with a circle region of 12.5 arcsec radius and all other source positions (with 6 arcsec radius circle regions each). The conversion of magnitudes to flux densities included a correction for Galactic extinction following the Cardelli et al. (1989) extinction function and the corresponding integration over the UVOT filter wavelength profile. We adopted a value of $R_V = 3.1$ and E(B-V) = 0.17, the latter extracted from the Schlegel et al. (1998) dust maps.

- **Tuorla and KAIT** 1ES 1959+650 has been observed in the optical R-band using the 1.03 m telescope at Tuorla Observatory as part of the Tuorla Observatory blazar monitoring[6] (Takalo et al. 2008). The observations and data reduction are described in detail in Nilsson et al. (2018). The observed fluxes were adjusted for galactic extinction, assuming a value of 0.384 mag.

  Simultaneous monitoring in the unfiltered optical band, which corresponds roughly to the R band, is provided by the Katzman Automatic Imaging Telescope (KAIT) (Filippenko et al. 2001). The data of the light curves for 163 objects are public[7], the KAIT light curve of 1ES 1959+650 is used in this work.

- **Radio observations** At 15 GHz, 1ES 1959+650 is monitored by the single-dish radio telescope operated by the Owens Valley Radio Observatory (OVRO) in California. The description of the OVRO monitoring program and data reduction are reported in Richards et al. (2011). The 100-m Effelsberg single-dish radio telescope monitors 1ES 1959+650 at multiple frequencies, from 14 GHz to 42 GHz, as part of the TELAMON ((Kadler et

[5] http://www.swift.ac.uk/user_objects
[6] https://users.utu.fi/kani/1m/
[7] http://herculesii.astro.berkeley.edu/kait/agn/

al. 2022)). The 43 GHz public VLBI data of 1ES 1959+650 are provided by the Boston University Blazar Group[8] which leads the Large VLBA Project Blazars Entering the Astrophysical Multi-Messenger Era (BEAM-ME). The VLBA is an array of ten antennas located in America working as an interferometer (see Section 1.2 for more details).

4.5 MWL results

4.5.1 Light curve

Fig. 4.8 shows the MWL light curve for the period 2020-2022. No major outbursts at any wavelengths are detected in the MWL light curves of Fig. 4.8 and the source is found in a low state compared with past flux levels (see, e.g., The MAGIC Collaboration et al. 2022, for a comparison). Despite the overall low state, significant changes in flux are found mainly in the VHE and X-rays bands. The variability at VHE and X-rays will be discussed in more detail in the following Sections. A few flares can be observed over the HE light curve (second panel in Fig. 4.8). However, they are consistent with the rest of the flux points within the errors. The optical light curves do not cover the entire 2020-2022 period. Large gaps are present in the KAIT light curve while the Tuorla light curve starts on MJD 59347, covering only about half of the period analysed here. During the first part of the Tuorla light curve, the flux is higher than the rest, exhibiting three flux maxima. The single-dish radio light curves show smoother evolution. The variations between radio flux points occur over longer periods as typical for blazars (e.g., Orienti et al. 2013a).

[8] https://www.bu.edu/blazars/BEAM-ME.html

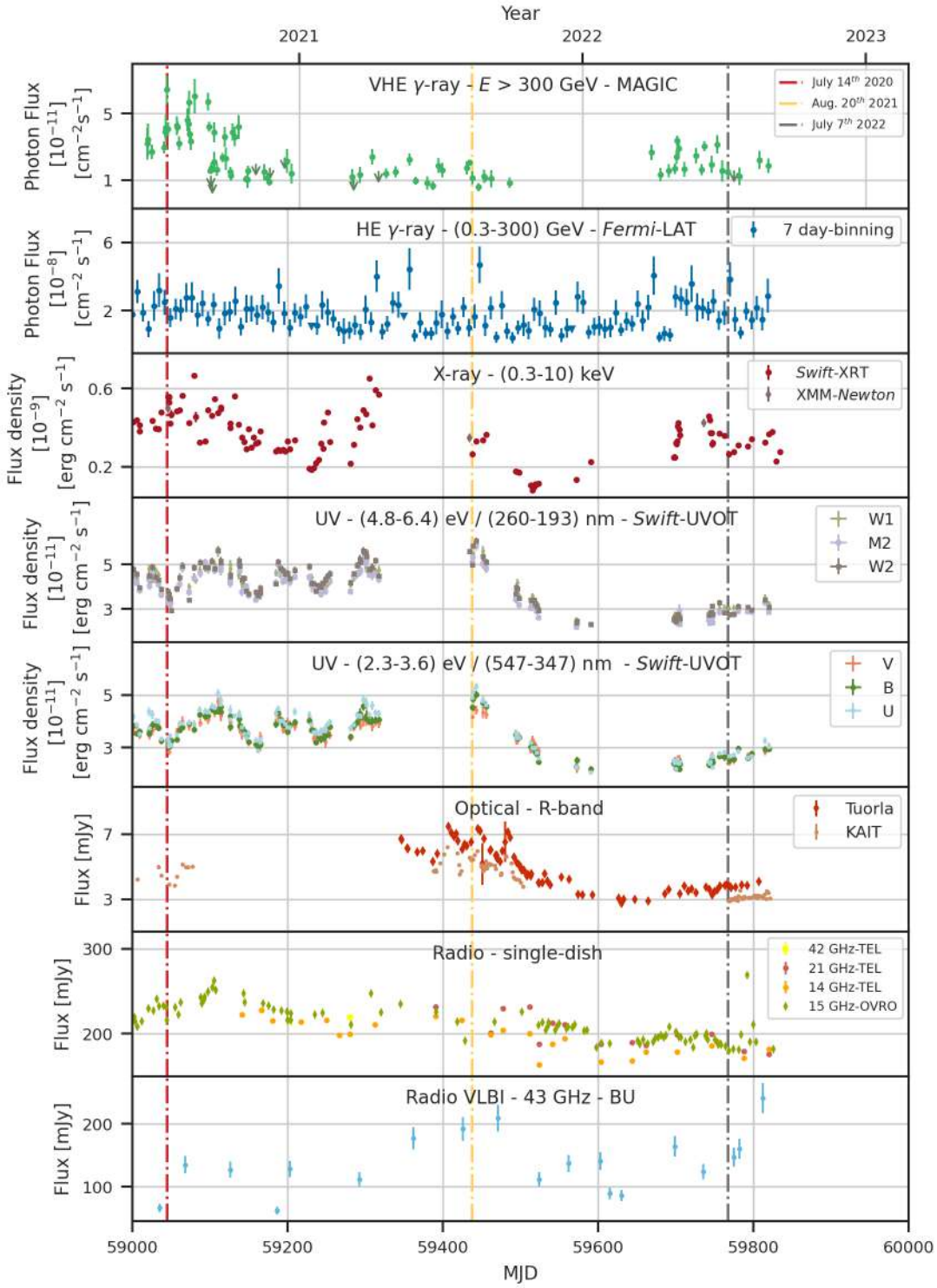

Figure 4.8: MWL light curves of 1ES 1959+650 during the period from 2020 to 2022. Top to bottom panels show: the VHE MAGIC gamma-ray data above 300 GeV, the HE *Fermi*-LAT gamma-ray data between 0.3-300 GeV, the XRT and XMM-*Newton* X-ray data between 0.3–10 keV, UVOT data in the UV band, between 4.8 eV and 6.4 eV, and the optical band, between 2.3 eV and 3.6 eV, and the Tuorla and KAIT data in the R-band. The last two panels show radio single-dish (OVRO and TELAMON) data between 15 GHz to 42 GHz and the VLBA (BEAM-ME) data at 43 GHz. The dashed red, yellow, and grey lines mark the day of highest VHE flux, low γ-ray-high optical state, and lowest VHE flux (see next Sections), respectively.

4.6 Flux Variability

In the following, we investigate the potential flux variability throughout the period 2020-2022. The variability study mainly focuses on the X-ray and VHE variability since these bands constitute the most variable energy bands in the case of 1ES 1959+650.

To assess the presence of variability we first conducted a χ^2 test using constant functions. Then, we applied the Bayesian Blocks (BB, Scargle et al. (2013)) method. This employs a Bayesian approach to determine time bins, or *blocks*, within which the photon flux can be assumed as constant. The method utilizes a geometric prior with the parameter ε. This prior assigns a lower probability to a subdivision in a larger number of blocks, reflecting the idea that, a priori, it is more likely to have fewer than more blocks. The BB approach is implemented in the `bayesian_blocks`[9] function of the `astropy.stats` module.

4.6.1 X-ray variability

As described in Section 4.4, XRT observations have been fitted with a logarithm parabola (Eq. 2.6). By testing the hypothesis of constant spectral parameters (α and β) and constant flux over the 2020-2022 period we found that these are rejected at the 3σ confidence level. The χ^2 test was utilized to assess the goodness of fit. The best fit constant function for the flux is $(3.0 \pm 0.07 \times 10^{-10})$ erg/cm^{-2} s^{-1}. The flux varied from a maximum of about 7.4×10^{-10} erg/cm^{-2} s^{-1} to a minimum of 7.9×10^{-11} erg/cm^{-2} s^{-1}. The α parameter varies in an interval between 2.3 and 1.24 while the β parameter is in an interval between 1.10 and 0.09. The constant functions are 1.852 ± 0.002 and 0.511 ± 0.006 for α and β, respectively. The flux, α and β light curves are shown in Fig. 4.9.

Given the observed variability, we have chosen to not compute cumulative spectra to avoid averaging data from different states. The averaging of data with substantial variations could impact the overall spectral representation, risking the distortion of specific features in each state. Therefore, we opted to maintain a temporal separation between variable states employing one-day spectra selected based on the MAGIC light curve inspection (see next Section). Wani et al. (2023) confirm the spectral variability in the *Swift*-XRT data during a time interval partially overlapping the 2020-2022 data analysed in this work.

4.6.2 VHE variability

By fitting the 2020-2022 VHE light curve with a constant function, the constant resulted to be $(1.11 \pm 0.14) \times 10^{-11}$ photon cm^{-2}s^{-1}. The null hypothesis which assumes constant emission is rejected at 3σ level. Due to the significant variability observed in the VHE light curve, an analysis assuming a steady state averaging the entire 2020-2022 data is not applicable. We then searched for time intervals representative of the states of the source with the BB approach.

In implementing the method, we tested a large set of priors ε. We found that the resulting splitting in blocks strongly depends on the prior choice and thus we judge the method too arbitrary. Applying the BB algorithm did not provide a satisfactory state subdivision. The effect could be because the BB algorithm is more effective when distinct variations or episodes of enhanced emission are in place. When dealing with a light curve showing emission without strong outbursts, as in our case, the BB algorithm finds it challenging to recognise meaningful blocks identifying actual different states of the source. The algorithm indeed relies on detecting changes in the statistical properties of the data, and if these changes are subtle or gradual, the

[9] https:docs.astropy.orgenstableapiastropy.stats.bayesian_blocks.html

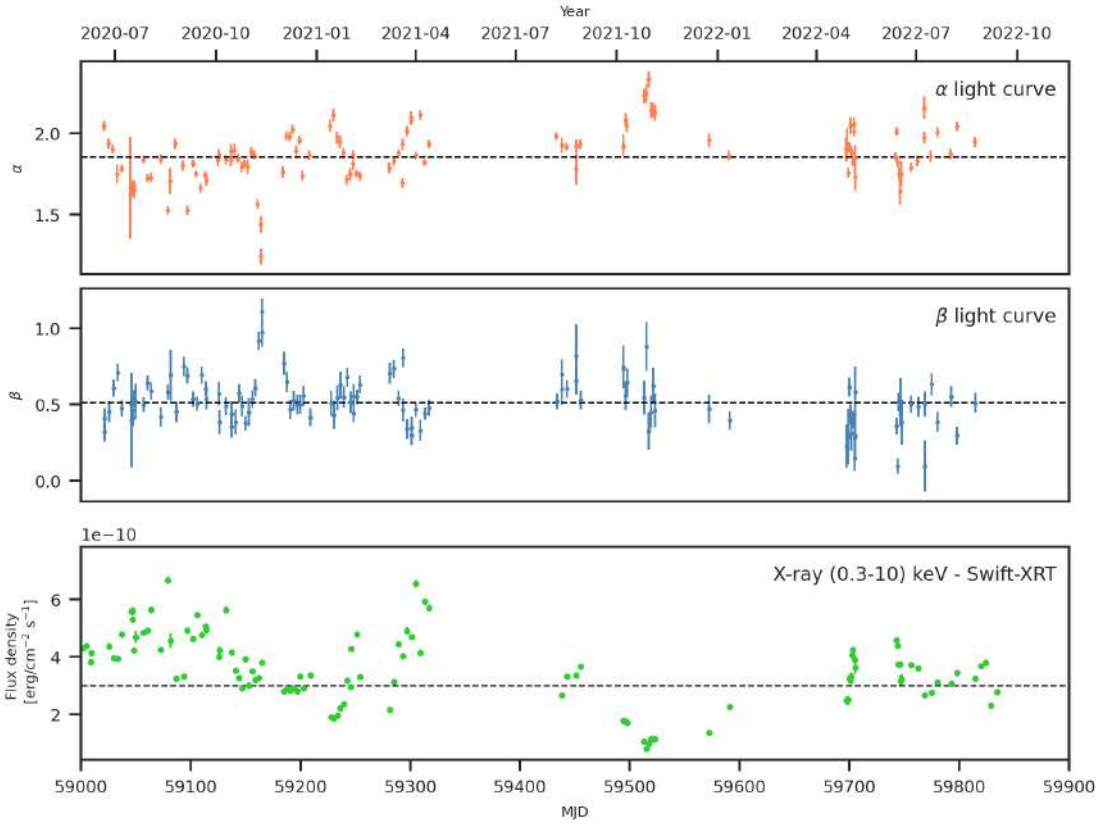

Figure 4.9: From top to bottom the panels show the α, β and XRT flux versus time, respectively, during the 2020-2022 period. The dashed lines indicate the fitted constant values for the three parameters.

algorithm may not identify clear boundaries. If the light curve is divided into time intervals that do not capture significant variations, the chosen time bins could fail to reflect underlying physical processes in the source, and a lack of strong outbursts may result in less informative time intervals.

The BB analysis, however, allows us to confirm a non-negligible variability in the VHE light curve. To account for possible fluctuations introduced by instrumental biases and data analysis uncertainties, statistic uncertainties on the flux points have been summed in quadrature to systematic errors in the BB analysis. The systematic errors on MAGIC data have been estimated at a level of 15%. Assuming as a prior $\varepsilon = 0.001$, the VHE light curve has been split into 20-time bins (top panel in Fig 4.10). The upper limits on the flux points have not been taken into account for this analysis. The main variability is observed in the first part of the light curve, from MJD 59020 to around MJD 59200. Within this time interval, the average flux in each block exhibits variations compared to the rest of the light curve.

4.6.3 MWL Bayesian Block

We applied the BB method to the MWL light curves to identify different states at all the wavelengths (Fig 4.10). Hints of variability are also found in the *Swift*-UVOT (UV band) and *Swift*-XRT (X-ray band) data points throughout the entire light curves. The latter result is in agreement with the X-ray variability previously reported. In the X-ray light curve, the flux level in the first blocks (from the beginning to MJD 59300) seems to be overall higher than the last seven blocks (from MJD 59700 to the end), aligning somewhat with the VHE trend. The X-ray occurs in shorter timescales compared to the VHE observations. Due to the 1-week binning, the

Fermi-LAT light curve has been divided into only four bins, within which the average flux does not vary significantly. No significant outbursts are detected simultaneously at all wavelengths as in 2016.

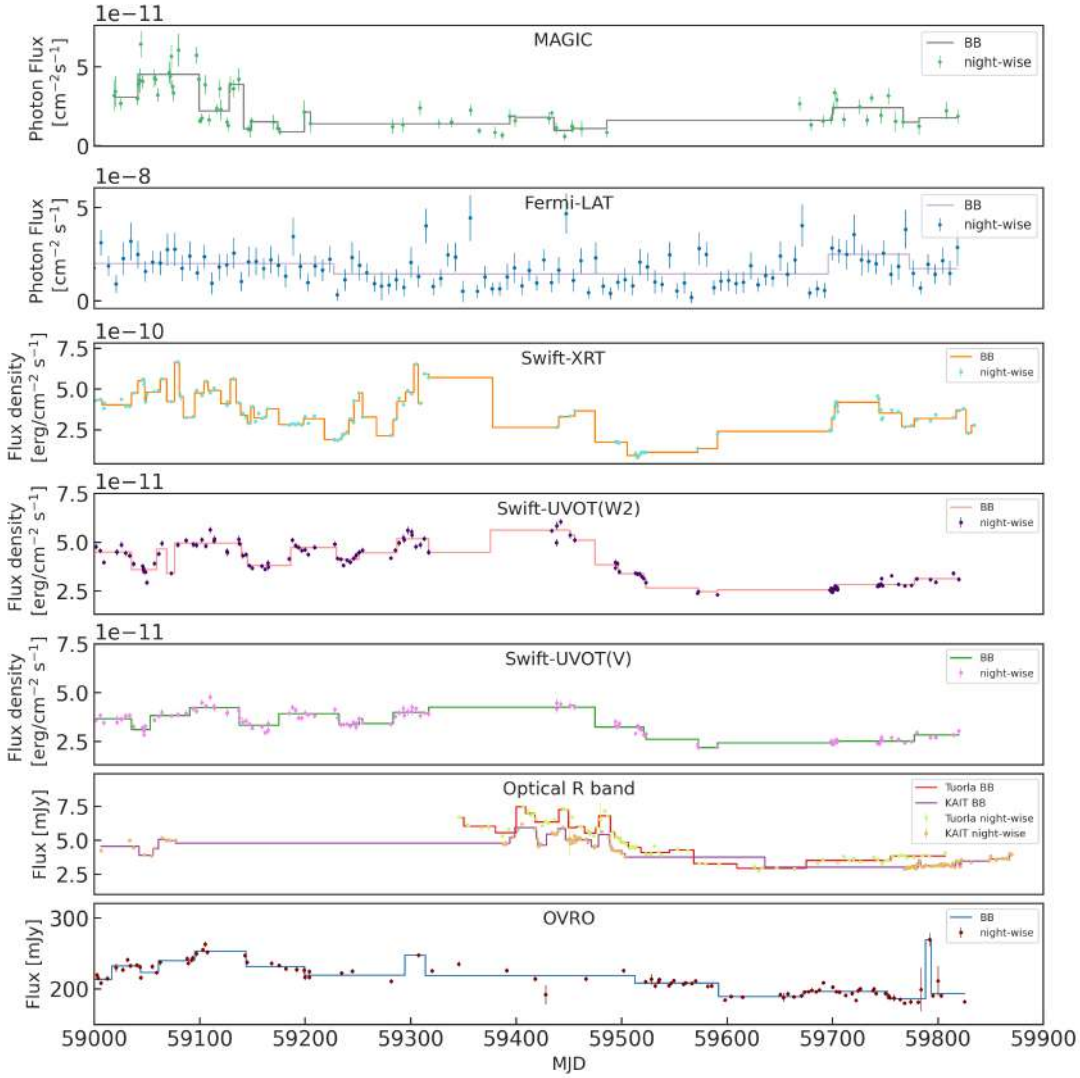

Figure 4.10: MWL light curves divided according to the BB analysis results. As discussed in the text, the BB analysis results depend on the prior. We selected those striking a balance between having a few but large time bins (which might combine different states) and a large number of short time bins that closely follow the observed light curve trend, thus not providing any useful division of the data sample. For *Swift*-UVOT analysis we show only the V-filter and the W2-filter as representative of the optical-side and UV-side bands of *Swift*-UVOT.

4.6.4 The fractional variability

Another quantitative estimate of the intrinsic variability is given by the *fractional variability*, $F_{\rm var}$ (Vaughan et al. 2003). For a sample of x_i flux-points with errors $\sigma_{{\rm err},i}$, $F_{\rm var}$ is defined by the formula:

$$F_{\rm var} = \sqrt{\frac{S^2 - \bar{\sigma}^2_{\rm err}}{\bar{x}^2}}, \tag{4.1}$$

in which S^2 is the variance of the flux-points sample, $\bar{\sigma_{\rm err}}^2$ is the mean square of the fluxes and the $\bar{x}^2$ is the mean flux. The uncertainty on $F_{\rm var}$ is:

$$\sigma_{F_{\rm var}} = \sqrt{\left(\sqrt{\frac{1}{2N}}\frac{\bar{\sigma}^2_{\rm err}}{\bar{x}^2 F_{\rm var}}\right)^2 + \left(\frac{\sqrt{\bar{\sigma}^2_{\rm err}}}{N}\frac{1}{\bar{x}}\right)^2}. \tag{4.2}$$

The computation of fractional variability is performed using the complete MWL dataset illustrated in Fig. 4.8. The $F_{\rm var}$ parameters versus energy for 1ES 1959+650 is plotted in Fig. 4.11.

The variation of $F_{\rm var}$ as a function of the energy is usually observed in HBLs. Consistent with previous studies, higher fractional variability in 1ES 1959+650 is detected at higher energies. This decreases towards lower energies.

Table 4.5 provides the results for each dataset. It is important to note that differences in temporal bins used to characterize variability may impact the comparability of $F_{\rm var}$ across different wavelength bands. In our case, we used the whole 2020-2022 period to investigate the overall behaviour of the source during a low state.

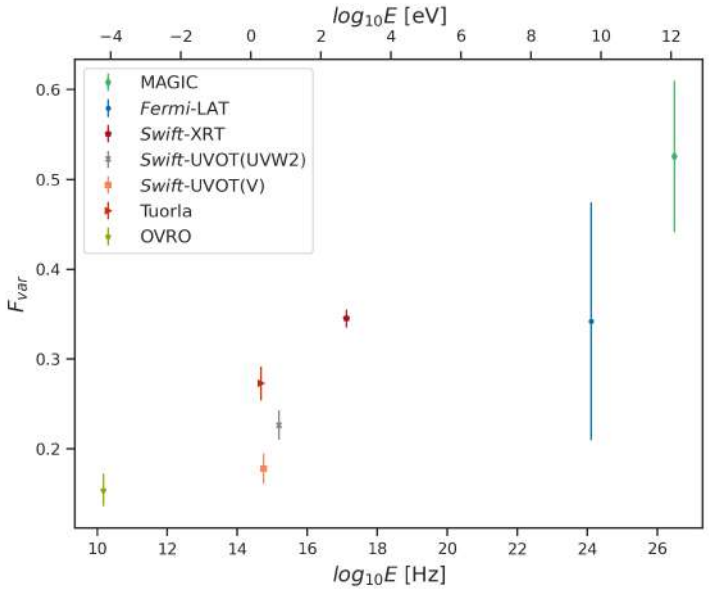

Figure 4.11: Fractional variability for each instrument as a function of energy. It is calculated using all data points collected during the 2020-2022 period (Fig. 4.8). The values of $F_{\rm var}$ are reported in Tab. 4.5.

4.7 Intra-band correlations

The correlation between different energy bands is crucial for understanding the underlying radiative processes driving emissions within those bands. Under the assumption of a leptonic

Table 4.5: Fractional variability in the different energy bands

Energy band (1)	F_{var} (2)
MAGIC	0.53 ± 0.08
Fermi-LAT	0.34 ± 0.13
Swift-XRT	0.35 ± 0.01
Swift-UVOT (UVW2)	0.23 ± 0.02
Swift-UVOT (V)	0.18 ± 0.02
Tuorla	0.27 ± 0.02
OVRO	0.15 ± 0.02

Notes: (1) Energy band; (2) $F_{\rm var} \pm \sigma_{F_{\rm var}}$ from Eq. 4.1 and Eq 4.2.

scenario, and specifically in the context of the one-zone SSC model, X-ray photons produced through synchrotron processes can act as target photons for IC interactions, leading to very high energy (VHE) emission. Similarly, high energy (HE) emission can stem from IC interactions with optical/UV target photons. In the SSC scenario, emissions across these energy bands are expected to vary almost simultaneously. Consequently, correlations between TeV and optical bands, as well as sub-TeV and X-ray bands, are predicted, driven by the specific energies of the photon fields involved. Any deviations from this simultaneity might suggest the presence of multiple emitting regions.

In TeV blazars, electrons can acquire extremely high energies. However, as electron energy increases, the efficiency of the Compton scattering process diminishes as it enters the Klein-Nishina regime, resulting in decreased interaction cross-sections. Consequently, the SSC spectrum steepens, and intra-band correlations become more complex (Boettcher et al. 2012; Katarzyński et al. 2005).

Keeping in mind the complexity of intra-band correlation implications, we analysed intra-band correlations between VHE, HE, X-ray, UV and optical bands for a first-order test for the assumption of a one-zone SSC scenario for our 2020-2022 data. Radio data have been excluded as the radio emission is expected to be contaminated by the large-scale emission from outer regions of the jet and so to be not connected to the emission in other energy bands.

To determine the presence of correlations between energy bands, we selected only observations performed within 2 days of those performed in the other energy bands. This choice allows us to test a reasonable number of data points. Only correlations with the HE band have been searched on a larger simultaneity window (10 days) to account for the 1-week binning of the data. The UVW2 filter fluxes were used as representatives of the UV emission.

We used the Pearson and Spearman tests (Myles Hollander & Douglas 1973) to describe the interplay between the energy bands. The main differences between the Pearson and Spearman correlation coefficients are in the type of relationship measured. Pearson measures the linear correlation between two variables, it is sensitive only to linear relationships, meaning it assesses whether there is a proportional relationship between variables. On the other hand, Spearman measures the monotonic correlation between two variables, not requiring the relationship to be linear. It only assesses whether, in general, an increase (or decrease) in one variable is associated with an increase (or decrease) in the other. The disadvantage of the Pearson coefficient computation is the assumption of Gaussian distributions of variables, while in the Spearman coefficient computation, there are no strong assumptions about the distribution of data. Another difference is that in the Pearson method, the correlation is measured using the actual values of

variables while in the Spearman method, it is measured using the ranks of variables, transforming the data into an ordinal scale before calculation. Both the correlation coefficients range between -1, 0, and 1, indicating anti-correlation, absence of correlation, and presence of correlation, respectively. Specifically, in the case of the Pearson coefficient, these correlations are linear. To compute the Pearson correlation coefficient we used the `scipy.stats.pearsonr`[10] function from the `scipy.stats` module in Python, part of the SciPy library, while for the Spearman correlation coefficient, we employed the `scipy.stats.spearmanr`[11] function also from the `scipy.stats` module.

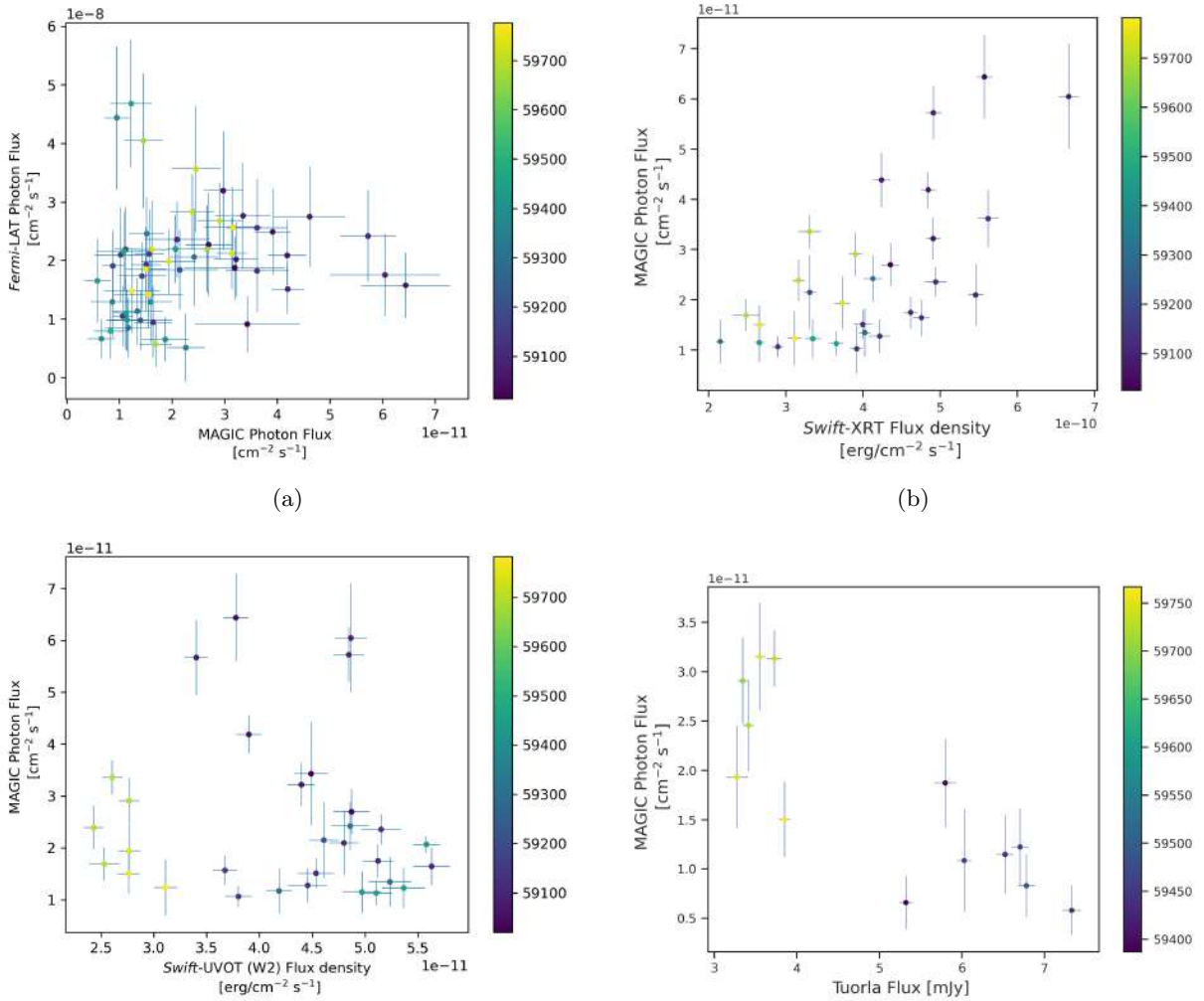

Figure 4.12: Correlations between the VHE photon flux and fluxes from other energy bands: from HE to X-rays, UV and optical (from top left to right bottom, respectively). The color-bar indicates the time of the observations.

VHE correlations Fig. 4.12b shows the VHE-X-ray correlation. 30 flux points were identified in the 2-day simultaneity window. The Pearson coefficient for the correlation is 0.68 with a p-value of 4.1×10^{-4}, confirming a hint of correlation, as expected for in a SSC model. The Spearman coefficient confirms this finding (0.64 with a p-value of 10^{-4}). No correlation is

[10] https:docs.scipy.orgdocscipyreferencegeneratedscipy.stats.pearsonr.html
[11] https://docs.scipy.org/doc/scipy/reference/generated/scipy.stats.spearmanr.html

found between VHE and UV emission (Fig. 4.12c). Only 16 simultaneous data points are found in the VHE and optical comparison (Fig. 4.12d). The results show a strong negative correlation (Pearson coeff. is −0.81) between VHE and optical emission. The inverse relation can be interpreted assuming an External Compton scenario. Alterations in the magnetic field may cause variation to the synchrotron low energy (optical) emission, not affecting the overall emission at high energy, that is instead produced by IC interactions with a different photon field (e.g., Chatterjee et al. 2013). However, the statistical results and the observed bimodal behaviour are influenced by the intermittent monitoring of the source in the optical band from 2020 to 2022. The split of the data points into high-optical and low-optical states in the VHE-optical correlation is due to the absence of transitional optical values, which were not recorded because the source being unobserved, rather than an intrinsic absence of the intermediate state.

HE correlations Both Pearson and Spearman correlation coefficients indicate a moderate positive relationship between the HE and X-ray emission (Fig. 4.13a). However, the correlation is less strong and statistically significant than the VHE and X-ray one. This can also be due to the smaller number of simultaneous data taken into account in the latter case (30 points in the VHE-Xray relation versus 55 points in the HE-X-ray relation). The Pearson statistic is indeed sensitive to outliers and can be influenced by extreme values (Moore 2009). In a larger sample of data, outliers are more frequent and can affect the Pearson coefficient computation. Moreover, large LAT errors in the data can affect the calculation of the Pearson correlation coefficient.

As for the VHE emission, also the HE does not correlate with the UV data (Fig. 4.13b). A correlation with the optical data is also missing. From the correlation in Fig 4.13c, it seems the source is acting in two different ways during the high optical flux days and the low optical flux ones. However, as in the VHE-optical correlation, this is due to the irregular monitoring of the source in the optical band and it is not related to physical changes in the source.

Although no correlation is found between HE and the optical fluxes, during the low γ-ray-high optical state, the LAT light curve shows one of the (7-day binned) highest flux levels detected over the 2020-2022 period (Fig 4.8).

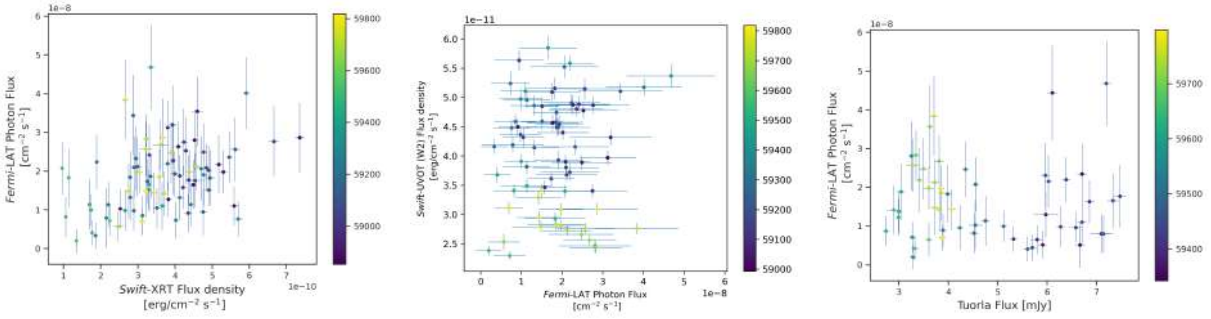

(a) (b) (c)

Figure 4.13: Same as Fig. 4.12 but for the HE intra-band correlations.

No correlation is found between X-ray and optical data, despite the artificial dual behaviour – due to the non-continuous monitoring in the optical band – recognised as in the correlation between the optical flux and the HE and VHE flux. According to the Pearson and Spearman test, neither the optical nor the UV light curves show a connection with the X-ray one. This also emerges from the correlation plots (Fig. 4.14b and Fig. 4.14a) showing the random distribution of the flux points. On the other hand, the UV and optical (R) bands correlate well, as expected, due to the proximity of the two energy ranges.

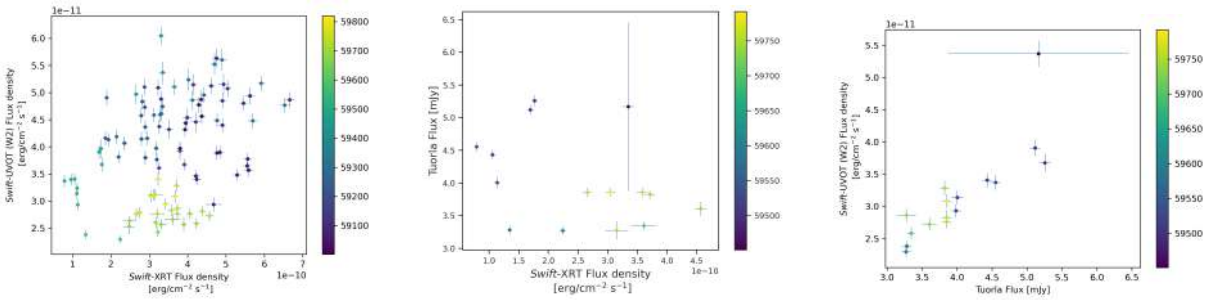

(a) (b) (c)

Figure 4.14: Same as Fig. 4.12 but for the UV-X-rays, Optical-X-rays and UV-optical correlations.

Table 4.6: Results of the intra-band correlation study

Correlation (1)	Pearson coeff. (2)	p-value (3)	Spearman coeff. (4)	p-value (5)	sim. days (6)	Fig. (7)
VHE vs HE	0.15	0.28	0.30	0.02	10	4.12a
VHE vs X-ray	0.68	4.10e−4	0.64	1.00e−4	2	4.12b
VHE vs UV	−0.10	0.63	−0.17	0.36	2	4.12c
VHE vs Optical	−0.81	8.00e−4	−0.79	0.001	2	4.12d
HE vs X-ray	0.40	0.001	0.36	1.00e−3	10	4.13a
HE vs UV	0.10	0.59	0.02	0.86	10	4.13b
HE vs Optical	−0.03	0.85	−0.09	0.53	10	4.13c
X-ray vs UV	0.33	1.00e−3	0.33	1.00e−3	2	4.14a
X-ray vs Optical	−0.34	0.22	−0.38	0.17	2	4.14b
UV vs Optical	0.85	3.6e−5	0.88	6.2e−6	2	4.14c

Notes: (1) Energy bands; (2) and (4) Pearson and Spearman correlation coefficient, respectively; (3) and (5) probability of the null hypothesis associated with the Pearson and Spearman coefficient, respectively; (6) time interval in days within which it is assumed simultaneity between the observations in the two bands; (7) reference to the figure.

VHE–X-ray correlation during the 2016 flare We tested the correlation between X-ray and VHE emission during the 2016 flare state. The 2016 MAGIC data used are from May 1^{st} (MJD 57509) to July 14^{th} (MJD 57583). In Fig. 4.15c the comparison between the two periods is shown in a single panel, while Fig. 4.15a and Fig. 4.15b represent the X-ray flux-VHE flux relation, separately, showing the 2020-2022 period the first and the 2016 period the latter. For the 2016 period, we found a Pearson coefficient of 0.78 with a probability of null hypothesis of 1.71×10^{-7} (the Spearman correlation coefficient is 0.81 and the p-value 3.21×10^{-8}), assuming the 2-day simultaneity window. By comparing this result with the low-state (2020-2022) VHE-X-ray correlation coefficients (i.e., the Pearson coefficient is 0.68 and the p-value 4.10×10^{-4}, Tab. 4.6) we observe that the correlation is stronger during the flaring state of the source.

4.8 Braodband SED

The strong dependence of the BB analysis from the prior choice together with the differences in the BB binning of the MWL light curves brings us to consider a distinct method for the definition of the time intervals for the spectral analysis. The goal of the project is to determine physical changes in the simultaneous broadband spectra of the source during different stages.

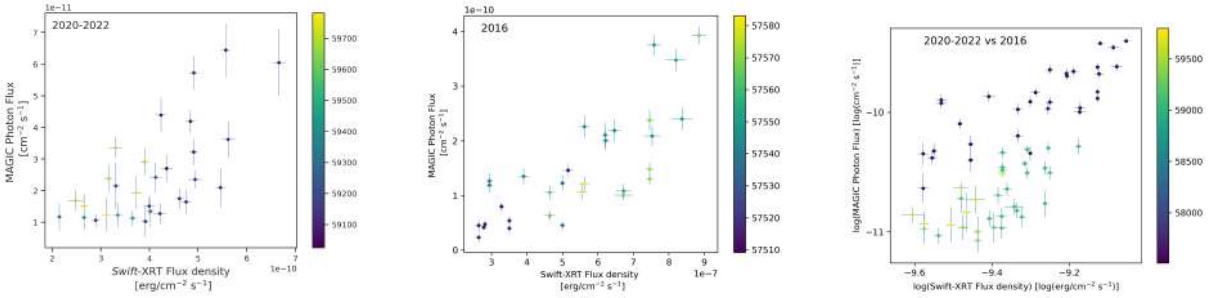

(a) (b) (c)

Figure 4.15: Correlations between the VHE band and X-ray band during 2020-2022 only (left panel), during a few months around the 2016 flare (middle panel). In the right panel, both the 2020-2022 and 2016 VHE-X-ray correlations are reported in a log-log plane for comparison.

In particular, we opted to identify three specific days to represent distinct states of the source at VHE in its low emission state. We selected the days with the highest and lowest VHE fluxes recorded and for which we have the maximum simultaneous MWL coverage.

During the first maximum detected at VHE, on July 14^{th}, 2020 (MJD 59044), there are simultaneous observations at all wavelengths, with simultaneity windows of up to three days. The VHE flux during the high state – hereafter referred to as the *high γ-ray state* – was $(6.44 \pm 0.84) \times 10^{-11}$ photons cm^{-2}s^{-1}.

There is no complete MWL coverage for the first three days of lowest VHE flux. Corresponding to the fourth lowest VHE flux point, occurring on August 20^{th}, 2021 (MJD 59446), the optical flux reached a maximum, as mentioned in the previous Section. The VHE flux during this day was $(1.15 \pm 0.40) \times 10^{-11}$ photons cm^{-2}s^{-1}. To achieve a 5σ significance for the source detection during this very low state, we considered three days around August 20^{th}, 2021, adding observations from August 12^{th} and August 27^{th} for the spectrum computation. In each BB subdivision (obtained by changing the prior), the three days are always included in the same block, confirming the flux can be assumed constant during the three days. During the observations of these three days, we have a complete MWL coverage. Despite including a block of three observations, for simplicity, we refer to this as a one-day observation (August 20^{th}, 2021), labelling it as *low γ-ray-high optical state*, considering the low state in the optical band and to distinguish it from the other low state introduced below.

For a complete view of the spectral changes during the whole 2020-2022 period, we selected a second day of lowest VHE flux at the end of the period, during which the optical flux is also at its minimum. After the fourth minimum (the low γ-ray-high optical state), the next day of lowest flux for which we have total MWL converge is on July 7^{th}, 2022 (MJD 59767), hereafter referred to as the *low γ-ray-low optical state*. The VHE flux during was $(1.50 \pm 0.38) \times 10^{-11}$ photons cm^{-2}s^{-1}.

We warn on the terms high and low state (γ-ray and optical). These refer to the overall low and high-flux phases analysed in this work (limited to the 2020-2022 time range) and should not be interpreted as absolute high and low states of the source. For example, in the VHE band, 1ES 1959+650 was in a high state during the 2016 flare, as well, in the optical band the source has experienced states of higher flux during its lifetime[12].

Upon visual inspection of the MAGIC light curve run-wise – where each run lasts about 15-20 minutes – we did not detect appreciable intranight flux variability over these time scales. We can exclude the presence of very fast variability, such as observed during the 2016 flare when

[12]The Tuorla monitoring of 1ES 1959+650 recorded peak fluxes of the order of 12 mJy (see https:users.utu.fikani1m1ES_1959+650_jy.html)

a variability timescale of 36 minutes was revealed.

4.8.1 Spectra

The VHE spectra for the three selected days, have been obtained with the unfolding procedure described in Section 2.3.10, accounting for the IRF. Fig. 4.16 illustrates the three spectra: July 14^{th}, 2020 (MJD 59044) for the high γ-ray state (Fig. 4.16a), July 7^{th}, 2022 (MJD 59767) for the low γ-ray-low optical state (Fig. 4.16b) and the August 20^{th}, 2021 (MJD 59446) block for the low γ-ray-high optical state (Fig. 4.16c). We tested both a power law (Eq.2.4) and a log parabola (Eq.2.6) function. The results are summarized in Tab 4.7. The LRTs statistic indicates that the preference for the log parabola over a simple power law is statically significant only for the high γ-ray state. During the other two states the simple power law is preferred over the log parabola. All the spectra are corrected for the EBL absorption model of Dominguez et al. (2011).

Table 4.7: Best-fit spectral paramters

Date (1)	Function (2)	α (3)	β (4)	Γ_γ (5)	χ^2/d.o.f (6)	Fig. (7)
July 14^{th} 2020	log parabola	$1.84^{+0.26}_{-0.24}$	$0.71^{+0.21}_{-0.27}$	–	10.8/8	4.16a
	power law	–	–	$2.19^{+0.11}_{-0.11}$	13.6/9	–
August 20^{th} 2021	log parabola	$2.32^{+0.12}_{-0.12}$	$(1.4^{+0.33}_{-0.32})$e–5	–	14.0/10	–
	power law	–	–	$2.32^{+0.12}_{-0.12}$	14.0/11	4.16c
July 7^{th} 2022	log parabola	$1.59^{+0.73}_{-0.55}$	$0.96^{+0.65}_{-0.47}$	–	6.0/7	
	power law	–	–	$2.14^{+0.24}_{-0.25}$	7.3/8	4.16b

Notes: (1) Date for the spectrum computation; (2) Spectral function assumed; (3) α and β best-fit parameters in case of log-parabola function; (4) Γ_γ best-fit parameter in case of simple power law function; (5) χ^2 over degrees of freedom (d.o.f); (6) reference to the relative figure.

To reach enough statistics for the spectra computation at HE, we divided the *Fermi*-LAT light curve into three blocks in correspondence to the three days selected at VHE. The blocks are between MJD 59020 and MJD 59146 for the high γ-ray state analysis, between MJD 59147 and MJD 59664 for the low γ-ray-high optical state analysis and between MJD 59665 and MJD 59818 for the low γ-ray state analysis.

The selected date of the XRT data corresponding to the VHE selected days are July 15^{th} 2020 (MJD 59045) for the high γ-ray state, July 8^{th} 2022 (MJD 59768) for the low γ-ray-low optical state (both 1-day delay to the MAGIC selected dates) and August 18^{th} 2021 (MJD 59445) for the low γ-ray-high optical state (2 days before the MAGIC selected date). The spectra are fitted with a log parabola. The corresponding spectra from the UVOT observations are produced for July 17^{th} 2020 (MJD 59047), July 8^{th} 2022 (MJD 59768) and July 16^{th} 2022 (MJD 59442) for the high γ-ray state, low γ-ray-low optical state and low γ-ray-high optical state, respectively. The optical spectral points are from the KAIT observation of July 15^{th} 2020 (MJD 59047) for the high γ-ray state, and from Tuorla observations of July 8^{th} 2022 (MJD 59768) and August 18^{th} 2021 (MJD 59445) for the low γ-ray-low optical state and the low γ-ray-high optical state, respectively. Radio data below 100 GHz were excluded from the SED fitting procedure due to the significant contribution from a distinct jet region at these frequencies, as discussed in Chapter 2, where emission at radio wavelengths is strongly self-absorbed. However, radio data are shown in the plots as upper limits for the low-energy emission even if excluded

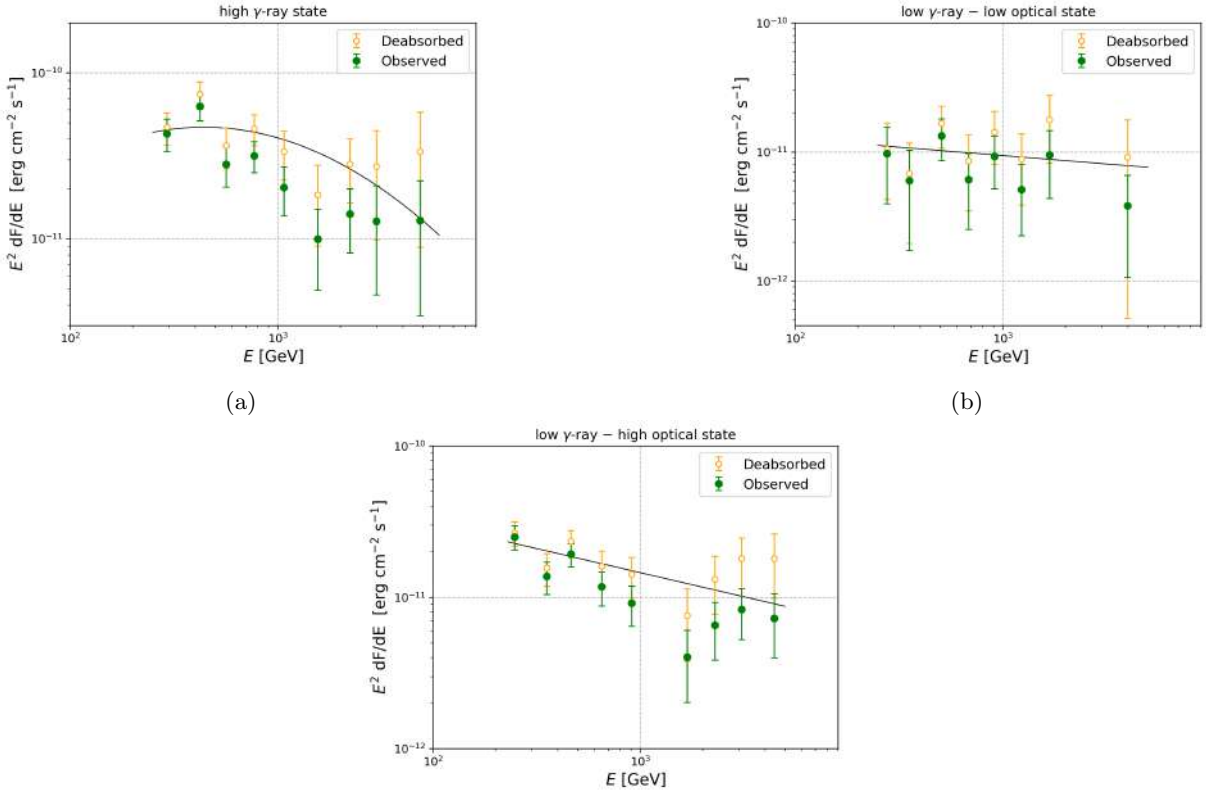

Figure 4.16: Unfolded VHE spectra for the high γ-ray state (top left, fitted with a log parabola function), low γ-ray-low optical state (top right, fitted with a power law function), and low γ-ray-high optical state day (bottom, fitted with a power law function). Observed and EBL-deabsorbed spectral points are shown. In the SED modelling analysis, the deabsorbed spectra are used. Spectral parameters are reported in Tab. 4.7.

during the fitting procedure. We used the radio observations closest in time to the VHE-selected days. Corresponding to the July 14^{th}, 2020 VHE SED, we show the July 14^{th} OVRO flux and an averaged BEAM-ME (VLBA) flux from the July 5^{th} and August 7^{th} observations. No TELAMON data are available for that day. Corresponding to July 7^{th}, 2022 VHE SED, we include BEAM-ME data from July 15^{th}; OVRO data from July 8^{th}; TELAMON-14 GHz data from June 6^{th} and July 27^{th} and TELAMON-21 GHz data from June 16^{th} and July 27^{th}. For the August 20^{th}, 2021 state, the plot reports the averaged BEAM-ME flux from September 14^{th} and July 31^{st} observations; the averaged OVRO flux from August 2^{nd} and September 9^{th} observations: the averaged TELAMON-14 GHz flux July 29^{th} and September 4^{th} observations and TELAMON-21 GHz data from September 4^{th}.

4.8.2 SED modelling

The MWL SED points overlapping with the best-fit models for high γ-ray, low γ-ray-low optical states, and low γ-ray-high optical state, are illustrated in Fig. 4.17, Fig. 4.19 and Fig. 4.18, respectively. A comparison between the observational data and modelling of the SEDs from the three days and the 2016 flare is shown in Fig. 4.20. The model of the 2016 flare day is reproduced using the parameters obtained by MAGIC Collaboration et al. (2020a).

We employed the `agnpy` software described in Section 2.3.3. For the data modelling, we

Table 4.8: Best fit SED parameters

Parameters (1)	July 14^{th} 2020 high γ-ray state (2)	August 20^{th} 2021 low γ-ray-low optical state (3)	July 7^{th} 2022 Opt. Flare (4)	June 13^{th} 2016 flare by MAGIC Collaboration et al. (2020a) (5)
p1	2.32±0.04	2.17±0.10	2.19±0.04	2.2
p2	2.60±0.20	3.28±0.12	3.22±0.21	3.2
$\gamma_{\rm b}$	$(1.9 \pm 1.1) \times 10^5$	$(9.4 \pm 1.5) \times 10^4$	$(1.8 \pm 0.5) \times 10^5$	4×10^5
$\gamma_{\rm min}^{(*)}$	500	500	500	700
$\gamma_{\rm max}^{(*)}$	5×10^6	10^6	10^6	10^6
$\delta_{\rm D}^{(*)}$	18	25	18	40
B [G]	0.055 ±0.003	0.034 ±0.002	0.040 ±0.003	0.1
$R_{\rm b}^{(*)}$ [10^{15} cm]	4.5	6.2	4.5	0.7
χ^2/d.o.f	56.9/42	22.8/28	39.4/28	

Notes: (1) Model parameters, the ones marked with $^{(*)}$ are frozen during the fitting; (2) best-fit parameters obtained for the July 14^{th} 2020 high γ-ray state; (3) best-fit parameters obtained for the August 20^{th} 2022 low γ-ray-high optical state; (4) best-fit parameters obtained for the July 7^{th} 2022 low γ-ray-low optical state; (5) best fit parameters of the SSC model assumed to describe the 2016 flare by MAGIC Collaboration et al. (2020a).

assumed a SSC scenario in which a uniform synchrotron radiation field in the spherical blob of radius R_b collides with the same population of electrons emitting the synchrotron radiation at low frequencies. We adopted a variability timescale $t_{\rm var}$ to derive the upper limit to the size of the emitting region: $R_{\rm b} \leq c t_{\rm var} \delta_D/(1+z)$, with δ_D being the Doppler factor, and z the redshift of the source. We fix $t_{\rm var}$ at 1 day, as there is no hint of faster variability, and the VHE spectra are averaged over the observing night.

The Doppler factor $\delta_{\rm D}$ could be retrieved from VLBI observations. However, Weaver et al. (2022) found no proper motion of the jet component at 43 GHz during any period of the source monitoring using the VLBA data from the BEAM-ME program. The authors estimated roughly the Doppler factor by adopting assumptions on the jet opening angle. They estimated a Doppler factor of 30.3. In order to reduce the free parameters we fixed $\delta_{\rm D}$ to 18 for the high γ-ray and low γ-ray-low optical states. This was the value reported by Tagliaferri et al. (2008) for the 2006 low state of 1ES 1959+650 (described below). For the low γ-ray-high optical state we needed to increase the $\delta_{\rm D}$ to 25 for a finer representation of the observational data.

As described in Section 2.3.3, the electron energy distribution is expressed as a function of the Lorentz factor γ. We used the typical values for blazars, in particular for HBL, for $\gamma_{\rm min}$ and $\gamma_{\rm max}$. The break energy is determined by balancing synchrotron cooling and electron escape timescale. Assuming that the break in the electron spectrum is induced by radiative cooling, the second index of the broken power law, p2, should constrained as p2 = p1 + 1. These are derived by consideration of the equilibrium between the cooling and acceleration processes (see Nigro et al. 2022, for more details). To reproduce the spectral feature as accurately as possible, we assumed a broken power-law for the electron energy distribution leaving the p1 and p2 indexes as free parameters.

To summarize, the free parameters are the differential energy density normalization, k, the two spectral indexes of the broken power law, p1 and p2, $\gamma_{\rm b}$ and the magnetic field strength, B. By freezing both $t_{\rm var}$ and the Doppler factor δ_D we pre-determine also $R_{\rm b}$. We tested different combinations of the parameters described above, alternatively freezing each parameter. Due to the large number of parameters and the degeneracy between them, we obtained several combinations of parameters fulfilling the χ^2 test. We finally selected the best models based on the visual best agreement between the model and the data and by ensuring reasonable values for the parameters (in agreement with theoretical expectations on particle acceleration processes). The best-fit parameters are reported in Tab. 4.8.

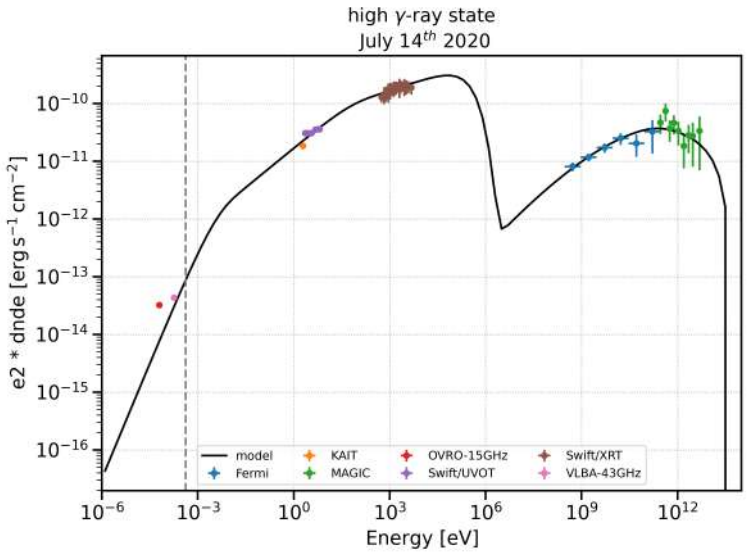

Figure 4.17: Broadband SED for the high γ-ray state (July 14*th* 2020) of 1ES 1959+650 during the 2020-2022 period. Data are taken almost simultaneously and include MAGIC, *Fermi*-LAT, *Swfit*-XRT, *Swfit*-UVOT, KAIT observations and radio data. The observational points are fitted with the one-zone SSC model described in the text and the best-fit parameters are reported in Tab. 4.8. The black solid line shows the model.

4.8.3 SED modelling results and discussion

The best-fit parameters obtained for the three states reveal some non-negligible variations over the analyzed three days, despite the system being in an overall quiescent state. In the subsequent discussion, we explore the main differences, comparing the models for the 2020-2022 days with the data from the 2016 flare and previous works on the source.

Elevated electron spectral break energy is required to reproduce the SED in EHBL. During the 2016 flare indeed the source was in a EHBL phase and spectral break energy was the highest recorded, at about 4×10^5 (MAGIC Collaboration et al. 2020a). In all three models of the 2020-2022 results, the break is located below 2×10^5.

During both the low γ-ray states of 2020-2022, the p1 and p2 spectral indexes are in agreement with the expected relation p2 = p1 + 1. This indicates the equilibrium between synchrotron losses and injection of accelerated particles is not violated. The possibility of a more complex particle injection function[13] can be suggested for the high γ-ray state, since, in this case, the expected relation is not satisfied. However, the disagreement can be due to our assumptions about the system. For example, it could be needed to account for the presence of multiple emitting zones or a non-uniform magnetic field in this case (e.g., Cerruti 2020). More sophisticated models introduce dynamic elements such as variable injection rates and the movement and expansion of the emission region within the jet (e.g., Graff et al. 2008). These improvements allow for a better representation of the observed flux variations in sources like Mrk 421 (MAGIC Collaboration et al. 2021).

The magnetic field density is the lowest in the 2020-2022 low γ-ray-high optical state, with a value of $B \sim 0.034$ G. The highest magnetic field strength ($B \sim 0.055$ G) is found during the high γ-ray state, which is, however, significantly lower than in the 2016 flare.

At the redshift of 1ES 1959+650 ($z = 0.047$) the conversion factor between linear and angular dimensions is 0.922 pc/mas. The resolving beam with which the 43 GHz VLBA data are imaged

[13]The particle injection between $\gamma_{\rm max}$ and $\gamma_{\rm min}$ is described by $Q(\gamma) = Q_0 \gamma^{(-q)}$, where γ represents the energy of the electrons and q is a spectral index.

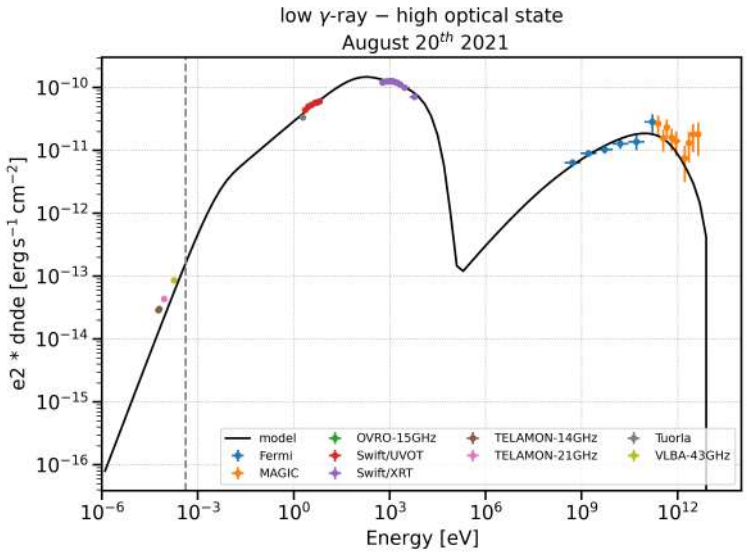

Figure 4.18: Broadband SED for the low γ-ray-high optical state day of 1ES 1959+650 during the 2020-2022 period. Data are taken almost simultaneously and include MAGIC, *Fermi*-LAT, *Swfit*-XRT, *Swfit*-UVOT, Tuorla observations and radio data. The observational points are fitted with the one-zone SSC model described in the text and the best-fit parameters are reported in Tab. 4.8. The black solid line shows the model.

is elliptical and has sizes of about 0.20 mas $\times$ 0.34 mas (Weaver et al. 2022). With such a spatial resolving power, the maximum resolvable size in pc is of the order of 0.2 pc. The emitting region is found to be $< 10^{16}$ cm (which means about 0.3 mpc). Therefore, the 43 GHz cannot resolve the emitting region and the exclusion of those data from the SED modelling is then justified.

Krawczynski et al. (2004) interpreted the 2002 orphan flare by assuming a SSC scenario with parameters that are closer to our high γ-ray state period than to the 2016 flare. In particular, they found $\delta_{\rm D} = 20$, $B = 0.04$ G and $R_{\rm b} = 5.8 \times 10^{15}$ cm. The SED modelling of data from a low state at VHE during 2006 (Tagliaferri et al. 2008) provided results similar to the ones found by us about the 2020-2022 period. During the 7 nights of MAGIC observations of this 2006 period, the VHE average flux was $(1.27 \pm 0.016) \times 10^{-11}$ photons cm^{-2}s^{-1} that is compatible within the errors with the VHE average flux of the 2020-2022 period ($(1.11 \pm 0.14) \times 10^{-11}$ photons cm^{-2}s^{-1}). In particular, assuming a one-zone SSC scenario, the 2006 SED parameters are $\delta_{\rm D} = 18$, $R_{\rm b} = 7.3 \times 10^{15}$ cm, $B = 0.25$ G, $\gamma_{\rm min} = 1$ and $\gamma_{\rm max} = 6 \times 10^5$, $\gamma_{\rm b} = 5.7 \times 10^4$, p1 = 2 and p2 = 3.4. The magnetic field strength deviates the most from our model while other parameters are somehow close to the 2006 period. Similar to the 2006 low state, our 2020-2022 SEDs show a synchrotron component dominating the IC one. In our modelling, we set the Doppler factor in the range from 18 in the high γ-ray and low γ-ray-low optical state to 25 during the low γ-ray-high optical state. Both these values are well below the Doppler factor required for the description of the 2016 flare, which was between 40 and 60, indicating this parameter may play a major role in the flaring activity of the source. A recent analysis of the 2016 flare of 1ES 1959+650 was conducted by Bégué et al. (2023) which utilized Convolutional Neural Networks for the SED modelling. They found results in agreement with what was found by MAGIC Collaboration et al. (2020a) reported in the last column of Tab. 4.8.

Despite the models aligning with expectations for HBLs and previous studies on 1ES 1959+650, ongoing refinement and deeper investigation of the parameters are still in progress. Indeed, the global picture emerging from the SED and the intra-band correlation analysis is not trivial. In the context of the SED analysis, the interpretation of the parameters is also challenged by the

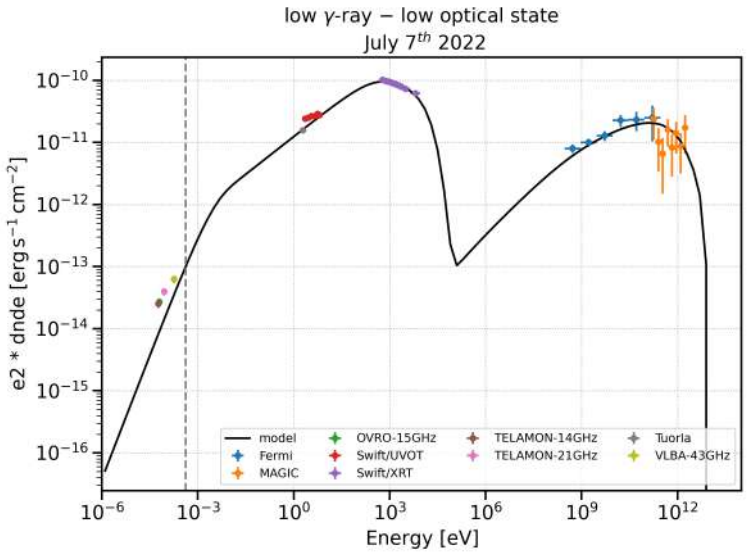

Figure 4.19: Broadband SED for the low γ-ray-low optical state of 1ES 1959+650 during the 2020-2022 period. Data are taken almost simultaneously and include MAGIC, *Fermi*-LAT, *Swfit*-XRT, *Swfit*-UVOT, Tuorla observations and radio data. The observational points are fitted with the one-zone SSC model described in the text and the best-fit parameters are reported in Tab. 4.8. The black solid line shows the model.

high degeneracy of the model's free parameters. At this stage of the work, we could provide a phenomenological description of the data while a physical interpretation requires further in-depth analysis. This will be a matter for the development of the work. Nevertheless, we found a set of parameters that well describe the data assuming a SSC scenario. We can estimate the synchrotron peak positions during the three states. These are at around 1.8×10^{19} Hz, 1.1×10^{17} Hz, 5.2×10^{16} during the high γ-ray state, low γ-ray-low optical state and low γ-ray-high optical state, respectively. By comparing the synchrotron peak positions with the VHE flux during the three states and the 13 June 2016 flare, we observe a trend in which the low energy peak moves to higher energies when the VHE flux increases (Fig. 4.21). In particular, if the SSC assumption presented in this work is accurate, we obtain a synchrotron peak value compatible with EHBL-like behaviour during the high γ-ray state as for the 2016 flare case.

4.9 Conclusion and future prospective

We have presented the MWL analysis of the HBL 1ES 1959+650 during the 2020-2022 period. The source was in a low state as the one reported in 2006 compared with past active periods, lasting from 2015 to 2019. For the 2020-2022 period, we collected data from various instruments, including MAGIC, *Fermi*-LAT, *Swift*-XRT, *Swift*-UVOT, and from blazar monitoring programs as Tuorla, OVRO, TELAMON, and BEAM-ME. It has to be noted that the datasets are not uniformly sampled in time with some light curves presenting significant time gaps. The primary objective of the project is to study the spectral features of the source during this very low state and how the SED changes depending on the flux state. We compared the results with the outburst detected in 2016.

Despite the low activity observed across all wavelengths during 2020-2022, we refrain from assuming that the source remained in a steady state throughout the entire period. Variability analysis revealed fluctuating fluxes and spectral parameters, especially in the VHE and X-ray bands.

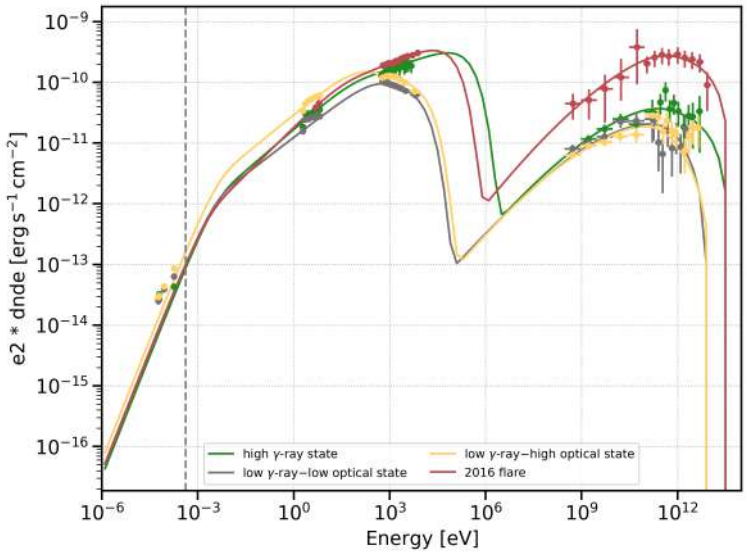

Figure 4.20: Broadband SEDs for the three days analyzed in this work and shown in Fig. 4.17, Fig. 4.19 and Fig. 4.18, compared with the 13^{th} June 2016 flare model adapted from MAGIC Collaboration et al. (2020a). This is indicated by the green solid line. The models for the high and low γ-ray-low optical state and the low γ-ray-high optical state are indicated in black, red, and grey, respectively.

The SED analysis focused on three representative states during this 2020-2022 low state. Days with the highest and lowest fluxes with maximum MWL coverage have been selected for the analysis. In particular, we identified a high γ-ray state day, a day of low γ-ray-low optical state, and three days with increased activity in the optical band referred to as low γ-ray-high optical state. A one-zone SSC model was applied, providing a reasonable representation of the observed SEDs with typical parameters of HBLs (e.g., Ahnen et al. 2016; Aleksić et al. 2013). However, the degeneracy of the model parameters allows us only to provide one of the possible phenomenological descriptions of the data. The pattern arising from intra-band correlation analysis, with the lack of relation between low-energy (UV and optical) and high-energy data, may suggest that a one-zone model oversimplifies the 1ES 1959+650 SEDs during the low state. Future plans involve adopting two-zone scenarios for a finer modelling. Moreover, a time-dependent approach would provide a more comprehensive view of the evolution of the model parameters giving more insights into the physical processes. Intraband cross-correlation study, employing Discrete Correlation Function (Edelson & Krolik 1988) analysis, could further provide information on the interplay between different bands and the presence of lags between active states.

Models accounting for the hadronic component in the 1ES 1959+650 jet, such as those proposed by Böttcher (2005), predict detectable neutrino fluxes. However, the SED modelling of the 2016 flare discards the possibility of a pure hadronic model due to the high magnetic field strength required, of about 150 G (MAGIC Collaboration et al. 2020a). The leptonic origin instead was the most plausible scenario in explaining the 1ES 1959+650 broadband SED during the 2016 flare. Due to the good agreement of the data with the SSC scenarios proposed for the 2020-2022 period, in this first analysis, we did not present the results for a hadronic origin of the high energy component. However, due to the hint of a connection between the AMANDA neutrino event and 1ES 1959+650 in 2002, hadronic and hybrid scenarios are still not ruled out. We are indeed testing these models for the 2020-2022 period and we will present the results in a dedicated paper.

The investigation of the broadband SED of this source over several years has drawn a complex

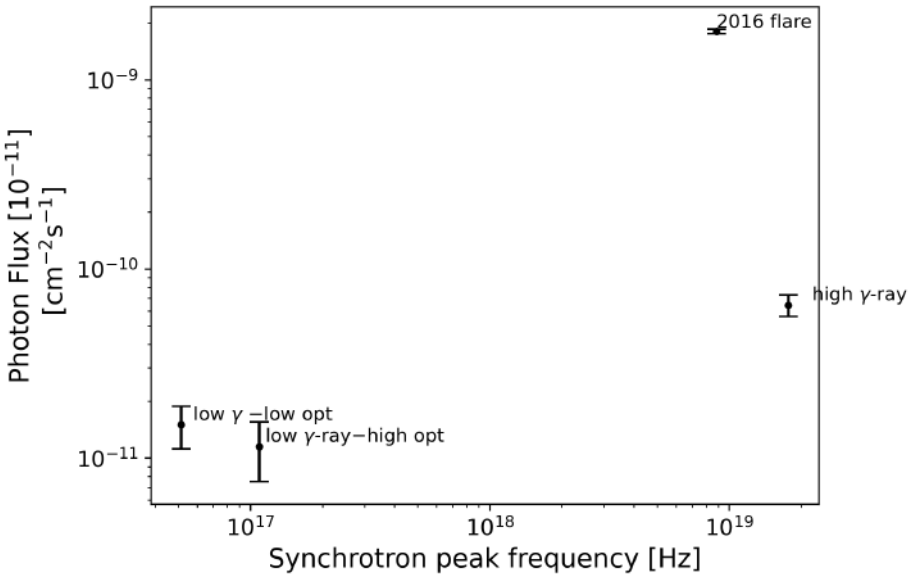

Figure 4.21: Synchrotron peak position from the SED models as a function of the MAGIC fluxes during the three days and the 2016 flare.

picture of the physical conditions during different phases, highlighting both its similarities with HBL sources and its rare features such as the intermittent EHBL nature and the orphan flare event. The prompt follow-up observations of MWL flares, such as the 2016 event, and their connection with EHBL phase, as well as peculiar occurrences like the VHE orphan flare in 2002, play a crucial role in determining recurring system conditions and ongoing processes. The MAGIC monitoring of 1ES 1959+650 is indeed still ongoing in coordination with other MWL facilities. Equally essential is the study of the source's low state, as presented in this work. Although more complex due to the low fluxes and statistics, understanding the source's behaviour during quiescent periods is the only way to get an unbiased view of the mechanisms at work. The improved sensitivity of the upcoming CTAO promises a groundbreaking advancement in characterizing blazar spectra in the VHE band also during these low states. This is particularly significant for HBLs and EHBLs, which emit the majority of their high-energy radiation in the TeV band despite exhibiting lower bolometric luminosity.

Part III

Conclusions

The physics of blazar jets

Jets ejected from the central regions of AGN play a crucial role in advancing our understanding of particle acceleration in cosmic environments, especially within the blazar subclass. Relativistic jets provide ideal conditions for accelerating particles to very high energies. In blazars, the alignment with the observer's line of sight enables a successful exploration of the interplay between particles and magnetic fields (refer to Chapter 2).

Throughout this thesis, we have investigated the substantial energy release from jets spanning the radio to the VHE band. Blazar emissions are predominantly non-thermal. The spectral energy distribution (SED) of blazars reveals a low-energy bump caused by synchrotron radiation from relativistic electrons spiralling along the jet's magnetic field lines and a high-energy bump, reaching up to TeV energy, produced through inverse Compton scattering of relativistic electrons off lower-frequency photons. Specifically, the SSC model asserts that the population of relativistic electrons, responsible for the first bump via the synchrotron mechanism, also contributes to the second one through inverse Compton scattering with the low-energy photon field. This theoretical framework attributes the entire non-thermal emission to the electron population within the jet.

On the other hand, hadronic models propose that the high-energy component of the blazar SED is produced by cosmic ray protons in the jet, either through proton synchrotron emission or by interacting with internal or external photon fields. These interactions also generate VHE neutrinos as byproducts. Theoretical studies predict that a fraction of astrophysical neutrinos may originate from blazars, but confirming this association observationally is challenging due to the low detection rate of neutrinos and the extensive error regions in which they are localized. It was only in 2017 that the gamma-ray blazar TXS 0506+056 was identified as a possible neutrino counterpart, providing support for the hadronic models. MWL observations were crucial to achieve this result (IceCube Collaboration et al. 2018a). Currently, this represents the only statistically significant association of a blazar with neutrino detection. Meanwhile, other classes of objects are proposed as possible neutrino emitters, with recent evidence also coming from the starburst galaxy NGC 1068 (IceCube Collaboration et al. 2022).

An additional distinctive feature of blazars is their variability. These sources frequently undergo episodes of enhanced activity during which their flux levels can double. These episodes can be observed over month timescales down to days or even hours and minutes, depending on the observed energy band and processes driving the change in the state. The interpretation of the flaring activity can be again attributed to the particle acceleration processes, during which part of the energy is released in the form of radiation.

The current state of knowledge regarding whether leptonic or hadronic mechanisms are at play in blazar jets remains uncertain, as does their connection with neutrino events. Observational insights, especially from studying blazars across the electromagnetic spectrum, are crucial in this context. The VLBI technique in the radio band allows for investigating the parsec-scale morphology of the jet, while MAGIC telescopes contribute with flux and spectral variability information in the VHE band. Both the energy bands and the respective facilities provide a close-up view of very compact regions within blazar jets. In the radio, VLBI allows for di-

rect imaging of parsec and sub-parsec regions, while in the VHE band, MAGIC observations constrain sizes by examining fast VHE variability. In the present project, we exploited VLBI observations and MAGIC (complemented with MWL) observations to investigate the blazar physics using different and complementary tools. The Thesis is indeed presented in two parts.

Neutrino-blazar connection study with VLBI

As mentioned before, in the hadronic framework, the presence of high-energy cosmic ray protons and an intense photon field in the parsec-scale regions of blazar jets leads to the production of neutrinos. In these sites, observable features that can be linked with particle acceleration processes are indeed observed with the high resolution achievable with VLBI. For example, limb brightening in blazar jets can be explained by the presence of velocity structures. The interplay between layers moving at different velocities leads to efficient particle acceleration (Tavecchio et al. 2014). Limb brightening has then been proposed as a possible indicator of efficient particle acceleration (Giroletti et al. 2004). Interestingly such a signature was observed at the parsec-scale site of TXS 0506+056 after the neutrino detection in 2017 (Ros et al. 2020). VLBI studies also allow us to infer important parameters to characterize the emission and particle acceleration mechanisms in TXS 0506+056 jet. In particular, among various parameters, Li et al. (2020) measured the Doppler factor increasing from an average value of almost 3 during a quiescent state up to about 10 during the high state recorded in 2017, and magnetic field decreasing from 0.43 G during the quiescent state to 0.23 G during the high state, estimated with the core-shift method, or from 0.69 G to 0.57 G, applying the variability estimation. They also identified a jet helical structure which is commonly attributed to the arising of instabilities that, in turn, lead to particle acceleration. Apart from TXS 0506+056 and population studies on VLBI blazar samples (Plavin et al. 2020; Plavin et al. 2021; Plavin et al. 2023), no additional observational proof for the connection between radio features in blazars and neutrino detection still exists.

The goal of this part of the project is then to build a radio-VLBI collection of candidate neutrino-emitting blazars in which the features described above and the overall radio characteristics are investigated. By exploiting the high angular resolution of VLBI observations we followed the evolution over several months of potential radio counterparts of four neutrino events detected between 2019 and 2020. The relevance of the new observations that we provided is in the temporal vicinity of the neutrino events and in the high sensitivity due to the long observing times. These characteristics are not guaranteed by archival observations. In particular, we carried out multi-frequency and multi-epoch follow-up observations, with the first epoch carried out soon after the IceCube Collaboration circulated a neutrino detection with $> 30\%$ probability of astrophysical origin. We dedicated the observations to blazar-like sources in the neutrino localization areas. We observed ten radio sources, eight of which are associated with gamma-ray counterparts. To collect the data, eight trigger proposals were approved by VLBA, EVN, e-MERLIN, KaVA (KVN plus VERA network).

We analyzed the VLBI characteristics of the ten radio sources shortly after the neutrino arrival, comparing them with archival VLBI observations and low-frequency radio surveys data. Five out of the ten potential neutrino-emitting blazars have been investigated in more detail because of their similarities with TXS 0506+056. Among these, we studied a high redshift BL Lac object, 1WHSP J104516.2+275133, located at $z = 1.914$, which was never observed with the VLBI angular resolution before. The other best candidates are two FSRQ and a blazar candidate and an X-ray source according to the NED and 4FGL classification. We measured radio luminosities between 10^{25} and 10^{26} W/Hz at frequencies from 1.5 and 5 GHz and flat or inverted radio spectral indices, ranging between -0.02 and 0.2, in the 1.5 – 23 GHz frequency range (Nanci et al. 2022). Spectral and morphological properties and large-scale characteristics

are presented in detail in Chapter 2. We discussed our findings in comparison with previous statistical works and studies on the case of TXS 0506+056. Our results suggest an enhanced state of activity for two out of the five sources, i.e., PKS 1725+123 and TXS 1100+122 (Fig. 1) for which we measured a variability index (Aller et al. (1992), Eq. 2.3) of the order or above 0.1, as found in TXS 0506+056. The high state in TXS 0506+056 was indicated as connected to an energetic particle injection responsible for neutrino production. We then propose PKS 1725+123 and TXS 1100+122 as favourable candidate neutrino emitters.

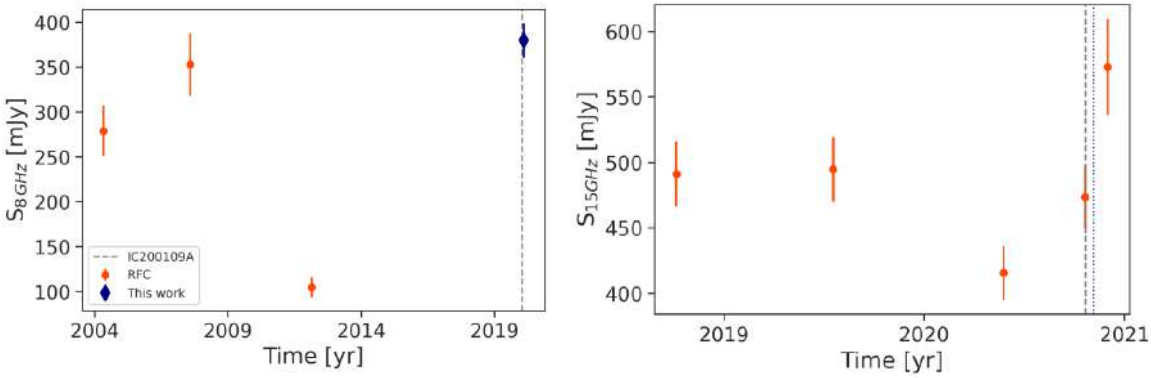

Figure 1: VLBI total flux density as functions of time of TXS 1100+122 (left) and of PKS 1725+123 (right). On the left panel, the red points represent total flux density data at 8 GHz for TXS 1100+122 from the RFC, while the blue point corresponds to the flux density obtained from our VLBA observation. The grey dashed line indicates the arrival time of the neutrino event. The left panel displays data from the MOJAVE monitoring of PKS 1725+123, with the neutrino arrival time marked by the grey dashed line. The blue dotted line marks the date of our e-MERLIN observation at 5 GHz. More details on the sources are in Chapter 2.

The lack of adequate monitoring before the neutrino events posed a limitation in tracing radio activity and morphological changes in the sources. Indeed, for other sources than PKS 1725+123 and TXS 1100+100, these first results alone do not suggest a connection between the radio activity state at the time of neutrino arrival. The work presented in this Thesis and published in Nanci et al. (2022) will be followed by the analysis of the ongoing monitoring of the sources presented here, focusing on the subsequent epochs of VLBI observation.

The research for a statistically significantly associations of neutrinos with astrophysical sources is often penalised by a large number of trial factors, and it would be important to have a limited number of source positions tested based on their potential association with neutrino events. Therefore, we suggest performing a dedicated analysis of neutrino data testing detections at the position of candidates as PKS 1725+123 and TXS 1100+122 for which the connection with the neutrino production is supported by some observational indications as in our VLBI analysis. In an optimistic scenario, this could lead to findings similar to the 2014–2015 neutrino excess from the direction of TXS 0506+056.

Given the relatively recent emergence of research focusing on observational constraints for the connection between astrophysical sources and neutrinos, it remains imperative to conduct a greater number of VLBI and MWL follow-up observations of neutrino events. Expanding the sample of the four follow-up observations of neutrino events analysed here is fundamental. From 2021 up to now, we dedicated follow-up observations to a total of seven new neutrino events, resulting in a collection of multi-frequency and multi-epoch VLBI observations of eight good candidate counterparts and a few other sources within the neutrino error areas. As for the first collection, the promising candidates show a blazar-like nature and have been found in MWL high state. Our ongoing analysis of these rich and diverse datasets aims to draw

statistically significant conclusions regarding the radio-VLBI properties of candidate neutrino sources. Moreover, this collection has the potential to become a database of images for future systematic studies on candidate neutrino sources. Padovani et al. (2022a) proposes the class of *masquerading* BL Lac as neutrino emitters. In this context, differences in the parsec-scale properties of masquerading and non-masquerading objects in relation to the neutrino production mechanism could be revealed by the sample that we will provide.

The HBL 1ES 1959+650

Among the first sources considered for a hadronic interpretation, the blazar 1ES 1959+650 stands out due to the observation of an orphan flare, presenting a challenge to the SSC interpretation. The source was indeed initially identified as a potential neutrino emitter (Halzen & Hooper 2005). In parallel to the VLBI investigation of a sample of blazars as possible neutrino counterparts, the focus of the project was centred on the exploration of emission mechanisms in this specific target by adopting a MWL approach. Characterizing blazars through MWL observations is pivotal in determining whether leptonic, hadronic, or hybrid lepto-hadronic mechanisms are at play and extracting key parameters driving the system. Flux and spectral variability are fundamental observables providing insights into the radiation mechanisms. Therefore, long-term monitoring of blazars can lead to a comprehensive understanding of the production and emission mechanisms around supermassive black holes.

Ongoing MWL monitoring of 1ES 1959+650, coordinated by the MAGIC Collaboration, spans from 2015 to 2022, with results already emerging from the 2015-2019 dataset (The MAGIC Collaboration et al. 2022). In the present project, the MAGIC and MWL data covering the 2020-2022 monitoring period have been presented. The MAGIC dataset encompasses data taken during both standard and non-standard observations. Non-standard data, i.e., taken under moon conditions, require additional data reduction procedures, starting from raw data (see Section 2.3.11 and the data analysis of 1ES 1959+650 in Section 4.2.1). The combined analysis of MAGIC observations at VHE with lower frequency data (X-ray, UV, optical and radio) serves for flux variability and spectral studies.

The correlation between low-energy and high-energy emissions is expected when the same population of electrons is responsible for both synchrotron and inverse Compton radiation as predicted in the SSC model. We tested the presence of such correlations finding hints of correspondence between VHE and X-ray fluxes, suggesting that a one-zone SSC model could be adopted. During the 2020-2022 period, the source is found in one of its lowest states ever reached in the VHE band, with a flux level of the order of 10% the Crab flux. No outstanding flares at VHE and other wavelengths have been recognized in the light curves simultaneously. However, a statistically significant variability both at VHE and at the X-rays has been revealed. Based on this result, to investigate the spectral changes of the sources during different stages, we focused the SED study for three different days taken as representative of different activity states. In particular, we identified two days for the lowest and the highest state for which we have maximum MWL coverage, along with a day when the source exhibited notable activity in the optical band while in low state at VHE. Also for the latter, we ensured the maximum MWL coverage.

The modelling of the 1ES 1959+650 broadband SED was conducted with the `agnpy` software (Nigro et al. 2022) which employs a fitting approach to the observed SED, determining model parameters through a χ^2 statistic. The best-fit parameters for the three days are in the range of typical values found for this class of objects (see Section 4.8.3 and Section 4.8.2). Smooth variations in the parameters are found between the different states considered. Among these, for the magnetic field density, the highest value is retrieved during the high state (around 0.055 G),

while during the low states, it ranges between 0.034 and 0.040 G. The electron energy distribution also slightly changes over time, both in slopes and in the γ_b, indicating the equilibrium between particle injection and synchrotron losses varies over time. Most of the parameters agree with previous studies on this source during quiescent states (such as 2006 Tagliaferri et al. (2008)), supporting the idea that the SSC model serves as a robust approximation for the emission mechanism of 1ES 1959+650 during low states.

We compared our results with the outburst observed in 2016. We observe a shift to the high energy of the two peaks of the SED during the flaring state. The synchrotron peak moves to higher energies in the case of our 2020-2022 high state as well, despite the VHE flux level being significantly lower than in 2016. This intermittent EHBL nature has been observed in other few HBLs as 1ES 2344+514 and Mrk 501 (Abe et al. 2023a; Ahnen et al. 2018, respectively) indicating common conditions in these sources. The general features of the SED during the 2016 flare are also satisfactorily described with a one-zone SSC model but with parameters different from the ones describing the 2020-2022 period. In particular, during the flare, the Doppler factor (about 40) and magnetic field strength ($\sim$ 0.1 G) result to be larger compared with the 2020-2022 low state. The parameters retrieved for the 2016 flare in 1ES 1959+650 can suggest that the activity is due to the presence of injected electrons accelerated by larger magnetic fields or a change in the configuration of the jet. MWL data catching future active states in 1ES 1959+650 would be crucial to further constrain the differences in the system during flares. This is one of the drivers of the ongoing MWL monitoring of the source. Although the one-zone SSC model can explain the observed data, the variability pattern observed in different high energy and low energy bands is not fully in agreement with the SSC interpretation. The lack of correlations between most of the low-energy and high-energy bands indicates the possibility of the presence of two emitting zones or more complex conditions. Future development of this work will be based on testing different scenarios such as a multi-zone SSC and hadronic models.

Final remarks

Both radio and VHE bands will undergo transformational changes in the near future. Major efforts from the international science and technology communities are ongoing, and the deployment of the first elements of both the SKAO, with its precursor Meerkat, and the CTAO, with LST-I installed and operative (currently in the commissioning phase) in La Palma. The SKAO in radio and the CTAO at VHE will lead observational capabilities to unprecedented levels in the two energy bands, boosting sensitivity, angular resolution, spectral resolution and so on. Beyond their scientific impact, these ambitious projects also entail substantial efforts in managerial, technological, and, in particular, computational domains. Recognizing the multiform importance of this historical moment, it becomes imperative to adopt a comprehensive approach to addressing the challenges and opportunities that SKAO, particularly its long-baseline component, and CTAO will bring.

The scientific rationale driving these projects spans a diverse range of research fields, promising revolutionary breakthroughs. In particular, with the remarkable results achieved in recent years, the field of MM astronomy field is significantly gaining importance and extending its influence across various branches of astrophysics. Consequently, the synergies between the upcoming generation of radio and VHE observatories, along with complementary state-of-the-art facilities such as KM3NeT, will be crucially important for investigating phenomena accessible through different messengers. In preparation for the pivotal moment in which the observatories will be fully operative, meticulous planning and strategic considerations are essential to exploit their observational capabilities to the fullest. At this stage, it is important to not only seek answers to scientific questions employing current facilities but also to clearly define the open

questions and topics of interest that will guide our exploration of the cosmos. The present PhD project aims to contribute to this, rather than with the scientific results, by testing existing tools for characterizing relativistic jets through radio and gamma-ray studies and refining the MWL approach using current telescopes.

Acknowledgements

The MAGIC and part of the *Swift*-XRT data analysis, along with the scientific analyses (variability study, intra-band correlation analysis and SED modelling) in the 1ES 1959+650 work have been carried out by the author of the Thesis. Additionally, all the radio data analysis, from calibration to scientific interpretation presented in Chapter 2, was undertaken by the author under the guidance and with the assistance of collaborators listed in the next section.

Acknowledgements for *Blazars at high angular resolution*

The work was done in collaboration with Marcello Giroletti, Monica Orienti, Giulia Migliori, Javier Moldon, Simone Garrappa, Matthias Kadler, Eduardo Ros, Sara Buson, Tao An, Miguel Perez-Torres, Filippo D'Ammando, Prashanth Mohan, Ivan Agudo, Bong W. Sohn, Alberto J. Castro-Tirado, and Yingkang Zhang.

JM and MPT acknowledge financial support from the State Agency for Research of the Spanish MCIU through the "Center of Excellence Severo Ochoa" award to the Instituto de Astrofísica de Andalucía (SEV-2017-0709) and through grants RTI2018-096228-B-C31 and PID2020-117404GB-C21 (MICIU/FEDER, EU). SB acknowledges financial support by the European Research Council for the ERC Starting grant *MessMapp*, under contract no. 949555. BWS is grateful for the support by the National Research Foundation of Korea (NRF) funded by the Ministry of Science and ICT (MSIT) of Korea (NRF-2020K1A3A1A78114060). We thank to L. Petrov for granting permission to use data from the Astrogeo VLBI FITS image database. The European VLBI Network is a joint facility of independent European, African, Asian, and North American radio astronomy institutes. Scientific results from data presented in this publication are derived from the following EVN project codes: RG011, EG108. The National Radio Astronomy Observatory is a facility of the National Science Foundation operated under cooperative agreement by Associated Universities, Inc. This work made use of the Swinburne University of Technology software correlator, developed as part of the Australian Major National Research Facilities Programme and operated under licence. e-MERLIN is a National Facility operated by the University of Manchester at Jodrell Bank Observatory on behalf of STFC. This research has made use of data from the MOJAVE database that is maintained by the MOJAVE team (Lister et al. 2018). This research has made use of the CIRADA cutout service at URL cutouts.cirada.ca, operated by the Canadian Initiative for Radio Astronomy Data Analysis (CIRADA). CIRADA is funded by a grant from the Canada Foundation for Innovation 2017 Innovation Fund (Project 35999), as well as by the Provinces of Ontario, British Columbia, Alberta, Manitoba and Quebec, in collaboration with the National Research Council of Canada, the US National Radio Astronomy Observatory and Australia's Commonwealth Scientific and Industrial Research Organisation. This research has made use of the NASA/IPAC Extragalactic Database (NED), which is operated by the Jet Propulsion Laboratory, California Institute of Technology, under contract with the National Aeronautics and Space Administration.

Acknowledgements for *Blazar at very high energy*

A MAGIC data analysis for cross-checking was performed by Cosimo Nigro from the Institut de Física d'Altes Energies (IFAE, Barcelona, Spain) and Cornelia Arcaro from the Dipartimento di Fisica e Astronomia dell'Università and Sezione INFN (Padova, Italy). The MWL data reduction has been conducted by MAGIC members involved in the project. In particular, the *Fermi*-LAT data analysis was performed by Axel Arbet-Engels from the Max-Planck-Institut für Physik (München, Germany); the *Swift*-UVOT data analysis by Mireia Nievas Rosillo from the Instituto de Astrofisica de Canarias (La Laguna, Tenerife, Spain); and the Tuorla, OVRO and TELAMON data have been provided by the respective collaborations. Filippo D'Ammando from the Dipartimento di Fisica e Astronomia dell'Università and Sezione INFN (Padova, Italy) carried out the XMM-*Newton* data analysis and helped in the *Swift*-XRT data analysis. Suggestions by Ettore Bronzini from the Astrophysics and Space Science Observatory of Bologna (INAF-OAS, Bologna, Italy) were extremely helpful for this work, particularly in the *Swift*-XRT data analysis and statistical analysis. Special thanks for assistance in part of the thesis writing are extended to Xavier Rodrigues from the European Southern Observatory, Garching bei München. Without any obligation, solely out of willingness to help, he kindly reviewed a portion of the thesis, providing valuable suggestions for its improvement.

The MAGIC Collaboration is acknowledged for allowing the use of proprietary observational data. MAGIC results presented in this thesis have not undergone the internal review procedure of MAGIC publications.

Acronyms

***e*-MERLIN** enhanced Multi-Element Radio Linked Interferometer Network.

3FHL The Third Catalog of Hard *Fermi*-LAT Sources.

4FGL *Fermi*-LAT Fourth Source Catalogue.

ACD Anti coincidence detector.

ADC Analog-to-Digital Converter.

AGILE Astrorivelatore Gamma ad Immagini LEggero.

AGN Active Galactic Nuclei.

AIPS Astronomical Image Processing System.

AMANDA Antarctic Muon And Neutrino Detector Array.

AMC Active Mirror Control.

ANTARES Astronomy with a Neutrino Telescope and Abyss environmental RESearch project.

ASTRI Astrofisica con Specchi a Tecnologia Replicante Italiana.

ATel Astronomer's Telegram.

BB Bayesian Blocks.

BEAM-ME Blazars Entering the Astrophysical Multi-Messenger Era.

BLR Broad Line Region.

CASA Common Astronomy Software Applications.

CGRO Compton Gamma Ray Observatory.

CH Counting House.

CIRADA Canadian Initiative for Radio Astronomy Data Analysis.

CMB Cosmic Microwave Background.

CoG Center of Gravity.

CORSIKA COsmic Ray SImulations for Kascade.

CTA Cherenkov Telescope Array.

CTAO Cherenkov Telescope Array Observatory.

CU Crab Units.

DAQ Data AcQuisition System.

DC Direct Current.

DESY Deutsches Elektronen-Synchrotron.

DL0 Data level 0.

DL1 Data level 1.

DL2 Data level 2.

DL3 Data level 3.

DR2 Data Release 2.

DT Discriminator Threshold.

EAS Extensive Air Shower.

EAVN East Asia VLBI Network.

EBL Extragalactic Background Light.

EGRET Energetic Gamma Ray Experiment Telescope.

EHBL Extreme-High-Frequency Peaked BL Lac.

EHE Extreme High Energy.

EHSP Extreme-High-Frequency Synchrotron Peaked.

ESO European Southern Observatory.

EVN European VLBI network.

EW Equivalent Width.

FIRST Faint Images of the Radio Sky at Twenty-cm.

FITS-IDI Flexible Image Transport System - Interferometry Data Interchange.

FoV field of view.

FR Fanaroff-Riley.

FSRQ Flat Spectrum Radio Quasar.

FWHM full width half maximum.

GCN GRB Coordinates Network.

GMVA Global millimeter VLBI array.

GPS Global Positioning System.

GRB Gamma-Ray Burst.

GVD Gigaton Volume Detector.

HAWC High-Altitude Water Cherenkov Observatory.

HBL High-Frequency Peaked BL Lac.

HE High Energy.

HEGRA High Energy Gamma Ray Astronomy.

HESS High Energy Stereoscopic System.

HSP High-Frequency Synchrotron Peaked.

HST Hubble Space Telescope.

HV High Voltage.

IACT Imaging Atmospheric Cherenkov Telescope.

IC Inverse Compton.

IF intermediate frequency.

IGMF Inter Galactic Magnetic Field.

IPC Einstein Imaging Proportional Counter.

IRAM Institut de radioastronomie millimétrique.

IRF instrument response function.

ISP Intermediate-Frequency Peaked BL Lac.

ISP Intermediate-Frequency Synchrotron Peaked.

JVLA Jansky Very Large Array.

KAGRA Kamioka Gravitational Wave Detector.

KAIT Katzman Automatic Imaging Telescope.

KAT Karoo Array Telescope.

KM3NeT Cubic Kilometre Neutrino Telescope.

KVN Korean VLBI Network.

L0 Level-0.

L1 Level-1.

L3 Level-3.

LAT Large Area Telescope.

LBA Long Baseline Array.

LCR Light Curve Repository.

LHAASO Large High Altitude Air Shower Observatory.

LIDAR Light Detection and Ranging.

LIGO Laser Interferometer Gravitational-Wave Observatory.

LISA Laser Interferometer Space Antenna.

LIV Lorentz Invariance Violation.

LOFAR Low Frequency Array.

LRT Likelihood Ratio Test.

LSP Low-Frequency Peaked BL Lac.

LSP Low-Frequency Synchrotron Peaked.

LST Large-Sized Telescope.

LUTs Look-Up Tables.

MAGIC Major Atmospheric Gamma-ray Imaging Cherenkov.

MARS MAGIC Analysis and Reconstruction Software.

MC Monte Carlo.

MM multi-messenger.

MOJAVE Monitoring Of Jets in Active Galactic Nuclei with VLBA Experiments.

MS Measurement Set.

MST Medium-Sized Telescope.

MWL multi-wavelength.

NED NASA/IPAC Extragalactic Database.

NEMO Neutrino Ettore Majorana Observatory.

NESTOR Neutrino Extended Submarine Telescope with Oceanographic Research.

NLR Narrow Line Regions.

NN Next-Neighbour.

NRAO National Radio Astronomy Observatory.

NSB Night Sky Background.

NVSS NRAO VLA Sky Survey.

OVRO Owens Valley Radio Observatory.

PA position angle.

phe photoelectron.

PMT Photomultiplier Tube.

PSF point spread function.

QE Quantum Efficiency.

RF Random Forest.

RFC Radio Fundamental Catalogue.

RFI Radio Frequency Interference.

RMS root mean square.

SED spectral energy distribution.

SKAO Square Kilometre Array Observatory.

SSC synchrotron-self Compton.

SST Small-Sized Telescope.

SWGO Southern Wide-field Gamma-ray Observatory.

TDE tidal disruption event.

TELAMON TeV Effelsberg Long-term Agn MONitoring.

UHE Ultra High Energy.

UHECRs Ultra High Energy Cosmic Rays.

UVOT Ultraviolet Optical Telescope.

VCS VLBA Calibrator Survey.

VERA VLBI Exploration of Radio Astrometry.

VERITAS Very Energetic Radiation Imaging Telescope Array System.

VHE Very High Energy.

VLA Very Large Array.

VLASS VLA Sky Survey.

VLBA Very Long Baseline Array.

VLBI very long baseline interferometry.

WT Windowed Timing.

XRT X-Ray Telescope.

Bibliography

Aartsen, M. G. et al. (July 2013). "First Observation of PeV-Energy Neutrinos with IceCube". In: *Phys. Rev. Lett.* 111.2, 021103, p. 021103. DOI: 10.1103/PhysRevLett.111.021103. arXiv: 1304.5356 [astro-ph.HE].

Aartsen, M. G. et al. (Jan. 2017). "The Contribution of Fermi-2LAC Blazars to Diffuse TeV-PeV Neutrino Flux". In: *The Astrophysical Journal* 835.1, 45, p. 45. DOI: 10.3847/1538-4357/835/1/45. arXiv: 1611.03874 [astro-ph.HE].

Aartsen, M. G. et al. (Feb. 2020). "Time-Integrated Neutrino Source Searches with 10 Years of IceCube Data". In: *Phys. Rev. Lett.* 124.5, 051103, p. 051103. DOI: 10.1103/PhysRevLett.124.051103. arXiv: 1910.08488 [astro-ph.HE].

Abbasi, R. et al. (Oct. 2021). "Search for Multi-flare Neutrino Emissions in 10 yr of IceCube Data from a Catalog of Sources". In: *The Astrophysical Journal Letters* 920.2, L45, p. L45. DOI: 10.3847/2041-8213/ac2c7b. arXiv: 2109.05818 [astro-ph.HE].

Abbasi, R. et al. (Nov. 2023). "IceCat-1: The IceCube Event Catalog of Alert Tracks". In: *Astrophysical Journal, Supplement* 269.1, 25, p. 25. DOI: 10.3847/1538-4365/acfa95. arXiv: 2304.01174 [astro-ph.HE].

Abbott, B. P. et al. (June 2016a). "GW151226: Observation of Gravitational Waves from a 22-Solar-Mass Binary Black Hole Coalescence". In: *Phys. Rev. Lett.* 116.24, 241103, p. 241103. DOI: 10.1103/PhysRevLett.116.241103. arXiv: 1606.04855 [gr-qc].

Abbott, B. P. et al. (Feb. 2016b). "Observation of Gravitational Waves from a Binary Black Hole Merger". In: *Phys. Rev. Lett.* 116.6, 061102, p. 061102. DOI: 10.1103/PhysRevLett.116.061102. arXiv: 1602.03837 [gr-qc].

Abbott, B. P. et al. (Oct. 2017a). "Gravitational Waves and Gamma-Rays from a Binary Neutron Star Merger: GW170817 and GRB 170817A". In: *The Astrophysical Journal Letters* 848.2, L13, p. L13. DOI: 10.3847/2041-8213/aa920c. arXiv: 1710.05834 [astro-ph.HE].

Abbott, B. P. et al. (Oct. 2017b). "GW170814: A Three-Detector Observation of Gravitational Waves from a Binary Black Hole Coalescence". In: *Phys. Rev. Lett.* 119.14, 141101, p. 141101. DOI: 10.1103/PhysRevLett.119.141101. arXiv: 1709.09660 [gr-qc].

Abbott, B. P. et al. (Oct. 2017c). "GW170817: Observation of Gravitational Waves from a Binary Neutron Star Inspiral". In: *Phys. Rev. Lett.* 119.16, 161101, p. 161101. DOI: 10.1103/PhysRevLett.119.161101. arXiv: 1710.05832 [gr-qc].

Abdollahi, S. et al. (Mar. 2020). "Fermi Large Area Telescope Fourth Source Catalog". In: *Astrophysical Journal, Supplement* 247.1, 33, p. 33. DOI: 10.3847/1538-4365/ab6bcb. arXiv: 1902.10045 [astro-ph.HE].

Abdollahi, S. et al. (Apr. 2023). "The Fermi-LAT Lightcurve Repository". In: *Astrophysical Journal, Supplement* 265.2, 31, p. 31. DOI: 10.3847/1538-4365/acbb6a. arXiv: 2301.01607 [astro-ph.HE].

Abe, H. et al. (Oct. 2023a). "Multi-year characterisation of the broad-band emission from the intermittent extreme BL Lac 1ES˜2344+514". In: *arXiv e-prints*, arXiv:2310.03922, arXiv:2310.03922. DOI: 10.48550/arXiv.2310.03922. arXiv: 2310.03922 [astro-ph.HE].

Abe, H. et al. (Oct. 2023b). "Observations of the Crab Nebula and Pulsar with the Large-sized Telescope Prototype of the Cherenkov Telescope Array". In: *The Astrophysical Journal* 956.2, 80, p. 80. DOI: 10.3847/1538-4357/ace89d. arXiv: 2306.12960 [astro-ph.HE].

Abeysekara, A. U. et al. (Jan. 2017). "A Search for Spectral Hysteresis and Energy-dependent Time Lags from X-Ray and TeV Gamma-Ray Observations of Mrk 421". In: *The Astrophysical Journal* 834.1, 2, p. 2. DOI: 10.3847/1538-4357/834/1/2. arXiv: 1611.04626 [astro-ph.HE].

Acciari, V. A. et al. (Mar. 2022). "Investigating the Blazar TXS 0506+056 through Sharp Multiwavelength Eyes During 2017-2019". In: *The Astrophysical Journal* 927.2, 197, p. 197. DOI: 10.3847/1538-4357/ac531d. arXiv: 2202.02600 [astro-ph.HE].

Acero, F. et al. (June 2015). "Fermi Large Area Telescope Third Source Catalog". In: *Astrophysical Journal, Supplement* 218.2, 23, p. 23. DOI: 10.1088/0067-0049/218/2/23. arXiv: 1501.02003 [astro-ph.HE].

Ackermann, M. et al. (Nov. 2012). "The Fermi Large Area Telescope on Orbit: Event Classification, Instrument Response Functions, and Calibration". In: *Astrophysical Journal, Supplement* 203.1, 4, p. 4. DOI: 10.1088/0067-0049/203/1/4. arXiv: 1206.1896 [astro-ph.IM].

Ackermann, M. et al. (Sept. 2015). "The Third Catalog of Active Galactic Nuclei Detected by the Fermi Large Area Telescope". In: *The Astrophysical Journal* 810.1, 14, p. 14. DOI: 10.1088/0004-637X/810/1/14. arXiv: 1501.06054 [astro-ph.HE].

Agudo, I. et al. (Apr. 2015). "Studies of Relativistic Jets in Active Galactic Nuclei with SKA". In: *Advancing Astrophysics with the Square Kilometre Array (AASKA14)*, 93, p. 93. DOI: 10.22323/1.215.0093. arXiv: 1501.00420 [astro-ph.GA].

Aharonian, F. et al. (July 2003). "Detection of TeV gamma-rays from the BL Lac 1ES 1959+650 in its low states and during a major outburst in 2002". In: *Astronomy and Astrophysics* 406, pp. L9–L13. DOI: 10.1051/0004-6361:20030838.

Aharonian, F. et al. (Aug. 2007). "An Exceptional Very High Energy Gamma-Ray Flare of PKS 2155-304". In: *The Astrophysical Journal Letters* 664.2, pp. L71–L74. DOI: 10.1086/520635. arXiv: 0706.0797 [astro-ph].

Aharonian, F. A. (Nov. 2000). "TeV gamma rays from BL Lac objects due to synchrotron radiation of extremely high energy protons". In: *New Astronomy* 5.7, pp. 377–395. DOI: 10.1016/S1384-1076(00)00039-7. arXiv: astro-ph/0003159 [astro-ph].

Ahlers, M. & K. Murase (July 2014). "Probing the Galactic origin of the IceCube excess with gamma rays". In: *Phys. Rev. D* 90.2, 023010, p. 023010. DOI: 10.1103/PhysRevD.90.023010. arXiv: 1309.4077 [astro-ph.HE].

Ahnen, M. L. et al. (July 2016). "Multiwavelength observations of the blazar 1ES 1011+496 in Spring 2008". In: *Monthly Notices of the Royal Astronomical Society* 459.3, pp. 2286–2298. DOI: 10.1093/mnras/stw710. arXiv: 1603.07308 [astro-ph.HE].

Ahnen, M. L. et al. (Sept. 2017). "Performance of the MAGIC telescopes under moonlight". In: *Astroparticle Physics* 94, pp. 29–41. DOI: 10.1016/j.astropartphys.2017.08.001. arXiv: 1704.00906 [astro-ph.IM].

Ahnen, M. L. et al. (Dec. 2018). "Extreme HBL behavior of Markarian 501 during 2012". In: *Astronomy and Astrophysics* 620, A181, A181. DOI: 10.1051/0004-6361/201833704. arXiv: 1808.04300 [astro-ph.HE].

Ajello, M. et al. (Oct. 2017). "3FHL: The Third Catalog of Hard Fermi-LAT Sources". In: *Astrophysical Journal, Supplement* 232.2, 18, p. 18. DOI: 10.3847/1538-4365/aa8221. arXiv: 1702.00664 [astro-ph.HE].

Alam, S. et al. (July 2015). "The Eleventh and Twelfth Data Releases of the Sloan Digital Sky Survey: Final Data from SDSS-III". In: *Astrophysical Journal, Supplement* 219.1, 12, p. 12. DOI: 10.1088/0067-0049/219/1/12. arXiv: 1501.00963 [astro-ph.IM].

Albert, J. et al. (Mar. 2006). "Observation of Very High Energy Gamma-Ray Emission from the Active Galactic Nucleus 1ES 1959+650 Using the MAGIC Telescope". In: *The Astrophysical Journal* 639.2, pp. 761–765. DOI: 10.1086/499421. arXiv: astro-ph/0508543 [astro-ph].

Albert, J. et al. (Nov. 2007). "Variable Very High Energy γ-Ray Emission from Markarian 501". In: *The Astrophysical Journal* 669.2, pp. 862–883. DOI: 10.1086/521382. arXiv: astro-ph/0702008 [astro-ph].

Albert, J. et al. (Apr. 2008). "Implementation of the Random Forest method for the Imaging Atmospheric Cherenkov Telescope MAGIC". In: *Nuclear Instruments and Methods in Physics Research A* 588.3, pp. 424–432. DOI: 10.1016/j.nima.2007.11.068. arXiv: 0709.3719 [astro-ph].

Aleksić, J. et al. (Feb. 2012). "Performance of the MAGIC stereo system obtained with Crab Nebula data". In: *Astroparticle Physics* 35.7, pp. 435–448. DOI: 10.1016/j.astropartphys.2011.11.007. arXiv: 1108.1477 [astro-ph.IM].

Aleksić, J. et al. (Aug. 2013). "The simultaneous low state spectral energy distribution of 1ES 2344+514 from radio to very high energies". In: *Astronomy and Astrophysics* 556, A67, A67. DOI: 10.1051/0004-6361/201220714. arXiv: 1211.2608 [astro-ph.HE].

Aleksić, J. et al. (Mar. 2015). "Measurement of the Crab Nebula spectrum over three decades in energy with the MAGIC telescopes". In: *Journal of High Energy Astrophysics* 5, pp. 30–38. DOI: 10.1016/j.jheap.2015.01.002. arXiv: 1406.6892 [astro-ph.HE].

Aleksić, J. et al. (Jan. 2016). "The major upgrade of the MAGIC telescopes, Part II: A performance study using observations of the Crab Nebula". In: *Astroparticle Physics* 72, pp. 76–94. DOI: 10.1016/j.astropartphys.2015.02.005. arXiv: 1409.5594 [astro-ph.IM].

Aliu, E. et al. (Jan. 2009). "Improving the performance of the single-dish Cherenkov telescope MAGIC through the use of signal timing". In: *Astroparticle Physics* 30.6, pp. 293–305. DOI: 10.1016/j.astropartphys.2008.10.003. arXiv: 0810.3568 [astro-ph].

Aliu, E. et al. (Dec. 2014). "Investigating Broadband Variability of the TeV Blazar 1ES 1959+650". In: *The Astrophysical Journal* 797.2, 89, p. 89. DOI: 10.1088/0004-637X/797/2/89. arXiv: 1412.1031 [astro-ph.HE].

Allakhverdyan, V. A. et al. (Jan. 2024). "High-energy neutrino-induced cascade from the direction of the flaring radio blazar TXS 0506 + 056 observed by Baikal-GVD in 2021". In: *Monthly Notices of the Royal Astronomical Society* 527.3, pp. 8784–8792. DOI: 10.1093/mnras/stad3653. arXiv: 2210.01650 [astro-ph.HE].

Aller, M. F., H. D. Aller & P. A. Hughes (Nov. 1992). "Pearson-Readhead Survey Sources: Properties of the Centimeter-Wavelength Flux and Polarization of a Complete Radio Sample". In: *The Astrophysical Journal* 399, p. 16. DOI: 10.1086/171898.

Antonucci, R. (Jan. 1993). "Unified models for active galactic nuclei and quasars." In: *Annual Review of Astron and Astrophys* 31, pp. 473–521. DOI: 10.1146/annurev.aa.31.090193.002353.

Araudo, A. T., V. Bosch-Ramon & G. E. Romero (Nov. 2010). "Gamma rays from cloud penetration at the base of AGN jets". In: *Astronomy and Astrophysics* 522, A97, A97. DOI: 10.1051/0004-6361/201014660. arXiv: 1007.2199 [astro-ph.HE].

Arnaud, K. A. (Jan. 1996). "XSPEC: The First Ten Years". In: *Astronomical Data Analysis Software and Systems V*. Ed. by G. H. Jacoby & J. Barnes. Vol. 101. Astronomical Society of the Pacific Conference Series, p. 17.

Arsioli, B., B. Fraga, P. Giommi, P. Padovani & P. M. Marrese (July 2015). "1WHSP: An IR-based sample of ~1000 VHE γ-ray blazar candidates". In: *Astronomy and Astrophysics* 579, A34, A34. DOI: 10.1051/0004-6361/201424148. arXiv: 1504.02801 [astro-ph.HE].

Astropy Collaboration et al. (Sept. 2018). "The Astropy Project: Building an Open-science Project and Status of the v2.0 Core Package". In: *Astronomical Journal* 156.3, 123, p. 123. DOI: 10.3847/1538-3881/aabc4f. arXiv: 1801.02634 [astro-ph.IM].

Atwood, W. B. et al. (June 2009). "The Large Area Telescope on the Fermi Gamma-Ray Space Telescope Mission". In: *The Astrophysical Journal* 697.2, pp. 1071–1102. DOI: 10.1088/0004-637X/697/2/1071. arXiv: 0902.1089 [astro-ph.IM].

Ballet, J., T. H. Burnett, S. W. Digel & B. Lott (May 2020a). "Fermi Large Area Telescope Fourth Source Catalog Data Release 2". In: *arXiv e-prints*, arXiv:2005.11208, arXiv:2005.11208. DOI: 10.48550/arXiv.2005.11208. arXiv: 2005.11208 [astro-ph.HE].

Ballet, J., T. H. Burnett, S. W. Digel & B. Lott (May 2020b). "Fermi Large Area Telescope Fourth Source Catalog Data Release 2". In: *arXiv e-prints*, arXiv:2005.11208, arXiv:2005.11208. arXiv: 2005.11208 [astro-ph.HE].

Barkov, M. V., F. A. Aharonian, S. V. Bogovalov, S. R. Kelner & D. Khangulyan (Apr. 2012). "Rapid TeV Variability in Blazars as a Result of Jet-Star Interaction". In: *The Astrophysical Journal* 749.2, 119, p. 119. DOI: 10.1088/0004-637X/749/2/119. arXiv: 1012.1787 [astro-ph.HE].

Barnacka, A., L. Bogacz, M. Grudzińska, M. Janiak, N. Komin, G. Lamanna & R. Moderski (2012). "Monte Carlo Simulations For The Cherenkov Telescope Array Observatory Using Pl-Grid E-Infrastructure". In: *Computer Science* 13, pp. 113–122.

Becker, R. H., R. L. White & D. J. Helfand (Jan. 1994). "The VLA's FIRST Survey". In: *Astronomical Data Analysis Software and Systems III*. Ed. by D. R. Crabtree, R. J. Hanisch & J. Barnes. Vol. 61. Astronomical Society of the Pacific Conference Series, p. 165.

Begelman, M. C., R. D. Blandford & M. J. Rees (Sept. 1980). "Massive black hole binaries in active galactic nuclei". In: *Nature* 287.5780, pp. 307–309. DOI: 10.1038/287307a0.

Begelman, M. C., A. C. Fabian & M. J. Rees (Feb. 2008). "Implications of very rapid TeV variability in blazars". In: *Monthly Notices of the Royal Astronomical Society* 384.1, pp. L19–L23. DOI: 10.1111/j.1745-3933.2007.00413.x. arXiv: 0709.0540 [astro-ph].

Bégué, D., N. Sahakyan, H. Dereli Bégué, P. Giommi, S. Gasparyan, M. Khachatryan, A. Casotto & A. Pe'er (Nov. 2023). "Modeling blazar broadband emission with convolutional neural networks – I. Synchrotron self-Compton model". In: *arXiv e-prints*, arXiv:2311.02979, arXiv:2311.02979. DOI: 10.48550/arXiv.2311.02979. arXiv: 2311.02979 [astro-ph.HE].

Benbow, W. (Jan. 2011). "Highlights of the VERITAS Blazar Observation Program". In: *International Cosmic Ray Conference*. Vol. 8. International Cosmic Ray Conference, p. 47. DOI: 10.7529/ICRC2011/V08/0746. arXiv: 1110.0038 [astro-ph.HE].

Bertero, M. (Jan. 1989). "Linear Inverse and III-Posed Problems". In: *Advances in Electronics and Electron Physics* 75, pp. 1–120. DOI: 10.1016/S0065-2539(08)60946-4.

Biermann, P. L. & P. A. Strittmatter (Nov. 1987). "Synchrotron Emission from Shock Waves in Active Galactic Nuclei". In: *The Astrophysical Journal* 322, p. 643. DOI: 10.1086/165759.

Biland, A. & FACT Collaboration (June 2016a). "FACT measures increased gamma-ray flux from the high-energy peaked BL Lac object 1ES 1959+650 since five nights". In: *The Astronomer's Telegram* 9139, p. 1.

Biland, A. & FACT Collaboration (July 2016b). "FACT measures new maximum flux from the HBL 1ES 1959+650 at TeV energies". In: *The Astronomer's Telegram* 9239, p. 1.

Biland, A., R. Mirzoyan, FACT Collaboration & MAGIC Collaboration (July 2016a). "FACT and MAGIC measure an increased gamma-ray flux from the HBL 1ES 1959+650". In: *The Astronomer's Telegram* 9203, p. 1.

Biland, A. et al. (June 2016b). "Further increase of gamma-ray emission from the HBL 1ES 1959+650". In: *The Astronomer's Telegram* 9148, p. 1.

Biteau, J. & B. Giebels (Dec. 2012). "The minijets-in-a-jet statistical model and the rms-flux correlation". In: *Astronomy and Astrophysics* 548, A123, A123. DOI: 10.1051/0004-6361/201220056. arXiv: 1210.2045 [astro-ph.HE].

Biteau, J. et al. (Feb. 2020). "Progress in unveiling extreme particle acceleration in persistent astrophysical jets". In: *Nature Astronomy* 4, pp. 124–131. DOI: 10.1038/s41550-019-0988-4. arXiv: 2001.09222 [astro-ph.HE].

Blandford, R. D. & A. Königl (Aug. 1979). "Relativistic jets as compact radio sources." In: *The Astrophysical Journal* 232, pp. 34–48. DOI: 10.1086/157262.

Blasi, M. G. et al. (Nov. 2013). "The TeV blazar Markarian 421 at the highest spatial resolution". In: *Astronomy and Astrophysics* 559, A75, A75. DOI: 10.1051/0004-6361/201321858. arXiv: 1310.4973 [astro-ph.HE].

Blumenthal, G. R. & R. J. Gould (Jan. 1970). "Bremsstrahlung, Synchrotron Radiation, and Compton Scattering of High-Energy Electrons Traversing Dilute Gases". In: *Reviews of Modern Physics* 42.2, pp. 237–271. DOI: 10.1103/RevModPhys.42.237.

Boccardi, B., E. Madika & L. Ricci (Nov. 2021). "Accretion mode and jet collimation in active galactic nuclei". In: *Astronomische Nachrichten* 342.1071, pp. 1071–1076. DOI: 10.1002/asna.20210085.

Boettcher, M., M. Fu, T. Govenor, Q. King & P. Roustazadeh (Apr. 2022). "Multiwavelength and Multimessenger Observations of Blazars and Theoretical Modeling: Blazars as Astrophysical Neutrino Sources". In: *arXiv e-prints*, arXiv:2204.12242, arXiv:2204.12242. DOI: 10.48550/arXiv.2204.12242. arXiv: 2204.12242 [astro-ph.HE].

Boettcher, M., D. E. Harris & H. Krawczynski (2012). *Relativistic Jets from Active Galactic Nuclei*.

Böttcher, M., A. Reimer, K. Sweeney & A. Prakash (May 2013). "Leptonic and Hadronic Modeling of Fermi-detected Blazars". In: *The Astrophysical Journal* 768.1, 54, p. 54. DOI: 10.1088/0004-637X/768/1/54. arXiv: 1304.0605 [astro-ph.HE].

Böttcher, M. (Mar. 2005). "A Hadronic Synchrotron Mirror Model for the "Orphan" TeV Flare in 1ES 1959+650". In: *The Astrophysical Journal* 621.1, pp. 176–180. DOI: 10.1086/427430. arXiv: astro-ph/0411248 [astro-ph].

Bradascio, F. (Oct. 2023). "Status of the Medium-Sized Telescopes for the Cherenkov Telescope Array Observatory". In: *arXiv e-prints*, arXiv:2310.02127, arXiv:2310.02127. DOI: 10.48550/arXiv.2310.02127. arXiv: 2310.02127 [astro-ph.IM].

Britzen, S., C. Fendt, M. Böttcher, M. Zajaček, F. Jaron, I. N. Pashchenko, A. Araudo, V. Karas & O. Kurtanidze (Oct. 2019). "A cosmic collider: Was the IceCube neutrino generated in a precessing jet-jet interaction in TXS 0506+056?" In: *Astronomy and Astrophysics* 630, A103, A103. DOI: 10.1051/0004-6361/201935422.

Burrows, A. & J. M. Lattimer (July 1987). "Neutrinos from SN 1987A". In: *The Astrophysical Journal Letters* 318, p. L63. DOI: 10.1086/184938.

Buson, S., S. Garrappa, C. Bartolini, J. Sinapius & Fermi-LAT Collaboration (Nov. 2023a). "Fermi-LAT gamma-ray observations of IceCube-231027A". In: *GRB Coordinates Network* 34932, p. 1.

Buson, S., S. Garrappa & C. C. Cheung (Nov. 2020a). "Fermi-LAT evidence for VHE emission from NVSS J065844+063711". In: *The Astronomer's Telegram* 14200, p. 1.

Buson, S., S. Garrappa, C. C. Cheung & M. Ajell (Oct. 2020b). "Fermi-LAT Gamma-ray Observations of IceCube-201021A and detection of a new gamma-ray source, Fermi J1725.5+1312". In: *The Astronomer's Telegram* 14111, p. 1.

Buson, S. et al. (Apr. 2016). "Fermi-LAT, FACT, MAGIC and VERITAS detection of increasing gamma-ray activity from the high-energy peaked BL Lac object 1ES 1959+650". In: *The Astronomer's Telegram* 9010, p. 1.

Buson, S., A. Tramacere, L. Oswald, E. Barbano, G. Fichet de Clairfontaine, L. Pfeiffer, A. Azzollini, V. Baghmanyan & M. Ajello (May 2023b). "Extragalactic neutrino factories". In: *arXiv e-prints*, arXiv:2305.11263, arXiv:2305.11263. DOI: 10.48550/arXiv.2305.11263. arXiv: 2305.11263 [astro-ph.HE].

Buson, S., A. Tramacere, L. Pfeiffer, L. Oswald, R. de Menezes, A. Azzollini & M. Ajello (July 2022). "Beginning a Journey Across the Universe: The Discovery of Extragalactic Neutrino Factories". In: *The Astrophysical Journal Letters* 933.2, L43, p. L43. DOI: 10.3847/2041-8213/ac7d5b. arXiv: 2207.06314 [astro-ph.HE].

Bustamante, M. & A. Connolly (Feb. 2019). "Extracting the Energy-Dependent Neutrino-Nucleon Cross Section above 10 TeV Using IceCube Showers". In: *Phys. Rev. Lett.* 122.4, 041101, p. 041101. DOI: 10.1103/PhysRevLett.122.041101. arXiv: 1711.11043 [astro-ph.HE].

Capel, F., J. M. Burgess, D. J. Mortlock & P. Padovani (Dec. 2022). "Assessing coincident neutrino detections using population models". In: *Astronomy and Astrophysics* 668, A190, A190. DOI: 10.1051/0004-6361/202243116. arXiv: 2201.05633 [astro-ph.HE].

Cardelli, J. A., G. C. Clayton & J. S. Mathis (Oct. 1989). "The Relationship between Infrared, Optical, and Ultraviolet Extinction". In: *The Astrophysical Journal* 345, p. 245. DOI: 10.1086/167900.

Cerruti, M., A. Zech, C. Boisson & S. Inoue (Mar. 2015). "A hadronic origin for ultra-high-frequency-peaked BL Lac objects". In: *Monthly Notices of the Royal Astronomical Society* 448.1, pp. 910–927. DOI: 10.1093/mnras/stu2691. arXiv: 1411.5968 [astro-ph.HE].

Cerruti, M. (Oct. 2020). "Leptonic and Hadronic Radiative Processes in Supermassive-Black-Hole Jets". In: *Galaxies* 8.4, 72, p. 72. DOI: 10.3390/galaxies8040072. arXiv: 2012.13302 [astro-ph.HE].

Chang, Y. .-., B. Arsioli, P. Giommi & P. Padovani (Feb. 2017). "2WHSP: A multi-frequency selected catalogue of high energy and very high energy γ-ray blazars and blazar candidates". In: *Astronomy and Astrophysics* 598, A17, A17. DOI: 10.1051/0004-6361/201629487. arXiv: 1609.05808 [astro-ph.HE].

Chang, Y. .-., C. H. Brandt & P. Giommi (Jan. 2020). "The Open Universe VOU-Blazars tool". In: *Astronomy and Computing* 30, 100350, p. 100350. DOI: 10.1016/j.ascom.2019.100350. arXiv: 1909.11455 [astro-ph.HE].

Chatterjee, R., G. Fossati, C. M. Urry, C. D. Bailyn, L. Maraschi, M. Buxton, E. W. Bonning, J. Isler & P. Coppi (Jan. 2013). "An Optical-Near-infrared Outburst with no Accompanying γ-Rays in the Blazar PKS 0208-512". In: *The Astrophysical Journal Letters* 763.1, L11, p. L11. DOI: 10.1088/2041-8205/763/1/L11. arXiv: 1212.2629 [astro-ph.HE].

Cherenkov Telescope Array Consortium et al. (2019). *Science with the Cherenkov Telescope Array*. DOI: 10.1142/10986.

Chiaberge, M., A. Celotti, A. Capetti & G. Ghisellini (June 2000). "Does the unification of BL Lac and FR I radio galaxies require jet velocity structures?" In: *Astronomy and Astrophysics* 358, pp. 104–112. DOI: 10.48550/arXiv.astro-ph/0003197. arXiv: astro-ph/0003197 [astro-ph].

Cologna, G. (Jan. 2016). "TeV observations of hard spectrum active galactic nuclei with HESS-I and HESS-II". PhD thesis. Ruprecht-Karls University of Heidelberg, Germany.

Condon, J. J., W. D. Cotton, E. W. Greisen, Q. F. Yin, R. A. Perley, G. B. Taylor & J. J. Broderick (May 1998). "The NRAO VLA Sky Survey". In: *Astronomical Journal* 115.5, pp. 1693–1716. DOI: 10.1086/300337.

Costamante, L., G. Bonnoli, F. Tavecchio, G. Ghisellini, G. Tagliaferri & D. Khangulyan (July 2018). "The NuSTAR view on hard-TeV BL Lacs". In: *Monthly Notices of the Royal Astronomical Society* 477.3, pp. 4257–4268. DOI: 10.1093/mnras/sty857. arXiv: 1711.06282 [astro-ph.HE].

Costamante, L. et al. (May 2001). "Extreme synchrotron BL Lac objects. Stretching the blazar sequence". In: *Astronomy and Astrophysics* 371, pp. 512–526. DOI: 10.1051/0004-6361:20010412. arXiv: astro-ph/0103343 [astro-ph].

Coulter, D. A. et al. (Dec. 2017). "Swope Supernova Survey 2017a (SSS17a), the optical counterpart to a gravitational wave source". In: *Science* 358.6370, pp. 1556–1558. DOI: 10.1126/science.aap9811. arXiv: 1710.05452 [astro-ph.HE].

Croke, S. M. & D. C. Gabuzda (May 2008). "Aligning VLBI images of active galactic nuclei at different frequencies". In: *Monthly Notices of the Royal Astronomical Society* 386.2, pp. 619–626. DOI: 10.1111/j.1365-2966.2008.13087.x. arXiv: 0809.3313 [astro-ph].

de Angelis, A., O. Mansutti, M. Persic & M. Roncadelli (Mar. 2009). "Photon propagation and the very high energy γ-ray spectra of blazars: how transparent is the Universe?" In: *Monthly Notices of the Royal Astronomical Society* 394.1, pp. L21–L25. DOI: 10.1111/j.1745-3933.2008.00602.x. arXiv: 0807.4246 [astro-ph].

Deil, C. et al. (July 2017). "Gammapy - A prototype for the CTA science tools". In: *35th International Cosmic Ray Conference (ICRC2017)*. Vol. 301. International Cosmic Ray Conference, 766, p. 766. DOI: 10.22323/1.301.0766. arXiv: 1709.01751 [astro-ph.IM].

Dembinski, H. et al. (Nov. 2020). *scikit-hep/iminuit: v1.5.4*. Zenodo. Version v1.5.4. DOI: 10.5281/zenodo.4283509.

Dermer, C. D. & G. Menon (2009). *High Energy Radiation from Black Holes: Gamma Rays, Cosmic Rays, and Neutrinos*.

Doe, S. et al. (Oct. 2007). "Developing Sherpa with Python". In: *Astronomical Data Analysis Software and Systems XVI*. Ed. by R. A. Shaw, F. Hill & D. J. Bell. Vol. 376. Astronomical Society of the Pacific Conference Series, p. 543.

Dominguez, A. et al. (Feb. 2011). "Extragalactic background light inferred from AEGIS galaxy-SED-type fractions". In: *Monthly Notices of the Royal Astronomical Society* 410.4, pp. 2556–2578. DOI: 10.1111/j.1365-2966.2010.17631.x. arXiv: 1007.1459 [astro-ph.CO].

Edelson, R. A. & J. H. Krolik (Oct. 1988). "The Discrete Correlation Function: A New Method for Analyzing Unevenly Sampled Variability Data". In: *The Astrophysical Journal* 333, p. 646. DOI: 10.1086/166773.

Elvis, M., D. Plummer, J. Schachter & G. Fabbiano (May 1992). "The Einstein Slew Survey". In: *Astrophysical Journal, Supplement* 80, p. 257. DOI: 10.1086/191665.

Essey, W., O. E. Kalashev, A. Kusenko & J. F. Beacom (Apr. 2010). "Secondary Photons and Neutrinos from Cosmic Rays Produced by Distant Blazars". In: *Phys. Rev. Lett.* 104.14, 141102, p. 141102. DOI: 10.1103/PhysRevLett.104.141102. arXiv: 0912.3976 [astro-ph.HE].

Evans, P. A. et al. (Aug. 2009). "Methods and results of an automatic analysis of a complete sample of Swift-XRT observations of GRBs". In: *Monthly Notices of the Royal Astronomical Society* 397.3, pp. 1177–1201. DOI: 10.1111/j.1365-2966.2009.14913.x. arXiv: 0812.3662 [astro-ph].

Evoli, C. (Dec. 2020). *The Cosmic-Ray Energy Spectrum*. DOI: 10.5281/zenodo.4396125. URL: https://doi.org/10.5281/zenodo.4396125.

Falomo, R., E. Pian & A. Treves (Sept. 2014). "An optical view of BL Lacertae objects". In: *Astronomy and Astrophysics Reviews* 22, 73, p. 73. DOI: 10.1007/s00159-014-0073-z. arXiv: 1407.7615 [astro-ph.HE].

Fang, K. & K. Murase (Apr. 2018). "Linking high-energy cosmic particles by black-hole jets embedded in large-scale structures". In: *Nature Physics* 14.4, pp. 396–398. DOI: 10.1038/s41567-017-0025-4. arXiv: 1704.00015 [astro-ph.HE].

Feng, S.-l., P. Fan, Y.-f. Hu, T.-y. Ma & Y. Xia (July 2021). "The Review of γ-ray Astronomical Observing Techniques". In: *Chinese Astronomy and Astrophysics* 45.3, pp. 281–300. DOI: 10.1016/j.chinastron.2021.08.002.

Fermi, E. (Apr. 1949). "On the Origin of the Cosmic Radiation". In: *Physical Review* 75.8, pp. 1169–1174. DOI: 10.1103/PhysRev.75.1169.

Filippenko, A. V., W. D. Li, R. R. Treffers & M. Modjaz (Jan. 2001). "The Lick Observatory Supernova Search with the Katzman Automatic Imaging Telescope". In: *IAU Colloq. 183: Small Telescope Astronomy on Global Scales*. Ed. by B. Paczynski, W.-P. Chen & C. Lemme. Vol. 246. Astronomical Society of the Pacific Conference Series, p. 121.

Fomin, V. P., A. A. Stepanian, R. C. Lamb, D. A. Lewis, M. Punch & T. C. Weekes (May 1994). "New methods of atmospheric Cherenkov imaging for gamma-ray astronomy. I. The false source method". In: *Astroparticle Physics* 2.2, pp. 137–150. DOI: 10.1016/0927-6505(94)90036-1.

Fossati, G., L. Maraschi, A. Celotti, A. Comastri & G. Ghisellini (Sept. 1998). "A unifying view of the spectral energy distributions of blazars". In: *Monthly Notices of the Royal Astronomical Society* 299.2, pp. 433–448. DOI: 10.1046/j.1365-8711.1998.01828.x. arXiv: astro-ph/9804103 [astro-ph].

Fruck, C. et al. (Sept. 2022). "Characterizing the aerosol atmosphere above the Observatorio del Roque de los Muchachos by analysing seven years of data taken with an GaAsP HPD-readout, absolutely calibrated elastic LIDAR". In: *Monthly Notices of the Royal Astronomical Society* 515.3, pp. 4520–4550. DOI: 10.1093/mnras/stac1563. arXiv: 2202.09561 [astro-ph.IM].

Garrappa, S., S. Buson, C. C. Cheung, J. Sinapius & Fermi-LAT Collaboration (Feb. 2022). "Fermi-LAT Gamma-ray Observations of IceCube-220205A". In: *GRB Coordinates Network* 31557, p. 1.

Garrappa, S., S. Buson, V. Paliya & Fermi-LAT Collaboration (Jan. 2020). "Fermi-LAT Gamma-ray Observations of IceCube-200109A and detection of a possible new gamma-ray source, Fermi J1055.8+1034". In: *The Astronomer's Telegram* 13402, p. 1.

Garrappa, S., S. Buson & T. Venters (July 2019a). "Fermi-LAT Gamma-ray Observations of IceCube-190704A and detection of the new gamma-ray source 1WHSP J104516.2+275133". In: *The Astronomer's Telegram* 12906, p. 1.

Garrappa, S. et al. (Aug. 2019b). "Investigation of Two Fermi-LAT Gamma-Ray Blazars Coincident with High-energy Neutrinos Detected by IceCube". In: *The Astrophysical Journal* 880.2, 103, p. 103. DOI: 10.3847/1538-4357/ab2ada. arXiv: 1901.10806 [astro-ph.HE].

Garrappa, S. et al. (Jan. 2024). "*Fermi*-LAT follow-up observations in seven years of realtime high-energy neutrino alerts". In: *arXiv e-prints*, arXiv:2401.06666, arXiv:2401.06666. DOI: 10.48550/arXiv.2401.06666. arXiv: 2401.06666 [astro-ph.HE].

Gehrels, N. et al. (Aug. 2004). "The Swift Gamma-Ray Burst Mission". In: *The Astrophysical Journal* 611.2, pp. 1005–1020. DOI: 10.1086/422091. arXiv: astro-ph/0405233 [astro-ph].

Geng, X. et al. (June 2022). "Exploring γ-Ray Flares in the Long-term Light Curves of CTA 102 at GeV Energies". In: *Astrophysical Journal, Supplement* 260.2, 48, p. 48. DOI: 10.3847/1538-4365/ac64f6.

Georganopoulos, M., E. S. Perlman & D. Kazanas (Nov. 2005). "Is the Core of M87 the Source of Its TeV Emission? Implications for Unified Schemes". In: *The Astrophysical Journal Letters* 634.1, pp. L33–L36. DOI: 10.1086/498714. arXiv: astro-ph/0510783 [astro-ph].

Ghirlanda, G. et al. (Mar. 2019). "Compact radio emission indicates a structured jet was produced by a binary neutron star merger". In: *Science* 363.6430, pp. 968–971. DOI: 10.1126/science.aau8815. arXiv: 1808.00469 [astro-ph.HE].

Ghisellini, G., A. Celotti & L. Costamante (May 2002). "Low power BL Lacertae objects and the blazar sequence. Clues on the particle acceleration process". In: *Astronomy and Astrophysics* 386, pp. 833–842. DOI: 10.1051/0004-6361:20020275. arXiv: astro-ph/0202367 [astro-ph].

Ghisellini, G., A. Celotti, G. Fossati, L. Maraschi & A. Comastri (Dec. 1998). "A theoretical unifying scheme for gamma-ray bright blazars". In: *Monthly Notices of the Royal Astronomical Society* 301.2, pp. 451–468. DOI: 10.1046/j.1365-8711.1998.02032.x. arXiv: astro-ph/9807317 [astro-ph].

Ghisellini, G., L. Maraschi & A. Treves (May 1985). "Inhomogeneous synchrotron-self-compton models and the problem of relativistic beaming of BL Lac objects." In: *Astronomy and Astrophysics* 146, pp. 204–212.

Ghisellini, G., P. Padovani, A. Celotti & L. Maraschi (Apr. 1993). "Relativistic Bulk Motion in Active Galactic Nuclei". In: *The Astrophysical Journal* 407, p. 65. DOI: 10.1086/172493.

Ghisellini, G., C. Righi, L. Costamante & F. Tavecchio (July 2017). "The Fermi blazar sequence". In: *Monthly Notices of the Royal Astronomical Society* 469.1, pp. 255–266. DOI: 10.1093/mnras/stx806. arXiv: 1702.02571 [astro-ph.HE].

Ghisellini, G. (Sept. 2011). "Extragalactic relativistic jets". In: *25th Texas Symposium on Relativistic AstroPhysics (Texas 2010)*. Ed. by F. A. Aharonian, W. Hofmann & F. M. Rieger. Vol. 1381. American Institute of Physics Conference Series, pp. 180–198. DOI: 10.1063/1.3635832. arXiv: 1104.0006 [astro-ph.CO].

Giommi, P., T. Glauch, P. Padovani, E. Resconi, A. Turcati & Y. L. Chang (Sept. 2020a). "Dissecting the regions around IceCube high-energy neutrinos: growing evidence for the blazar connection". In: *Monthly Notices of the Royal Astronomical Society* 497.1, pp. 865–878. DOI: 10.1093/mnras/staa2082. arXiv: 2001.09355 [astro-ph.HE].

Giommi, P., P. Padovani & T. Glauch (Nov. 2020b). "Swift observations of blazars and blazar candidates in and around the error regions of the gold neutrinos IC201114A and IC201115A". In: *The Astronomer's Telegram* 14225, p. 1.

Giroletti, M. et al. (Jan. 2004). "Parsec-Scale Properties of Markarian 501". In: *The Astrophysical Journal* 600.1, pp. 127–140. DOI: 10.1086/379663. arXiv: astro-ph/0309285 [astro-ph].

Giroletti, M. et al. (Apr. 2015). "The connection between radio and high energy emission in black hole powered systems in the SKA era". In: *Advancing Astrophysics with the Square Kilometre Array (AASKA14)*, 153, p. 153. DOI: 10.22323/1.215.0153. arXiv: 1501.03330 [astro-ph.HE].

Goldstein, A. et al. (Oct. 2017). "An Ordinary Short Gamma-Ray Burst with Extraordinary Implications: Fermi-GBM Detection of GRB 170817A". In: *The Astrophysical Journal Letters* 848.2, L14, p. L14. DOI: 10.3847/2041-8213/aa8f41. arXiv: 1710.05446 [astro-ph.HE].

Gordon, Y. A., M. M. Boyce, C. P. O'Dea, L. Rudnick, H. Andernach, A. N. Vantyghem, S. A. Baum, J.-P. Bui & M. Dionyssiou (Oct. 2020). "A Catalog of Very Large Array Sky Survey Epoch 1 Quick Look Components, Sources, and Host Identifications". In: *Research Notes of the American Astronomical Society* 4.10, 175, p. 175. DOI: 10.3847/2515-5172/abbe23.

Graff, P. B., M. Georganopoulos, E. S. Perlman & D. Kazanas (Dec. 2008). "A Multizone Model for Simulating the High-Energy Variability of TeV Blazars". In: *The Astrophysical Journal* 689.1, pp. 68–78. DOI: 10.1086/592427. arXiv: 0808.2135 [astro-ph].

Gregory, P. C. & J. J. Condon (Apr. 1991). "The 87GB Catalog of Radio Sources Covering 0 degrees ¡ delta ¡ +75 degrees at 4.85 GHz". In: *Astrophysical Journal, Supplement* 75, p. 1011. DOI: 10.1086/191559.

Greisen, E. W. (Mar. 2003). "AIPS, the VLA, and the VLBA". In: *Information Handling in Astronomy - Historical Vistas*. Ed. by A. Heck. Vol. 285. Astrophysics and Space Science Library, p. 109. DOI: 10.1007/0-306-48080-8_7.

Gurvits, L. I. (June 2023). "A Brief History of Space VLBI". In: *arXiv e-prints*, arXiv:2306.17647, arXiv:2306.17647. DOI: 10.48550/arXiv.2306.17647. arXiv: 2306.17647 [astro-ph.IM].

Hada, K., A. Doi, M. Kino, H. Nagai, Y. Hagiwara & N. Kawaguchi (Sept. 2011). "An origin of the radio jet in M87 at the location of the central black hole". In: *Nature* 477.7363, pp. 185–187. DOI: 10.1038/nature10387.

Hallinan, G. et al. (Dec. 2017). "A radio counterpart to a neutron star merger". In: *Science* 358.6370, pp. 1579–1583. DOI: 10.1126/science.aap9855. arXiv: 1710.05435 [astro-ph.HE].

Halzen, F. (Nov. 2021). "High-Energy Neutrinos from the Cosmos". In: *Annalen der Physik* 533.11, 2100309, p. 2100309. DOI: 10.1002/andp.202100309.

Halzen, F. & D. Hooper (July 2002). "High-energy neutrino astronomy: the cosmic ray connection". In: *Reports on Progress in Physics* 65.7, pp. 1025–1078. DOI: 10.1088/0034-4885/65/7/201. arXiv: astro-ph/0204527 [astro-ph].

Halzen, F. & D. Hooper (July 2005). "High energy neutrinos from the TeV Blazar 1ES 1959 + 650". In: *Astroparticle Physics* 23.6, pp. 537–542. DOI: 10.1016/j.astropartphys.2005.03.007. arXiv: astro-ph/0502449 [astro-ph].

Halzen, F. & A. Kheirandish (May 2019). "Multimessenger Search for the Sources of Cosmic Rays using Cosmic Neutrinos". In: *Frontiers in Astronomy and Space Sciences* 6, 32, p. 32. DOI: 10.3389/fspas.2019.00032.

Hardee, P. E. (July 1987). "Spatial Stability of Relativistic Jets: Application to 3C 345". In: *The Astrophysical Journal* 318, p. 78. DOI: 10.1086/165352.

Harris, C. R. et al. (Sept. 2020). "Array programming with NumPy". In: *Nature* 585.7825, pp. 357–362. DOI: 10.1038/s41586-020-2649-2. arXiv: 2006.10256 [cs.MS].

Hayasaki, K. & R. Yamazaki (Dec. 2019). "Neutrino Emissions from Tidal Disruption Remnants". In: *The Astrophysical Journal* 886.2, 114, p. 114. DOI: 10.3847/1538-4357/ab44ca. arXiv: 1908.10882 [astro-ph.HE].

Heckmann, L., D. Paneque & A. Reimer (Sept. 2023). "A novel approach to identify blazar emission states using clustering algorithms". In: *arXiv e-prints*, arXiv:2309.13120, arXiv:2309.13120. DOI: 10.48550/arXiv.2309.13120. arXiv: 2309.13120 [astro-ph.HE].

Henri, G. & L. Saugé (Mar. 2006). "The Bulk Lorentz Factor Crisis of TeV Blazars: Evidence for an Inhomogeneous Pileup Energy Distribution?" In: *The Astrophysical Journal* 640.1, pp. 185–195. DOI: 10.1086/500039. arXiv: astro-ph/0511610 [astro-ph].

Hillas, A. M. (Jan. 1984). "The Origin of Ultra-High-Energy Cosmic Rays". In: *Annual Review of Astron and Astrophys* 22, pp. 425–444. DOI: 10.1146/annurev.aa.22.090184.002233.

Hillas, A. M. (Aug. 1985). "Cerenkov Light Images of EAS Produced by Primary Gamma Rays and by Nuclei". In: *19th International Cosmic Ray Conference (ICRC19), Volume 3*. Vol. 3. International Cosmic Ray Conference, p. 445.

Hoerbe, M. R., P. J. Morris, G. Cotter & J. Becker Tjus (Aug. 2020). "On the relative importance of hadronic emission processes along the jet axis of active galactic nuclei". In: *Monthly Notices of the Royal Astronomical Society* 496.3, pp. 2885–2901. DOI: 10.1093/mnras/staa1650. arXiv: 2006.05140 [astro-ph.HE].

Högbom, J. A. (June 1974). "Aperture Synthesis with a Non-Regular Distribution of Interferometer Baselines". In: *Astronomy and Astrophysics, Supplement* 15, p. 417.

Holder, J. et al. (Jan. 2003). "Detection of TeV Gamma Rays from the BL Lacertae Object 1ES 1959+650 with the Whipple 10 Meter Telescope". In: *The Astrophysical Journal Letters* 583.1, pp. L9–L12. DOI: 10.1086/367816. arXiv: astro-ph/0212170 [astro-ph].

Hooper, D., T. Linden & A. Vieregg (Feb. 2019). "Active galactic nuclei and the origin of IceCube's diffuse neutrino flux". In: *Journal of Cosmology and Astroparticle Physics* 2019.2, 012, p. 012. DOI: 10.1088/1475-7516/2019/02/012. arXiv: 1810.02823 [astro-ph.HE].

Hovatta, T. et al. (June 2021). "Association of IceCube neutrinos with radio sources observed at Owens Valley and Metsähovi Radio Observatories". In: *Astronomy and Astrophysics* 650, A83, A83. DOI: 10.1051/0004-6361/202039481. arXiv: 2009.10523 [astro-ph.HE].

IceCube Collaboration (Nov. 2013). "Evidence for High-Energy Extraterrestrial Neutrinos at the IceCube Detector". In: *Science* 342.6161, 1242856, p. 1242856. DOI: 10.1126/science.1242856. arXiv: 1311.5238 [astro-ph.HE].

IceCube Collaboration et al. (July 2018a). "Multimessenger observations of a flaring blazar coincident with high-energy neutrino IceCube-170922A". In: *Science* 361.6398, eaat1378, eaat1378. DOI: 10.1126/science.aat1378. arXiv: 1807.08816 [astro-ph.HE].

IceCube Collaboration et al. (July 2018b). "Neutrino emission from the direction of the blazar TXS 0506+056 prior to the IceCube-170922A alert". In: *Science* 361.6398, pp. 147–151. DOI: 10.1126/science.aat2890. arXiv: 1807.08794 [astro-ph.HE].

IceCube Collaboration et al. (Nov. 2022). "Evidence for neutrino emission from the nearby active galaxy NGC 1068". In: *Science* 378.6619, pp. 538–543. DOI: 10.1126/science.abg3395. arXiv: 2211.09972 [astro-ph.HE].

Inoue, Y., D. Khangulyan & A. Doi (Mar. 2020). "On the Origin of High-energy Neutrinos from NGC 1068: The Role of Nonthermal Coronal Activity". In: *The Astrophysical Journal Letters* 891.2, L33, p. L33. DOI: 10.3847/2041-8213/ab7661. arXiv: 1909.02239 [astro-ph.HE].

Jansen, F. et al. (Jan. 2001). "XMM-Newton observatory. I. The spacecraft and operations". In: *Astronomy and Astrophysics* 365, pp. L1–L6. DOI: 10.1051/0004-6361:20000036.

Jansky, K. G. (July 1933). "Radio Waves from Outside the Solar System". In: *Nature* 132.3323, p. 66. DOI: 10.1038/132066a0.

Jethwa, P., R. Saxton, M. Guainazzi, P. Rodriguez-Pascual & M. Stuhlinger (Sept. 2015). "When is pile-up important in the XMM-Newton EPIC cameras?" In: *Astronomy and Astrophysics* 581, A104, A104. DOI: 10.1051/0004-6361/201425579.

Jonas, J. & MeerKAT Team (Jan. 2016). "The MeerKAT Radio Telescope". In: *MeerKAT Science: On the Pathway to the SKA*, 1, p. 1. DOI: 10.22323/1.277.0001.

Jorstad, S. & A. Marscher (Oct. 2016). "The VLBA-BU-BLAZAR Multi-Wavelength Monitoring Program". In: *Galaxies* 4.4, 47, p. 47. DOI: 10.3390/galaxies4040047.

Jorstad, S. G. et al. (Sept. 2017). "Kinematics of Parsec-scale Jets of Gamma-Ray Blazars at 43 GHz within the VLBA-BU-BLAZAR Program". In: *The Astrophysical Journal* 846.2, 98, p. 98. DOI: 10.3847/1538-4357/aa8407. arXiv: 1711.03983 [astro-ph.GA].

Kadler, M. et al. (June 2008). "The Trails of Superluminal Jet Components in 3C 111". In: *The Astrophysical Journal* 680.2, pp. 867–884. DOI: 10.1086/529539. arXiv: 0801.0617 [astro-ph].

Kadler, M. et al. (Aug. 2016). "Coincidence of a high-fluence blazar outburst with a PeV-energy neutrino event". In: *Nature Physics* 12.8, pp. 807–814. DOI: 10.1038/nphys3715. arXiv: 1602.02012 [astro-ph.HE].

Kadler, M. et al. (Mar. 2022). "TELAMON: Monitoring of AGN with the Effelsberg 100-m Telescope in the Context of Astroparticle Physics". In: *37th International Cosmic Ray Conference*, 974, p. 974. DOI: 10.22323/1.395.0974. arXiv: 2108.00383 [astro-ph.HE].

Kadler, M. et al. (2021). "TELAMON: Monitoring of AGN with the Effelsberg 100-m Telescope in the Context of Astroparticle Physics". In: *Proceedings of 37th International Cosmic Ray Conference — PoS(ICRC2021)*. Vol. 395, p. 974. DOI: 10.22323/1.395.0974.

Kalashev, O., D. Semikoz & I. Tkachev (Mar. 2015). "Neutrinos in IceCube from active galactic nuclei". In: *Soviet Journal of Experimental and Theoretical Physics* 120.3, pp. 541–548. DOI: 10.1134/S106377611503022X. arXiv: 1410.8124 [astro-ph.HE].

Kalberla, P. M. W., W. B. Burton, D. Hartmann, E. M. Arnal, E. Bajaja, R. Morras & W. G. L. Pöppel (Sept. 2005). "The Leiden/Argentine/Bonn (LAB) Survey of Galactic HI. Final data release of the combined LDS and IAR surveys with improved stray-radiation corrections". In: *Astronomy and Astrophysics* 440.2, pp. 775–782. DOI: 10.1051/0004-6361:20041864. arXiv: astro-ph/0504140 [astro-ph].

Kapanadze, B., D. Dorner & S. Kapanadze (July 2016). "A new highest historical X-ray State in 1ES 1959+650". In: *The Astronomer's Telegram* 9205, p. 1.

Kardashev, N. S. (Nov. 2000). "Radio Synchrotron Emission by Protons and Electrons in Pulsars and the Nuclei of Quasars". In: *Astronomy Reports* 44.11, pp. 719–724. DOI: 10.1134/1.1320497.

Katarzyński, K., G. Ghisellini, F. Tavecchio, L. Maraschi, G. Fossati & A. Mastichiadis (Apr. 2005). "Correlation between the TeV and X-ray emission in high-energy peaked BL Lac objects". In: *Astronomy and Astrophysics* 433.2, pp. 479–496. DOI: 10.1051/0004-6361:20041556. arXiv: astro-ph/0412405 [astro-ph].

Keivani, A. et al. (Sept. 2018). "A Multimessenger Picture of the Flaring Blazar TXS 0506+056: Implications for High-energy Neutrino Emission and Cosmic-Ray Acceleration". In: *The Astrophysical Journal* 864.1, 84, p. 84. DOI: 10.3847/1538-4357/aad59a. arXiv: 1807.04537 [astro-ph.HE].

Kellermann, K. I. (Jan. 2002). "Brightness Temperature Constraints to Compact Synchrotron Source Radiation Obtained from IDV and VLBI Observations". In: *Publications of the Astron. Soc. of Australia* 19.1, pp. 77–82. DOI: 10.1071/AS01103.

Kellermann, K. I. & I. I. K. Pauliny-Toth (Feb. 1969). "The Spectra of Opaque Radio Sources". In: *The Astrophysical Journal Letters* 155, p. L71. DOI: 10.1086/180305.

Kellermann, K. I., R. Sramek, M. Schmidt, D. B. Shaffer & R. Green (Oct. 1989). "VLA Observations of Objects in the Palomar Bright Quasar Survey". In: *Astronomical Journal* 98, p. 1195. DOI: 10.1086/115207.

Kiepenheuer, K. O. (Aug. 1950). "Cosmic Rays as the Source of General Galactic Radio Emission". In: *Physical Review* 79.4, pp. 738–739. DOI: 10.1103/PhysRev.79.738.

Kimura, S. S., K. Murase & K. Toma (June 2015). "Neutrino and Cosmic-Ray Emission and Cumulative Background from Radiatively Inefficient Accretion Flows in Low-luminosity Active Galactic Nuclei". In: *The Astrophysical Journal* 806.2, 159, p. 159. DOI: 10.1088/0004-637X/806/2/159. arXiv: 1411.3588 [astro-ph.HE].

Komossa, S. (Feb. 2013). "A new probe of black holes and their environment: Luminous flares from tidally disrupted stars". In: *Feeding Compact Objects: Accretion on All Scales*. Ed. by C. M. Zhang, T. Belloni, M. Méndez & S. N. Zhang. Vol. 290, pp. 53–56. DOI: 10.1017/S1743921312019199.

Kotera, K. & A. V. Olinto (Sept. 2011). "The Astrophysics of Ultrahigh-Energy Cosmic Rays". In: *Annual Review of Astron and Astrophys* 49.1, pp. 119–153. DOI: 10.1146/annurev-astro-081710-102620. arXiv: 1101.4256 [astro-ph.HE].

Kovalev, Y. Y., M. L. Lister, D. C. Homan & K. I. Kellermann (Oct. 2007). "The Inner Jet of the Radio Galaxy M87". In: *The Astrophysical Journal Letters* 668.1, pp. L27–L30. DOI: 10.1086/522603. arXiv: 0708.2695 [astro-ph].

Kovalev, Y. Y., S. V. Troitsky, Y. A. Kovalev & A. V. Plavin (Jan. 2020a). "Flat spectrum radio quasar TXS 1100+122 has a bright VLBI-compact core - as expected for neutrino candidate sources". In: *The Astronomer's Telegram* 13397, p. 1.

Kovalev, Y. A., Y. V. Sotnikova, A. K. Erkenov, Y. Y. Kovalev, A. V. Plavin & S. V. Troitsky (Jan. 2020b). "The RATAN-600 2-22 GHz continuum spectrum of the neutrino association quasar TXS 1100+122 is slightly rising". In: *The Astronomer's Telegram* 13405, p. 1.

Krawczynski, H. et al. (Jan. 2004). "Multiwavelength Observations of Strong Flares from the TeV Blazar 1ES 1959+650". In: *The Astrophysical Journal* 601.1, pp. 151–164. DOI: 10.1086/380393. arXiv: astro-ph/0310158 [astro-ph].

Kun, E., P. L. Biermann & L. Á. Gergely (Feb. 2019). "Very long baseline interferometry radio structure and radio brightening of the high-energy neutrino emitting blazar TXS 0506+056".

In: *Monthly Notices of the Royal Astronomical Society* 483.1, pp. L42–L46. DOI: 10.1093/mnrasl/sly216. arXiv: 1807.07942 [astro-ph.HE].

Lacy, M. et al. (Mar. 2020). "The Karl G. Jansky Very Large Array Sky Survey (VLASS). Science Case and Survey Design". In: *PASP* 132.1009, 035001, p. 035001. DOI: 10.1088/1538-3873/ab63eb. arXiv: 1907.01981 [astro-ph.IM].

Lamanna, G. et al. (July 2015). "Cherenkov Telescope Array Data Management". In: *34th International Cosmic Ray Conference (ICRC2015)*. Vol. 34. International Cosmic Ray Conference, 947, p. 947. DOI: 10.22323/1.236.0947. arXiv: 1509.01012 [astro-ph.IM].

Larson, M. J. et al. (2021). "Testing the AGN Radio and Neutrino correlation using the MOJAVE catalog and 10 years of IceCube Data". In: *Proceedings of 37th International Cosmic Ray Conference — PoS(ICRC2021)*. Vol. 395, p. 949. DOI: 10.22323/1.395.0949.

Levenberg, K. (1944). "Method for the solution of certain problems in least squares siam". In: *J Numer Anal* 16, 588–A604.

Li, T. .-. & Y. .-. Ma (Sept. 1983). "Analysis methods for results in gamma-ray astronomy." In: *The Astrophysical Journal* 272, pp. 317–324. DOI: 10.1086/161295.

Li, X., T. An, P. Mohan & M. Giroletti (June 2020). "The Parsec-scale Jet of the Neutrino-emitting Blazar TXS 0506+056". In: *The Astrophysical Journal* 896.1, 63, p. 63. DOI: 10.3847/1538-4357/ab8f9f. arXiv: 2005.00300 [astro-ph.GA].

Linfield, R. (Nov. 1981). "A precessing jet model of compact radio sources". In: *The Astrophysical Journal* 250, pp. 464–468. DOI: 10.1086/159393.

Liodakis, I. et al. (Oct. 2022). "The hunt for extraterrestrial high-energy neutrino counterparts". In: *Astronomy and Astrophysics* 666, A36, A36. DOI: 10.1051/0004-6361/202244551. arXiv: 2208.07381 [astro-ph.HE].

Liodakis, I. & M. Petropoulou (Apr. 2020). "Proton Synchrotron Gamma-Rays and the Energy Crisis in Blazars". In: *The Astrophysical Journal Letters* 893.1, L20, p. L20. DOI: 10.3847/2041-8213/ab830a. arXiv: 2003.10460 [astro-ph.HE].

Lister, M. L., M. F. Aller, H. D. Aller, M. A. Hodge, D. C. Homan, Y. Y. Kovalev, A. B. Pushkarev & T. Savolainen (Jan. 2018). "MOJAVE. XV. VLBA 15 GHz Total Intensity and Polarization Maps of 437 Parsec-scale AGN Jets from 1996 to 2017". In: *Astrophysical Journal, Supplement* 234.1, 12, p. 12. DOI: 10.3847/1538-4365/aa9c44. arXiv: 1711.07802 [astro-ph.GA].

Lister, M. L., M. H. Cohen, D. C. Homan, M. Kadler, K. I. Kellermann, Y. Y. Kovalev, E. Ros, T. Savolainen & J. A. Zensus (Dec. 2009a). "MOJAVE: Monitoring of Jets in Active Galactic Nuclei with VLBA Experiments. VI. Kinematics Analysis of a Complete Sample of Blazar Jets". In: *Astronomical Journal* 138.6, pp. 1874–1892. DOI: 10.1088/0004-6256/138/6/1874. arXiv: 0909.5100 [astro-ph.CO].

Lister, M. L. et al. (Mar. 2009b). "MOJAVE: Monitoring of Jets in Active Galactic Nuclei with VLBA Experiments. V. Multi-Epoch VLBA Images". In: *Astronomical Journal* 137.3, pp. 3718–3729. DOI: 10.1088/0004-6256/137/3/3718. arXiv: 0812.3947 [astro-ph].

Lister, M. L. et al. (Mar. 2019). "MOJAVE. XVII. Jet Kinematics and Parent Population Properties of Relativistically Beamed Radio-loud Blazars". In: *The Astrophysical Journal* 874.1, 43, p. 43. DOI: 10.3847/1538-4357/ab08ee. arXiv: 1902.09591 [astro-ph.GA].

Liu, S. & F. Melia (July 2002). "Spin-induced Disk Precession in the Supermassive Black Hole at the Galactic Center". In: *The Astrophysical Journal Letters* 573.1, pp. L23–L26. DOI: 10.1086/341991. arXiv: astro-ph/0205487 [astro-ph].

Lobanov, A. P. & J. Roland (Mar. 2005). "A supermassive binary black hole in the quasar 3C 345". In: *Astronomy and Astrophysics* 431.3, pp. 831–846. DOI: 10.1051/0004-6361:20041831. arXiv: astro-ph/0411417 [astro-ph].

Lobanov, A. P. & J. A. Zensus (Oct. 2001). "A Cosmic Double Helix in the Archetypical Quasar 3C273". In: *Science* 294.5540, pp. 128–131. DOI: 10.1126/science.1063239.

Maggi, G., IceCube Collaboration, K. D. de Vries & N. van Eijndhoven (Jan. 2017). "Investigation of Obscured Flat Spectrum Radio AGN with the IceCube Neutrino Observatory". In: *35th International Cosmic Ray Conference (ICRC2017)*. Vol. 301. International Cosmic Ray Conference, 1000, p. 1000.

MAGIC Collaboration et al. (Mar. 2019). "A fast, very-high-energy γ-ray flare from BL Lacertae during a period of multi-wavelength activity in June 2015". In: *Astronomy and Astrophysics* 623, A175, A175. DOI: 10.1051/0004-6361/201834010. arXiv: 1901.01733 [astro-ph.HE].

MAGIC Collaboration et al. (June 2020a). "Broadband characterisation of the very intense TeV flares of the blazar 1ES 1959+650 in 2016". In: *Astronomy and Astrophysics* 638, A14, A14. DOI: 10.1051/0004-6361/201935450. arXiv: 2002.00129 [astro-ph.HE].

MAGIC Collaboration et al. (Mar. 2020b). "Monitoring of the radio galaxy M 87 during a low-emission state from 2012 to 2015 with MAGIC". In: *Monthly Notices of the Royal Astronomical Society* 492.4, pp. 5354–5365. DOI: 10.1093/mnras/staa014. arXiv: 2001.01643 [astro-ph.HE].

MAGIC Collaboration et al. (Aug. 2020c). "Testing two-component models on very high-energy gamma-ray-emitting BL Lac objects". In: *Astronomy and Astrophysics* 640, A132, A132. DOI: 10.1051/0004-6361/202037811. arXiv: 2006.04493 [astro-ph.HE].

MAGIC Collaboration et al. (Nov. 2021). "Investigation of the correlation patterns and the Compton dominance variability of Mrk 421 in 2017". In: *Astronomy and Astrophysics* 655, A89, A89. DOI: 10.1051/0004-6361/202141004. arXiv: 2106.05516 [astro-ph.HE].

Mannheim, K. (Mar. 1993). "The proton blazar." In: *Astronomy and Astrophysics* 269, pp. 67–76. DOI: 10.48550/arXiv.astro-ph/9302006. arXiv: astro-ph/9302006 [astro-ph].

Mannheim, K. (May 1995). "High-energy neutrinos from extragalactic jets". In: *Astroparticle Physics* 3.3, pp. 295–302. DOI: 10.1016/0927-6505(94)00044-4.

Margutti, R. & R. Chornock (Sept. 2021). "First Multimessenger Observations of a Neutron Star Merger". In: *Annual Review of Astron and Astrophys* 59, pp. 155–202. DOI: 10.1146/annurev-astro-112420-030742. arXiv: 2012.04810 [astro-ph.HE].

Marquardt, D. W. (1963). "An algorithm for least-squares estimation of nonlinear parameters". In: *Journal of the society for Industrial and Applied Mathematics* 11.2, pp. 431–441.

Marscher, A. P. & W. K. Gear (Nov. 1985). "Models for high-frequency radio outbursts in extragalactic sources, with application to the early 1983 millimeter-to-infrared flare of 3C 273." In: *The Astrophysical Journal* 298, pp. 114–127. DOI: 10.1086/163592.

Marscher, A. P. et al. (Feb. 2010). "Probing the Inner Jet of the Quasar PKS 1510-089 with Multi-Waveband Monitoring During Strong Gamma-Ray Activity". In: *The Astrophysical Journal Letters* 710.2, pp. L126–L131. DOI: 10.1088/2041-8205/710/2/L126. arXiv: 1001.2574 [astro-ph.CO].

Massaro, F., M. Giroletti, A. Paggi, R. D'Abrusco, G. Tosti & S. Funk (Oct. 2013). "Blazar Spectral Properties at 74 MHz". In: *Astrophysical Journal, Supplement* 208.2, 15, p. 15. DOI: 10.1088/0067-0049/208/2/15. arXiv: 1308.0594 [astro-ph.HE].

Matthews, J. H., A. R. Bell & K. M. Blundell (Sept. 2020). "Particle acceleration in astrophysical jets". In: *New A Rev.* 89, 101543, p. 101543. DOI: 10.1016/j.newar.2020.101543. arXiv: 2003.06587 [astro-ph.HE].

Mazin, D. & M. Raue (Aug. 2007). "New limits on the density of the extragalactic background light in the optical to the far infrared from the spectra of all known TeV blazars". In: *Astronomy and Astrophysics* 471.2, pp. 439–452. DOI: 10.1051/0004-6361:20077158. arXiv: astro-ph/0701694 [astro-ph].

Mazin, D., M. Raue, B. Behera, S. Inoue, Y. Inoue, T. Nakamori, T. Totani & CTA Consortium (Mar. 2013). "Potential of EBL and cosmology studies with the Cherenkov Telescope Array".

In: *Astroparticle Physics* 43, pp. 241–251. DOI: 10.1016/j.astropartphys.2012.09.002. arXiv: 1303.7124 [astro-ph.CO].

McMullin, J. P., B. Waters, D. Schiebel, W. Young & K. Golap (Oct. 2007). "CASA Architecture and Applications". In: *Astronomical Data Analysis Software and Systems XVI*. Ed. by R. A. Shaw, F. Hill & D. J. Bell. Vol. 376. Astronomical Society of the Pacific Conference Series, p. 127.

Menezes, R. de et al. (2021). "Multi-Messenger observations of the Fermi-LAT blazar 4FGL J0658.6+0636 consistent with an IceCube high-energy neutrino". In: *Proceedings of 37th International Cosmic Ray Conference — PoS(ICRC2021)*. Vol. 395, p. 955. DOI: 10.22323/1.395.0955.

Mészáros, P., D. B. Fox, C. Hanna & K. Murase (Oct. 2019). "Multi-messenger astrophysics". In: *Nature Reviews Physics* 1.10, pp. 585–599. DOI: 10.1038/s42254-019-0101-z. arXiv: 1906.10212 [astro-ph.HE].

Mirzoyan, R. (Jan. 1997). "On the Calibration Accuracy of Light Sensors in Atmospheric Cherenkov Fluorescence and Neutrino Experiments". In: *International Cosmic Ray Conference*. Vol. 7. International Cosmic Ray Conference, p. 265.

Mohan, P., T. An, Y. Zhang, J. Yang, X. Yang & A. Wang (Mar. 2022). "High-resolution VLBI Observations of and Modeling the Radio Emission from the Tidal Disruption Event AT2019dsg". In: *The Astrophysical Journal* 927.1, 74, p. 74. DOI: 10.3847/1538-4357/ac4cb2. arXiv: 2106.15799 [astro-ph.HE].

Moldon, J. (Sept. 2021). *eMCP: e-MERLIN CASA pipeline*. ascl: 2109.006.

Moore, D. S. (2009). *Introduction to the Practice of Statistics*. WH Freeman and company.

Mücke, A., R. J. Protheroe, R. Engel, J. P. Rachen & T. Stanev (Mar. 2003). "BL Lac objects in the synchrotron proton blazar model". In: *Astroparticle Physics* 18.6, pp. 593–613. DOI: 10.1016/S0927-6505(02)00185-8. arXiv: astro-ph/0206164 [astro-ph].

Murase, K., S. S. Kimura & P. Mészáros (July 2020a). "Hidden Cores of Active Galactic Nuclei as the Origin of Medium-Energy Neutrinos: Critical Tests with the MeV Gamma-Ray Connection". In: *Phys. Rev. Lett.* 125.1, 011101, p. 011101. DOI: 10.1103/PhysRevLett.125.011101. arXiv: 1904.04226 [astro-ph.HE].

Murase, K., S. S. Kimura, B. T. Zhang, F. Oikonomou & M. Petropoulou (Oct. 2020b). "High-energy Neutrino and Gamma-Ray Emission from Tidal Disruption Events". In: *The Astrophysical Journal* 902.2, 108, p. 108.

Myles Hollander, M. & A. W. Douglas (1973). *Nonparametric statistical methods*.

Nanci, C. et al. (July 2022). "Observing the inner parsec-scale region of candidate neutrino-emitting blazars". In: *Astronomy and Astrophysics* 663, A129, A129. DOI: 10.1051/0004-6361/202142665. arXiv: 2203.13268 [astro-ph.HE].

Nanci, C. et al. (Aug. 2023). "A VLBI investigation of high-energy neutrino emitter candidates". In: *15th European VLBI Network Mini-Symposium and Users' Meeting*, 16, p. 16.

Narayan, R. & T. Piran (Feb. 2012). "Variability in blazars: clues from PKS 2155-304". In: *Monthly Notices of the Royal Astronomical Society* 420.1, pp. 604–612. DOI: 10.1111/j.1365-2966.2011.20069.x. arXiv: 1107.5812 [astro-ph.HE].

Neronov, A. Y. & D. V. Semikoz (Dec. 2002). "Which blazars are neutrino loud?" In: *Phys. Rev. D* 66.12, 123003, p. 123003. DOI: 10.1103/PhysRevD.66.123003. arXiv: hep-ph/0208248 [hep-ph].

Neronov, A. & I. Vovk (Apr. 2010). "Evidence for Strong Extragalactic Magnetic Fields from Fermi Observations of TeV Blazars". In: *Science* 328.5974, p. 73. DOI: 10.1126/science.1184192. arXiv: 1006.3504 [astro-ph.HE].

Netzer, H. (2013). *The Physics and Evolution of Active Galactic Nuclei*.

Nigro, C., J. Sitarek, P. Gliwny, D. Sanchez, A. Tramacere & M. Craig (Apr. 2022). "agnpy: An open-source python package modelling the radiative processes of jetted active galactic nu-

clei". In: *Astronomy and Astrophysics* 660, A18, A18. DOI: 10.1051/0004-6361/202142000. arXiv: 2112.14573 [astro-ph.IM].

Nigro, C. & A. Tramacere (July 2022). "Open-Source Radiative Modeling Tools for Extragalactic VHE Gamma-ray Sources". In: *Galaxies* 10.4, 85, p. 85. DOI: 10.3390/galaxies10040085. arXiv: 2207.13525 [astro-ph.IM].

Nilsson, K., T. Pursimo, C. Villforth, E. Lindfors, L. O. Takalo & A. Sillanpää (Nov. 2012). "Redshift constraints for RGB 0136+391 and PKS 0735+178 from deep optical imaging". In: *Astronomy and Astrophysics* 547, A1, A1. DOI: 10.1051/0004-6361/201219848. arXiv: 1209.4755 [astro-ph.CO].

Nilsson, K. et al. (Dec. 2018). "Long-term optical monitoring of TeV emitting blazars. I. Data analysis". In: *Astronomy and Astrophysics* 620, A185, A185. DOI: 10.1051/0004-6361/201833621. arXiv: 1810.01751 [astro-ph.HE].

Nishiyama, T. (Aug. 1999). "Detection of a new TeV gamma-ray source of BL Lac object 1ES 1959+650". In: *26th International Cosmic Ray Conference (ICRC26), Volume 3*. Vol. 3. International Cosmic Ray Conference, p. 370.

Oikonomou, F., K. Murase, P. Padovani, E. Resconi & P. Mészáros (Nov. 2019). "High-energy neutrino flux from individual blazar flares". In: *Monthly Notices of the Royal Astronomical Society* 489.3, pp. 4347–4366. DOI: 10.1093/mnras/stz2246. arXiv: 1906.05302 [astro-ph.HE].

Ojha, R. et al. (Sept. 2010). "TANAMI: tracking active galactic nuclei with austral milliarcsecond interferometry . I. First-epoch 8.4 GHz images". In: *Astronomy and Astrophysics* 519, A45, A45. DOI: 10.1051/0004-6361/200912724. arXiv: 1005.4432 [astro-ph.CO].

Orienti, M., F. D'Ammando, M. Giroletti, D. Dallacasa, T. Venturi & G. Giovannini (Dec. 2013a). "On the connection between radio and gamma rays. Variability and polarization properties in relativistic jets". In: *European Physical Journal Web of Conferences*. Vol. 61. European Physical Journal Web of Conferences, 04009, p. 04009. DOI: 10.1051/epjconf/20136104009. arXiv: 1309.5286 [astro-ph.HE].

Orienti, M. et al. (Jan. 2013b). "Radio and γ-ray follow-up of the exceptionally high-activity state of PKS 1510-089 in 2011". In: *Monthly Notices of the Royal Astronomical Society* 428.3, pp. 2418–2429. DOI: 10.1093/mnras/sts201. arXiv: 1210.4319 [astro-ph.HE].

Padovani, P., B. Boccardi, R. Falomo & P. Giommi (Apr. 2022a). "PKS 1424+240: yet another masquerading BL Lac object as a possible IceCube neutrino source". In: *Monthly Notices of the Royal Astronomical Society* 511.4, pp. 4697–4701. DOI: 10.1093/mnras/stac376. arXiv: 2202.04363 [astro-ph.HE].

Padovani, P., P. Giommi, R. Falomo, F. Oikonomou, M. Petropoulou, T. Glauch, E. Resconi, A. Treves & S. Paiano (Feb. 2022b). "The spectra of IceCube neutrino (SIN) candidate sources - II. Source characterization". In: *Monthly Notices of the Royal Astronomical Society* 510.2, pp. 2671–2688. DOI: 10.1093/mnras/stab3630. arXiv: 2112.05394 [astro-ph.HE].

Padovani, P., F. Oikonomou, M. Petropoulou, P. Giommi & E. Resconi (Mar. 2019). "TXS 0506+056, the first cosmic neutrino source, is not a BL Lac". In: *Monthly Notices of the Royal Astronomical Society* 484.1, pp. L104–L108. DOI: 10.1093/mnrasl/slz011. arXiv: 1901.06998 [astro-ph.HE].

Padovani, P., A. Turcati & E. Resconi (July 2018). "AGN outflows as neutrino sources: an observational test". In: *Monthly Notices of the Royal Astronomical Society* 477.3, pp. 3469–3479. DOI: 10.1093/mnras/sty877. arXiv: 1804.01386 [astro-ph.HE].

Padovani, P. et al. (Aug. 2017). "Active galactic nuclei: what's in a name?" In: *Astronomy and Astrophysics Reviews* 25.1, 2, p. 2. DOI: 10.1007/s00159-017-0102-9. arXiv: 1707.07134 [astro-ph.GA].

Padovani, P. (Aug. 2017). "On the two main classes of active galactic nuclei". In: *Nature Astronomy* 1, 0194, p. 0194. DOI: 10.1038/s41550-017-0194. arXiv: 1707.08069 [astro-ph.GA].

Paiano, S., R. Falomo, A. Treves & R. Scarpa (Feb. 2018). "The Redshift of the BL Lac Object TXS 0506+056". In: *ApJL* 854.2, L32, p. L32. DOI: 10.3847/2041-8213/aaad5e. arXiv: 1802.01939 [astro-ph.GA].

Paragi, Z. et al. (Apr. 2015). "Very Long Baseline Interferometry with the SKA". In: *Advancing Astrophysics with the Square Kilometre Array (AASKA14)*, 143, p. 143. DOI: 10.22323/1.215.0143. arXiv: 1412.5971 [astro-ph.IM].

Peirson, A. L. et al. (Mar. 2022). "New Tests of Milli-lensing in the Blazar PKS 1413 + 135". In: *The Astrophysical Journal* 927.1, 24, p. 24. DOI: 10.3847/1538-4357/ac469e. arXiv: 2201.01110 [astro-ph.GA].

Perlman, E. S., J. T. Stocke, J. F. Schachter, M. Elvis, E. Ellingson, C. M. Urry, M. Potter, C. D. Impey & P. Kolchinsky (June 1996). "The Einstein Slew Survey Sample of BL Lacertae Objects". In: *Astrophysical Journal, Supplement* 104, p. 251. DOI: 10.1086/192300.

Petropoulou, M., S. Dimitrakoudis, P. Padovani, A. Mastichiadis & E. Resconi (Apr. 2015). "Photohadronic origin of γ -ray BL Lac emission: implications for IceCube neutrinos". In: *Monthly Notices of the Royal Astronomical Society* 448.3, pp. 2412–2429. DOI: 10.1093/mnras/stv179. arXiv: 1501.07115 [astro-ph.HE].

Petropoulou, M., D. Giannios & S. Dimitrakoudis (Nov. 2014). "Implications of a PeV neutrino spectral cut-off in gamma-ray burst models". In: *Monthly Notices of the Royal Astronomical Society* 445.1, pp. 570–580. DOI: 10.1093/mnras/stu1757. arXiv: 1405.2091 [astro-ph.HE].

Petropoulou, M. et al. (Mar. 2020). "Multi-epoch Modeling of TXS 0506+056 and Implications for Long-term High-energy Neutrino Emission". In: *The Astrophysical Journal* 891.2, 115, p. 115. DOI: 10.3847/1538-4357/ab76d0. arXiv: 1911.04010 [astro-ph.HE].

Plavin, A. V., Y. Y. Kovalev, Y. A. Kovalev & S. V. Troitsky (Aug. 2023). "Growing evidence for high-energy neutrinos originating in radio blazars". In: *Monthly Notices of the Royal Astronomical Society* 523.2, pp. 1799–1808. DOI: 10.1093/mnras/stad1467. arXiv: 2211.09631 [astro-ph.HE].

Plavin, A. V., Y. Y. Kovalev, Y. A. Kovalev & S. V. Troitsky (Feb. 2021). "Directional Association of TeV to PeV Astrophysical Neutrinos with Radio Blazars". In: *The Astrophysical Journal* 908.2, 157, p. 157. DOI: 10.3847/1538-4357/abceb8. arXiv: 2009.08914 [astro-ph.HE].

Plavin, A., Y. Y. Kovalev, Y. A. Kovalev & S. Troitsky (May 2020). "Observational Evidence for the Origin of High-energy Neutrinos in Parsec-scale Nuclei of Radio-bright Active Galaxies". In: *The Astrophysical Journal* 894.2, 101, p. 101. DOI: 10.3847/1538-4357/ab86bd. arXiv: 2001.00930 [astro-ph.HE].

Prandini, E. & G. Ghisellini (Feb. 2022). "The Blazar Sequence and Its Physical Understanding". In: *Galaxies* 10.1, 35, p. 35. DOI: 10.3390/galaxies10010035. arXiv: 2202.07490 [astro-ph.HE].

Pushkarev, A. B., Y. Y. Kovalev, M. L. Lister & T. Savolainen (Nov. 2009). "Jet opening angles and gamma-ray brightness of AGN". In: *Astronomy and Astrophysics* 507.2, pp. L33–L36. DOI: 10.1051/0004-6361/200913422. arXiv: 0910.1813 [astro-ph.CO].

Raiteri, C. M. et al. (Dec. 2017). "Blazar spectral variability as explained by a twisted inhomogeneous jet". In: *Nature* 552.7685, pp. 374–377. DOI: 10.1038/nature24623. arXiv: 1712.02098 [astro-ph.HE].

Readhead, A. C. S. et al. (Feb. 2021). "The Relativistic Jet Orientation and Host Galaxy of the Peculiar Blazar PKS 1413+135". In: *The Astrophysical Journal* 907.2, 61, p. 61. DOI: 10.3847/1538-4357/abd08c. arXiv: 2012.04045 [astro-ph.GA].

Reimer, A., M. Böttcher & S. Buson (Aug. 2019). "Cascading Constraints from Neutrino-emitting Blazars: The Case of TXS 0506+056". In: *The Astrophysical Journal* 881.1, 46, p. 46. DOI: 10.3847/1538-4357/ab2bff. arXiv: 1812.05654 [astro-ph.HE].

Richards, J. L. et al. (June 2011). "Blazars in the Fermi Era: The OVRO 40 m Telescope Monitoring Program". In: *Astrophysical Journal, Supplement* 194.2, 29, p. 29. DOI: 10.1088/0067-0049/194/2/29. arXiv: 1011.3111 [astro-ph.CO].

Rieger, F. M. (Nov. 2004). "On the Geometrical Origin of Periodicity in Blazar-type Sources". In: *The Astrophysical Journal Letters* 615.1, pp. L5–L8. DOI: 10.1086/426018. arXiv: astro-ph/0410188 [astro-ph].

Righi, C., F. Tavecchio & S. Inoue (Feb. 2019). "Neutrino emission from BL Lac objects: the role of radiatively inefficient accretion flows". In: *Monthly Notices of the Royal Astronomical Society* 483.1, pp. L127–L131. DOI: 10.1093/mnrasl/sly231. arXiv: 1807.10506 [astro-ph.HE].

Rodrigues, X., S. Gao, A. Fedynitch, A. Palladino & W. Winter (Apr. 2019). "Leptohadronic Blazar Models Applied to the 2014-2015 Flare of TXS 0506+056". In: *The Astrophysical Journal Letters* 874.2, L29, p. L29. DOI: 10.3847/2041-8213/ab1267. arXiv: 1812.05939 [astro-ph.HE].

Rodrigues, X., V. S. Paliya, S. Garrappa, A. Omeliukh, A. Franckowiak & W. Winter (July 2023). "Leptohadronic Multimessenger Modeling of 324 Gamma-Ray Blazars". In: *arXiv e-prints*, arXiv:2307.13024, arXiv:2307.13024. DOI: 10.48550/arXiv.2307.13024. arXiv: 2307.13024 [astro-ph.HE].

Roming, P. W. A. et al. (Oct. 2005). "The Swift Ultra-Violet/Optical Telescope". In: *Space Science Reviews* 120.3-4, pp. 95–142. DOI: 10.1007/s11214-005-5095-4. arXiv: astro-ph/0507413 [astro-ph].

Ros, E., M. Kadler, M. Perucho, B. Boccardi, H. .-. Cao, M. Giroletti, F. Krauß & R. Ojha (Jan. 2020). "Apparent superluminal core expansion and limb brightening in the candidate neutrino blazar TXS 0506+056". In: *Astronomy and Astrophysics* 633, L1, p. L1. DOI: 10.1051/0004-6361/201937206. arXiv: 1912.01743 [astro-ph.GA].

Rossi, B. & K. Greisen (Oct. 1941). "Cosmic-Ray Theory". In: *Reviews of Modern Physics* 13.4, pp. 240–309. DOI: 10.1103/RevModPhys.13.240.

Rybicki, G. B. & A. P. Lightman (1986). *Radiative Processes in Astrophysics*.

Sahakyan, N., P. Giommi, P. Padovani, M. Petropoulou, D. Bégué, B. Boccardi & S. Gasparyan (Feb. 2023). "A multimessenger study of the blazar PKS 0735+178: a new major neutrino source candidate". In: *Monthly Notices of the Royal Astronomical Society* 519.1, pp. 1396–1408. DOI: 10.1093/mnras/stac3607. arXiv: 2204.05060 [astro-ph.HE].

Sahu, S., C. E. Lopez Fortin, L. H. Castaneda Hernandez & S. Rajpoot (Jan. 2021). "A Two-zone Photohadronic Interpretation of the EHBL-like Behavior of the 2016 Multi-TeV Flares of 1ES 1959+650". In: *The Astrophysical Journal* 906.2, 91, p. 91. DOI: 10.3847/1538-4357/abc9c6. arXiv: 2011.00082 [astro-ph.HE].

Sahu, S., A. F. O. Oliveros & J. C. Sanabria (May 2013). "Hadronic-origin orphan TeV flare from 1ES 1959+650". In: *Phys. Rev. D* 87.10, 103015, p. 103015. DOI: 10.1103/PhysRevD.87.103015. arXiv: 1305.4985 [hep-ph].

Scargle, J. D., J. P. Norris, B. Jackson & J. Chiang (Feb. 2013). "Studies in Astronomical Time Series Analysis. VI. Bayesian Block Representations". In: *The Astrophysical Journal* 764.2, 167, p. 167. DOI: 10.1088/0004-637X/764/2/167. arXiv: 1207.5578 [astro-ph.IM].

Schlegel, D. J., D. P. Finkbeiner & M. Davis (June 1998). "Maps of Dust Infrared Emission for Use in Estimation of Reddening and Cosmic Microwave Background Radiation Foregrounds". In: *The Astrophysical Journal* 500.2, pp. 525–553. DOI: 10.1086/305772. arXiv: astro-ph/9710327 [astro-ph].

Schmelling, M. (Feb. 1994). "The method of reduced cross-entropy A general approach to unfold probability distributions". In: *Nuclear Instruments and Methods in Physics Research A* 340.2, pp. 400–412. DOI: 10.1016/0168-9002(94)90119-8.

Shaw, M. S. et al. (Mar. 2012). "Spectroscopy of Broad-line Blazars from 1LAC". In: *The Astrophysical Journal* 748.1, 49, p. 49. DOI: 10.1088/0004-637X/748/1/49. arXiv: 1201.0999 [astro-ph.HE].

Shepherd, M. C., T. J. Pearson & G. B. Taylor (May 1994). "DIFMAP: an interactive program for synthesis imaging." In: *Bulletin of the American Astronomical Society*. Vol. 26, pp. 987–989.

Shukla, A. & K. Mannheim (Aug. 2020). "Gamma-ray flares from relativistic magnetic reconnection in the jet of the quasar 3C 279". In: *Nature Communications* 11, 4176, p. 4176. DOI: 10.1038/s41467-020-17912-z.

Sikora, M., M. C. Begelman & M. J. Rees (Jan. 1994). "Comptonization of Diffuse Ambient Radiation by a Relativistic Jet: The Source of Gamma Rays from Blazars?" In: *The Astrophysical Journal* 421, p. 153. DOI: 10.1086/173633.

Sinapius, J., S. Garrappa, S. Buson, C. Bartolini & L. Pfeiff (Jan. 2024). "Fermi-LAT detection of increased gamma-ray activity of blazar PKS 0446+11, located inside the IceCube-240105A error region". In: *The Astronomer's Telegram* 16398, p. 1.

Singh, K. K. et al. (Dec. 2018). "Study of short term enhanced TeV γ- ray emission from Mrk 421 observed with TACTIC on December 28, 2014". In: *Astroparticle Physics* 103, pp. 122–130. DOI: 10.1016/j.astropartphys.2018.08.003. arXiv: 1808.02670 [astro-ph.HE].

Singh, K. K. & P. J. Meintjes (July 2020). "Characterization of variability in blazar light curves". In: *Astronomische Nachrichten* 341.713, pp. 713–725. DOI: 10.1002/asna.202013731. arXiv: 2006.05166 [astro-ph.HE].

Sinha, A., R. Khatoon, R. Misra, S. Sahayanathan, S. Mandal, R. Gogoi & N. Bhatt (Oct. 2018). "The flux distribution of individual blazars as a key to understand the dynamics of particle acceleration". In: *Monthly Notices of the Royal Astronomical Society* 480.1, pp. L116–L120. DOI: 10.1093/mnrasl/sly136. arXiv: 1807.09073 [astro-ph.HE].

Soares, G. & R. Nemmen (June 2020). "Jet efficiencies and black hole spins in jetted quasars". In: *Monthly Notices of the Royal Astronomical Society* 495.1, pp. 981–991. DOI: 10.1093/mnras/staa1241. arXiv: 2005.00381 [astro-ph.HE].

Sol, H. & A. Zech (Nov. 2022). "Blazars at Very High Energies: Emission Modelling". In: *Galaxies* 10.6, 105, p. 105. DOI: 10.3390/galaxies10060105. arXiv: 2211.03580 [astro-ph.HE].

Sol, H. et al. (July 2013). "Prospect on intergalactic magnetic field measurements with gamma-ray instruments". In: *Solar and Astrophysical Dynamos and Magnetic Activity*. Ed. by A. G. Kosovichev, E. de Gouveia Dal Pino & Y. Yan. Vol. 294, pp. 459–470. DOI: 10.1017/S1743921313002925.

Stathopoulos, S. I., M. Petropoulou, P. Giommi, G. Vasilopoulos, P. Padovani & A. Mastichiadis (2021). "Probing Neutrino Emission from X-ray Blazar Flares observed with Swift-XRT". In: *Proceedings of 37th International Cosmic Ray Conference — PoS(ICRC2021)*. Vol. 395, p. 1008. DOI: 10.22323/1.395.1008.

Steffen, W., J. A. Zensus, T. P. Krichbaum, A. Witzel & S. J. Qian (Oct. 1995). "A helical model for the compact jet in 3C345." In: *Astronomy and Astrophysics* 302, p. 335. DOI: 10.48550/arXiv.astro-ph/9505075. arXiv: astro-ph/9505075 [astro-ph].

Stein, R. et al. (Jan. 2021). "A tidal disruption event coincident with a high-energy neutrino". In: *Nature Astronomy* 5, pp. 510–518. DOI: 10.1038/s41550-020-01295-8. arXiv: 2005.05340 [astro-ph.HE].

Stickel, M., J. W. Fried & H. Kuehr (Feb. 1988). "The redshifts of the BL Lac objects 1749+096 and 2254+074." In: *Astronomy and Astrophysics* 191, pp. L16–L18.

Tagliaferri, G. et al. (June 2008). "Simultaneous Multiwavelength Observations of the Blazar 1ES 1959+650 at a Low TeV Flux". In: *The Astrophysical Journal* 679.2, pp. 1029–1039. DOI: 10.1086/586731. arXiv: 0801.4029 [astro-ph].

Takalo, L. O., K. Nilsson, E. Lindfors, A. Sillanpää, A. Berdyugin & M. Pasanen (Dec. 2008). "Tuorla Blazar Monitoring Program". In: *American Institute of Physics Conference Series*. Ed. by F. A. Aharonian, W. Hofmann & F. Rieger. Vol. 1085. American Institute of Physics Conference Series, pp. 705–707. DOI: 10.1063/1.3076774.

Tamborra, I., S. Ando & K. Murase (Sept. 2014). "Star-forming galaxies as the origin of diffuse high-energy backgrounds: gamma-ray and neutrino connections, and implications for starburst history". In: *Journal of Cosmology and Astroparticle Physics* 2014.9, pp. 043–043. DOI: 10.1088/1475-7516/2014/09/043. arXiv: 1404.1189 [astro-ph.HE].

Tanaka, Y. T., S. Buson & D. Kocevski (Sept. 2017). "Fermi-LAT detection of increased gamma-ray activity of TXS 0506+056, located inside the IceCube-170922A error region." In: *The Astronomer's Telegram* 10791, p. 1.

Tavecchio, F., G. Ghisellini, G. Bonnoli & G. Ghirlanda (June 2010a). "Constraining the location of the emitting region in Fermi blazars through rapid γ-ray variability". In: *Monthly Notices of the Royal Astronomical Society* 405.1, pp. L94–L98. DOI: 10.1111/j.1745-3933.2010.00867.x. arXiv: 1003.3475 [astro-ph.CO].

Tavecchio, F., G. Ghisellini, L. Foschini, G. Bonnoli, G. Ghirlanda & P. Coppi (July 2010b). "The intergalactic magnetic field constrained by Fermi/Large Area Telescope observations of the TeV blazar 1ES0229+200". In: *Monthly Notices of the Royal Astronomical Society* 406.1, pp. L70–L74. DOI: 10.1111/j.1745-3933.2010.00884.x. arXiv: 1004.1329 [astro-ph.CO].

Tavecchio, F., G. Ghisellini, G. Ghirlanda, L. Costamante & A. Franceschini (Oct. 2009). "The hard TeV spectrum of 1ES 0229+200: new clues from Swift". In: *Monthly Notices of the Royal Astronomical Society* 399.1, pp. L59–L63. DOI: 10.1111/j.1745-3933.2009.00724.x. arXiv: 0905.0899 [astro-ph.CO].

Tavecchio, F., G. Ghisellini, G. Ghirlanda, L. Foschini & L. Maraschi (Jan. 2010c). "TeV BL Lac objects at the dawn of the Fermi era". In: *Monthly Notices of the Royal Astronomical Society* 401.3, pp. 1570–1586. DOI: 10.1111/j.1365-2966.2009.15784.x. arXiv: 0909.0651 [astro-ph.HE].

Tavecchio, F. & G. Ghisellini (Mar. 2008). "Spine-sheath layer radiative interplay in subparsec-scale jets and the TeV emission from M87". In: *Monthly Notices of the Royal Astronomical Society* 385.1, pp. L98–L102. DOI: 10.1111/j.1745-3933.2008.00441.x. arXiv: 0801.0593 [astro-ph].

Tavecchio, F., G. Ghisellini & D. Guetta (Sept. 2014). "Structured Jets in BL Lac Objects: Efficient PeV Neutrino Factories?" In: *The Astrophysical Journal Letters* 793.1, L18, p. L18. DOI: 10.1088/2041-8205/793/1/L18. arXiv: 1407.0907 [astro-ph.HE].

The MAGIC Collaboration et al. (Mar. 2022). "Studying the long-term spectral and temporal evolution of 1ES 1959+650". In: *37th International Cosmic Ray Conference*, 858, p. 858. DOI: 10.22323/1.395.0858.

Thompson, A. R., J. M. Moran & G. W. Swenson (2017). *Interferometry and synthesis in radio astronomy*. Springer Nature.

Tikhonov, A. N. & V. Y. Arsenin (1977). "Solutions of ill-posed problems". In: URL: https://api.semanticscholar.org/CorpusID:122072756.

Troja, E. et al. (Nov. 2017). "The X-ray counterpart to the gravitational-wave event GW170817". In: *Nature* 551.7678, pp. 71–74. DOI: 10.1038/nature24290. arXiv: 1710.05433 [astro-ph.HE].

Ulrich, M.-H., L. Maraschi & C. M. Urry (Jan. 1997). "Variability of Active Galactic Nuclei". In: *Annual Review of Astron and Astrophys* 35, pp. 445–502. DOI: 10.1146/annurev.astro.35.1.445.

Urry, C. M., P. Padovani & M. Stickel (Dec. 1991). "Fanaroff-Riley I Galaxies as the Parent Population of BL Lacertae Objects. III. Radio Constraints". In: *The Astrophysical Journal* 382, p. 501. DOI: 10.1086/170736.

Urry, C. M. & P. Padovani (Sept. 1995). "Unified Schemes for Radio-Loud Active Galactic Nuclei". In: *PASP* 107, p. 803. DOI: 10.1086/133630. arXiv: astro-ph/9506063 [astro-ph].

Valtonen, M. & P. Pihajoki (Sept. 2013). "A helical jet model for OJ287". In: *Astronomy and Astrophysics* 557, A28, A28. DOI: 10.1051/0004-6361/201321754. arXiv: 1307.1364 [astro-ph.HE].

Vaughan, S., R. Edelson, R. S. Warwick & P. Uttley (Nov. 2003). "On characterizing the variability properties of X-ray light curves from active galaxies". In: *Monthly Notices of the Royal Astronomical Society* 345.4, pp. 1271–1284. DOI: 10.1046/j.1365-2966.2003.07042.x. arXiv: astro-ph/0307420 [astro-ph].

Vedantham, H. K. et al. (Aug. 2017). "The Peculiar Light Curve of J1415+1320: A Case Study in Extreme Scattering Events". In: *The Astrophysical Journal* 845.2, 90, p. 90. DOI: 10.3847/1538-4357/aa7741. arXiv: 1702.05519 [astro-ph.GA].

Wagner, R. M. (2007). "Measurement of Very High Energy Gamma-Ray Emission from Four Blazars Using the MAGIC Telescope and a Comparative Blazar Study". In: *Publications of the Astronomical Society of the Pacific* 119.860, pp. 1201–1203.

Wani, K., H. Gaur & M. K. Patil (July 2023). "X-Ray Studies of Blazar 1ES 1959+650 Using Swift and XMM-Newton Satellite". In: *The Astrophysical Journal* 951.2, 94, p. 94. DOI: 10.3847/1538-4357/acd186. arXiv: 2305.03246 [astro-ph.HE].

Weaver, Z. R. et al. (May 2022). "Kinematics of Parsec-scale Jets of Gamma-Ray Blazars at 43 GHz during 10 yr of the VLBA-BU-BLAZAR Program". In: *Astrophysical Journal, Supplement* 260.1, 12, p. 12. DOI: 10.3847/1538-4365/ac589c. arXiv: 2202.12290 [astro-ph.HE].

White, G. L., D. L. Jauncey, A. Savage, A. E. Wright, M. J. Batty, B. A. Peterson & S. Gulkis (Apr. 1988). "Redshifts of Southern Radio Sources. VII." In: *The Astrophysical Journal* 327, p. 561. DOI: 10.1086/166216.

Wiklind, T. & F. Combes (Dec. 1997). "Molecular absorption lines at high redshift: PKS 1413+135 (z=0.247)". In: *Astronomy and Astrophysics* 328, pp. 48–68. DOI: 10.48550/arXiv.astro-ph/9708051. arXiv: astro-ph/9708051 [astro-ph].

Wilms, J., A. Allen & R. McCray (Oct. 2000). "On the Absorption of X-Rays in the Interstellar Medium". In: *The Astrophysical Journal* 542.2, pp. 914–924. DOI: 10.1086/317016. arXiv: astro-ph/0008425 [astro-ph].

Winter, W. & C. Lunardini (Jan. 2021). "A concordance scenario for the observed neutrino from a tidal disruption event". In: *Nature Astronomy* 5, pp. 472–477. DOI: 10.1038/s41550-021-01305-3. arXiv: 2005.06097 [astro-ph.HE].

Zandanel, F. & S. Ando (May 2014). "Constraints on diffuse gamma-ray emission from structure formation processes in the Coma cluster". In: *Monthly Notices of the Royal Astronomical Society* 440.1, pp. 663–671. DOI: 10.1093/mnras/stu324. arXiv: 1312.1493 [astro-ph.HE].

Zanin, R. et al. (Jan. 2013). "MARS, The MAGIC Analysis and Reconstruction Software". In: *International Cosmic Ray Conference*. Vol. 33. International Cosmic Ray Conference, p. 2937.

Zech, A. & M. Lemoine (Oct. 2021). "Electron-proton co-acceleration on relativistic shocks in extreme-TeV blazars". In: *Astronomy and Astrophysics* 654, A96, A96. DOI: 10.1051/0004-6361/202141062. arXiv: 2108.12271 [astro-ph.HE].

Zhang, B. T., K. Murase, F. Oikonomou & Z. Li (Sept. 2017). "High-energy cosmic ray nuclei from tidal disruption events: Origin, survival, and implications". In: *Phys. Rev. D* 96.6, 063007, p. 063007. DOI: 10.1103/PhysRevD.96.063007. arXiv: 1706.00391 [astro-ph.HE].

Zhang, Y. H. et al. (Dec. 1999). "Rapid X-Ray Variability of the BL Lacertae Object PKS 2155-304". In: *The Astrophysical Journal* 527.2, pp. 719–732. DOI: 10.1086/308116. arXiv: astro-ph/9907325 [astro-ph].

Zhirkov, K. et al. (Apr. 2022). "IceCube-220425A: MASTER: flaring blazar TXS 1742-078 as the possible neutrino source candidate". In: *GRB Coordinates Network* 31948, p. 1.